Synergic effect of metal and graphene oxide loading on metal titanates for enhanced photocatalytic activity

Thesis submitted for the award of degree of

Doctor of Philosophy

Submitted by:

Manjusha

(Reg. No. 901809017)

Under the Supervision of

Dr. Bonamali Pal
(Professor)

DEPARTMENT OF CHEMISTRY AND BIOCHEMISTRY
THAPAR INSTITUTE OF ENGINEERING AND TECHNOLOGY,
PATIALA-147004, INDIA

December, 2023

Certificate

This is to certify that thesis entitled **"Synergic effect of metal and graphene oxide loading on metal titanates for enhanced photocatalytic activity"** being submitted by Manjusha, in the fulfillment of the requirement for the award of the Degree of Philosophy to the Department of Chemistry and Biochemistry, Thapar Institute of Engineering and Technology, Patiala, is an authentic record of candidate's own work carried out by her under my supervision and guidance. The matter presented in this thesis has not been submitted in part or full for the award of any degree in any other university or institute.

(Supervisor)

Dr. Bonamali Pal

Professor

Department of Chemistry and Biochemistry

Thapar Institute of Engineering and Technology

Patiala, Punjab (India)

(Head)

Dr. Satnam Singh

Professor

Department of Chemistry and Biochemistry

Thapar Institute of Engineering and Technology

Patiala, Punjab (India)

Candidate's Declaration

I hereby declare that the work presented in the thesis entitled **"Synergic effect of metal and graphene oxide loading on metal titanates for enhanced photocatalytic activity"** in the fulfillment of the award of the Degree of Philosophy to the Department of Chemistry and Biochemistry, Thapar Institute of Engineering and Technology, Patiala, is an authentic record of my own work carried out under the supervision of Dr. Bonamali Pal (Professor & Former Head), Department of Chemistry and Biochemistry, Thapar Institute of Engineering and Technology, Patiala, India. The matter embodied in this thesis has not been submitted in part or full to any other university or institute for the award of any degree in India or abroad.

Manjusha

Dr. Bonamali Pal
Professor and Supervisor
Department of Chemistry and Biochemistry
Thapar Institute of Engineering and Technology
Patiala-147004

Dedicated

To

My Family

Acknowledgement

First and foremost, I wholeheartedly thank the Almighty God for giving me courage, patience, vision, and endurance to accomplish this research work.

The completion of this thesis would not have been possible without the support and encouragement of several special people. Hence, I would like to take this opportunity to show my gratitude to those who have assisted me in a myriad of ways.

I want to express my heartfelt gratitude and unpayable indebtedness to my doctorate advisor, Dr. Bonamali Pal, Professor, for the privilege of working in his research group. His constant support, skillful guidance, proficient supervision and encouragement, allowed me to gain experience with various research issues, that helped this work to reach its destination.

I sincerely acknowledge Dr. Padamakumar Nair, Honourable Director, Dr. N. Tejo Prakash, Dean of Research and Development Centre (DRDC), and Dr. Bhupendrakumar Chudasama, Associate Dean RDC, T.I.E.T, Patiala, for providing all the necessary facilities that have been immensely helpful in carrying out this research.

My sincere appreciation to Dr. Satnam Singh, Professor and Head, Department of Chemistry and Biochemistry, Thapar Institute of Engineering and Technology, Patiala for his ever-helping attitude and encouragement.

I extend my deep sense of gratitude to my doctoral committee members Dr. Vikas Tyagi, Dr. Bhupesh Goyal, and Dr. Bhupendrakumar Chudasama who were involved in the validation survey for this research project. Their valuable suggestions and scientific discussions help me represent my research work in a better way.

The kind help extended by all the faculty members of DCB, TIET, Patiala, is gratefully acknowledged. Greatly appreciative of all the authorities, technical and office staff in the DCB, especially Mr. Mayank Sharma for their cooperation, and support during the tenure of my work.

The help from different institutes and laboratories like SAI, Lab TIET, Patiala, SAIF Lab, Panjab University Chandigarh, CeNS, Bengaluru Sprint Testing Solutions Mumbai, etc. is highly acknowledged.

I express my warm thanks to my lab seniors, Dr. Samriti Thakur and Dr. Aadil Bathla, for their knowledgeable help, and also grateful to my colleagues and labmates for their company during this period.

My Ph.D. journey was definitely an experience of a lifetime and indeed a huge learning process for me in every aspect, making me a much stronger person.

I can't put my thoughts or feelings in to words to show my heartfelt appreciation to my respected parents, Mr. Gulshan Passi and Mrs. Navita Passi. Their blessings, beliefs, and encouragement have shown me the path to pursue my goals in life. They have always provided the main impetus for commuting me into the person I am today. Regardless of whether I was around them or far from them during this research tenure, their pearls of enlightenment and counseling were always felt in furtherance of this research. I have learned discipline from my father and diligence from my mother. My father is truly my best friend and my supporter. My mother pushes me to be better every day.

I also want to thank my grandparents, Mr. Satpal Passi and Mrs. Raj Rani Passi for their relentless encouragement, prayer, care, pure love, and unmatched affection that made this work to reach this destination.

My dearest grandmother is in heaven, and she has left me with her memories while writing this thesis. Losing her left an indelible imprint on me as she was a constant source of encouragement throughout my education and career. I will miss her with all my teary eyes for the rest of my life. Even though I can't see her, I know she's by my side at all times.

The most special "thankyou" from the depths of my heart, is for my loving brother Mr. Girish Passi, for his unmatched affection, care, patience, and love. Thank you for every little thing you've done for me to fill my days with joy and happiness, especially during this challenging time.

I don't think I would ever be able to repay whatever my family, "the pillars of my strength," have done for me.

Besides this, I am eternally thankful to everyone who has been a part of my journey and knowingly and unknowingly helped me during the completion of this work.

Manjusha

Manjusha

Table of Contents

CHAPTER-1

Introduction and Literature review

CHAPTER-2

Fabrication and photocatalytic activity of Ag and Cu photodeposited CaTiO3 nanocatalysts for the degradation of Rhodamine B dye under UV light irradiation

CHAPTER-3

Preparation, characterization and photocatalytic activity of a novel Ag-$BaTiO_3$/GO ternary nanocomposite under LED-light irradiation

CHAPTER-4

Fe(III) and GO loaded $SrTiO_3$ nanocomposite for the LED-light -driven photocatalytic degradation of norfloxacin antibiotic

CHAPTER-5

Cu decorated $CaTiO_3$-GO hybrid composite for the improved photocatalytic degradation of cefixime and dehydrogenation of alcohol under LED light

List of Abbrevations

a.u.	Arbitary unit
BET	Brunauer Emmett Teller
BJH	Barrett-Joyner-Halenda
CB	Conduction band
VB	Valence band
DRS	Diffuse reflectance spectroscopy
SEM	Scanning electron microscopy
EDS	Energy dispersive X-ray spectroscopy
FESEM	Field emission scanning electron microscopy
TEM	Transmission electron microscopy
HRTEM	High resolution transmission electron microscopy
SAED	Selected area diffraction
XPS	X-ray photoelectron spectroscopy
XRD	X-ray diffraction spectroscopy
PL	Photoluminiscence
GC	Gas chromatography
LC-MS	Liquid chromatography-Mass spectroscopy
IPA	Isopropyl alcohol
TiO_2 (P25)	Commercially available TiO_2
JCPDS	Joint committee on powder diffraction standards
M	Metal
SC	Semiconductor
CTO	Calcium titanate
$BaTiO_3$	Barium titanate
$SrTiO_3$	Strontium titanate
mL	Milli-litre

mM	Milli molar
nM	Nanometre
NPs	Nanoparticles
SPR	Surface plasmon resonance
UV	Ultraviolet
Vis	Visible
µl	Micro-liter
wt%	Weight percentage
mg	Milli gram
Ar	Argon
B.E.	Binding energy
LSPR	Localized surface plasmon resonance
IFCT	Interfacial charge transfer effect
DI	Distilled
E_{CB}	Conduction band edge position
E_{VB}	Valence band edge position
E_g	Band gap
eV	Electron volt
GO	Graphene oxide
ppm	Parts per million
TOC	Total organic carbon
λ_{max}	Wavelength of maximum absorption
RhB	Rhodamine B
CV	Crystal violet
CFX	Cefixime
OFL	Ofloxacin
NOF	Norfloxacin
H_2	Hydrogen
min	minute

List of symbols

e^-	Electron
h^+	Hole
$O_2^{\bullet-}$	Superoxide radical
•OH	Hydroxyl radical
Å	Angstrom
α	Absorption coefficient
A	Absorbance
°	Degree
λ	Wavelength
Ag	Silver
Cu	Copper
Fe	Iron
%	Percentage
μ	Micro
m	Meter
h	Hour
υ	Light frequency
θ	Theta
s	Second
V	Volt
Φ	Work function
g	Gram
mg	Milligram
E_f	Fermi energy
W	Watt
h	Planck constant
k	Pseudo first order rate constant min^{-1}

Abstracts

Chapter-1

This chapter provides a brief introduction to the basic principles of semiconductor photocatalysis and discusses the use of perovskite-structured metal titanates ($ATiO_3$, A= Ca, Ba, Sr) as SC photocatalysts for the degradation of hazardous water pollutants and the generation of hydrogen energy. Metal titanates advantages, limitations, and strategies for improving their photocatalytic activity have been outlined. The related literature has been systematically reviewed, and a brief description of characterization techniques for assessing the properties of synthesized $ATiO_3$ nanocomposites has been provided. The significance of using a synergic approach that incorporates metal and GO concurrently for $ATiO_3$ enhancement over its pristine and binary counterparts is presented. An overview of the photocatalytic activity evaluation tests performed on these titanates, including information concerning model pollutants and the H_2 reaction is provided. In this regard, the realized research gaps were mentioned with the objective of the current research work.

Chapter-2

This study aims to develop an efficient photocatalyst based on perovskite structured $CaTiO_3$ (CTO) for environmental concerns. Pure $CaTiO_3$ nanoparticles were first fabricated by simple sol-gel method followed by modification with Ag, Cu via photodeposition. Different amounts (1 to 5 wt%) of Ag and Cu were loaded over CTO to form Ag/Cu-CTO nanocomposites. Several characterization techniques such as XRD, UV-DRS, SEM, EDS, HRTEM and PL were employed to study their structural and physicochemical properties. TEM analysis reveals, successful deposition of nanosized Ag (6-12 nm) and Cu NPs (3-20 nm) on the surface of CTO nanostructures (40-150 nm). The UV-vis study discloses a decrease in band-gap energies after Ag and Cu surface modification The photocatalytic performance of as-prepared samples was assessed by degrading Rhodamine B dye under UV light irradiation. Results indicate that Ag/Cu deposition significantly enhanced the photocatalytic activity of CTO depending upon the amount of metal loading. 1wt% Ag-CTO composite exhibited the highest (98%) photoactivity within 90 mins in contrast to 82% and 57% degradation achieved by 1wt% Cu-CTO and bare CTO respectively. The degradation process followed pseudo-first-order kinetics with rate constants of $k = 4.5 \times 10^{-2}$ min^{-1} for Ag-CTO

relative to k = 1.8 x 10^{-2} min^{-1} of Cu-CTO and k = 0.86 x 10^{-2} min^{-1} of bare. The amazingly improved photocatalytic performance was credited to the increased optical absorption, and quick transfer of photoinduced electrons from $CaTiO_3$ conduction band to Ag and Cu deposits that probably retards the charge-carriers recombination as evident by their observed photoluminance behavior. Further, the degradation pathway and removal mechanism of RhB by this Ag/Cu-CTO system are also elaborated. Considering the ease of the preparation process, this study provides an efficient way for boosting $CaTiO_3$ performance and demonstrates the immense potential of these synthesized Ag/Cu-CTO nanocatalysts in photocatalytic wastewater treatment applications.

Chapter-3

This chapter deals with the fabrication of a visible-light responsive, photocatalyst (Ag-$BaTiO_3$/GO*)* where Ag nanoparticles and GO sheets were deposited onto the surface of $BaTiO_3$ nanorods via a combination of photodeposition and hydrothermal methods. The as-prepared ternary photocatalyst was comprehensively characterized for its structural, morphological, and optical properties using XRD, XPS, Raman, HR-TEM, FE-SEM, EDS-mapping, BET, EIS, UV-vis DRS, and PL analysis. The photoactivity was assessed by degrading crystal violet dye (CV) and antibiotic ofloxacin (OFL) under visible light illumination. In comparison with pristine $BaTiO_3$, and binary composites Ag-$BaTiO_3$, $BaTiO_3$-GO, the newly designed ternary hybrid exhibited superior activity with ~98.5% and 96.1% degradation efficiency for CV and OFL at high-rate constants (0.053 and 0.033 min^{-1}, respectively). The heightened photocatalytic performance is attributed to the SPR effect of Ag, which broadens the visible light range, as well as strong adsorption capacity, excellent electron mobility, and greater surface area of GO that facilitates the charge transfer process. Moreover, the catalyst could be easily reused for four sequential cycles, maintaining up to 78.83% efficiency for CV removal. Trapping experiments disclosed the eloquent role played by the •OH and $O_2^{\bullet-}$ radicals in pollutant degradation. Also, the degradation pathways of CV and OFL were determined based on the LC-MS analysis. Even the TOC analysis reveals that Ag-$BaTiO_3$/GO is capable of effectively mineralizing both pollutants. Eventually, on account of the results, a photocatalytic reaction mechanism was presumed. This work offers a propitious strategy, for successful eradication of multiple perilous pollutants from wastewater using a combination of metal titanates, plasmonic Ag NPs, and GO based highly efficient ternary photocatalyst.

Chapter-4

The widespread production and use of pharmaceutical antibiotics is wreaking havoc on the environment. To address this issue, a semiconductor photocatalyst with high photocatalytic efficiency must be developed in order to eliminate antibiotics from wastewater. Herein, an effective and novel ternary photocatalyst (Fe(III)-$SrTiO_3$-GO) is synthesized by anchoring Fe(III) species and GO sheets over the surface of $SrTiO_3$ nanotubes. The GO nanosheets function as an electron-transfer mediator while the Fe(III) cocatalyst serves as an electron-reduction active site. The optimized (2Fe(III)-$SrTiO_3$-10GO) nanocomposite displayed superior photoactivity by degrading 92.3% of NOF within 120 min of LED light exposure in contrast with pristine $SrTiO_3$, (33.6%) and binary composites ($SrTiO_3$-10GO) (68.5%), (2Fe(III)-$SrTiO_3$) (79.2%). The meliorative performance is credited to synergic effects of GO (with high conductivity), $SrTiO_3$ (specialized morphology) and Fe(III) species (IFCT effect) all together in the trio-hybrid that accelerated the transference and separation of photoinduced carriers, and extends the visible-light responsive range. The scavenging experiments confirmed (h^+), (•OH) as the predominant reactive species liable for the degradation process. Approximately 60% of NOF was mineralized at the end of the photodegradation process, according to TOC analyses. The catalyst's reusable feature was validated by post-photocatalytic characterization studies (9.6% reduction in efficacy after 4 cycles). Further, the plausible photocatalytic mechanism and degradation pathways of NOF were speculated with several intermediates identified. The current study provides a new perspective on construction of innovative, reusable and cost-effective photocatalyst based on transition metal ion and GO co-catalyzed metal titanates for wastewater remediation.

Chapter-5

To combat the issues of energy scarcity and environmental pollution, a new visible-light responsive, ternary photocatalyst (Cu-$CaTiO_3$-GO*)* has been fabricated in this work, by photo-depositing Cu nanoparticles over a $CaTiO_3$-GO binary nanocomposite. The physicochemical characteristics of Cu-$CaTiO_3$-GO were thoroughly investigated using XRD, HR-TEM, FE-SEM, EDS-mapping XPS, Raman, FT-IR, BET, EIS, UV-vis DRS, and PL techniques. In comparison with pristine $CaTiO_3$, and binary composites (Cu-$CaTiO_3$, $CaTiO_3$-GO), the ternary hybrid exhibited superior photocatalytic activity for H_2 generation as well as antibiotic cefixime (CFX) degradation. Under LED light exposure, the rate of H_2 generation over Cu-$CaTiO_3$-GO

accumulated to 57.6 $mmolh^{-1}$ in 6 hours, while the photodegradation efficiency of CFX reached 94.1% in 100 minutes. The upgraded performance is credited to the synergistic effects of Cu NPs (SPR effect), $CaTiO_3$ (specialized cuboid-like morphology), and GO (high conductivity), co-existing in the trio-hybrid, which resulted in a greatly increased surface area, an expanded spectral response range, a stronger adsorption property, and efficient charge migration and separation extent. Ternary catalyst performed well even in the recycling tests (retaining 79.4% CFX removal efficiency even after 4 sequential cycles). Scavenging experiments revealed reactive ($O_2^{\bullet-}$) and (•OH) as the primary drivers for CFX degradation. Besides, degradation intermediates of CFX were elucidated using LC-MS, and the decomposition pathway was suggested. Finally, the probable photocatalytic reaction mechanism was deduced for both the degradation and H_2 generation processes. The current study proposes a non-noble transition metal-based perovskite-type photocatalytic material for both clean energy generation and wastewater treatment.

CHAPTER-1

Introduction and literature review

Section-A

1.1 Introduction

Nowadays, due to the dramatic increase in global population, industrialization, and natural resource consumption, the world is grappling with two major issues: environmental protection and remediation, as well as energy control, storage, and alternative conversion. As a result, it is necessary to find the efficient way to combat energy scarcity and environmental pollution problem. "Semiconductor-based photocatalysis" has been regarded as one of the viable solutions for a clean and sustainable future due to its cleanliness, inexhaustibility, efficiency, and low-cost[1]. It basically involves speeding up the chemical process by use of a light-activated SC catalyst.

Basic principle of the SC mediated Photocatalytic Process

Generally, there are five essential key steps in the heterogenous photocatalysis on the surface of SC, namely, the (i) photoexcitation (absorption of light photons and charge carriers' generation), (ii) transportation of electrons and holes to the surface of the photocatalyst, (iii) adsorption of the reactants on the surface and (iv) redox reaction (v) formation of final products and desorption of products

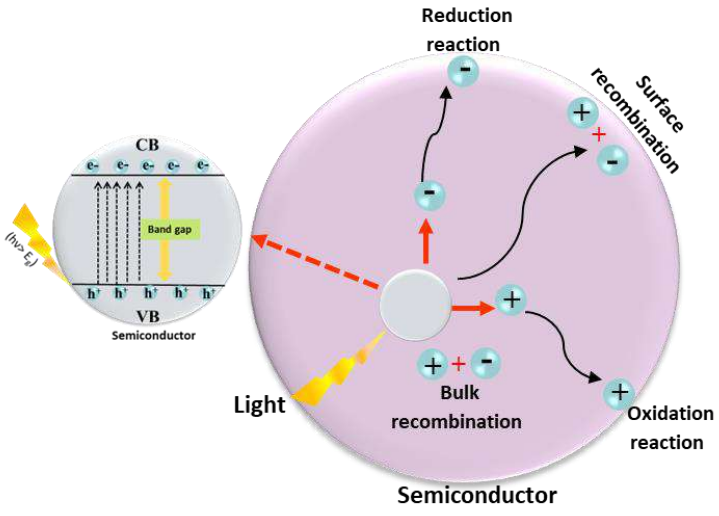

Scheme1.1: General mechanism of a typical photocatalytic reaction occurring on SC surface.

The most significant photocatalyst materials, semiconductors, have a distinct band gap between their valence band (VB) (with full electron) and conduction band (CB) (with higher energy and no electron). When a light of sufficient energy equivalent or greater than the bandgap of a SC ($E_{hv} \geq E_g$), strikes its surface, excitation happens and e^- from the VB of a SC transfers to its CB thereby leaving holes (h^+) at its VB. Photogenerated electrons and holes (charge carriers) often recombine on the surface or bulk of a SC, w.r.t to acceptor or donor centers. This process is accompanied by he release of energy in the form of heat or photons. In addition, the charge carriers may move to SC surfaces. The migrated photoproduced e^--h^+ pair subsequently starts the redox reaction at the SC's surface. This redox process (oxidation-reduction reactions) can be used to degrade water contaminants and transform abundant earth elements (H_2O, CO_2, and N_2) into useful fuel (clean H_2, or organic fuel like CH_4, CH_3OH, and NH_3)[2].

$SC + h\nu \rightarrow h^+(VB) + e^- (CB)$

1.1.1 Photocatalytic applications

(i) Photocatalytic degradation of toxic pollutants (Wastewater treatment)

Recent years have seen water contamination becoming a major issue. A wide range of harmful contaminants, including industrial dyes, pesticides, fertilizers, personal care products, disinfectants, pharmaceuticals drugs, and inorganic pollutants, i.e heavy metals are daily being discharged into the water bodies without any treatment. Long-term persistence of these carcinogenic contaminates in water bodies is threatening both human and aquatic life.

The textile and tanning industries massive outputs of colored effluent are a major source of water pollution. Cationic and anionic synthetic dyes used in textiles, such as rhodamine B (RhB), and crystal violet (CV)) eosin Y (EY), phenol red (PR), and Congo red (CR)) are actually toxic pollutants that could hinder the photosynthesis in aquatic plants and may harm the living creature health through food and drinking water supply.

Likewise, Pharmaceutical pollutants such as antibiotics, analgesics, and disinfectants have been detected in surface water at amounts ranging from ng/L to g/L. About 70–90% of antibiotics are excreted either chemically unaltered or as active metabolites from the human or animal body. The low metabolic rate, excessive consumption and exploitation, and inadequate absorption of these substances leave environmental resources vulnerable to pollution. Reports reveals that these are not entirely removed at sewage treatment plants[3]. Given the serious consequences of water pollution caused by dye and pharmaceutical

contaminants, researchers have attempted several attempts to eliminate these hazardous pollutants from wastewater. [4] However, among the various wastewater treatment methods, SC-based photocatalytic chemical degradation is seen as an effective strategy to tackle this pressing issue. This advanced oxidation process offers several advantages such as minimum operational costs, reusability, contaminant removal from different media, capability to use solar energy, and complete mineralizes the organic pollutants to CO_2, H_2O and mineral acids. It uses reactive oxygen species (ROS) such hydroxyl (•OH) and superoxide (O_2^-•) radicals to degrade organic pollutants and eliminate persistent chemicals. The oxidation potentials of most contaminants range between -1 to 2 eV. Thus, a reactor with ROS have potential to oxidize or reduce an organic component into CO_2, H_2O, and mineral acids. Degrading harmful pollutants by semiconductor photocatalysis is thus a safe and sustainable process.

For pollutant degradation,

After transferring photogenerated charge carriers to the SC photocatalyst surface, excited electrons in the CB react with electron acceptors such O_2 on the SC surface or in water, resulting in $•O_2^-$ species. Hole scavenging produces •OH radicals from H_2O and OH^- molecules. Both of these reactive species are capable of mineralizing any adsorbed organic molecules. Thus, finally, after interaction with the photocatalyst surface, highly reactive oxygen species (h^+, $^•OH$, $^•O_2^-$, H_2O_2, $^•OOH$) decomposes the pollutant molecules forming water, carbon dioxide and other harmless products. **(Scheme-1.2(a))**

The following equations show the sequence of oxidative and reductive reactions that occur during pollutant photodegradation:

Photons (hv) + semiconductor→ h^+(VB) + e^-(CB)

$h^+ + H_2O \rightarrow H^+ + OH^-$

$h^+ + OH^- \rightarrow OH•$

$e^- + O_2 \rightarrow {}^•O_2^-$

$2e^- + O_2 + H_2O \rightarrow H_2O_2$

$e^- + H_2O_2 \rightarrow 2{}^•OH$

$^•O_2^- + H^+ \rightarrow {}^•OOH$

Pollutant molecules (h^+,$^•OH$, $^•O_2^-$, H_2O_2, $^•OOH$) → CO_2 + H_2O + other harmless products

(ii) Photocatalytic hydrogen production reaction

Hydrogen gas (H_2), being a clean energy source with high energy density and no carbon emissions, is one of the most promising energy carriers for replacing traditional fossil fuels and addressing energy scarcity.

Several Countries like Britain and China are adopting H_2 as a transportation fuel to minimize the greenhouse gas emissions in urban cities. Generating H_2 directly from water using photocatalyst has garnered interest as an economically viable, adaptable, and renewable way to address global energy demands by converting unlimited solar energy to H_2. After Fujishima and Honda reported photocatalytic hydrogen synthesis from water using semiconductor (TiO_2) in 1972, various researchers got interested in searching semiconductor materials for H_2 evolution reactions [5].

Process of H_2 generation

For H_2 production through photocatalytic water splitting, after the separation process of photoinduced e^- and h^+ in a semiconductor, H_2O molecules on the SC surface are reduced by these e^- to form H_2 and also oxidized by h^+ to give O_2.

The oxidation and reduction reactions are described below:

Oxidation: $H_2O + 2\ h^+ \rightarrow ½\ O_2 + 2\ H^+ + 2\ e^-$

Reduction: $2H^+ + 2\ e^- \rightarrow H_2$

To facilitate the water splitting reaction, SC photocatalyst should have CB edge potential more negative than H^+/H_2 (0 V vs. NHE, pH = 0) redox potential and VB edge position more positive than the O_2/H_2O (+1.23 V vs. NHE, pH = 0) redox potentials **Scheme-2(b)** [6].

However, Still, it's challenging to set up large-scale H_2 production facilities based on water splitting to meet the world's H_2 need. From a thermodynamics view, water splitting is an uphill and nonspontaneous reaction because of the higher positive Gibbs free energy of (+ 237 KJ/mole).

$2\ H_2O\ (l) \rightarrow O_2\ (g) + 2\ H_2\ (g)$ ($\Delta G° = +237.14$ kJ/mol) However, the presence of alcohols such as methanol, ethanol, propanol in the reaction medium reduces the energy required for H_2 generation. Methanol, the simplest alcohol with one hydroxyl group and one carbon atom, is the model molecule for photocatalytic H_2 generation.

$CH_3OH \leftrightarrow HCHO + H_2$ $\Delta G° = 64.1$ kJ/mol

$HCHO + H_2O \leftrightarrow HCOOH + H_2$ $\Delta G° = 47.8$ kJ/mol

$HCOOH \leftrightarrow CO + H_2$ $\Delta G° = -95.8$ kJ / mol

Overall reaction

$CH_3OH + H_2O \leftrightarrow CO + 3H_2$ $\Delta G° = 16.1$ kJ / mol

This reaction demonstrates that decomposing methanol is far more practical than water [7]. Thus,

photodehydrogenation of alcohols to assist H_2 is appealing as a liquid, alcohols can be easily stored and transported. Besides, these can be easily produced from several biomass-derived feedstocks and organic residues such as sewage sludge. Compared with water splitting, its H_2 production reaction is thermodynamically advantageous which less decreases the energy input requirement. Even the lower band gap SC can also generate H_2 through the alcohol's dehydrogenation.

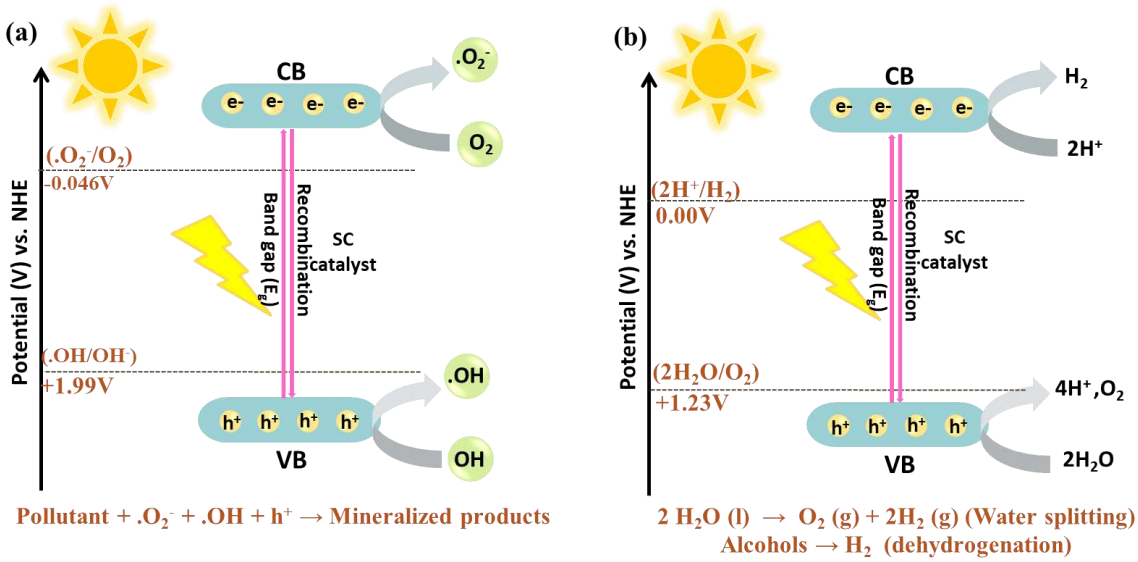

Scheme-1.2: (a) Photocatalytic mechanism of pollutant degradation and (b) H_2 production

1.1.2 Preferred semiconductor photocatalyst

A suitable photocatalyst should have a bandgap of ≥1.2 eV for energetic electrons and ≤3.0 eV for solar spectrum absorption, accessible photogenerated charge carriers, and photocorrosion resistance. Other benefits include low cost, easy preparation, and bandgap tuning.

Among a wide range of semiconductors, Perovskite based materials have been intensively studied due to their outstanding performance as a photocatalyst in UV irradiation and affordability. The German scientist Gustave Rose made the initial discovery of 'perovskite materials' in the Ural Mountains in 1839. And it was given this name in honor of the Russian mineralogist Lev Alekseyevich von Perovski. Among these, $ATiO_3$ perovskite-type oxides known as metal titanates are much popular[8].

1.1.3. Metal titanates as Photocatalyst

Metal titanates (general formula is $ATiO_3$) refer to inorganic compounds containing titanium, oxygen, and

at least one additional metallic element. Owing to their unique structural, optical, physicochemical, magnetic, and electrical properties, these ternary oxides have revolutionized various sectors of applications, including energy storage and conversion, environmental remediation, catalysis, chemical sensing, and electronic devices. Most ternary titanates possess a special perovskite crystal structure of type (ABX_3), where the larger ion 'A' is a member of the alkali/alkaline earth or rare-earth family. The 'B' ion with a smaller radius represents the d-block transition elements, and 'X' is the oxygen atom that binds to both cations. $ATiO_3$ perovskite oxide, in its ideal cubic structure, has an "A" atom are at the body corners, "Ti" at the body centre, and oxygen at the face-centered positions (**Fig.1.1**). Octahedral coordination of cation 'B' (6-fold) and dodecahedral coordination of cation 'A' (12-fold) are responsible for the stability of perovskites [9].

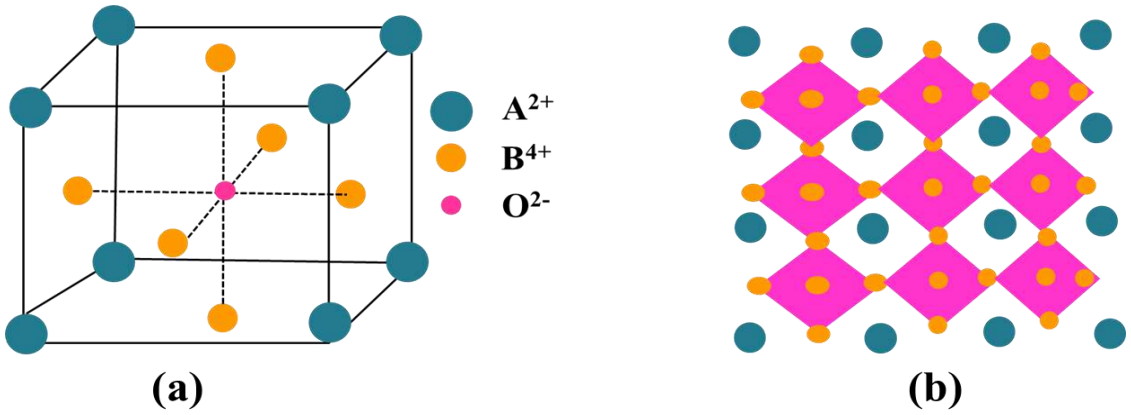

Fig.1.1: (a) Ideal cubic structure perovskite of (ABO_3) (b) the perovskite framework

Alkaline earth titanates such as calcium titanate ($CaTiO_3$), barium titanate ($BaTiO_3$), and strontium titanate ($SrTiO_3$), have been intensively explored for their potential applications in both environmental remediation and energy conversion.[10] Because of their intriguing properties, such as multifunctionality, efficient photoactivity, superconductivity, ferroelectricity, high stability, low cost, easy synthesis, high dielectric constant, piezoelectricity, modest dielectric loss, and eco-friendliness, these materials have been a game changer in many different fields of study[11–14]. The cubic structure of these titanates is depicted in **Fig1.2**, where the (Ca, Ba, Sr) ions are situated at the "A" site, the Ti ions are positioned at the "B" site, and the O ion represents the oxygen anion.

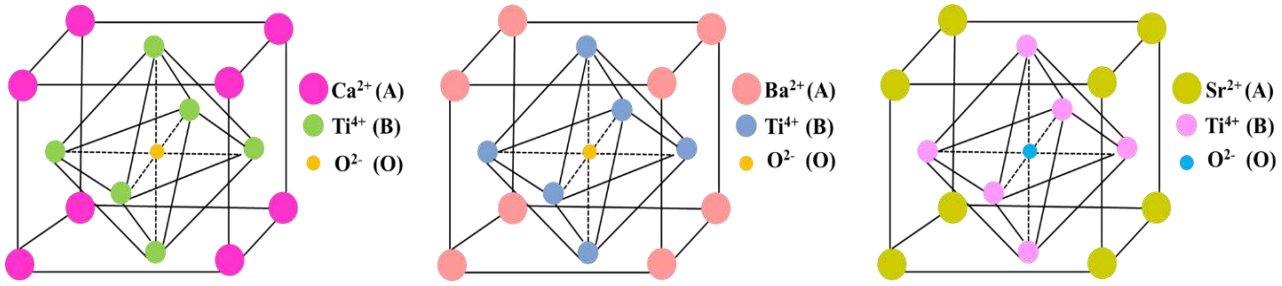

Fig.1.2: Ideal cubic crystal structures of (a) $CaTiO_3$, (b) $BaTiO_3$, and (c) $SrTiO_3$

S.No	Photocatalyst	Application	Light Source	Result	References
1.	$CaTiO_3$	Arsenic degradation	UV (254 nm)	98.4% removal	[15]
2.	$CaTiO_3$	Methyl orange dye degradation (1ppm)	UV (254 nm)	96% removal in 3h	[16]
3.	$BaTiO_3$	Pendimethalin (Herbicide) degradation (10 ppm)	UV (350-400 nm)	100% removal in 6.25h	[17]
4.	$BaTiO_3$ (E_g -2.93 eV)	Crystal violet dye degradation (10 ppm)	UV (365 nm)	100% removal in 48h	[18]
5.	$SrTiO_3$ (E_g -3.21 eV)	Methyl orange degradation (10 ppm)	365 nm	> 95% in 180 min	[19]
6.	$SrTiO_3$ (E_g -2.59 eV)	H_2 production reaction	Hg lamp (500 W)	3200.00 (mmol/h)	[20]

Table 1.1. Summary of the photocatalytic performances of pure ($MTiO_3$, M=Ca, Ba, Sr) nanocatalysts

In addition to being resistant to photocorrosion, their stable crystalline structure, high activity sites, compositional versatility, easily tunable band gap, and structural morphology, make them effective photocatalysts.

Moreover, their band potentials are suitably aligned, with a more negative conduction band (CB) potential allowing the photo-induced electrons to display greater reduction ability and a more positive valence band (VB) potential allowing the holes to display higher oxidation tendency. The CB potential is even much higher than the benchmark TiO_2 photocatalyst, this is beneficial for various reactions including H_2 generation and photoreduction reactions.

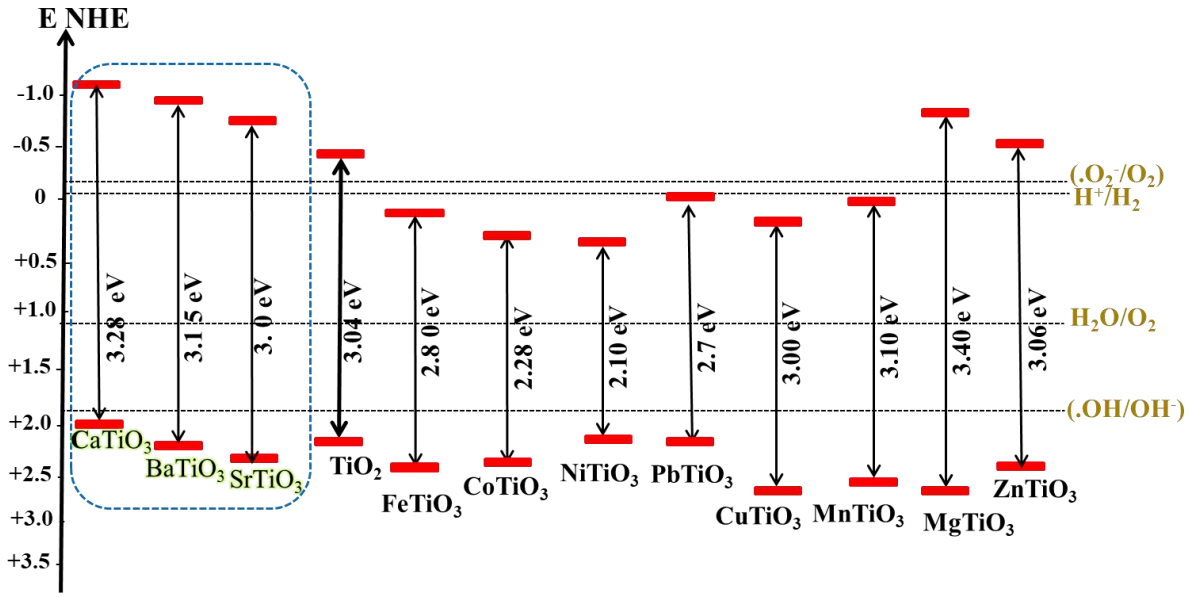

Scheme-1.3: Representation of band gaps and band edges potentials of several titanates w.r.t redox potentials for photocatalytic degradation and H_2 production reactions

1.1.4 Limitations of $ATiO_3$ photocatalyst

Despite the great potential of these benchmark metal titanates ($CaTiO_3$, $BaTiO_3$, $SrTiO_3$) for photocatalytic applications, their efficiency is still confined by the smaller specific surface areas, quick recombination of photogenerated charge carriers and limited solar or visible light utilization efficiency owing to their wide band gaps. **Table 1.1.**indicates that these despite the remarkable photo efficiency, these titanates are photocatalytically active only under UV light (which comprises only 3% of solar spectrum) These drawbacks severely restrict the large-scale use of these materials[11].With regard to the improvement in light-absorption features and the charge carrier's lifetime, enormous efforts have been channeled towards metal titanate modification.

1.1.5 Strategies for the improvement of photocatalysis:

Several strategies such as metals deposition, coupling with carbonaceous material, and modifications of

transition metals etc. have been addressed to tune their photocatalytic properties discussed below:

(i) Plasmonic metal deposition

Depositing plasmonic metal NPs like Ag, Au, Cu, Pt with semiconductor to develop M-SC hybrid nanostructures surface seems to be a viable technique for tuning the physicochemical-optical properties of the SC's. According to studies, deposited metal plays a number of critical roles, like: (i) serves as electron sinks by capturing the photoinduced electrons from the SC, this restricts the recombination of charge species; (ii) facilitates dioxygen reduction to generate reactive free radicals; (iii) enhances the visible light response of SC through induced SPR absorbance feature; (iv) modifies the surface properties of the SC [21].

Metal-semiconductor integration promotes photo reactivity by a synergistic effect of two features, namely (i) Plasmonic effect and (ii) Schottky barrier formation at the M-SC contacts

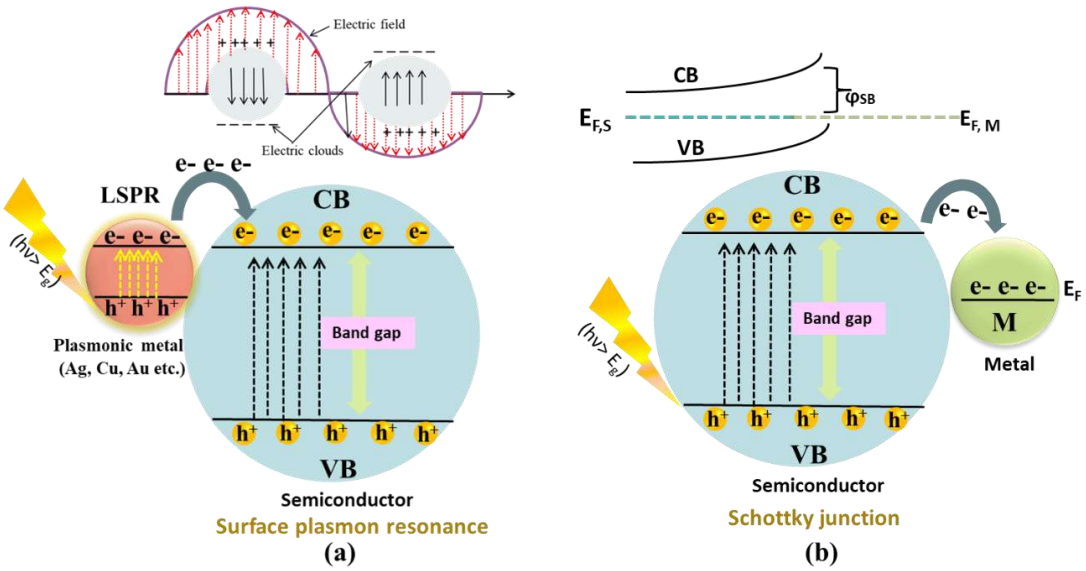

Scheme-1.4: Schematic illustration of charge transfer mechanism in M-SC junction with (a) LSPR effect of metal (M) nanoparticles (b) formation of Schottky barrier

(a) Enhanced Charge Separation through Schottky barrier formation

The effective separation of the charge carriers in M-SC composite results from electron transport across the M-SC interface. When a semiconductor (SC) is in close proximity to a metal (with a higher work function), electrons diffusion from the SC to the metal will take place. This process will continue until the fermi energy levels of both the components reach an equilibrium. As a result of this electron diffusion, a space charge region develops. Additionally, the band edges (CB) in the SC bends upward. Due to the deformation of the band structure at the M–SC interface, a small barrier known as the "Schottky barrier" is created which serves

as an electron trap. The trapped electrons then proceed to the adsorbed species surface to carry out the reduction reactions. The efficiency of electron transfer across the M-SC interface improves as the Schottky barrier rises in height [22]. Here, the Schottky barrier, prevents the return of the migrating electrons to the SC, thus inhibiting the reunion of e^--h^+ couples. This upgrades the photocatalytic reaction rate by allowing the active charge carriers on the surface of (SC) and metal to engage in redox reactions independently of one another [23].

(b) Enhanced Visible Light Absorption through Surface plasmon mechanism

In addition to the Schottky barrier, deposition of nano sized plasmonic metals on the SC can boost the light absorption via localized surface plasmonic resonance (LSPR). LSPR occurs when the valence electrons of plasmonic metal nanoparticles collectively oscillate in response to the electric field of incident light, resulting in effective light absorption and dramatically elevated local electric fields near the M-SC interface. In surface plasmon resonances (SPRs), deposited metal NPs typically function as antennas, converting light to localized electrical fields that eventually decay into highly energetic hot electrons [24]. These LSPR generated hot electrons have the potential to increase the photocatalytic reaction rate by multiple times. Thus, in the photocatalytic process, plasmon could promote the redox reaction mainly through the following routes: enlarging light trapping ability, speeding up charge separation, producing the hot electrons, and plasmon-induced energy transfer [25].

Several binary M/$ATiO_3$ nanostructures have been successfully synthesized by photo-deposition and impregnation methods, including Ag/$CaTiO_3$[26], Cu-$BaTiO_3$,[27] Ag/$SrTiO_3$[28], Au/$BaTiO_3$[29]. All of these combinations have been proven to have upgraded photoactivity when compared to unmodified $ATiO_3$. NTB was efficiently photoconverted to aniline using Pt/$CaTiO_3$, and the process took only 40 minutes [30]. Likewise, piezoelectric Ag-$BaTiO_3$ catalysts degrade 83% RhB in 75min[31]. The Ag(0)/$CaTiO_3$ photocatalyst outperformed pure $CaTiO_3$ in H_2 production because of the enhanced e^--h^+ separation and promoter effect of the Ag metal [32]. Similarly, under simulated UV irradiation, Au-loaded $CaTiO_3$ composite [33] degraded 99.6% of RhB in 120 min, compared to 76.4% for pure $CaTiO_3$. Three factors contributed to Au@$CaTiO_3$'s outstanding performance. (i) Au NPs, operating as electron sinks, resulting in improve charge segregation; (ii) LSPR effect of Au NPs leading to extension in light harvesting ability; (iii) Involvement of Au NPs LSPR-induced electrons in photodegradation processes. Thus, deposition of Au NPs on $CaTiO_3$ significantly upgraded the photocatalytic activity.

(ii) Surface modification with transition metal ions:

Surface grafting of transition metal ions, particularly Ce(III), Cu(II), Cr(III), or Fe(III), is another competent and economic approach to promote the photocatalytic efficacy of wide-band gap semiconductors through a well-known IFCT process.

In this photocatalytic system **(Scheme-1.5)**, when transition metal ions are grafted or loaded onto the surface of SC to create the interface contact, the photoinduced electrons on the SC's VB have a tendency to directly migrate to these ionic species, leaving behind holes in the VB. Owing to the strong electron capturing ability of these grafted species, effective separation between the electrons and holes is achieved. This process allows the separated excitons to engage in catalytic reactions to form reactive species. The trapped electrons could efficiently reduce the O_2 via multi-electron reduction routes to form superoxide anion radicals, whereas the holes with strong oxidizing power accumulated in SC;s VB could either react with H_2O molecules forming .OH species or directly participate in the reaction.

In this IFCT charge transfer mechanism(M^{n+}-SC) system, the transition metal ions serve as efficient e- trapping centers to prevent the rejoining of charges and activate the molecular O_2, and also broadens the light absorption range, resulting in an improved photocatalysis response [34,35].

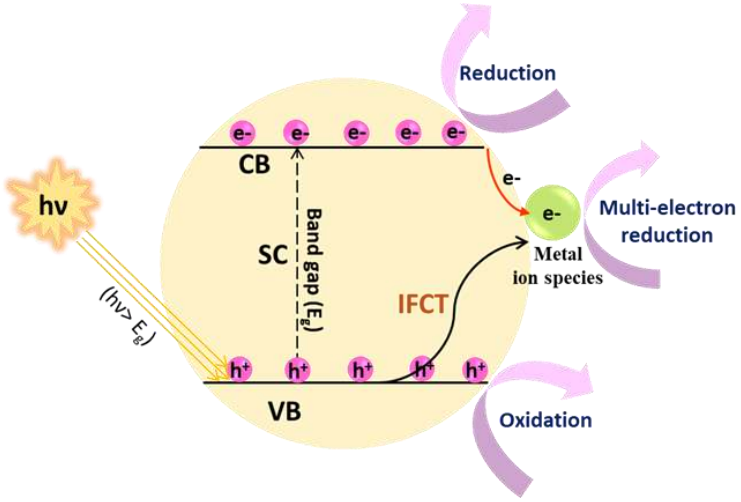

Scheme-1.5: Schematic representation of photocatalytic mechanism of Metal ion (M^{n+}) loaded semiconductor (SC)

According to Qiu et al.[36], grafting Fe(III) clusters onto the surface of flower-like BiOCl, could enhance BiOCl performance, due to IFCT interaction between the Fe(III) clusters and BiOCl. Hashimoto et al. [37] reported Cu(II) grafted TiO_2 photocatalysts for efficient decomposition of 2-propanol(g) to CO_2. Dai group[38] synthesized Fe(III) modified Bi_2O_4 photocatalyst that accelerated the degradation of RhB dye by

almost 2.7 times (0.098min^{-1}) compared to bare Bi_2O_4 nanorods (0.036 min^{-1}). Grafting Cu(II) nanoclusters onto TiO_2 increases the degradation rate of imidacloprid[39]. Likewise, the Alam group [34] found that the IFCT in the Fe(III)-modified MoO_3 system was extremely efficient in the visible light mediated degradation of numerous pollutants, such as MB, RhB, and 4-NP. In all these studies, the IFCT effect has been encountered to provide an efficient channel to simultaneously extend the optical response and minimize the charge transportation distance in the existing photocatalytic material.

(iii) Modification with Graphene oxide:

Recent years have seen a surge in interest in carbonaceous materials such graphitic carbon nitride, fullerenes, carbon nanotubes, graphene, and diamond as potential building blocks for developing highly stable and effective photocatalysts. Among these is graphene oxide (GO), a sparkling star in the arena of material science. GO is a $sp^2$and sp^3-hybridized carbon monolayer with oxygen functional groups on both the basal (hydroxyl and epoxy) and edge planes (carboxyl, carbonyl).

GO possesses some intriguing and peculiar properties **(Scheme-1.6.)** including a rich pore structure, huge surface area, outstanding mechanical strength, high flexibility and absorptivity, unique conjugated structure with (π–π) interactions, better charge carrier mobility, a high degree of thermal conductivity, raised optical transmittance, incredible elastic modulus, and chemical stability [40]. These fascinating features of GO make it an enticing material with several potential applications such as in catalysis, solar cells, energy conversion-storage, nano-electronics, drug-delivery, water splitting, batteries, sensors, and water treatment etc.

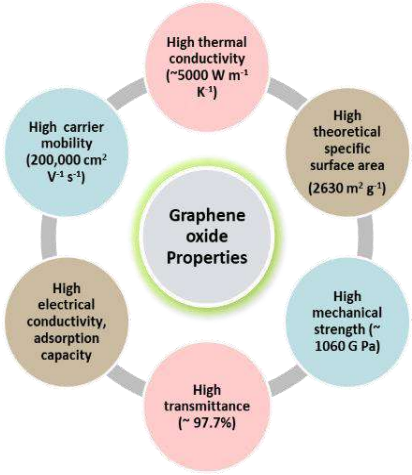

Scheme-1.6: Schematic depiction of properties of Graphene oxide

Especially, in the field of photocatalysis, GO has emerged as a prominent candidate and a frequently used ideal support material to integrate with wide band gap SC to accomplish spectacular photoactivity enhancement[41].

Mechanism of electron transference in SC-GO composites

When the GO-SC photocatalyst is excited by a light irradiation, photogenerated charge carriers are created in SC. From the CB of SC, the electrons could potentially migrate towards the GO aromatic structure. Here,

GO works as an electron trap, preventing the recombination of electrons with the VB holes. The electrons accumulated on the graphene surface react with the dissolved or adsorbed oxygen to form superoxide radicals. Meanwhile, the photogenerated holes in SC's VB react with water molecules to produce hydroxyl (·OH) radicals. These active species then facilitate the photocatalytic reactions. This promotion in the electron transference through numerous graphene oxide layers improves the overall efficiency of the attached SC [42].

When combined to semiconductors, GO exhibits diverse promoting effects. The enhancement in photocatalytic capabilities occurs because of the synergy between the two components: GO and SC, which generally results in:

(i) Extended light absorption range, resulting in band gap narrowing; (ii) enlarged surface area of the obtained catalyst due to the interaction with the 2-D structure of GO; (iii) Improved adsorption capacity for pollutants via strong π-π interactions among the pollutants and the aromatic network of GO; (iv) adequate charge separation and transfer ability of e^--h^+ couples, extended charge carrier lifespan due to the substantial electronic conductivity of GO that act as an electron sink for the photo-generated electrons accumulated on the SC surface; (v) Reduced Photocatalysts' self-oxidation, leading to improved stability and reusability; (vi)The emergence of more potent oxidizing species.[43,44] To date, many GO-based dual component SC photocatalysts have been reported. By using a two-step sol-gel deposition process, Durmus et al.[45] synthesized a binary GO/ZnO nanocomposite and showed that it is superior to pure ZnO at degrading basic fuchsin (BF) dye. When exposed to visible light, the GO-CdS composites developed by Gao et al. [46] were extremely effective at killing Gram-negative E. coli and Gram-positive B. subtilis and degrading AO7 dye. Unlike the segregated CuO NPs and GO, the hybrid (CuO-GO) have shown exceptional reduction performance in terms of yield and selectivity for the conversion of different nitroaromatics[47]. A 13- and 3.3-fold increase in H_2 production was observed for the hierarchical GO-TiO_2 composite compared to the TiO_2 microsphere and GO-P25, respectively (305.6 $mmolh^{-1}$). [48]

GO-modified metal titanates have also been reported. Ling et al [49], synthesized $SrTiO_3$-RGO composites and investigated that in comparison to $SrTiO_3$, $SrTiO_3$-RGO composites exhibited much higher photocatalytic H_2 generation activity due to the reduced charge carrier re[50]combination rate. Zhu Mengting et.al [51] reported $BaTiO_3$/GO composite with high degradation efficiency for MB degradation.

While binary photocatalysts are superior, the ternary photocatalysts formed by combining metal and GO have even greater activity. For instance, Labhane et al.[52] developed Mn-doped ZnO/graphene nanocomposite for visible-light MB degradation. The as-synthesized ternary nanocomposite outperformed

pure ZnO samples in photocatalysis due to improved light absorption and charges segregation, and their transference. Jin and colleagues synthesized a Cu-P25-graphene composite, that degraded MB faster than pure P25 and P25-graphene binary composite [50]. The activity of pure BiOBr catalyst was greatly enhanced via simultaneous addition of Ag and GO when comparing the developed (Ag/BiOBr/GO) catalyst to its counterparts BiOBr, Ag/BiOBr, and GO/BiOBr[53]. Yang et al. reported Ag-P25-GR (APG) nanocomposites with a wider light absorption range and better charge separation than binary P25 and PG. APG exhibited 7.6 times and 2.6 times higher H_2 evolution rates than pure P25 and PG respectively. The presence of graphene and Ag's SPR effect together boosted the photocatalytic activity.[54]

All of these studies point to a synergistic impact between graphene and metal, which boosts the photocatalytic activity of the combined material.

Similarly, in the case of Ca, Ba, and $SrTiO_3$, whereas dual-ingredient M-$ATiO_3$ and GO-$ATiO_3$ composites improved the photocatalytic performance of pure $ATiO_3$ nanostructures, multi-component nanomaterials are expected to provide substantially better photoactivity. The increase in the photocatalytic activity of the ternary GO/M-$ATiO_3$ nanocomposites can be expected from the synergic impact of GO, the loaded metal (M) and $ATiO_3$ nanostructures. Firstly, the metal nanoparticles deposited on $ATiO_3$ nanostructures can serve as electron trappers, limiting the reunion of e^--h^+ couples. Second, GO's enhanced surface area means it can absorb more of these harmful contaminants, which in turn makes photodegradation more effective. Thirdly, the deposited metals unique SPR effect, can enlarge the light absorption extent to higher wavelengths. Lastly, the high electron conductivity of GO favors charge transfer, which accelerates charge carrier separation.

Therefore, it is rational to create GO/M-$ATiO_3$ type ternary composites in order to reap the benefits of $ATiO_3$, metal nanoparticles (M), and GO all at once. This approach has the potential to produce a highly efficient GO/M-$ATiO_3$ photocatalyst that makes use of a wide spectrum of light and has robust interfacial charge transfer characteristics.

The proposed mechanism for the charge transference in GO/M-$ATiO_3$ nanocomposite is proposed and illustrated in **Scheme-1.7.**

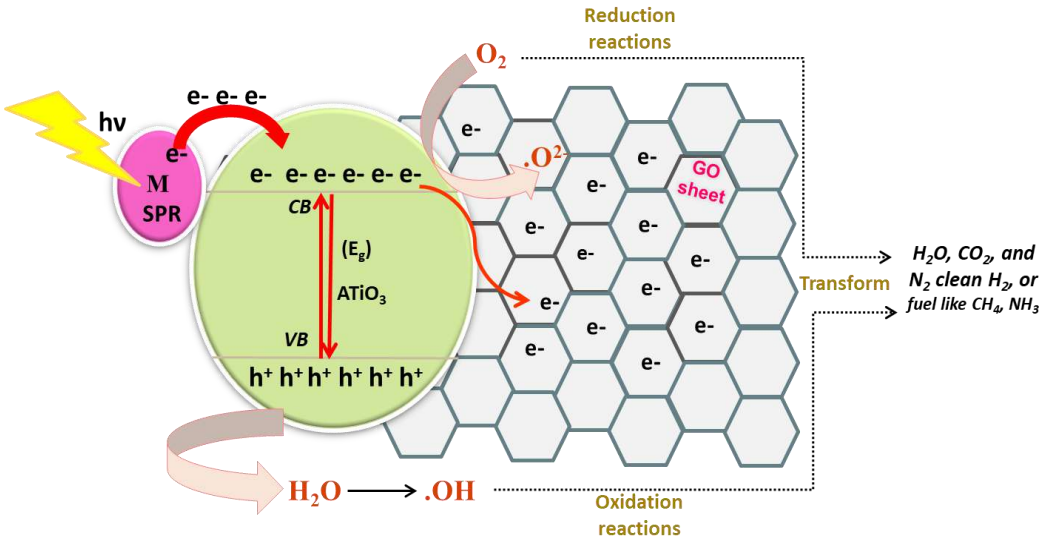

Scheme-1.7: Scheme description of possible route of charge transference in GO/M-$ATiO_3$

Section-B

1.2 Research Gaps

From the literature survey, we came across the fact that although photocatalytic activity over metal- $ATiO_3$ hybrids and graphene-$ATiO_3$ composites is well documented. However, there is still plenty of room to further increase the photocatalytic performance of metal titanates. Recent studies have evidenced that the combined effect of graphene oxide and metals on the SC photocatalyst can effectively improve the photocatalytic activity. Considering the advantages of these multicomponent composites, fabricating GO/M-$ATiO_3$ nanocomposites, with the benefits of good electron conductivity, the specific Schottky barrier of the metal, improved light-absorption characteristics, and a large specific surface area, will be highly beneficial for further enhancement of metal titanates. At present, only one research focuses on the fabrication of this kind of nanocomposite using metal titanates. But to the best of our knowledge, no study has been reported on the construction of such GO/M-$ATiO_3$ nanocomposite for improving the photocatalytic activity of metal titanates like $CaTiO_3$, $BaTiO_3$ and $SrTiO_3$. Besides this, it would also be valuable to investigate the comparative activity of bare $ATiO_3$, M-$ATiO_3$, and GO/M-$ATiO_3$ nanocomposites for various photocatalytic studies. Despite the fact that these metal titanates have been well considered for the degradation of many environmental pollutants like dyes and many other organic hazardous compounds. Yet significant work can be done to further upgrade their photocatalytic efficiency for various photodegradation reactions by synthesizing a ternary GO/M-$ATiO_3$ system with the benefits of both high surface area graphene oxide

providing more adsorption sites for pollutants and metals retarding charge carrier recombination as well as improving the light response. Moreover, numerous previous studies have proven that these metal titanates can effectively generate H_2 by direct water splitting. However, only limited reports are available on the use of metal titanates to produce H_2 via the dehydrogenation of alcohols.

Additionally, the synergistic effect of the two components, metallic nanoparticles and graphene oxide, can lead to increased H_2 generation rates in metal titanates, which needs to be investigated.

With the aforementioned considerations in mind, the following objectives are designed.

1.3 Objectives

1) Preparation and characterization of metal titanates ($ATiO_3$ where A-Ca, Ba, Sr) nanostructures.

2) To prepare metal (M=Ag, Cu, Ni, Fe)-loaded (M-$ATiO_3$) and graphene oxide-modified GO/M- $ATiO_3$ nanocomposites.

3) To study the photocatalytic degradation and dehydrogenation of waste alcohols by GO/M-$ATiO_3$ nanocomposites.

1.4 Characterization techniques

Several modified and self-planned synthetic protocols were followed for the fabrication of pristine ATiO3 (A = Ca, Ba, Sr), binary (M-$ATiO_3$, GO-$ATiO_3$) and ternary (GO/M-$ATiO_3$) nanocomposites. (Details are provided in the respective chapters). The synthesized nanocomposites were examined using a variety of structural, optical, surface and morphology determining characterization techniques as detailed below:

1.4.1. X-ray powder diffraction (XRD)

The crystal structure, phase composition, diffraction pattern and crystallinity, of the prepared samples were investigated using a PANalytical-Xpert-PRO diffractometer equipped with Cu-Kα target as radiation source (λ =1.54 Ao) operating at 45 kV with diffraction angle (2θ) ranging from 5°-90° at a scan rate of 5°/min.

1.4.2. X-ray photoelectron spectroscopy (XPS)

The surface chemistry, elemental composition and oxidation states were elucidated using an XPS analysis. The XPS data was recorded on (Thermo Fisher ESCALAB Xi+) spectrometer using a monochromatic Al K Alpha X-ray source (1486 eV) and the calibration of the binding energies was conducted using C1s peak at 284.6 eV as an internal standard.

1.4.3. UV-Vis spectroscopy

The optical absorption properties of powder solid samples were explored using an Avantes DRS instrument and a UV-vis spectrophotometer (JASCO, V-750), over a spectral range of 200-800 nm, with $BaSO_4$ as a reference standard.

1.4.4. Photoluminescence spectroscopy (PL)

The separation of photoinduced e--h+ pairs was examined by measuring the PL emission spectrum at room temperature. The analysis was carried out by dispersing samples in distilled water and recording data on a spectrofluorometer (Perkin-Elmer LS55) and a (SHIMADZU, RF-6000) excited at 320-380 nm wavelengths.

1.4.5. Surface area and Porosity characteristics

A Quanta chrome Nova-1000 surface analyzer was used to determine the surface area, pore volume and pore size distributions with BET and BJH methods, respectively. (Analysis gas: nitrogen; outgas and bath temperatures: 180ºC and 77.3 K, respectively; outgas time: 6 hours).

1.4.6. Morphological analysis

Electron microscopy techniques such as transmission electron microscopy (TEM), high-resolution TEM (HRTEM), and scanning electron microscopy (SEM) were used to examine morphological characteristics such as shape, size, and arrangement of the nanoparticles. The TEM analysis was carried out on both HR-TEM (JEOL, JEM 2100 PLUS) and (TALOS F200S G2) instruments at a 200 kV accelerating voltage. SEM and FE-SEM analysis were performed on JEOL JSM-7600F operated at 30 kV and Carl Zeiss SIGMA 500) respectively. Furthermore, elemental composition and colored dot mapping scans were determined using a Bruker energy-dispersive X-ray spectrometer (EDS) linked to the scanning module of the previously mentioned SEM microscopes.

1.4.7. Raman spectroscopy

Raman spectroscopic measurements were conducted on a Labram HR, a Horiba micro-Raman spectrometer with a 532 nm excitation laser.

1.4.8. Fourier transform infrared spectroscopy (FT-IR)

The functional groups were appraised using an IR Tracer-100, FT-IR spectrophotometer (SHIMADZU, Kyoto, Japan) with KBr pellets as a reference.

1.4.9. Conductivity study

Conductivity measurements were carried out at room temperature using electrochemical Impedance spectroscopy (EIS), with a Solartron analytical impedance analyzer (Model: SI 1260).

1.4.10. Gas-chromatography (GC)

The H_2 evolved during the dehydrogenation reaction was quantified by manually injecting 1 mL of the produced H_2 gas into a gas chromatography system (GC, Nucon Ltd, India) equipped with a thermal conductivity detector (TCD) and a molecular sieve column (5Å). The temperatures of the oven, injector, and detector were set to 40^{o}C, 40^{o}C, and 50^{o}C, respectively. The amount of H_2 produced was then determined by comparing it with standard 505 ppm H_2 + 503 ppm CO_2 balanced Argon Sigma gases from India).

Section-C

1.5 Photocatalytic activity

The photocatalytic efficiency of prepared $ATiO_3$-based nanostructures was assessed by studying the following two photocatalytic reactions:

1.5.1. Photocatalytic degradation of environmental pollutants (such as dyes and pharmaceutical drugs)

The photodegradation of several toxic pollutants (listed in **Table 1.2**) was carried out in a test tube with the required amount of catalyst suspended in 5 mL of aqueous pollutant solution. Prior to light illumination, the prepared suspension was magnetically stirred in darkness for a certain time period to ensure adsorption-desorption equilibrium between the catalyst and pollutant molecules. The test tubes were then exposed to different light sources with UV (125W Hg arc, 104 mW/cm^2) and visible light irradiations (50W LED lamp, Wipro Garnet B22, having an intensity of ~100W/m^2, λ > 360 nm). After regular intervals of time, the catalyst was withdrawn from the test tube by centrifugation to eliminate any residual solid catalyst particles, and the changes in the pollutant concentration were then analyzed by monitoring its absorbance spectra with a UV-visible spectrophotometer. (SHIMADZU, UV-2600). The degradation efficiency and reaction kinetics were also estimated. (Related equations are explained in the respective chapters.) Further, the mineralization capability of catalysts was assessed by executing the TOC analysis. A LC-MS technique (Waters, SYNAPT-XS HDMS MASS spectrometer, U.K.). was used to investigate the intermediates produced during the pollutant degradation. For different pollutants, mixtures of formic acid with water and acetonitrile served as the mobile phase.

1.5.2. Photocatalytic H_2 production via alcohol dehydrogenation

To carry out the dehydrogenation reactions for H_2 production, a desired amount of catalyst was added in a test tube containing 10 mL of an aqueous alcoholic solution (50 vol%). The test tube was purged with high

purity argon gas for 20 minutes before being sealed with a gas tight rubber septum to create an inert atmosphere. The reaction was then initiated by exposing the prepared test tube containing the reaction mixture to LED light irradiations (50W LED lamp, Wipro Garnet B22, intensity ~100W/m^2, $\lambda > 360$ nm) for a specified time period, while being continuously magnetically stirred. H_2 evolved from the aqueous solution was identified and monitored periodically using a GC instrument (Nucon, India, TCD, Ar carrier) with a 5 Å molecular sieve column **(Scheme-1.9)**. The GC chromatogram was then compared to a standard, with a 505 ppm H_2 concentration and 503 ppm CO_2 balanced Argon as obtained from Sigma Gases, India) to measure the amount of H_2 gas generated.

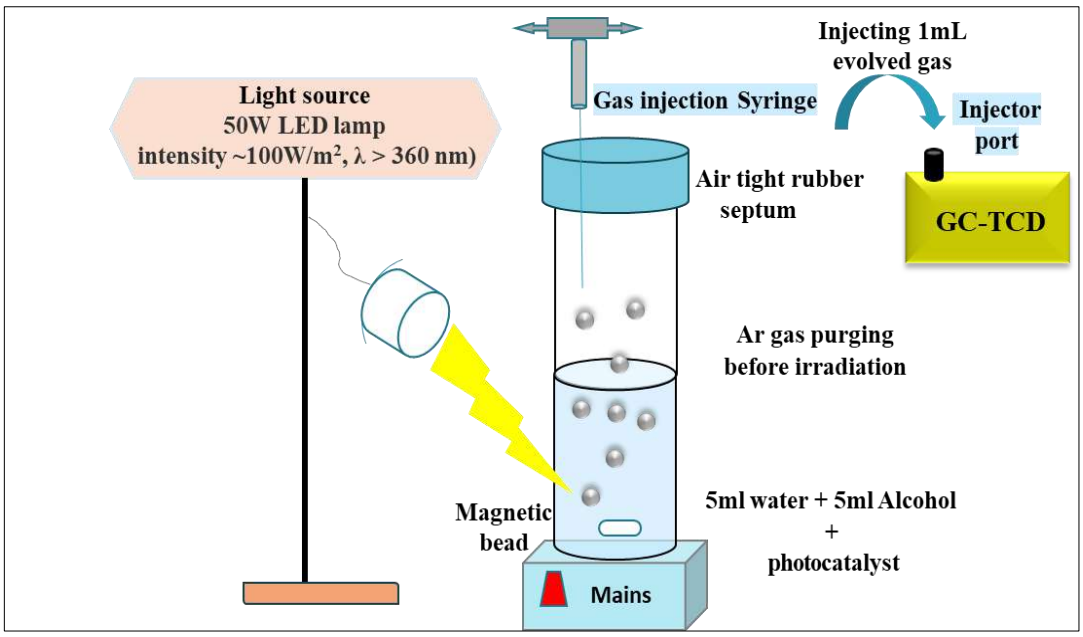

Scheme-1.9: Schematic depiction of the reaction set-up for photocatalytic H_2 generation reaction

Chemical name	Chemical formula	λ_{max}	Chemical structure
Rhodamine B	$C_{28}H_{31}ClN_2O_3$	554 nm	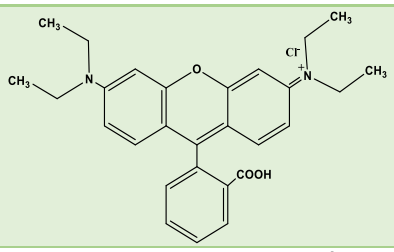
Ofloxacin	$C_{18}H_{20}FN_3O_4$	288 nm	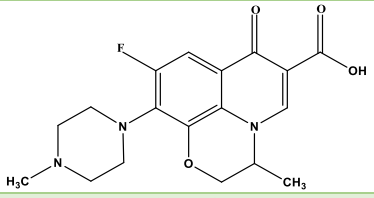
Crystal Violet	$C_{25}H_{30}N_3Cl$	589 nm	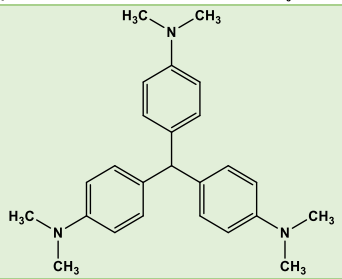
Norfloxacin	$C_{16}H_{18}FN_3O_3$	272 nm	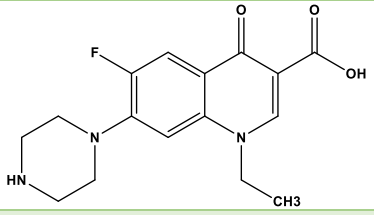
Cefixime	$C_{16}H_{15}N_5O_7S_2$	278 nm	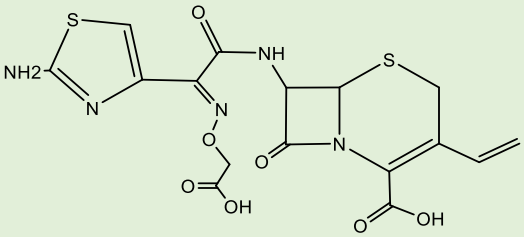

Table-1.2: Model pollutants tested for photodegradation using GO/M-ATiO_3 nanocomposites.

References

[1] X. Zhang, X. Yuan, L. Jiang, J. Zhang, H. Yu, H. Wang, G. Zeng, Chemical Engineering Journal 390 (2020).

[2] F. Zhang, X. Wang, H. Liu, C. Liu, Y. Wan, Y. Long, Z. Cai, Applied Sciences (Switzerland) 9 (2019).

[3] P. Kar, K. Shukla, P. Jain, G. Sathiyan, R.K. Gupta, Nano Materials Science 3 (2021) 25–46.

[4] A.D. Folawewo, M.D. Bala, Water (Switzerland) 14 (2022).

[5] S. Escobedo, H. de Lasa, Catalysts 11 (2021).

[6] R. Singh, S. Dutta, Fuel 220 (2018) 607–620.

[7] B. Gupta, A.A. Melvin, Renewable and Sustainable Energy Reviews 76 (2017) 1384–1392.

[8] E. Grabowska, Applied Catalysis B: Environmental 186 (2016) 97–126.

[9] R. Djellabi, M.F. Ordonez, F. Conte, E. Falletta, C.L. Bianchi, I. Rossetti, Journal of Hazardous Materials 421 (2022) 126792.

[10] Amika, R. Sharma, A. Sharma, A. Chandrani, J. Singh, D. Kumar, Journal of Physics: Conference Series 2267 (2022).

[11] R.R. Solís, J. Bedia, J.J. Rodríguez, C. Belver, R.R. Solís, J. Bedia, J.J. Rodríguez, C. Belver, Chemical Engineering Journal (2020) 128110.

[12] S.K. Ray, J. Cho, J. Hur, Journal of Environmental Management 290 (2021) 112679.

[13] B.L. Phoon, C.W. Lai, J.C. Juan, P.L. Show, W.H. Chen, International Journal of Energy Research 43 (2019) 5151–5174.

[14] M. Passi, B. Pal, Powder Technology 388 (2021) 274–304.

[15] R. Tamayo, R. Espinoza-González, F. Gracia, U.P. Rodrigues-Filho, M. Flores, E. Sacari, Nanomaterials 9 (2019).

[16] Y.S. Huo, H. Yang, T. Xian, J.L. Jiang, Z.Q. Wei, R.S. Li, W.J. Feng, Journal of Sol-Gel Science and Technology 71 (2014) 254–259.

[17] L.N. Gomathi Devi, G. Krishnamurthy, Journal of Environmental Science and Health - Part B Pesticides, Food Contaminants, and Agricultural Wastes 43 (2008) 553–561.

[18] W.W. Lee, W.H. Chung, W.S. Huang, W.C. Lin, W.Y. Lin, Y.R. Jiang, C.C. Chen, Journal of the Taiwan Institute of Chemical Engineers 44 (2013) 660–669.

[19] T. Puangpetch, T. Sreethawong, S. Yoshikawa, S. Chavadej, Journal of Molecular Catalysis A: Chemical 287 (2008) 70–79.

[20] Y. Liu, L. Xie, Y. Li, R. Yang, J. Qu, Y. Li, X. Li, Journal of Power Sources 183 (2008) 701–707.

[21] A. Kumar, P. Choudhary, A. Kumar, P.H.C. Camargo, V. Krishnan, Small (2021).

[22] M.R. Khan, T.W. Chuan, A. Yousuf, M.N.K. Chowdhury, C.K. Cheng, Catalysis Science and Technology 5 (2015) 2522–2531.

[23] Y.S. Fu, J. Li, J. Li, Nanomaterials 9 (2019).

[24] N. Zhang, C. Han, X. Fu, Y.J. Xu, Chem 4 (2018) 1832–1861.

[25] W. Hou, S.B. Cronin, Advanced Functional Materials 23 (2013) 1612–1619.

[26] S.W. Lee, L.M. Lozano-Sánchez, V. Rodríguez-González, Journal of Hazardous Materials 263 (2013) 20–27.

[27] A.S. Basaleh, R.M. Mohamed, Journal of Materials Research and Technology 9 (2020) 9550–9558.

[28] Q. Zhang, Y. Huang, L. Xu, J.J. Cao, W. Ho, S.C. Lee, ACS Applied Materials and Interfaces 8 (2016) 4165–4174.

[29] C. Chao, Y. Zhou, T. Han, Y. Yang, J. Wei, H. Li, W. He, Journal of Alloys and Compounds 825 (2020) 154060.

[30] A. Shawky, M. Alhaddad, K.S. Al-Namshah, R.M. Mohamed, N.S. Awwad, Journal of Molecular Liquids 304 (2020) 3–10.

[31] S. Xu, Z. Liu, M. Zhang, L. Guo, Journal of Alloys and Compounds 801 (2019) 483–488.

[32] A. Alzahrani, D. Barbash, A. Samokhvalov, Journal of Physical Chemistry C 120 (2016) 19970–19979.

[33] Y. Yan, H. Yang, Z. Yi, R. Li, X. Wang, Micromachines 10 (2019) 1–16.

[34] U. Alam, S. Kumar, D. Bahnemann, J. Koch, C. Tegenkamp, M. Muneer, Physical Chemistry Chemical Physics 20 (2018) 4538–4545.

[35] S. Li, L. Chen, Z. Liu, M. Zhang, B. Li, C. Lai, Applied Surface Science 566 (2021) 150658.

[36] C. Huang, J. Hu, S. Cong, Z. Zhao, X. Qiu, "Applied Catalysis B, Environmental" 174–175 (2015) 105–112.

[37] H. Irie, S. Miura, K. Kamiya, K. Hashimoto, Chemical Physics Letters 457 (2008) 202–205.

[38] X. Dai, S. Yan, L. Cui, L. Shi, Ceramics International 46 (2020) 11261–11267.

[39] T. Čižmar, I. Panžić, I. Capan, A. Gajović, Applied Surface Science 569 (2021).

[40] M.R. Gandhi, S. Vasudevan, A. Shibayama, M. Yamada, ChemistrySelect 1 (2016) 4358–4385.

[41] N. Zhang, Y. Zhang, Y.J. Xu, Nanoscale 4 (2012) 5792–5813.

[42] J. Prakash, Photochem 2 (2022) 651–671.

[43] M. Al Kausor, D. Chakrabortty, Inorganic Chemistry Communications 129 (2021) 108630.

[44] H.A.A. Jamjoum, K. Umar, R. Adnan, M.R. Razali, M.N. Mohamad Ibrahim, Frontiers in Chemistry 9 (2021) 1–24.

[45] Z. Durmus, B.Z. Kurt, A. Durmus, ChemistrySelect 4 (2019) 271–278.

[46] P. Gao, J. Liu, D.D. Sun, W. Ng, Journal of Hazardous Materials 250–251 (2013) 412–420.

[47] K. Zhang, J.M. Suh, T.H. Lee, J.H. Cha, J.W. Choi, H.W. Jang, R.S. Varma, M. Shokouhimehr, Nano Convergence 6 (2019) 0–6.

[48] P. Gao, D.D. Sun, Chemistry - An Asian Journal 8 (2013) 2779–2786.

[49] G.L. He, Y.H. Zhong, M.J. Chen, X. Li, Y.P. Fang, Y.H. Xu, Journal of Molecular Catalysis A: Chemical 423 (2016) 70–76.

[50] Z. Jin, W. Duan, B. Liu, X. Chen, F. Yang, J. Guo, Applied Surface Science 356 (2015) 707–718.

[51] Z. Mengting, T.A. Kurniawan, S. Fei, T. Ouyang, M.H.D. Othman, M. Rezakazemi, S. Shirazian, Environmental Pollution 255 (2019).

[52] P.K. Labhane, L.B. Patle, G.H. Sonawane, S.H. Sonawane, Chemical Physics Letters 710 (2018) 70–77.

[53] C. Li, B. Wang, F. Zhang, N. Song, G. Liu, C. Wang, S. Zhong, Journal of Materials Research and Technology 9 (2020) 610–621.

[54] Y. Yang, E. Liu, H. Dai, L. Kang, H. Wu, J. Fan, X. Hu, H. Liu, International Journal of Hydrogen Energy 39 (2014) 7664–7671.

CHAPTER-2

Fabrication and photocatalytic activity of Ag and Cu photodeposited $CaTiO_3$ nanocatalysts for the degradation of Rhodamine B dye under UV light irradiation

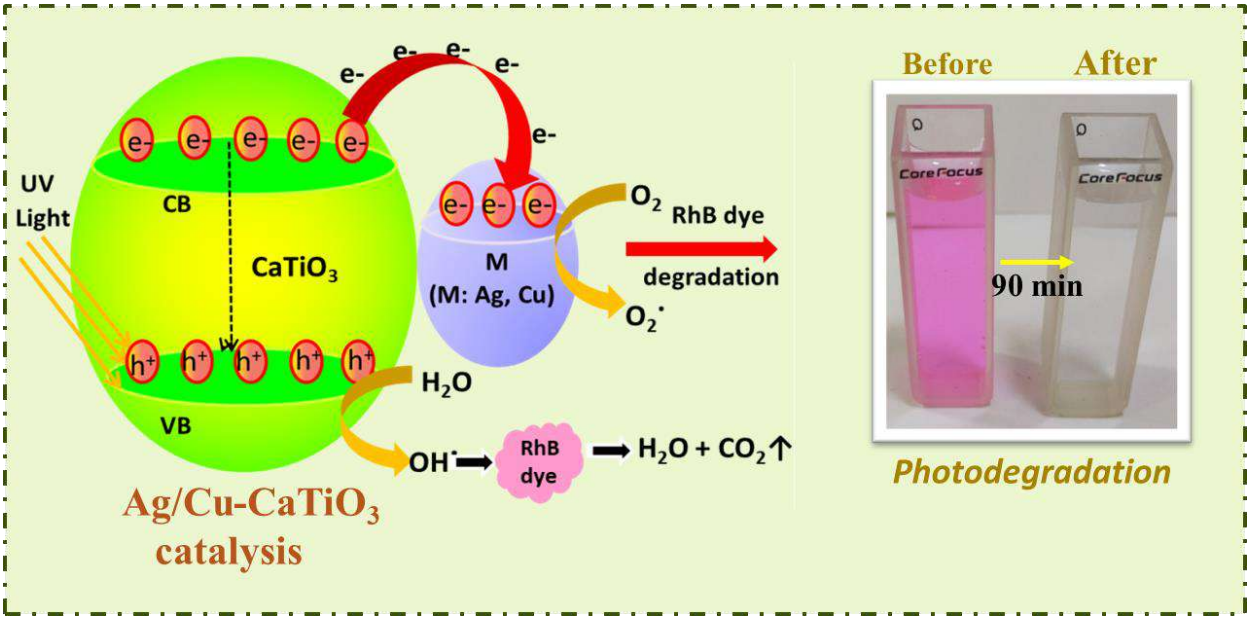

Schematic summary

This study reveals the superior co-catalysis effect of Ag and Cu nanoparticles photo deposited on $CaTiO_3$ (CTO) nanoparticles for the removal of toxic Rhodamine B dye under UV light illumination. Both Ag and Cu depositions promoted $CaTiO_3$ photoactivity. Optimal 1wt%Ag-$CaTiO_3$ nanocomposite, degraded RhB dye with the highest effectiveness (97.72%) within 90 minutes of reaction. Increased optical absorption and the creation of a Schottky barrier at the interface of (Ag/Cu) and $CaTiO_3$ are credited for the remarkable improvement in photocatalytic performance.

2.1. Introduction

Global environmental problems have become more of more concern due to severe pollution, especially the recalcitrant toxic organic pollutants. For its effectiveness, simplicity, and environmentally-friendly nature, semiconductor-based photocatalysis, one of the advanced oxidation technologies has been regarded as the most appealing method in treating the waste water. It basically involves absorption of photons with energy equal to or higher than the band gap of the semiconductor to produce electron-hole pairs which then reacts with the oxygen and hydroxyl ions to generate active radicals that can degrade the water contaminants readily and quickly [1,2]. In this regard, variety of semiconductor systems and their composites have been extensively developed and studied so far. Among the large assemblage of catalytic materials explored to date, perovskites oxides of the form ABO_3 are gaining huge attention because of their immense potential in diverse applications [3–5]. Owing to their remarkable physicochemical and optoelectronic properties such as structural flexibility, electron-mobility, band gap tunability, low-cost fabrication, high thermal and photo-corrosion stability enormous efforts have been made on utilizing perovskite oxides as photocatalysts [6–8]. Recently, Calcium titanate ($CaTiO_3$), a typical titanium-containing oxide semiconductor with a perovskite-type structure has been examined in various fields including energy conversion [9–12], environmental remediation [13–15] and industrial processes [16,17]. Its unique perovskite structure offers a large platform for designing new and efficient photocatalytic materials by alteration at its A, B and O sites [18]. In addition, this n-type semiconductor, even possesses conduction band potential value more negative than the benchmark photocatalyst TiO_2, making it a good substitute for the industrial catalyst TiO_2 [19,20]

Although $CaTiO_3$ is a highly photoactive material however, because of its wide bandgap and low quantum efficiency, its overall photocatalytic performance is restricted. Several factors are of relevance, but majorly two are important: ultrafast recombination of photoexcited electron-hole pairs and the limit of optical response only to UV-light [21]. Thus, the two most crucial points for achieving the high photocatalytic performance of $CaTiO_3$ are necessity to efficiently separate the photogenerated charge carriers and to expand its absorption range to the visible region. Up to now, many attempts have been made for its modification including elemental doping [22–24], metal deposition [25,26], surface functionalization [27], heterojunction formation [28–30], and coupling with carbon materials [31–33]. Among these depositing metal nanoparticles on semiconductors, has been an important strategy to overcome these shortcomings. Generally, metal deposition on semiconductors is known to form a metal-semiconductor (M-SC) interface or Schottky barrier that furnishes an effective pathway for capturing, storing and discharging of

photogenerated electrons. The contact metal actually serves as an electron trap. The Schottky barrier created at the interface permits the flow of electrons from the semiconductor to the deposited metal till the equilibration of Fermi levels. This process is influenced by nature, electronegativity, reduction potential and Fermi energy/work function of the metal [34]. Metals with lower reduction potential than CB of semiconductor ($CaTiO_3$) are suitable choice for this.

Many literature reports reveal the significant enrichment in its photocatalytic activity by metal deposition. Recently, A. Shawky *et al.* [35] synthesized Pt-decorated $CaTiO_3$ nanocrystals with varying amounts of Pt loadings and evaluated the photoreduction of nitrobenzene to aniline. The conversion rate was found to be notably improved by Pt deposition. Alzahrani *et al.* reported Ag(0)/$CaTiO_3$ photocatalysts with higher rates of hydrogen generation than pure $CaTiO_3$ [36]. Ag metals also show considerable antibacterial and antifungal effect. Complete deactivation of T. suecica algae was achieved in just 12 min of UV light irradiation by $CaTiO_3$ cuboids functionalized with Ag nanoparticles [37]. Au@$CaTiO_3$ nanocomposites displayed increased rates of RhB degradation under both UV and visible light irradiations [38]. Thus, it is evident that decorating metals over $CaTiO_3$ surface greatly improvise its photocatalytic activity. However, only a few reports are available on its modification by Ag and Cu. Furthermore, herein we present the first report displaying the comparative effect of Ag, Cu as effective co-catalysts for $CaTiO_3$.

With this perspective, the present report deals with the preparation, characterization, and comparative study of the photocatalytic performance of series of Ag/Cu modified $CaTiO_3$ nanocomposites (with 1 to 5 wt% of Ag and Cu). Sol-gel method was applied to synthesize $CaTiO_3$ photocatalyst and then Ag and Cu were deposited onto it by the photo-deposition method. Because of their easy availability, cost-effectiveness and suitable redox potentials (Ag = 0.799 V and Cu = 0.337 V) [39] w.r.t conduction band of $CaTiO_3$, these metals were selected for this study. The as-synthesized samples were then characterized using various techniques and their photocatalytic performances were evaluated by removal of commercial dye rhodamine B under the illumination of UV light. The influence of loading amount of Ag and Cu on the light absorbency and photocatalytic activity was studied individually. Based on the photocatalytic results their loading amount was optimized. A possible photocatalysis mechanism has been proposed. The main importance of this work is to study the enlargement in photocatalytic performance of wide band gap semiconductor $CaTiO_3$ with metallic Ag and Cu and to predict the most superior co-catalyst among the two.

2.2. Experimental Section

2.2.1 Chemicals and Reagents

Titanium dioxide (P25-TiO_2) was obtained from Degussa Corporation, Germany. Calcium carbonate ($CaCO_3$), Cupric acetate monohydrate $(CH_3COO)_2Cu.H_2O$), Rhodamine B dye ($C_{28}H_{31}N_2O_3Cl$), Isopropyl alcohol (C_3H_8O), ethanol (C_2H_5OH), all were acquired from Loba Chemie (India). Silver nitrate ($AgNO_3$) was purchased from Sigma-Aldrich (India). Double distilled water (D.I.) utilized during the whole study was obtained from Milli-Q (Millipore), an ultra-filtration system (conductivity = 35 mho cm^{-1} at 25°C).

2.2.2. Preparation of $CaTiO_3$ nanoparticles

The experimental details are presented in the flow chart of the preparation method, as shown in **Scheme-2.1.** In brief, $CaCO_3$ and TiO_2 powders in equimolar ratios were mixed together in 10 ml of de-ionized (DI) water in a beaker for 30 minutes. The mixed solution was continuously stirred for 12 h at room temperature and the slurry dried in an oven at 80°C for 3h. The resultant dried solid was grounded in a mortar pestle for 10 min until a fine and homogenous powder was obtained and then finally, calcined at 900°C for 2 h, in a muffle furnace with a heating rate of 5ºC/min, yielding white-colored $CaTiO_3$ nanoparticles which were then stored in dry container and kept in a desiccator. The as-prepared $CaTiO_3$ nanoparticles were abbreviated as (CTO).

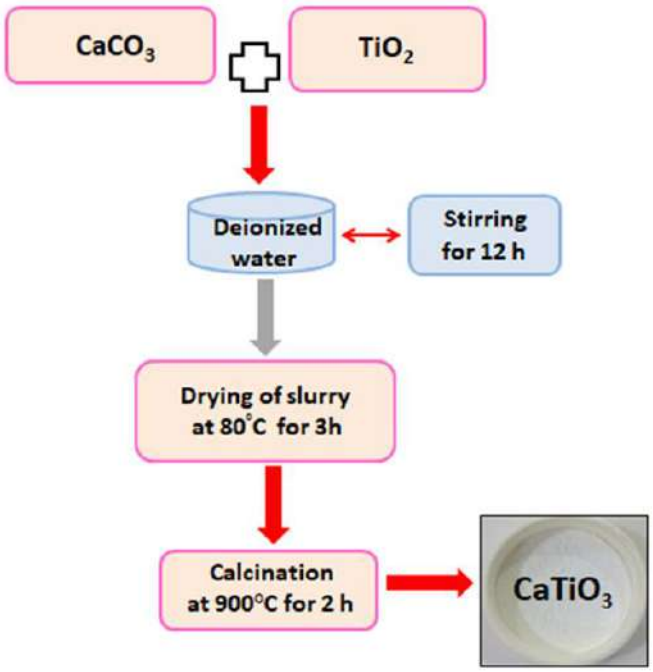

Scheme-2.1. Flow chart of synthesis of $CaTiO_3$ (CTO)

2.2.3. Preparation of Ag/Cu-$CaTiO_3$ nanocomposites

Photodeposition of Ag and Cu on $CaTiO_3$ surface was carried out by the following protocol as displayed in **Scheme-2.2.** As prepared 100 mg of CTO powder was suspended in different test tubes containing distilled water and isopropyl alcohol as hole scavenger (5 ml each). The requisite amount of metal salts $AgNO_3$ (0.01M; 928-4636µL) and $Cu(CH_3COO)_2.H_2O$ (0.01M; 1574–7870µL) corresponding to different wt% (1, 3 and 5 wt%) was added to these suspension. Test tubes were then purged with argon (Ar) gas for 20 min to create an inert atmosphere and closed tightly by a rubber septum. The contents in the test tubes were photo-irradiated with UV light (125 W, 10.4 mW/cm^2) for 3h under continuous magnetic stirring in photochemical

reactor. Finally, the metal deposited solutions were centrifuged (8000 rpm), washed repeatedly with distilled water and ethanol followed by drying in oven at 70°C for 2 h. The obtained Ag/Cu deposited nanocomposites were named as 1, 3 and 5 wt% Ag/Cu-CTO respectively.

Scheme-2.2: Experimental procedure for photodeposition of M (M=Ag, Cu) NPs onto $CaTiO_3$

2.2.4. Characterization

The crystallographic studies of the prepared samples were carried out by X-ray powder diffraction PANalytical-Xpert-PRO machine equipped with a Cu-Kα radiation source (1.54 Å) operating at 45 kV with diffraction angle (2θ) ranging from 10°-80° at a scan rate of 5°/min. The optical properties were measured using a diffuse reflectance spectrophotometer (DRS, Avantes) in the region 400-900 nm, with $BaSO_4$ bar as a reference. Separation of photogenerated electron-hole pairs was examined by measuring the photoluminescence (PL) emission spectrum using a spectrofluorometer (Perkin-Elmer LS55). The shape and size analysis of the samples was done by both scanning electron microscopy (SEM;) JEOL JSM-7600F operated at 30kV) and high-resolution transmission electron microscopy (HRTEM TALOS F200S G2 model operating at 200 kV voltage). Elemental analysis and mapping were carried out by an energy-dispersive X-

ray spectrometer (EDS) linked to another SEM of the same model as mentioned above.

2.2.5. Photocatalytic activity test

The photocatalytic performance of the prepared samples (bare CTO, Ag/Cu-CTO), was examined by Rhodamine B (RhB) dye degradation. The photocatalytic reaction was conducted at room temperature in different test tubes. In a typical reaction, 15 mg of each catalyst was dispersed in 5 mL of 0.01mM RhB aqueous solution. Prior to the irradiation, the suspensions were stirred in the dark for 30 min to achieve the adsorption-desorption equilibrium condition between the dye molecules and catalyst surface. Then the test tubes containing different catalysts were exposed to UV light irradiation (125W Hg arc, 104 mW/cm^2). After definite time intervals of 15 min, the samples were withdrawn from each test tube and centrifuged at 8000 rpm for 5 min to remove any residual solid catalyst particles. After separation, the absorbance spectra of RhB were monitored at λ_{max}= 554 nm using a UV-vis spectrophotometer. As the concentration was directly proportional to the absorbance so in accordance with Beer-Lambert's law, the photodegradation efficiency was obtained using the following formula:

Degradation rate (%) = $(A_o - A_t)/A_o \times 100 = (C_o - C_t)/C_o \times 100$ (1)

where, A_o, C_o denote the initial absorbance and concentration of RhB before irradiation at time‘0’ and A_t, C_t be the absorbance and concentration of RhB after light irradiation at time ‘t’.

2.3. Results and discussion

2.3.1 Structural studies

XRD analysis

XRD analysis was performed to predict the crystal structure and phase composition of the as-prepared samples. **Fig.2.1** displays the XRD patterns of the bare and the Ag, Cu deposited $CaTiO_3$ samples for the optimum 1wt% respectively. Six major reflection peaks appear at diffraction angle (2θ) values of 23.23°, 33.11°, 47.49°, 59.36°, 69.48°, and 79.22° which corresponds to the (110), (112), (220), (312), (224), (116) crystal planes of the $CaTiO_3$ structure, respectively. It can be seen that all these diffraction peaks of the CTO nanoparticles can be perfectly indexed to a perovskite-type structure well-crystallized in the orthorhombic phase with Pbnm space group (ICSD PDF# 01-078-1013), verifying that a pure single-phase was obtained. No significant diffraction peaks of Ag and Cu were witnessed probably due to their low loading amount (1 wt%) which is consistent with previous reports [37,40]. However, a small decrease in the intensities of these peaks was observed on metal loading, which might be attributed to the suppression of the electron scattering

of bare CTO upon loading of these heavy metals to its surface [41]. As the diffraction patterns of the loaded samples almost coincide with the bare CTO this also gives indication of homogenous dispersion of Ag and Cu on CTO surface.

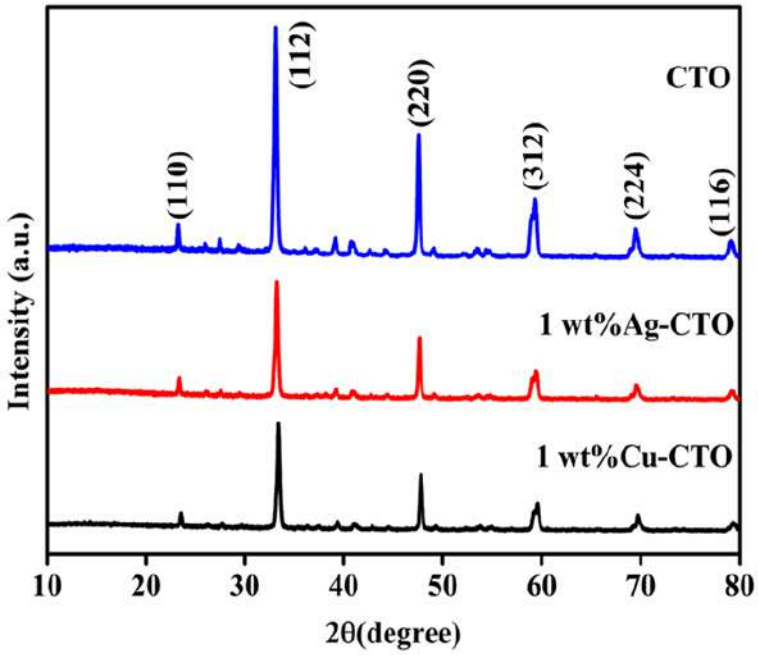

Fig.2.1: X-ray diffraction patterns of different photocatalysts

2.3.2 Morphological studies

SEM, EDS-Mapping and HR-TEM analysis

The surface morphology of the catalysts was identified by SEM. **Fig.2.2(a)-(c)** displays the SEM images of bare CTO and optimum 1wt%Ag/Cu-CTO composites. Mostly spherical aggregates or clusters were obtained for all the samples. Appearance of agglomerates may be due to high calcination temperature of 900°C. The deposited Ag, Cu nanoparticles and the bare CTO could not be differentiated by SEM due to low resolution of the instrument. But the elemental composition and mapping results confirm their presence on CTO surface. EDS study was used for determining the quantity of various elements present in the composites. Fig.2 (a)-(c) shows their respective EDS spectra along with tables indicating the elemental content values. The expected loading amount was 1wt% of Ag and Cu but the observed values were 0.68% and 0.64%. The lower amount of Ag, Cu content might be due to selective area selection for EDX or because of some mass loss occurred either during the photodeposition process or by the washing procedure. In addition, with all

the necessary elements like (Ca, Ti, O, Ag, Cu) one additional signal of element carbon (C) was detected in all the samples that could have come from the carbon tape employed in SEM-EDX analysis to attach samples to sample holders or may be because of the presence of some carbonate traces.

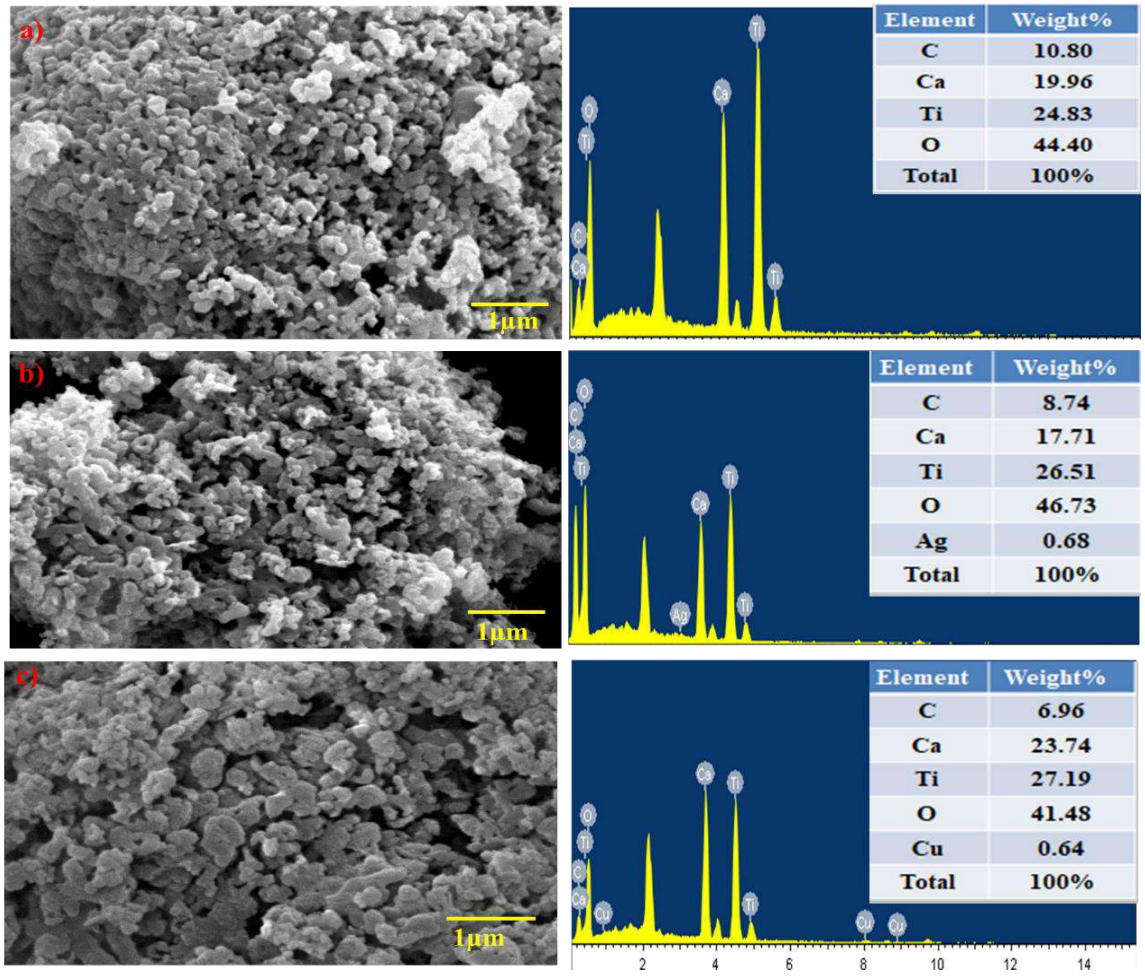

Fig.2.2: SEM images of (a) bare CTO, (b) 1 wt% Ag-CTO, (c) 1 wt% Cu-CTO and their corresponding EDX profiles.

The mapping results of Ag/Cu-CTO samples along with the corresponding image are shown in **Fig.2.3.** The dot pattern of 1wt% Ag-CTO sample **{Fig.2.3 (a-d)}** clearly shows the presence of elements Ca, Ti, O, Ag appearing in green, blue, yellow and pink colors respectively. Similar confirmation of elements most importantly the presence of Cu was also detected in the dot pattern of 1wt% Cu-CTO nanocomposite **{Fig.2.3 (e-h)}.**

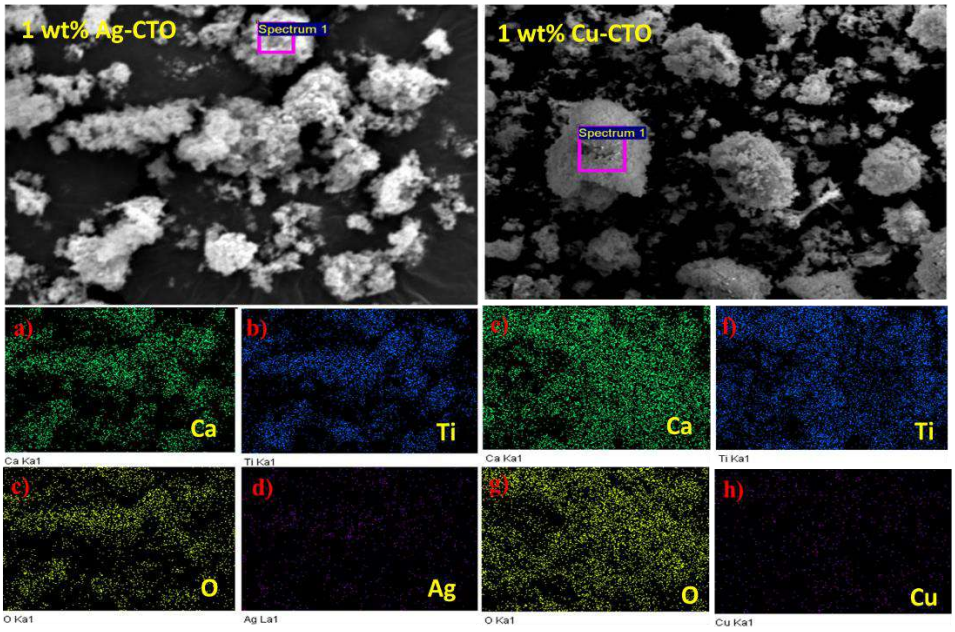

Fig.2.3: Elemental dot mapping of different elements present in (a-d) 1 wt% Ag-CTO and (e-h) 1wt% Cu-CTO photocatalysts.

Further, the clear morphologies as well as the way of distribution of Ag and Cu nanoparticles on $CaTiO_3$ surface were elucidated from their TEM and HRTEM images. The TEM images of bare CTO **(Figs.2.4(a-b))** show mixed morphological characteristics.

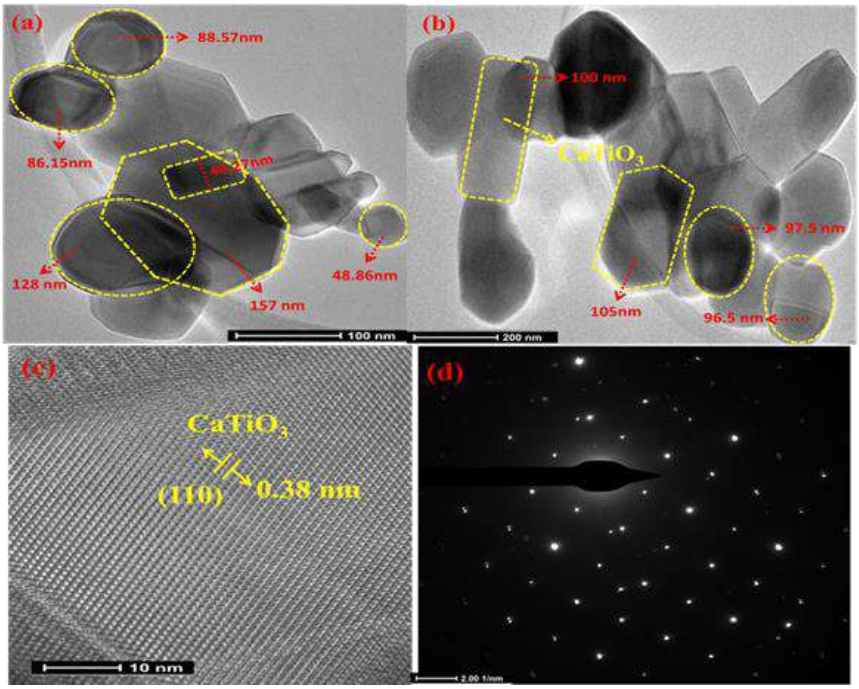

Fig. 2.4: HRTEM morphology (a, b), lattice fringes (c) and SAED pattern (d) of bare $CaTiO_3$.

Most of the nanoparticles attained spherical shape while variable morphologies such as rectangular, hexagonal and cubical were also observed. Size of the CTO particles was measured and found to be in the range of 40-150nm. Occurrence of large sized particles could be related to the consequence of high calcination temperature which causes growth of the crystal. **Fig. 2.4(c),** displays the high resolution TEM image of bare CTO which represents clear lattice fringes of CTO

with an interplanar ‘d’ spacing of 0.38 nm coinciding with the (110) crystal plane of pure perovskite phase CTO [42].

Fig. 2.5(a) and (b) represent the TEM images of 1wt% Ag-CTO nanocomposite. Many smaller spherical Ag nanoparticles (marked by red arrows) of average size 6-12 nm were found to be uniformly deposited on CTO surface in the form of nanodots. Its HRTEM image displayed in **Fig.2.5(c)**, further confirms the presence of Ag. The interplanar spacing (d) of 0.23 nm [43] and 0.38 nm shows the presence of (111) plane of Ag nanoparticles [30] anchored on (110) plane of CTO surface, respectively.

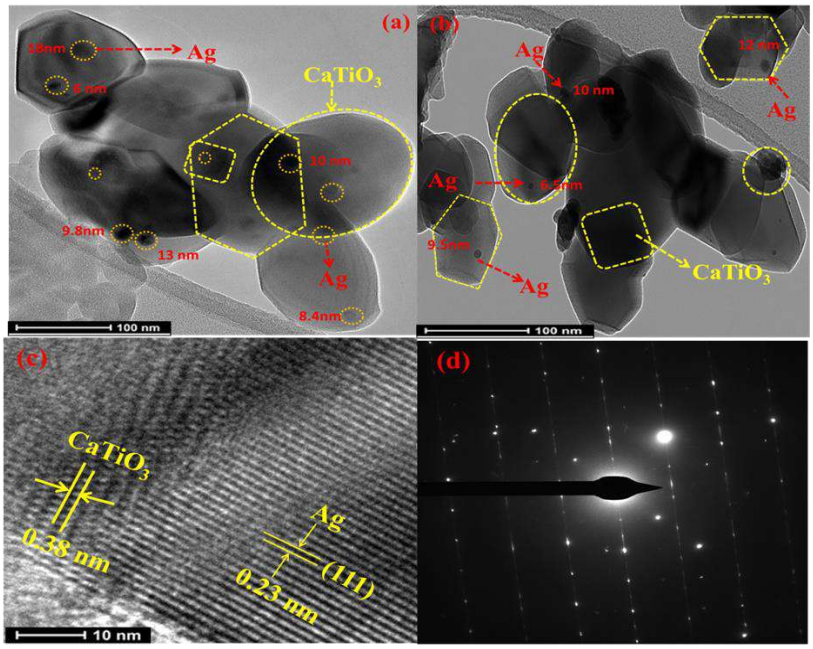

Fig.2.5. HRTEM morphology (a, b), lattice fringes (c) and SAED pattern (d) of optimum 1wt% Ag-$CaTiO_3$ nanocomposite.

Similar kind of TEM and HRTEM images were also obtained in case of 1wt% Cu-CTO nanocomposite as presented in **Fig.2.6(a)-(c).**

Cu nanodots of average sizes 3 to 20 nm were found to be anchored on CTO surface. Distinct fringes were also observed for Cu and CTO where, spacing ‘d’ of 0.21 and 0.38 nm attributes to (121) plane of Cu [44] and (110) plane of CTO. Such results indicate the deposition of Ag and Cu nanoparticles on $CaTiO_3$ perovskite. Moreover, SAED pattern of these samples was also analyzed as shown in **Figs.2.4(d), 2.5(d) and 2.6(d)** respectively. A series of bright spots were observed in contrast to ring

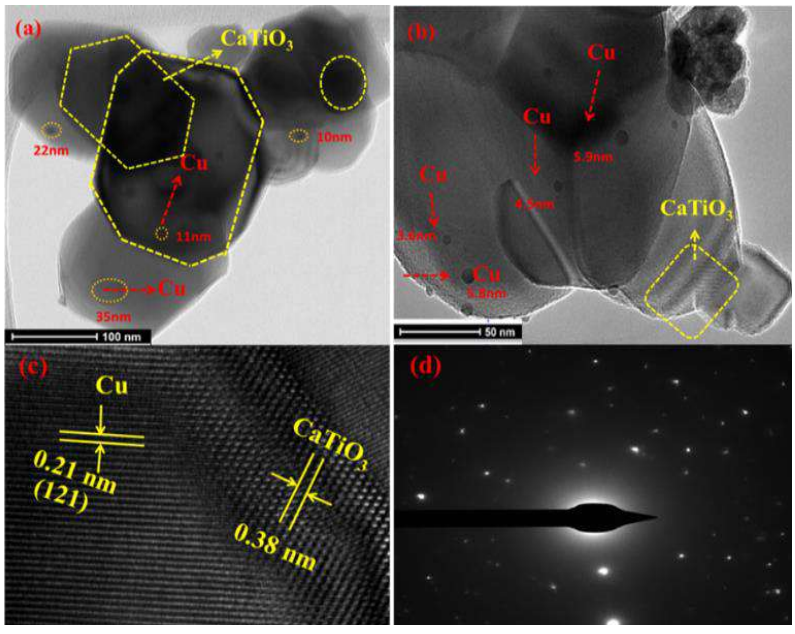

Fig.2.6. HRTEM morphology (a, b), lattice fringes (c) and SAED pattern (d) of optimum 1wt% Cu-$CaTiO_3$ nanocomposite.

pattern. The typical spot pattern reveals the high crystallinity of all the prepared samples.

2.3.3. Optical and charge transfer properties

UV-Vis Diffuse reflectance spectra

Fig.2.7 presents the results of ultraviolet-visible spectra of bare and 1, 3, 5 wt% Ag/Cu-CTO nanocomposites. A characteristic peak of CTO was observed at 370 nm in a UV region which could be due to the electronic transition from the valence band to the conduction band. After deposition of Ag and Cu, the absorption range of the composites was found to be significantly shifted towards the visible-light region. The typical surface plasmon resonance bands of Ag and Cu in the composites were seen in the range of 480 and 700 nm respectively. Moreover, with the increase in their amount from 1 to 5 wt% the intensities of these plasmon bands were also found to increase gradually. Accordingly, the existence of UV as well as visible absorbance maxima in case of Ag/Cu-CTO composites clearly indicates that the material turns out to be highly photoactive, with ability to be able to respond in full range spectrum. After depositing these metals on CTO surface, the colors of the samples were also found to be changed (as inserted in Scheme 2) from the typical white color of CTO to light brown and grey in the case of Ag and Cu-CTO respectively. This further confirms the change in the light absorption capacity of CTO by the deposited metals.

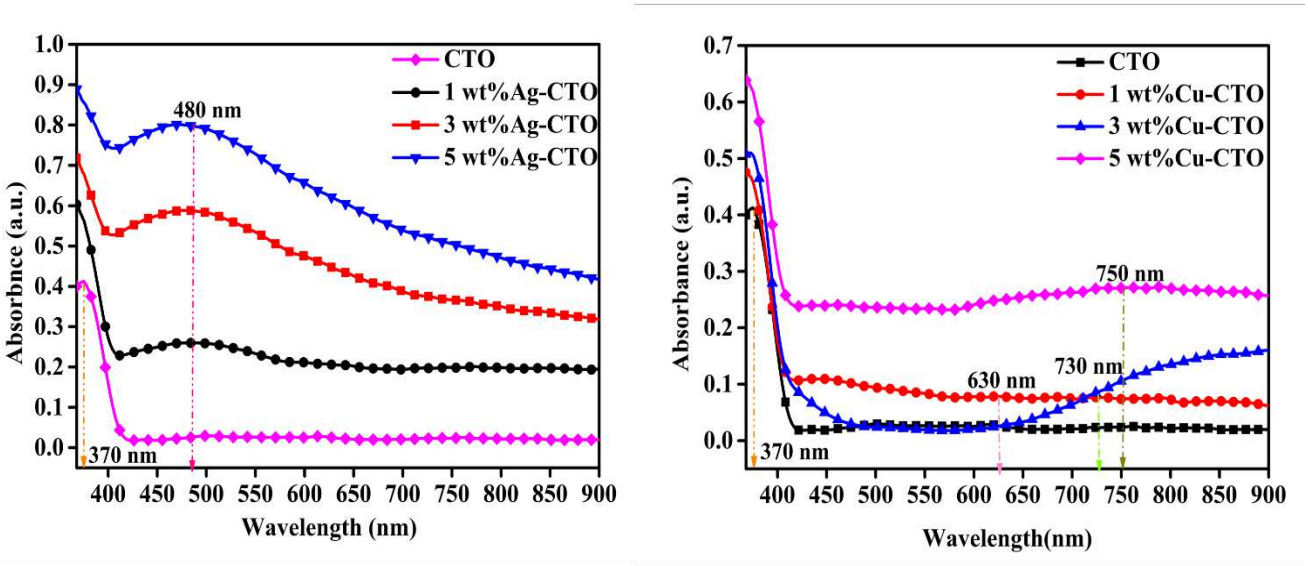

Fig.2.7. Diffused reflectance spectra of various Ag and Cu loaded CTO nanocomposites

Further, the band gap energies of the samples were estimated by the use of Tauc relation [39], given by:

$$\alpha h\nu = A\,(h\nu - E_g)^n \qquad \textbf{(2)}$$

where α = absorption coefficient, $h\nu$ = photon energy, A = constant, E_g = is the band gap of the material and n is the exponent coefficient (n=1/2 for $CaTiO_3$). The exact band gap values (listed in **Table-2.1**) were

calculated by plotting graph between $(\alpha h\nu)^{1/2}$ versus the hν. Results revealed that the band gap energy values of all the prepared catalysts were lower than bare CTO (2.99eV). The reduction in the band gap upon modification with Ag and Cu was attributed to decrease in the extent of recombination of photogenerated charge carriers. However, it was also noticed that this band gap lowering occured only up to 3 wt%, further increasing the loading amount of Ag and Cu to 5wt%, increases the band gap. This could be due to excessive loading of metal nanoparticles which acts as recombination centers, and affects the band gap. The maximum decrease in the band gap of 2.90 eV was observed in case of 3 wt%Ag-CTO sample.

	Ag-CTO		**Cu-CTO**	
Metal content	λ_{max} (nm)	Band gap (eV)	λ_{max} (nm)	Band gap (eV)
1 wt%	480	2.91	630	2.96
3 wt%	480	2.90	730	2.95
5 wt%	480	2.94	750	2.98

Table-2.1: The absorption peaks and band gap values for bare CTO and various (1, 3 and 5 wt%) Ag/Cu-CTO nanocomposites

Photoluminescence measurement

PL spectroscopy was used to examine the extent of charge carrier separation in various samples. It is well reported that the PL intensity is directly proportional to the recombination rate of electron-hole pairs, i.e. the higher the extent of recombination, the more intense is the PL signal, and vice-versa [45]. **Fig.2.7** shows the room temperature PL spectra of bare and Ag/Cu-CTO nanocomposites with excitation wavelength of 370nm. Several peaks at 423, 486 and 530 nm were obtained for all the samples. The peak at 423nm is ascribed to near band edge emission (NBE) and the latter peaks at 486 and 530 nm defined as deep level emissions (DLE). The NBE emission peak mainly centered in the UV region originates due to recombination of charge carriers formed upon excitation by radiation with energy equal to or greater than the bandgap energy. The other two deep level emissions centered in the visible region would be the result of intrinsic defects such as oxygen vacancies (V_O), Ti vacancies (V_{Ti}) or surface defects. The deposition of Ag and Cu however, did not change much the position of band edges, but resulted in significant quenching of PL intensity in comparison to the intensity of bare CTO, indicating suppression in the recombination rate of photoinduced electron-hole pairs in Ag/Cu-CTO composites. This could be credited to the electron trapping ability of Ag and Cu leading to efficient transfer of charges from CTO surface to these islands which strongly hinders the recombination

process and in turn prolongs the lifetime of charge carriers. Besides, it was observed that the highest PL quenching happens in case of 1wt% amount of Ag/Cu-CTO nanocomposites which implies that there is an optimal value for the quantity of metal (Ag, Cu) in order to obtain the adequate electron transportation. On further increasing the metal content beyond 1wt%, the PL emission shows rise in intensity due to high electron-hole recombination rate. This might be due to excessive metal deposition which can cover the CTO surface, eventually leading to decrease in the concentration of photoexcited charge carriers and also the photocatalytic activity of composites. Among all the samples, the most depressed PL signal is obtained in case of 1wt% Ag loaded CTO.

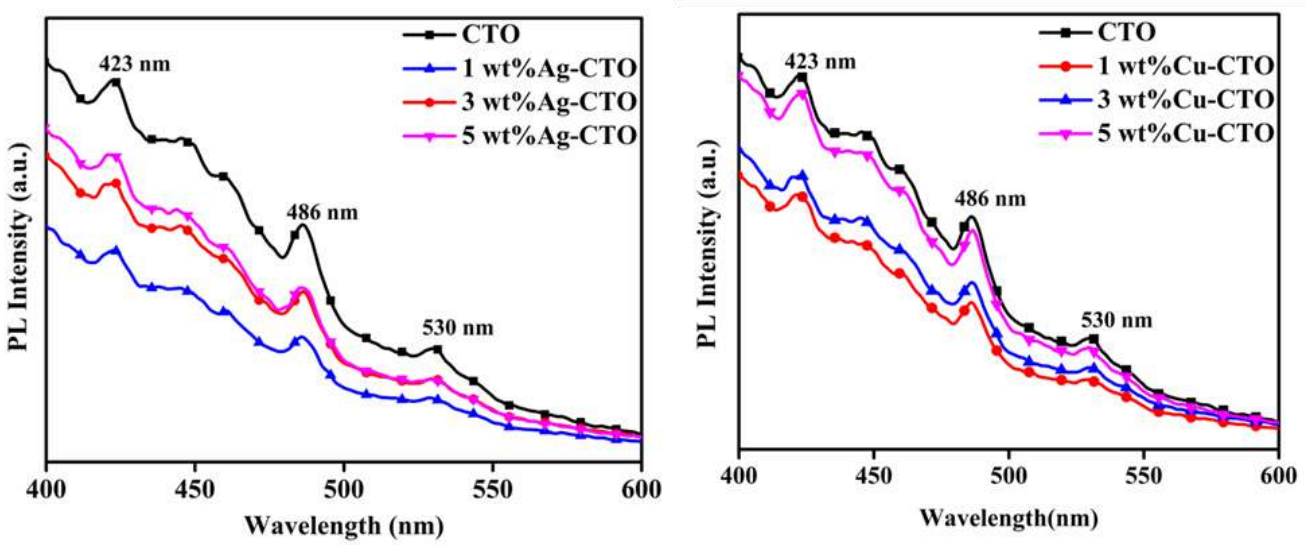

Fig. 2.7: Photoluminescence (λ_{max} = 370 nm) spectra of various nanocomposites

2.4. Photocatalytic activity

2.4.1. Photodegradation reaction

(a) With Ag-$CaTiO_3$

The UV-visible absorption spectra **Fig.2.8(a)** shows comparative change in absorbance of RhB dye after its photodegradation by bare and different Ag-loaded CTO nanocomposites under 90 min UV irradiation. It can be seen that absorption intensity is decreased in a varied extent depending on the amount of Ag (1 to 5 wt%) deposition, signifying the differences in RhB photodegradation efficiency among various catalysts. Definitely Ag loading notably improved the photoactivity of CTO, and 1 wt% Ag deposition exhibits maximum catalytic activity and thereby decreased on further (3 to 5 wt%) loading. To further confirm the optimum amount of Ag loading on CTO for RhB degradation, the time course **(Fig.2.8(b))** plot and kinetic

graphs **(Fig.2.9(c))** were studied and found that the photodegradation process follows pseudo-first-order rate law in all cases. **Fig.2.9(d)** representing the histogram showed comparative reaction rate constant values. Out of various Ag loaded catalysts, the maximum rate constant (4.50 x 10^{-2}) is obtained in case of 1wt% Ag loaded CTO sample under similar experimental condition.

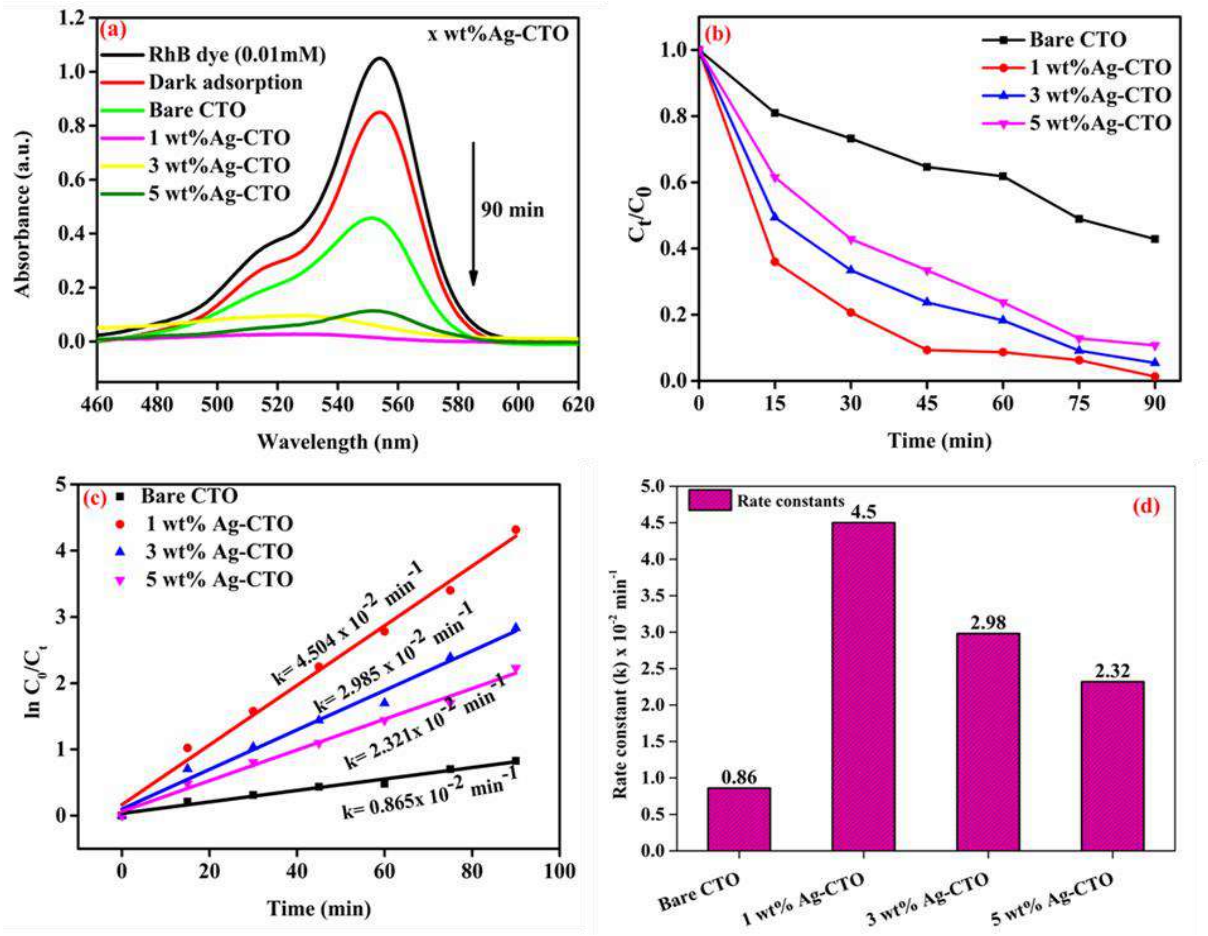

Fig.2.9: (a) Comparative changes in absorption spectra of RhB dye degradation by different Ag- CTO catalysts after 90 min UV irradiation, (b and c) time course-kinetic plot, (d) their relative rate constants (k).

(b) <u>With Cu-$CaTiO_3$</u>

Similar results are obtained for various amounts of Cu-loaded CTO for RhB dye photodegradation as shown in **Fig.2.10.** The changes in the absorption spectral intensity, time course plot and kinetic rate law are also varying depending upon the amount of Cu loaded on CTO as displayed in **Fig.2.10(a)-(c).** The photocatalytic activity of Cu-CTO catalysts is seen to follow the same trend as observed by Ag loaded catalysts where 1wt%Cu loading also exhibited the best photoactivity (1.80 x10^{-2}) for RhB degradation as evident in **Fig.2.10(d)** histogram.

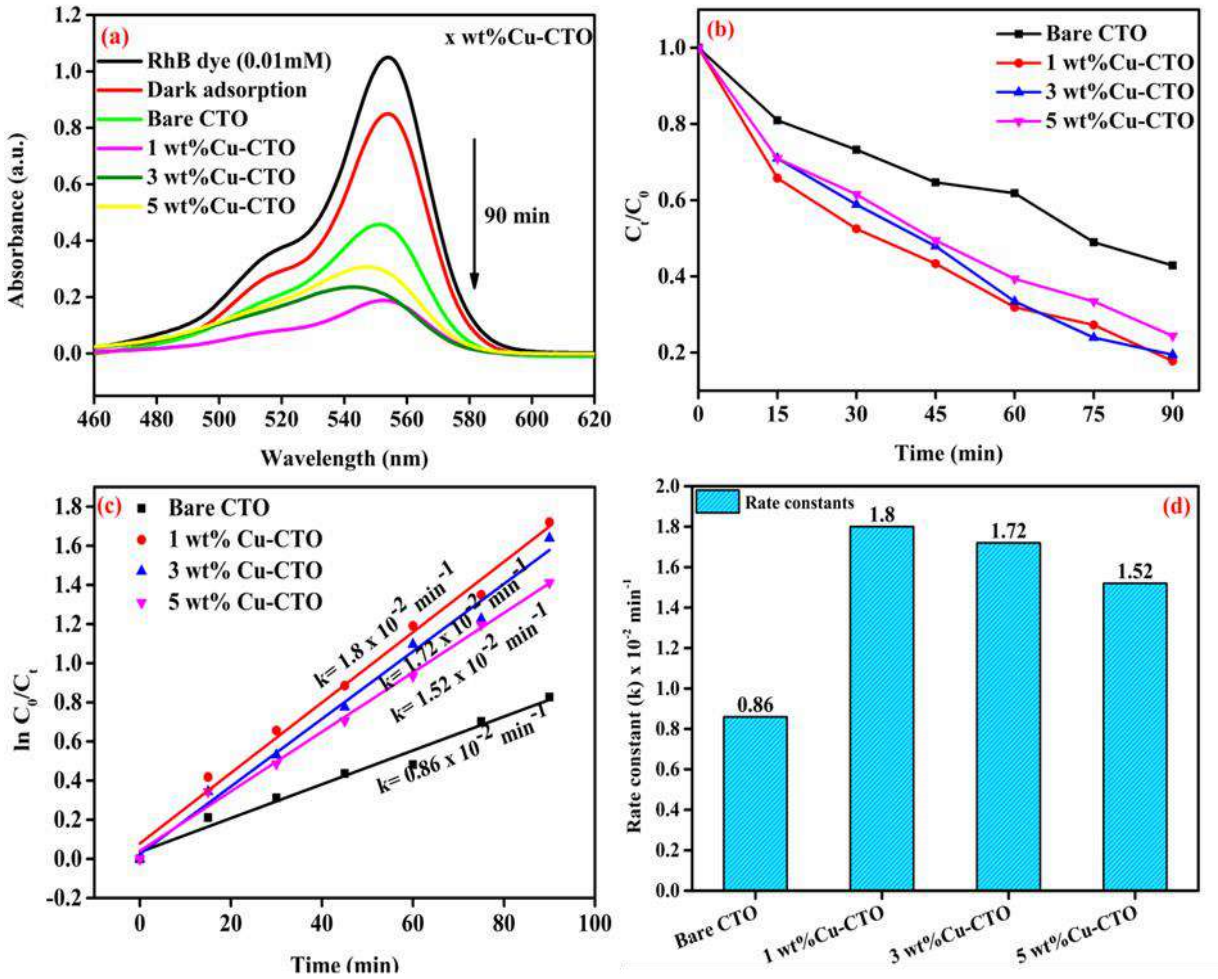

Fig.2.10: (a) Comparative changes in absorption spectra of RhB dye degradation by different Cu-CTO catalysts after 90 min UV irradiation, (b and c) time course-kinetic plot, (d) their relative rate constants (k).

The experimental result suggests that degradation ability of $CaTiO_3$ gets remarkably enhanced by depositing Ag and Cu on its surface. These metal deposits behave like electron accumulation sites and effectively traps the photo-excited electrons from CTO surface and then transferred it to oxygen molecule. Followed by increase in the formation of highly reactive hydroxyl (.OH-) radicals and superoxide radical anion ($.O_2$-) which can be used effectively for degradation of RhB. To further understand the improved behavior of CTO photoactivity, the CB (conduction band) and VB (valence band) potentials of CTO v/s (NHE) normal hydrogen electrode were determined based on its band gap by Equations **(3)-(4).**

$$E_{CB} = X - E_e - 0.5E_g \quad \textbf{(3)}$$

$$E_{CB} = X - E_e + 0.5E_g \quad \textbf{(4)}$$

where X is the absolute electronegativity of CTO (5.105 eV) [46]; E_e is the energy of free electrons on the hydrogen scale (4.5 eV), E_g is the band gap of CTO (2.99eV). The CB and VB potentials were obtained as -

0.89V and +2.1V vs NHE, respectively.

Comparative analysis of the co-catalytic effect imparted by Ag/Cu to $CaTiO_3$ photoactivity is presented in **Fig.2.11.**

The histogram clearly shows the differences in the degradation efficiency of RhB by various samples. 1wt%Ag-CTO revealed the maximum RhB removal efficiency (98%) within 90 min. Since the amount of metal loading and the average particle size are almost the same in both the Ag and Cu deposited composites, the observed difference in the photoactivity of Ag/Cu-CTO catalysts can be elucidated on the basis of electronic properties like electron affinity and electronegativity and also the work function of the deposited metal. As it can be seen from **Table- 2.2**, Ag metal because of its high electron affinity (125.6 KJ/mol) and high electronegativity (1.93 on Pauling scale) value [47] act as more efficient electron trap in comparison to the relatively lower values of Cu. Moreover, the lower work function of Ag metal (4.26eV) than of Cu (4.93eV), allows easy transference of the CB electrons of CTO to the Ag deposits. Further, the higher reduction potential of Ag^{+} ions (0.79V) accepts the electrons first from the CB while Cu^{+2} ions with lower reduction potential (0.33V) get reduced afterwards.

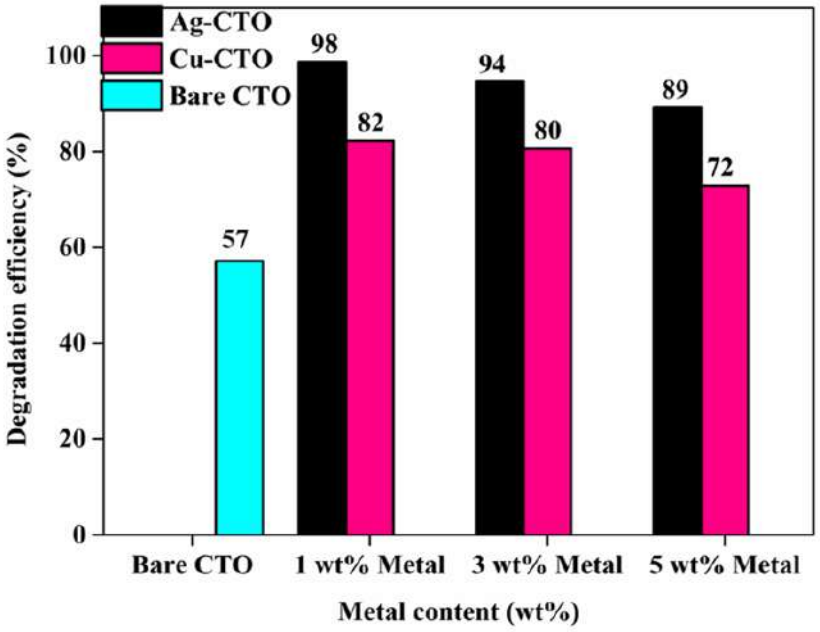

Fig.2.11: Comparative photodegradation efficiency of different photocatalysts

Co-catalyst	Electron affinity (KJ/mol)	Electronegativity (Pauling)
Ag	125.6	1.93
Cu	118.4	1.90

Table-2.2: The electronic properties of Ag and Cu used as co-catalysts.

As a result, much better separation of charges is achieved in the case of, Ag loaded samples leading to its

superior degradation ability. Both the PL measurements and bandgap analysis also support the observed degradation results. The lower bandgap value of (E_g = 2.91 eV) as well as much depressed PL intensity in case of 1 wt% Ag-CTO composites in contrast with the one deposited with Cu-CTO of (E_g=2.96 eV) act as evidence for better efficiency of the Ag cocatalyst.

Further, the lower degrading efficiency beyond 1wt% deposition could be attributed to the fact that after exceeding this amount, the deposited Ag and Cu nanodots may cover the large portion of CTO surface, leading to blockage of its many active sites and partially shielding of UV light absorption [48,49]. All these events probably reduce the number of photoinduced excitons (e^-/h^+). Furthermore, high amount of metal loading can also induce the agglomeration of metal particles which in turn might be responsible for reducing the photoactivity. Thus, it is revealed that nature of metal and their amount also effects the photoactivity of $CaTiO_3$ for degrading RhB.

2.4.2. Possible degradation mechanism

Scheme-2.3 illustrates the possible mechanism responsible for the degradation of RhB under UV light irradiation by the as-prepared catalysts. In CTO, during light illumination, the electrons get excited from the VB to the CB, with the simultaneous generation of holes (h^+) in the VB. Then the photoexcited electrons and holes react with adsorbed oxygen and water molecule to generate the reactive oxygen species, such as superoxide radical anions ($O_2^{\cdot -}$) and hydroxyl radicals. These strong oxidative species such as $O_2^{\cdot -}$ and $OH^{\cdot}$ radicals works together to further degrade or mineralize RhB [50]. Whereas, in case of Ag/Cu-CTO, owing to the lower redox potentials of Ag (+0.799 V vs. NHE) and Cu (+0.337V vs. NHE) in comparison with the CB potential of CTO (-0.89 V), the photoexcited electrons can be eagerly transferred from CTO to Ag and Cu surface which further speeds up the separation of the electron-hole pairs in CTO. Here, the deposited metals Ag, Cu act as electron sinks or traps for the photogenerated electrons migrated from CTO. This obstructs the immediate electron-hole recombination process. The overall reactions during photocatalysis under UV light with metal (M) deposited (CTO) photocatalyst are shown below [51]:

$CTO + h\nu\ (UV) \rightarrow CTO\ (e_{CB}^- + h_{VB}^+)$

$CTO\ (e_{CB}^-) + M\ (Ag, Cu) \rightarrow CTO\text{-}M\ (e^-)$

$CTO\text{-}M\ (e^-) + O_2 \rightarrow CTO\text{-}M + \cdot O_2^-$

$h_{VB}^+ + OH^- \rightarrow \cdot OH$

$\cdot O_2^- + 2H^+ \rightarrow 2 \cdot OH$

$\cdot OH + RhB \rightarrow$ decomposed product

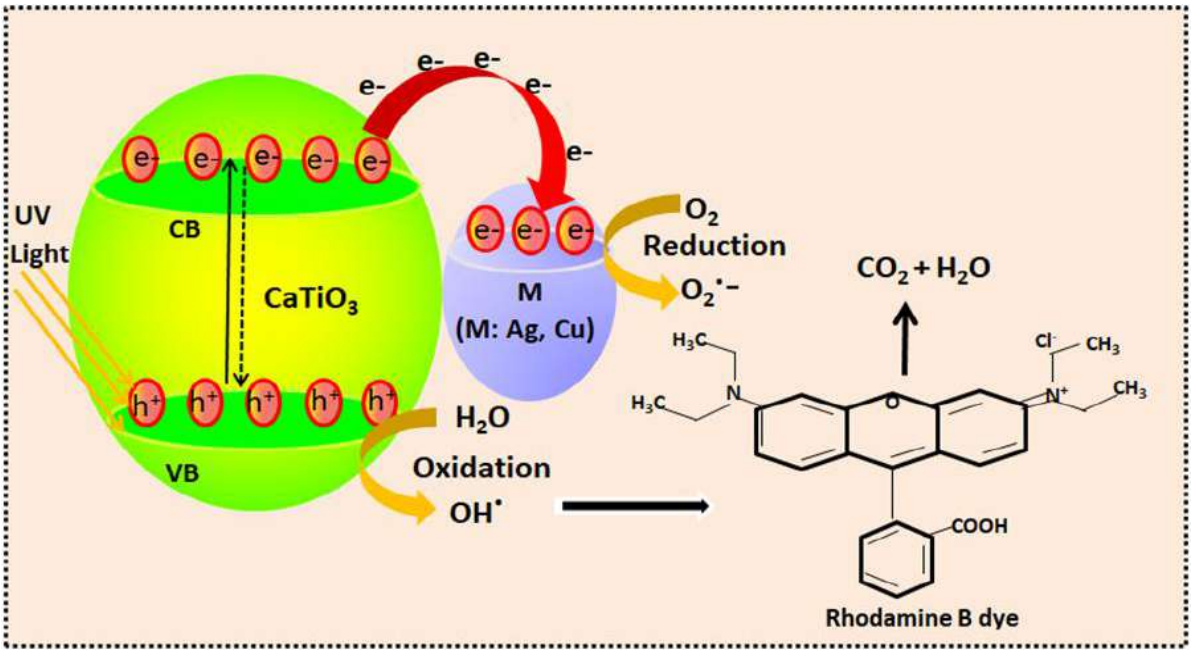

Scheme-2.3: Plausible mechanism of RhB degradation by under UV light irradiation.

2.4.3. Photodegradation pathway

To perceive the major intermediates of RhB produced during its photodegradation, the LC-MS experiment was conducted. Based on the results of the detected oxidation products by LC-MS and earlier studies, a possible degradation pathway of RhB in the Ag-$CaTiO_3$ process is proposed and illustrated in **Scheme-2.4.** The LC-MS spectra revealed that the fragment with m/z value 443 belonging to the parent RhB dye molecule was rarely found after the degradation process. The major steps engaged in the decomposition pathway of RhB are: chromophore cleavage, ring-opening and mineralization process. The cleavage of the conjugated xanthene structure of deethylated products of RhB results in destroying the chromophore structures and giving rise to low-molecular-weight intermediates like, P1 (m/z = 239), P2 (m/z = 215), P3 (m/z = 199), P4 (m/z = 172) and P5 (m/z = 110). After that, the ring opening process occurred, wherein the benzene ring structures of the aforementioned intermediates were continually attacked and oxidized resulting in products into acid such as

glutaric acid [P6 (m/z = 132)] and also the smallest molecular weight P7 (m/z = 84). Finally, these low molecular weight products might be mineralized to CO_2 and H_2O NO_3^-, NH_4^+, etc. The existence of these breakdown products in the mass spectra indicates dye cleavage, implying that the photocatalyst is extremely effective at promoting dye photodegradation.

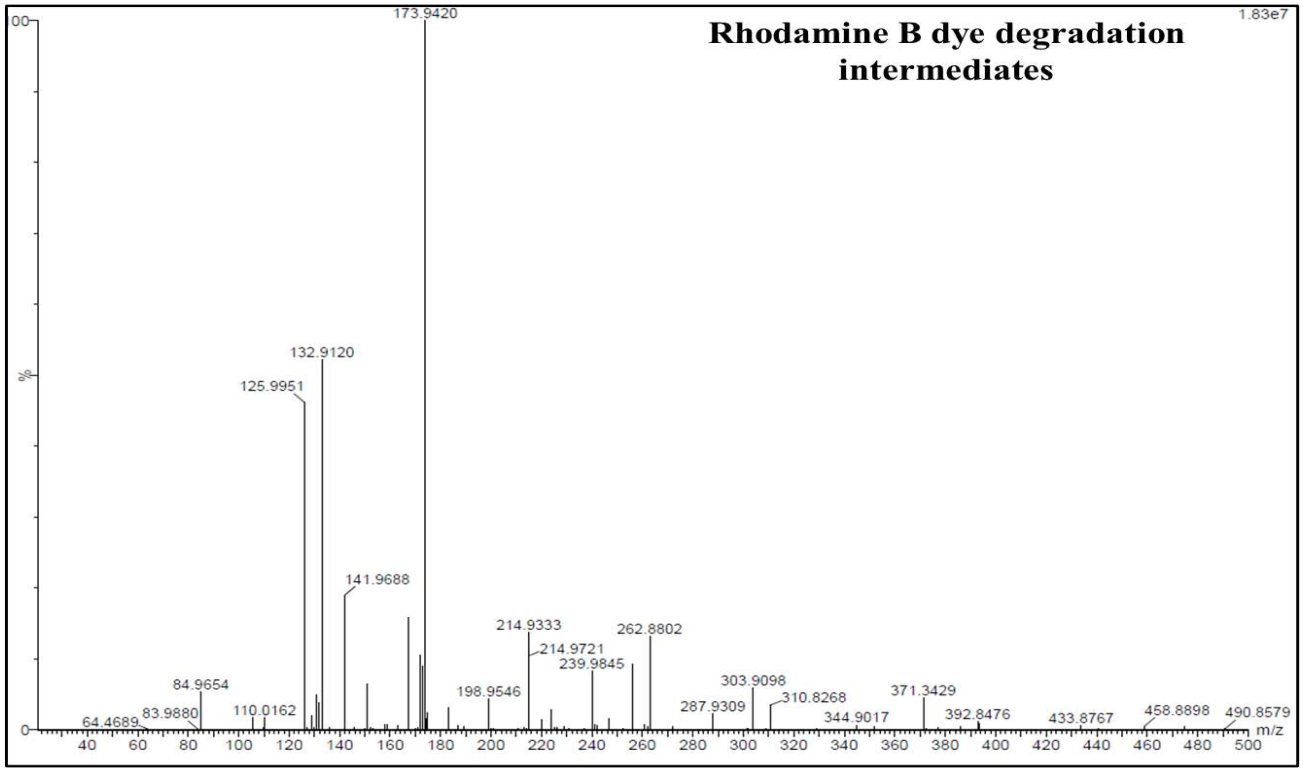

Scheme-2.4 (a) The mass spectra of RhB dye after photodegradation using Ag-$CaTiO_3$ catalyst

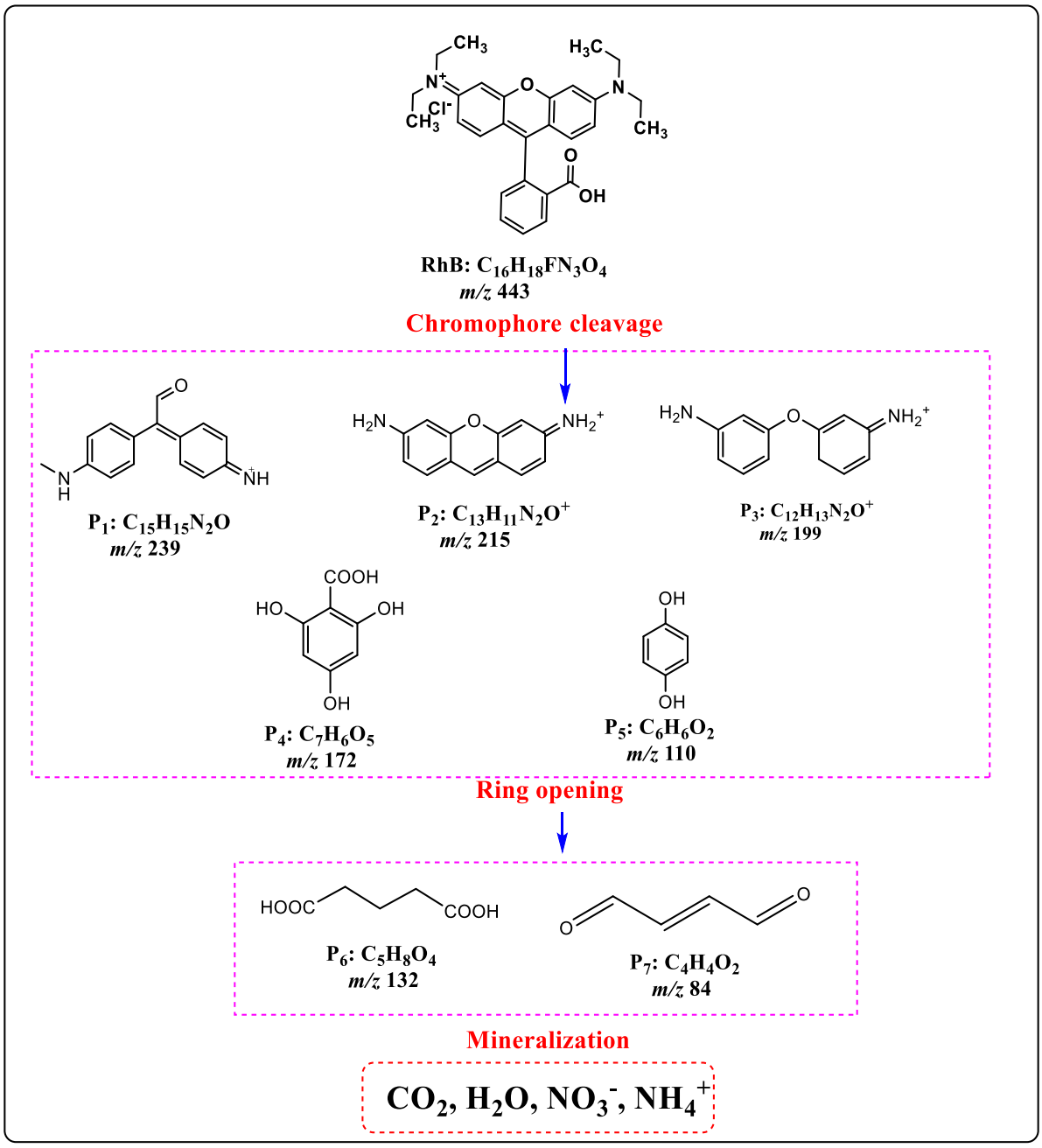

Scheme-2.4 (b): Degradation pathway of Rhodamine B dye using Ag-$CaTiO_3$ photocatalyst under UV light.

Conclusion

The effect of nature and amount of metal deposited on $CaTiO_3$ for its enhanced activity in degrading RhB dye under UV light irradiation is studied. A series of Ag/Cu-CTO nanocomposites with varying wt% (1, 3 and 5) of Ag, Cu were synthesized by photodeposition method. Their photocatalytic activity for the degradation of Rhodamine B was found to be dramatically higher than that of bare CTO. Both Ag and Cu deposition promoted enlarged photoactivity by shifting the absorption edges towards longer wavelengths with reduced bandgaps and suppressing the charge carriers (electron-hole pairs) recombination probability, as confirmed by UV-DRS and PL spectroscopy, respectively. Optimal Ag and Cu loading (1wt% in the present case) ensures the maximum degradation, whereas the rates were gradually reduced with higher metal loadings. Also, in comparison to Cu, much superior reaction rates = 4.5×10^{-2} min^{-1} were achieved by deposition of Ag onto CTO. So, based on the experimental results, Ag was found to be a promising co-catalyst for $CaTiO_3$. In addition, the as-prepared composites not only show enhanced activity under UV light but also possesses strong absorption in the visible light region as seen by the UV-DRS plot. This study will enlighten the usage of these materials applications for developing other visible-light responsive perovskites photocatalysts with high photocatalytic activity in various environmental and energy issues.

References

[1] M. Kurian, Cleaner Engineering and Technology 2 (2021) 100090.

[2] A.G. Gutierrez-Mata, S. Velazquez-Martínez, A. Álvarez-Gallegos, M. Ahmadi, J.A. Hernández-Pérez, F. Ghanbari, S. Silva-Martínez, International Journal of Photoenergy 2017 (2017).

[3] N.F. Atta, A. Galal, E.H. El-Ads, Perovskite Materials - Synthesis, Characterisation, Properties, and Applications (2016).

[4] E.A.R. Assirey, Saudi Pharmaceutical Journal 27 (2019) 817–829.

[5] X. Huang, G. Zhao, G. Wang, J.T.S. Irvine, Chemical Science 9 (2018) 3623–3637.

[6] A. Kumar, A. Kumar, V. Krishnan, ACS Catalysis 10 (2020) 10253–10315.

[7] P. Kanhere, Z. Chen, Molecules 19 (2014) 19995–20022.

[8] V.H. Nguyen, H.H. Do, T. Van Nguyen, P. Singh, P. Raizada, A. Sharma, S.S. Sana, A.N. Grace, M. Shokouhimehr, S.H. Ahn, C. Xia, S.Y. Kim, Q. Van Le, Solar Energy 211 (2020) 584–599.

[9] E. Jiang, L. Yang, N. Song, X. Zhang, C. Liu, H. Dong, Journal of Colloid and Interface Science 576

(2020) 21–33.

[10] J. Pan, Z. Jiang, S. Feng, C. Zhao, Z. Dong, B. Wang, J. Wang, C. Song, Y. Zheng, C. Li, International Journal of Hydrogen Energy 43 (2018) 19019–19028.

[11] J. Han, Y. Liu, F. Dai, R. Zhao, L. Wang, Applied Surface Science 459 (2018) 520–526.

[12] M. Passi, B. Pal, Powder Technology 388 (2021) 274–304.

[13] Y. Yan, H. Yang, Z. Yi, R. Li, T. Xian, Solid State Sciences 100 (2020).

[14] J. Zhuang, Q. Tian, S. Lin, W. Yang, L. Chen, P. Liu, Applied Catalysis B: Environmental 156–157 (2014) 108–115.

[15] Y. Yan, H. Yang, Z. Yi, T. Xian, X. Wang, Environmental Science and Pollution Research 26 (2019) 29020–29031.

[16] S. Lanfredi, J. Matos, S.R. da Silva, E. Djurado, A.S. Sadouki, A. Chouaih, P.S. Poon, E.R.P. González, M.A.L. Nobre, Applied Catalysis B: Environmental 272 (2020) 118986.

[17] K. V. Yatish, H.S. Lalithamba, R. Suresh, H.K.E. Latha, Renewable Energy 147 (2020) 310–321.

[18] H. Yang, C. Han, X. Xue, JES (2014) 1–7.

[19] X. Chen, L. Di, H. Yang, T. Xian, Journal of the Ceramic Society of Japan 127 (2019) 221–231.

[20] B. Deng, P. Si, L. Bauman, J. Luo, M. Rao, Z. Peng, T. Jiang, G. Li, B. Zhao, (2019).

[21] L. Bai, Q. Xu, Z. Cai, Journal of Materials Science: Materials in Electronics 29 (2018) 17580–17590.

[22] L.H. Oliveira, A.P. De Moura, F.A. La Porta, I.C. Nogueira, E.C. Aguiar, T. Sequinel, I.L.V. Rosa, E. Longo, J.A. Varela, Materials Research Bulletin 81 (2016) 1–9.

[23] R. Wang, S. Ni, G. Liu, X. Xu, 225 (2018) 139–147.

[24] L.H. Oliveira, J. Savioli, A.P. De Moura, I.C. Nogueira, M.S. Li, E. Longo, J.A. Varela, I.L.V. Rosa, Journal of Alloys and Compounds 647 (2015) 265–275.

[25] C. Science, G. Jiajian, F. Gu, Z. Zhong, (2013).

[26] K. Shimura, H. Yoshida, Energy and Environmental Science 3 (2010) 615–617.

[27] C. Han, J. Liu, W. Yang, Q. Wu, H. Yang, X. Xue, “Journal of Photochemistry & Photobiology, A: Chemistry” (2016).

[28] J. Lin, J. Hu, C. Qiu, H. Huang, L. Chen, Y. Xie, Z. Zhang, H. Lin, X. Wang, Catalysis Science and Technology 9 (2019) 336–346.

[29] Z. Jiang, J. Pan, B. Wang, C. Li, Applied Surface Science 436 (2018) 519–526.

[30] Y. Liu, J. Pan, H. Li, W. Ou, S. Li, W. Zhao, J. Wang, C. Song, Y. Zheng, C. Li, Journal of Alloys and Compounds 811 (2019).

[31] T. Xian, H. Yang, Y.S. Huo, Physica Scripta 89 (2014).

[32] A. Kumar, S. Kumar, A. Bahuguna, A. Kumar, V. Sharma, V. Krishnan, Materials Chemistry Frontiers 1 (2017) 2391–2404.

[33] A. Kumar, C. Schuerings, S. Kumar, A. Kumar, V. Krishnan, Beilstein Journal of Nanotechnology 9 (2018) 671–685.

[34] Y.S. Fu, J. Li, J. Li, Nanomaterials 9 (2019).

[35] A. Shawky, M. Alhaddad, K.S. Al-Namshah, R.M. Mohamed, N.S. Awwad, Journal of Molecular Liquids 304 (2020) 3–10.

[36] A. Alzahrani, D. Barbash, A. Samokhvalov, Journal of Physical Chemistry C 120 (2016) 19970–19979.

[37] S.W. Lee, L.M. Lozano-Sánchez, V. Rodríguez-González, Journal of Hazardous Materials 263 (2013) 20–27.

[38] Y. Yan, H. Yang, Z. Yi, R. Li, X. Wang, Micromachines 10 (2019) 1–16.

[39] S. Bhardwaj, B. Pal, Advanced Powder Technology 29 (2018) 2119–2128.

[40] H. Zhang, G. Chen, Y. Li, Y. Teng, International Journal of Hydrogen Energy 35 (2010) 2713–2716.

[41] J. Kaur, B. Pal, (2013) 3956–3964.

[42] W. Dong, Q. Bao, X. Gu, G. Zhao, (2015) 643–648.

[43] V.D. Doan, B.A. Huynh, T.D. Nguyen, X.T. Cao, V.C. Nguyen, T.L.H. Nguyen, H.T. Nguyen, V.T. Le, Journal of Nanomaterials 2020 (2020).

[44] Y. Zhai, Y. Ji, G. Wang, Y. Zhu, H. Liu, Z. Zhong, F. Su, RSC Advances 5 (2015) 73011–73019.

[45] J. Liqiang, Q. Yichun, W. Baiqi, L. Shudan, J. Baojiang, Y. Libin, F. Wei, F. Honggang, S. Jiazhong, Solar Energy Materials and Solar Cells 90 (2006) 1773–1787.

[46] X. Yan, X. Huang, Y. Fang, Y. Min, Z. Wu, W. Li, J. Yuan, 9 (2014) 5155–5163.

[47] S. Oros-Ruiz, R. Zanella, B. Prado, Journal of Hazardous Materials 263 (2013) 28–35.

[48] A. Gnanaprakasam, V.M. Sivakumar, M. Thirumarimurugan, Water Science and Technology 74

(2016) 1426–1435.

[49] B. Luo, D. Xu, D. Li, G. Wu, M. Wu, W. Shi, M. Chen, ACS Applied Materials and Interfaces 7 (2015) 17061–17069.

[50] P. Fageria, S. Gangopadhyay, S. Pande, RSC Advances 4 (2014) 24962–24972.

[51] Ş.Ş. Türkyılmaz, N. Güy, M. Özacar, Journal of Photochemistry and Photobiology A: Chemistry 341 (2017) 39–50.

CHAPTER-3

Preparation, characterization and photocatalytic activity of a novel Ag-$BaTiO_3$/GO ternary nanocomposite under LED-light irradiation

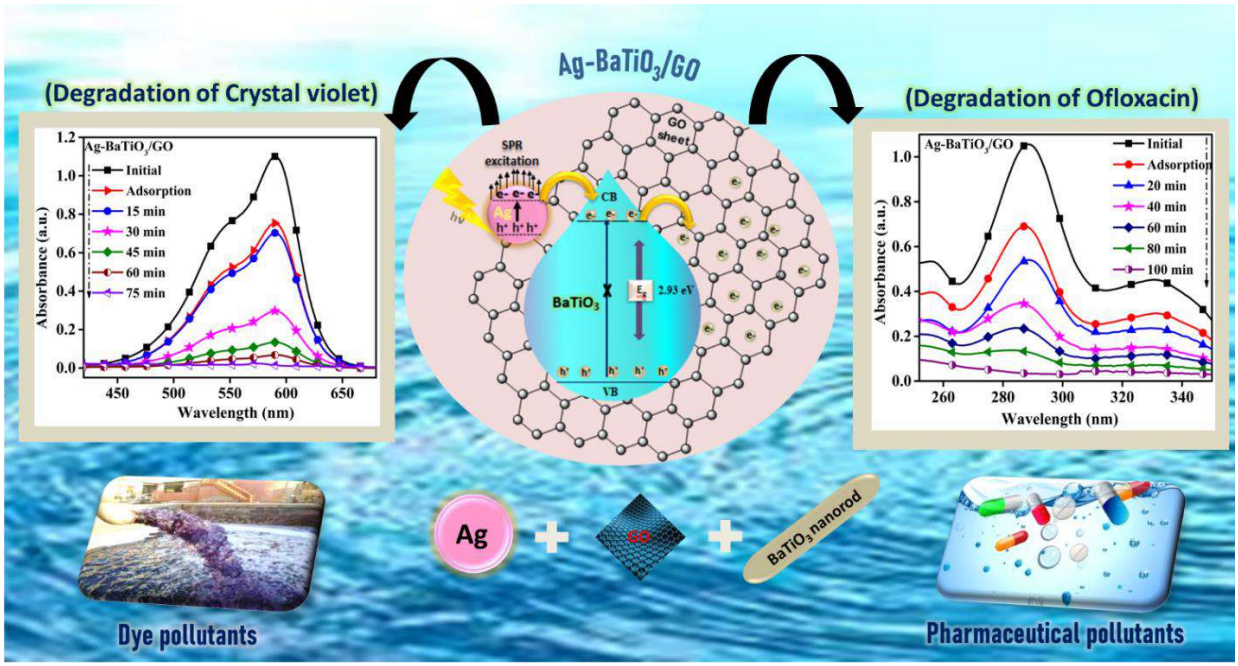

Schematic summary

Synergic effect of Ag and GO on the photocatalytic performance of $BaTiO_3$ was examined. Under LED light, the developed ternary photocatalyst (Ag-$BaTiO_3$/GO) effectively degraded hazardous contaminants with a removal efficiency of 98.5% for CV dye and 96.1% for OFL antibiotic. Ag NPs increase this photocatalyst's optical response to a wider range, while GO improves photoinduced charge separation and transport and adsorption capacity, thus improving BaTiO3's photocatalytic behavior.

3.1. Introduction

The relentless expansion of industrialization and urbanization has exacerbated some of the world's most pressing issues, such as the energy crisis and environmental pollution. Particularly, the accumulation of hazardous contaminants (lethal dyes, pharmaceutical drugs etc.) in natural water bodies is a major threat to human beings as well as the aquatic life [1–3]. Crystal violet (CV), a well-known synthetic cationic dye belonging to the triphenylmethane group, is extensively utilized in a variety of ways, including biological staining, veterinary medicine, dermatological agents, bacteriostatic agents, and as a poultry feed additive etc. This recalcitrant dye enters the aquatic systems through the effluents of the textile and paint industries, as well as the medical and biotechnology industries. Because of its mutagenic, teratogenic, carcinogenic, and mitotic poisoning properties, it has a considerable deleterious impact on flora and fauna[4,5]. Similarly, antibiotics, which account for a large proportion of pharmaceutical and personal care products are another common emerging organic micropollutant. Dumping of pharmaceutical industrial effluents into water streams and improper disposal of tones of unwanted medications into the environment are two of the pathways through which these contaminants predominate in our water resources [6]. For instance, Ofloxacin (OFL), an antibacterial synthetic drug from the fluoroquinolone family, widely employed in the treatment of infections like bronchitis, diarrhea, pneumonia, eye, ear and skin infections, gastrointestinal diseases, gonorrhea, respiratory and urinary tract infections. However, 48 h after ingestion, approximately 90% of the drug is excreted in its active form via urination. As a result, it has a direct impact on domestic sewage. Surface water (10-535ng/L), hospital wastewater (25000-35000 ng/L), and municipal wastewater effluent (53-1800 ng/L), have all been shown to have a significant concentration of OFL. Bacteria exposed to this antibiotic residue in the aquatic environment may go through genetic mutations, resulting in bacteria that are resistant to OFL itself [7,8]. These antibiotic-resistant bacteria act as infection spreaders, and their diseases are more difficult to treat. Clearly, widespread usage of both CV and OFL is harmful to one's health and the environment. Therefore, the use of environmentally friendly and sustainable treatment technologies is urgently required to resolve the aforementioned problems.

SC photocatalysis, one of the advanced oxidation processes (AOPs), is considered the most compelling and promising approach for treating these toxic moieties in wastewater due to its potential advantages such as the complete mineralization of pollutants to CO_2, water and mineral acids, no waste-solids disposal problem, its applicability at ambient conditions (temperature and pressure), absence of fouling, lack of mass transfer limitations, less chemical component input, use of a photoactive, chemically

inert, environment-friendly catalysts with super-hydrophilicity as well as remarkable oxidation strength and photostability.[9,10].

Alkaline earth metal titanates, a distinctive category of oxide SC's has emerged as an important class of photocatalysts[11,12]. Among them is barium titanate ($BaTiO_3$), a multifunctional n-type titanium oxide with a perovskite-like structure that has sparked tremendous interest. Owing to its peculiar and fascinating characteristics like excellent ferroelectric/piezoelectric properties, strong oxidizing ability, structural simplicity, flexibility, good stability, compatibility with other materials, multiple crystal phases (cubic, tetragonal, orthorhombic, rhombohedral) as well as nontoxicity, it has been extensively used in numerous photocatalytic energy and environmental applications[13]. However, limited light absorption (due to broad band gap usually > than 3 eV) and quick rejoining of the photoinduced charge carrier is a persistent bottleneck in this material which hampers its applicability scope and utilization efficiency. Designing and creating highly effective visible light-active catalyst is therefore essential for upgrading its photocatalytic activity.[14–16].

It is widely believed that the deposition of plasmonic metal NPs (i.e. Ag, Au, Cu, Pt) onto the surface of a SC is an effective strategy for the increment in its photocatalytic properties. Specifically, with their extraordinary localized surface plasmon resonance (LSPR) features, plasmonic metal NPs can profoundly enlarge and boost the spectral response to visible region by generating hot electrons, favoring the production of more active species, and enhancing the charge carrier separation extent of the system [17–22]. For instance, Wu et al.[23] fabricated flower like $Ag@SrTiO_3$ nanocomposite, which displayed excellent capability in reduction of 4-nitrophenol and the degradation of MO. Yan et al. $Au@CaTiO_3$ photocatalyst [24] was observed to accelerate the degradation of RhB dye by almost 3.9 times (0.04701 min^{-1}) compared to bare $CaTiO_3$ NCs (0.01195 min^{-1}). Likewise, $Au/ZnTiO_3$ nanocomposites delivered an amazingly increased rate of H_2 evolution in presence of both UV and visible light [25]. Due to its comparatively low cost, outstanding electrical conductivity and the powerful LSPR effect, Ag has been recognized as one of the most auspicious contender for developing plasmonic photocatalysts [26].

Another strategy to boost $BaTiO_3$'s activity is to prevent the electron-hole pairs from reconciling in the bulk and on the surface during the photocatalytic process. Graphene oxide (GO), an important member of the carbonaceous family, is an excellent choice for scavenging photoinduced electrons due to its potentially ballistic transport capabilities, owing to its numerous graphene layers along which e^-'s can pass through when in contact with $BaTiO_3$. Additionally, because of its high surface area and 2-D planar conjugated structure (π–π), GO deliver a large platform for embedding diverse substrates [27]. These distinctive

properties of GO make it superb applicant to build hybrid structures.[28–31]. Wang et al. [32] reported $BaTiO_3$-graphene composite, that was found to be extremely effective in removing MB when exposed to visible light. Using a $NiTiO_3$/graphene composite, Diab and coworkers were able to achieve H_2 evolution rates of up to 8383 mol/s (h.g) [33]. These GO-incorporated composites allow photoinduced electrons to be quickly get arrested by GO, which not only reduce the e^--h^+ reunion, in addition expands the light absorbency of a SC.

Motivated by the distinguished properties of Ag, $BaTiO_3$, and GO, it is fascinating to integrate their benefits into one ternary system, like Ag-$BaTiO_3$/GO to develop an excellent photocatalyst with multiplex synergism among all the components [34–36].

Taking into account the above facts, we address for the first time the design and synthesis of an Ag-$BaTiO_3$/GO composite by photo-deposition and hydrothermal methods. Inclusion of Ag NPs to this photocatalyst is deemed to enlarge its optical response to a broader range. On the other hand, GO will advance the separation and transportation of photoinduced charges, together with the increase in the photocatalyst's adsorption capacity, thus ameliorating $BaTiO_3$'s photocatalytic behavior. The photocatalytic efficacy of such a ternary composite is examined by removal of CV and OFL, under visible-light illumination. A plausible explanation for its significantly enhanced degrading activities has been proposed based on the findings of PL, EIS and scavenger studies. Moreover, the role of GO and the influence of Ag on degrading activity are thoroughly investigated. Additionally, the photocatalyst's stability, mineralization power is inspected. Furthermore, LC-MS analysis has been used for the identification of the intermediate compounds produced. As far as we know, no prior work has been put forward to date pertaining the development of an Ag-$BaTiO_3$/GO three-component system with multi-channel e- transfer pathways for maximizing the photocatalytic performance of $BaTiO_3$. Such an innovative architecture would offer enormous potential for expansion in light harvesting property, shorter diffuse distances for better charge separation and interfacial charge transport route with greater contact areas as well as abundant active sites for elimination of hazardous pollutants.

3.2. Experimental section

3.2.1. Chemicals and Reagents

Barium chloride dihydrate ($BaCl_2.2H_2O$, 99%), graphite powder (98%), hydrogen peroxide (H_2O_2, 30wt%), ethylenediaminetetraacetic acid ($C_{10}H_{16}N_2O$, 99%), sodium nitrate ($NaNO_3$, 99%), crystal violet dye ($C_{25}H_{30}ClN_3$, 96%), potassium permanganate ($KMnO_4$, 97%), sodium hydroxide (NaOH, 97%), isopropyl

alcohol (C_3H_8O, 99.5%), ascorbic acid ($C_6H_8O_6$, 99%), sulphuric acid (H_2SO_4, 98%), hydrochloric acid (HCl, 35%), ethanol (C_2H_5OH, 99.9%), were procured from Loba Chemie (India). Titanium dioxide (P25-TiO_2, [70% anatase + 30 % rutile form]) was gifted by Degussa Corporation, Germany. Silver nitrate ($AgNO_3$, ≥ 99.0%) was acquired from Sigma-Aldrich. All these chemicals were of analytical grade and were utilized without being purified further. Ofloxacin ($C_{18}H_{20}FN_3O_4$) tablet (50mg) was procured from the pharmaceutical company Cipla Ltd. Triple deionized water utilized throughout the entire study was attained from Organo Biotech Laboratories Pvt. Ltd.

3.2.2. Synthesis of $BaTiO_3$ nanorods

$BaTiO_3$ nanorods were synthesized by a hydrothermal method. The first step was to form solution A, by dissolving 3 mmol of $BaCl_2.2H_2O$ in 20 mL of distilled water. Similarly, suspension B was obtained, by uniformly dispersing 3 mmol of P25-TiO_2 into 20 mL of distilled water. Further, Solution C was formed by dissolving 0.2 mol NaOH in 40 mL of water. The resulting solutions A and B were separately stirred for 1h. Further, the suspension B was progressively poured into the solution A, followed by the solution C, drop by drop. After uniformly mixing and stirring for 1h the resulting mixture was loaded to a Teflon-lined autoclave (100 mL) and then hydrothermally treated at 180°C for 12h. After being allowed to naturally cool to room temperature, the precipitates were centrifuged, washed repeatedly with distilled water and absolute ethanol, then dried at 60°C for 6 hours. The as-obtained white powder was further submitted for a calcination treatment in the muffle furnace at 700ºC for 3h, finally yielding $BaTiO_3$ nanorods.

3.2.3. Synthesis of Ag-$BaTiO_3$ nanocomposite

Ag loaded $BaTiO_3$ nanocomposite was fabricated by a photo-deposition method. As prepared $BaTiO_3$ powder (100 mg) was added in a test tube having 10 ml of isopropanol-water (1:1) mixture along with 2796 □L of (0.01 mM) $AgNO_3$ solution for 5wt% Ag loaded $BaTiO_3$. The test tube was purged with argon gas for 10-15 min under magnetic stirring and then capped with a rubber septum to create an inert atmosphere inside it. Further the mixture in the test tube was illuminated with UV radiations (125W Hg arc, 10.4mW/cm^2) with a constant magnetic stirring for 3 h in a photochemical reactor. The obtained suspension was centrifuged, washed few times with distilled water as well as ethanol, followed by drying at 50°C for nearly half an hour.

3.2.4. Synthesis of Graphene oxide

A modified Hummer's method was employed for synthesizing graphene oxide (GO) from graphite powder[37].

3.2.5. Synthesis of Ag-$BaTiO_3$/GO ternary nanocomposite

Fabrication of the ternary Ag-$BaTiO_3$/GO nanocomposite was carried out by a hydrothermal method. Briefly, 5 mg of GO was ultrasonically dispersed in distilled water-ethanol (40/20 mL) mixture for 2 h, and then 100 mg of as-prepared Ag-$BaTiO_3$ was added to this GO dispersion. After 1 h of stirring the obtained homogeneous suspension was shifted to an autoclave, and hydrothermally treated at 120°C for 3 h. The resulting solution was centrifuged, product was washed thoroughly, and then finally dried in oven at 60°C for 4 h to get the desired Ag-$BaTiO_3$/GO nanocomposite. (5% Ag, 5% GO by wt%).

The overall synthesis route adopted for the formation of Ag-$BaTiO_3$/GO nanocomposite is depicted schematically in **Scheme-3.1.**

3.2.6. Synthesis of $BaTiO_3$-GO nanocomposite

For comparative study, a similar procedure was also followed to prepare the $BaTiO_3$-GO nanocomposite. In brief, GO (5mg) was dispersed in ethanol: water mixture (40:20ml) by ultrasonication followed by the addition of the as-prepared $BaTiO_3$ nanorods (100 mg) to it. After uniformly mixing and stirring for 1h the obtained mixed solution was treated hydrothermally at 120˚C for 3 h. Ultimately, the $BaTiO_3$-GO composite was procured after a centrifugation, washing and drying process.

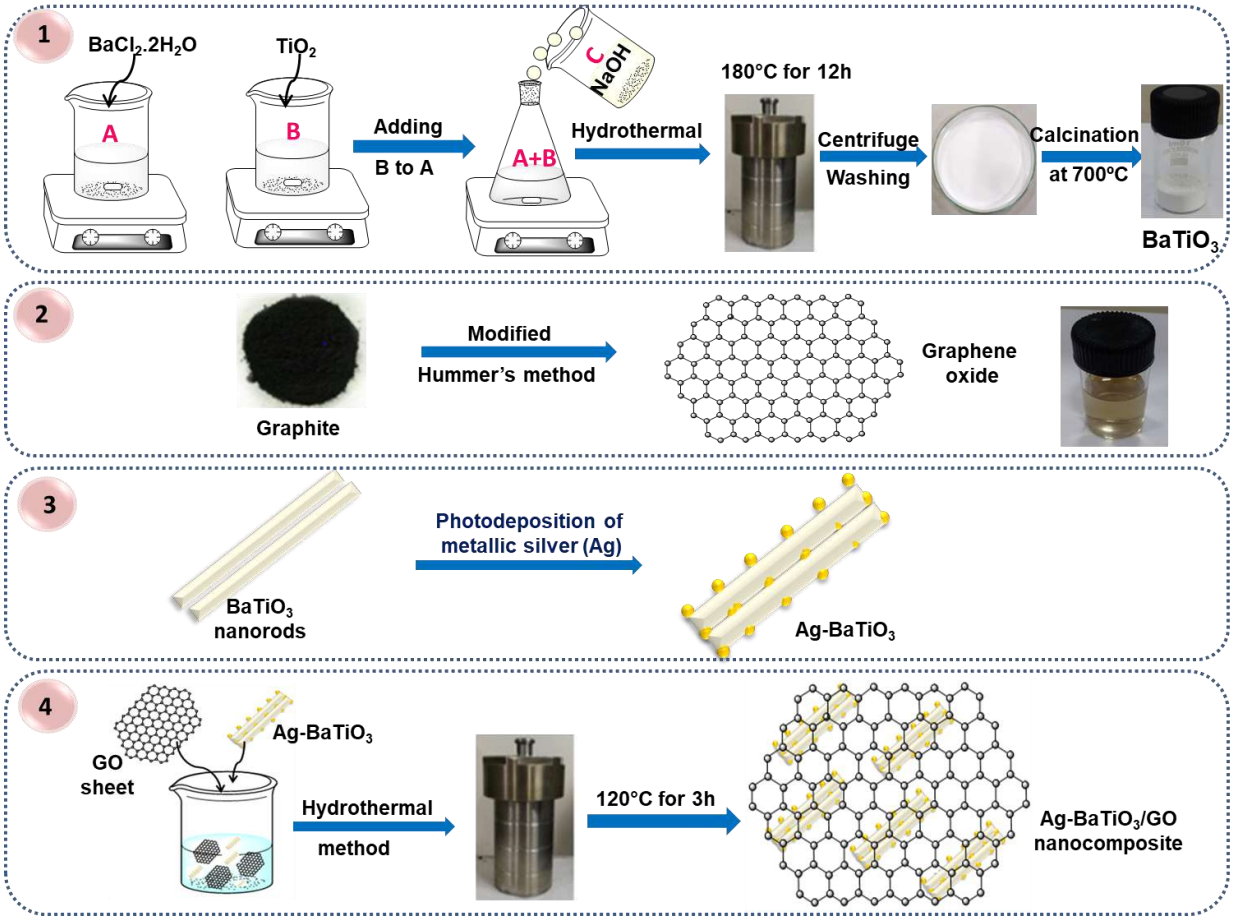

Scheme-3.1: The schematic representation of synthesis of ternary Ag-$BaTiO_3$/GO nanocomposite.

3.2.7. Characterization

The crystal phase of the as-prepared photocatalysts was identified with X-ray diffractometer (PANalytical X'Pert PRO) operating at 45KV with Cu-Kα radiation (k=1.54060˚ Å) Measurements were performed in the range of 10°–90° (2θ). Morphology and structural studies were conducted using FESEM (Carl Zeiss SIGMA 500), HRTEM (JEOL, JEM 2100 PLUS) and elemental composition along with colored mapping were investigated by collaborating the scanning module of the microscope with an EDX analyzer. Besides, the oxidation states of the photocatalysts were identified with XPS (Thermo Fisher ESCALAB Xi+). Raman spectroscopic measurements were performed on a Labram HR, Horiba micro-Raman spectrometer with an 532 nm laser excitation. The optical absorption studies were explored using Avantes DRS instrument with reference standard-$BaSO_4$. A photoluminescence (PL) spectrum of each sample was recorded using a spectrofluorimeter by SHIMADZU, RF-6000 at room temperature at an excitation wavelength of 380 nm. Electrical conductivity measurements were carried out at room temperature using an Solartron analytical

impedance analyzer (Model: SI 1260). UV–Vis spectrophotometer (Shimadzu, UV-2600) was employed for the kinetic investigation of photodegradation of toxic pollutants. Surface area and porosity were analyzed by a surface analyzer Quantachrome Nova-1000, using the BET N_2 adsorption–desorption isotherm at 77.3K. Further, BJH method was utilized for the investigative study of pore size distribution curves.

3.2.8. Photocatalytic activity tests

The photocatalytic performance of pristine $BaTiO_3$, and the various composites (Ag-$BaTiO_3$, $BaTiO_3$-GO, and Ag-$BaTiO_3$/GO) was evaluated by degrading toxic dye CV along with a colorless antibiotic OFL. The photocatalytic reactions were carried out in different test tubes. For the degradation of CV, about 5 mg of each photocatalyst was dispersed in 5 mL of 10 ppm CV solution. Before exposure to light, the above suspensions were magnetically stirred in the dark for 30 minutes to achieve adsorption-desorption equilibrium. After that, the test tubes consisting different catalysts were illuminated with a visible light source (50W LED lamp, Wipro Garnet B22, having an intensity ~100W/m^2, $\lambda > 360$ nm) for 75 min. Similarly, 10 mg of each photocatalyst was mixed with a 5 mL solution of 20 ppm OFL in different test tubes and stirred in dark for 60 minutes and later on irradiated with visible light for 100 min. At definite intervals of time, the catalysts were removed from the test tubes by centrifugation at 7,000 rpm for 5 min so as to eliminate any residual solid catalyst particles. Following the separation, the absorbance spectra of CV and OFL were examined at λ_{max}= 589 nm and λ_{max} = 288 nm, respectively.

The photodegradation efficiency was calculated by the below-mentioned equation:

$$(\%)\ \text{Degradation} = \{(C_0 - C_t)/C_0\} \times 100 \quad (1)$$

where, C_0 and C_t represents the initial and residual concentration of pollutants before and after the light irradiation at time '0' and certain time 't' respectively.

To examine the mineralization ability of Ag-$BaTiO_3$/GO, the total organic carbon (TOC) analysis was carried out through titrimetric technique.

The TOC value using distilled water as blank was determined by the below equation:

$$TOC\ (mg/L) = \frac{(Blank - Sample) \times Normality\ of\ FAS \times 12000}{Sample\ volume \times 4} \quad (2)$$

The mineralization at the end of the reaction was evaluated using the following equation:

$$Mineralization\ (\%) = \frac{TOC\ initial - TOC\ final}{TOC\ inital} \times 100\% \quad (3)$$

Apparent quantum yield (AQY) of Ag-$BaTiO_3$/GO ternary photocatalyst was estimated by [38] :

$$AQY\ (\%) = \frac{2 \times No.of\ pollutant\ molecules\ degraded\ in\ given\ time}{No.of\ incident\ photons} \times 100\% \quad (4)$$

The photodegradation intermediates of CV and OFL were further determined by LC-MS technique, (Waters QTOF Micro). For OFL, the mobile phase comprised of acetonitrile and 1% formic acid mixture (30:70 v/v), whereas water and acetonitrile (50:50, v/v) worked as mobile phase for CV detection.

3.3. Results and Discussion

3.3.1. Structural study

XRD analysis

Fig. 3.1 presents the XRD diffractogram of as-fabricated GO, $BaTiO_3$ and $BaTiO_3$-GO, Ag-$BaTiO_3$, Ag-$BaTiO_3$/GO samples. Pure GO exhibits a characteristic diffraction peak at about 2θ = 11.6˚ which belongs to the (001) crystal plane, indicating the successful oxidation of graphite to graphene oxide [39]. Further, the diffraction peaks located at 2θ values 22.46˚, 31.59˚, 39.0˚, 45.60˚, 50.92˚, 56.43˚, 65.76˚, 70.82˚, 75.26˚, 79.41˚, 83.72˚ matches well with the (100), (101), (111), (200), (210), (211), (220), (212), (310), (311) and (322) lattice planes of tetragonal structure $BaTiO_3$ (JCPDS No. 75-2122) respectively [40]. The two binary samples: $BaTiO_3$-GO, Ag-$BaTiO_3$ as well as the ternary Ag-$BaTiO_3$/GO sample, were found to have diffraction peaks that were identical to those of pristine $BaTiO_3$. However, along with the prominent peaks of $BaTiO_3$, the XRD pattern of the Ag-$BaTiO_3$ and Ag-$BaTiO_3$/GO shows one additional low-intensity peak, at 2θ value 38.1˚, corresponding to (111) plane of metallic Ag (JCPDS No. 040783) marked with "♣" asterisks in the graph [41]. The fact that there was no evident change in the $BaTiO_3$ peak position, further supports the idea that the Ag NPs are well loaded or dispersed on the surface rather than being incorporated into the $BaTiO_3$ lattice. It is noteworthy that the typical XRD peak of GO was not observed in the patterns of $BaTiO_3$-GO and Ag-$BaTiO_3$/GO, most likely because of its relatively low content. Besides, the appearance of relatively sharp peaks as well as absence of any other extra peaks indorses the high purity and crystalline nature of all the synthesized photocatalysts.

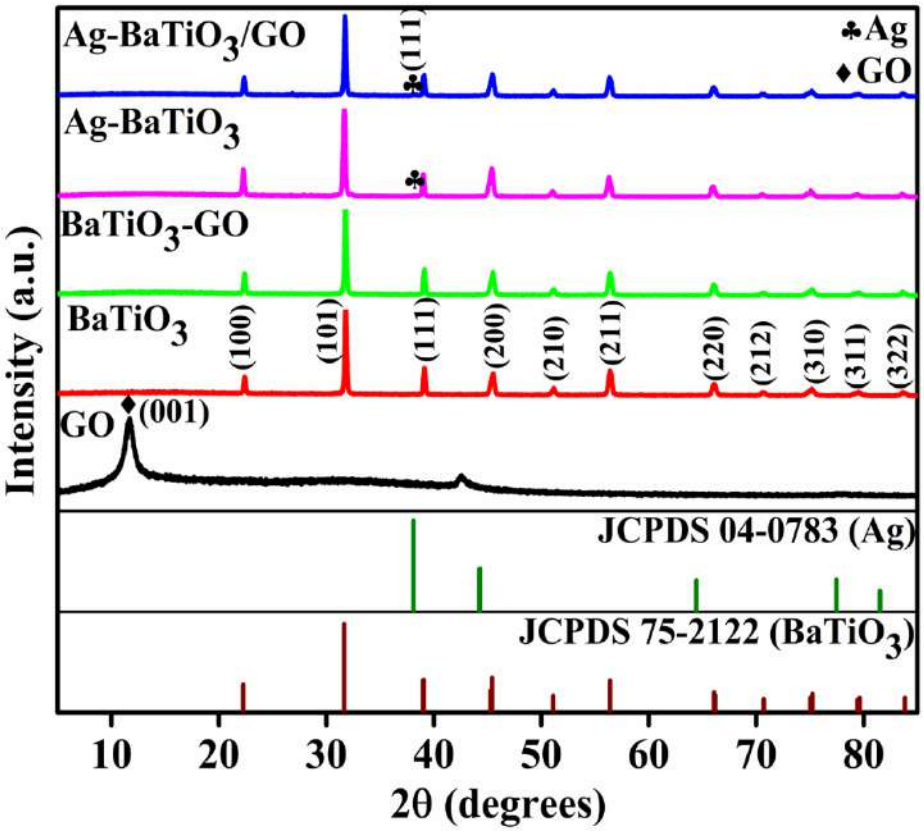

Fig. 3.1: XRD patterns of as-synthesized GO, bare $BaTiO_3$, binary $BaTiO_3$-GO, Ag-$BaTiO_3$ and ternary Ag-$BaTiO_3$/GO nanocomposites.

3.3.2. Morphological study

FE-SEM, EDS-Mapping and HR-TEM analysis

To understand the morphological and structural characteristics of prepared photocatalysts, FESEM **(Fig. 3.2, Fig. 3.3)**, TEM and HRTEM **(Fig. 3.3(a)-(f))** analysis were performed. As can be seen from **Fig. 3.2(a)**, graphene oxide (GO) exhibits a rippled and crumpled layered morphology with several stacking layers of 2-D graphene sheets. The FESEM image of the Ag-$BaTiO_3$/GO nanocomposite **(Fig. 3.2(b)-(d))** reveals that pure $BaTiO_3$ exhibits a nanorod like structure with a average length ranging from 400-450 mm and diameter of 200-250 nm along with a decoration of spherical Ag nano-particles (brilliant bright spots) all homogeneously embedded onto the surface of the GO nanosheets. These images imply perfect formation of the desired ternary hybrid with intimate contact.

Additionally, EDS spectrum and elemental colored mapping images **(Fig. 3.3 (a-b))** validated the co-existence and uniform distribution of Ba (yellow), Ti (azure), O (Kelly green), Ag (emerald green) and C (red) elements in the hybrid.

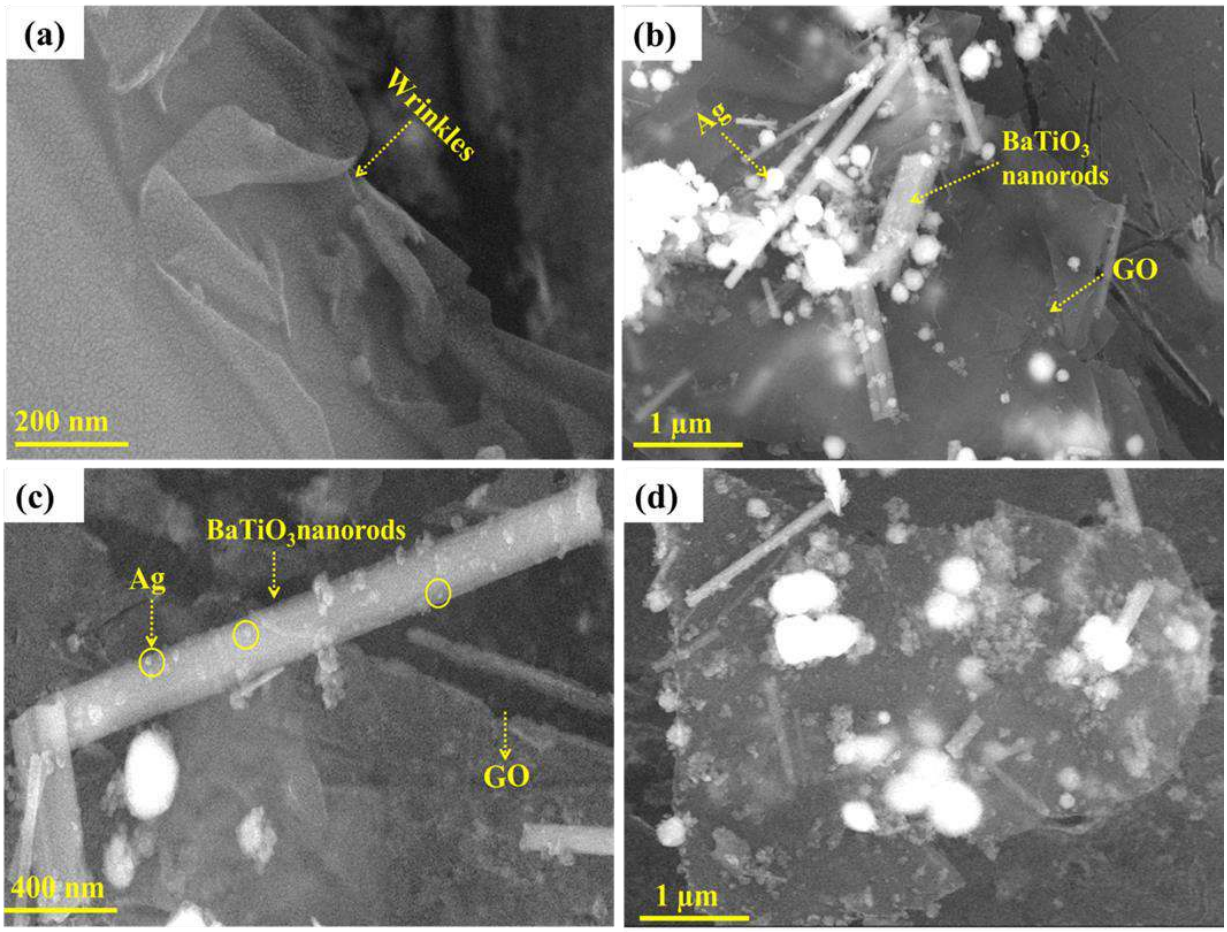

Fig. 3.2: FE-SEM images of (a) GO, and (b-d) Ag-$BaTiO_3$/GO nanocomposite.

TEM analysis was carried out to further examine the effective integration of Ag, $BaTiO_3$, and GO into the ternary system. **Fig. 3.4(a)** provides evidence for the stacked layered morphology of GO sheets with micrometer-long wrinkles. **Fig. 3.4(b-d)** depicts the TEM images of the ternary composite. The photographs clearly reveal the accumulation of Ag-deposited $BaTiO_3$ nanorods on wrinkled sheets like GO. Metallic Ag NP_S with size of 25-35 nm can be spotted as dark-colored dots. These results are consistent with the corresponding FESEM images. Besides, the HRTEM micrographs **(Fig. 3.4(e))** clearly displays two separate sets of lattice fringes one belonging to the (111) diffraction plane of metallic Ag with interplanar distance (d) of 0.28 nm between them and the other with a lattice fringe of 0.23 nm, which corresponded to the (110) crystal plane of tetragonal $BaTiO_3$. In addition, GO nanosheets served as the ground for both photo-deposited Ag and $BaTiO_3$, as indicated in **Fig. 3.4(e)**. Similarly, the SAED pattern **Fig. 3.4(f)**, displaying several discrete concentric rings with superimposed bright spots, corresponding to characteristic rings of Ag [(111), (220)], [(101), (220), (200), (322)] of $BaTiO_3$ and (001) plane of GO, which further indicates that Ag

deposited $BaTiO_3$ nanostructures are nicely grown over graphene oxide sheets [42]. Overall, both the FE-SEM and HR-TEM investigations confirm the formation of close contact and multiple electron transfer pathways existing among the individual components (Ag NPs, $BaTiO_3$ NRs and GO sheets) in ternary system, which would be resulting in an overall enrichment in its photocatalytic efficiency.

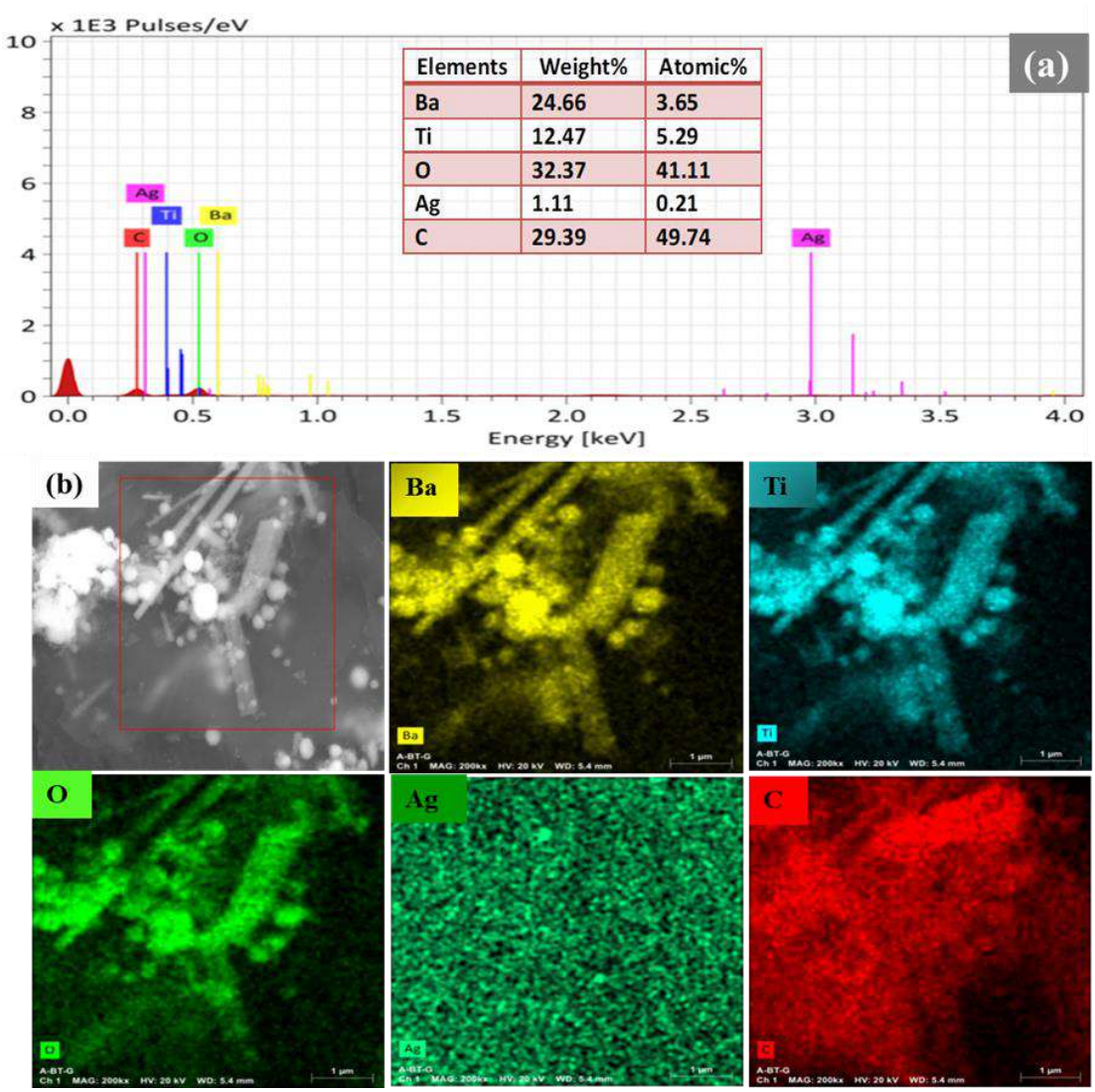

Fig. 3.3: (a) EDX spectrum; (b) elemental color mapping images of different elements (Ba, Ti, O, Ag, C) present in Ag-$BaTiO_3$/GO nanocomposite.

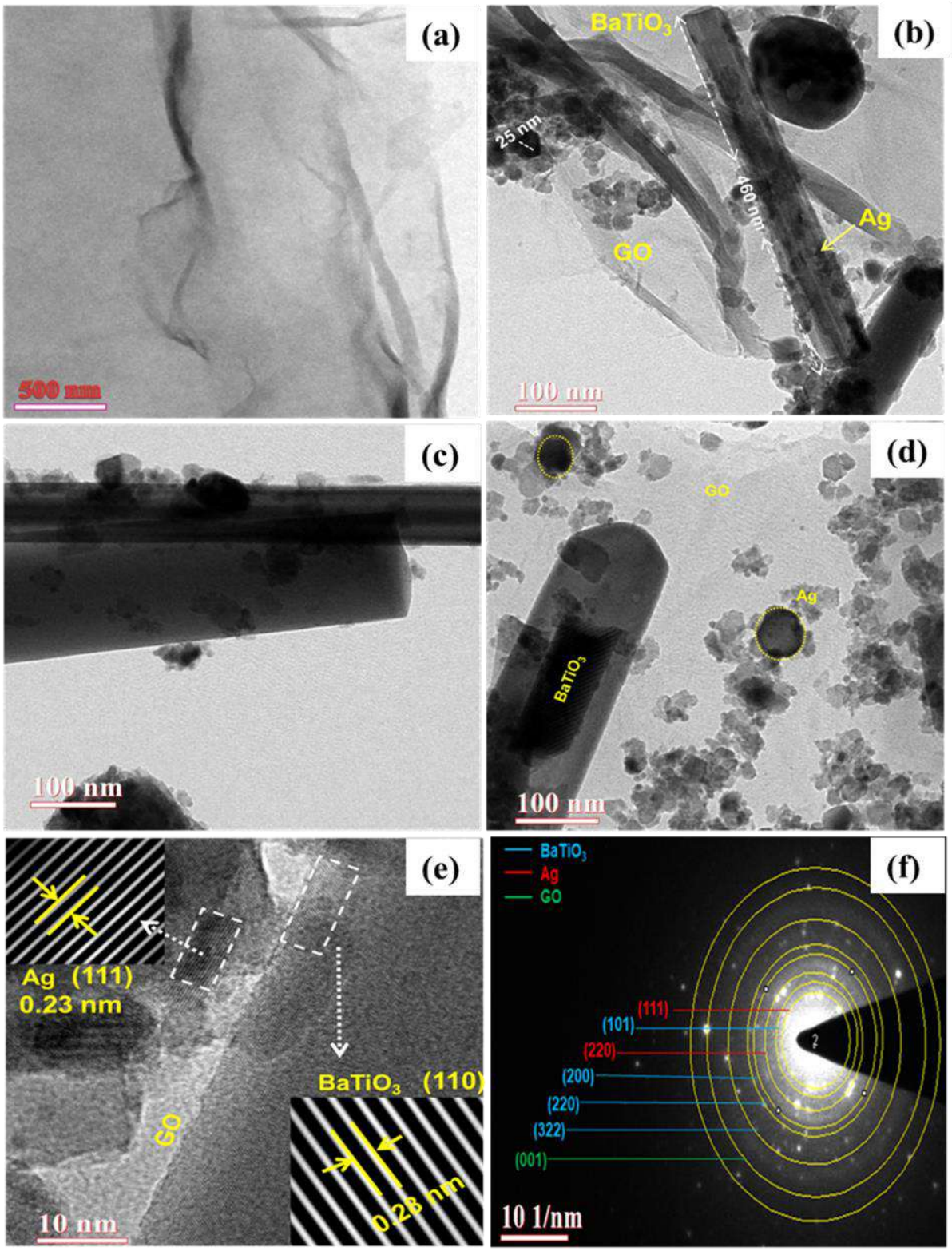

Fig. 3.4: HR-TEM images of (a) GO, (b-d) Ag-$BaTiO_3$/GO nanocomposite (e) corresponding Lattice fringes and (f) SAED pattern for Ag-$BaTiO_3$/GO photocatalyst.

3.3.3. XPS analysis

For analyzing the surface chemical composition and oxidation state of each element in the ternary Ag-$BaTiO_3$/GO composite, XPS measurements were performed, and the outcomes are presented in **Fig. 3.5**.

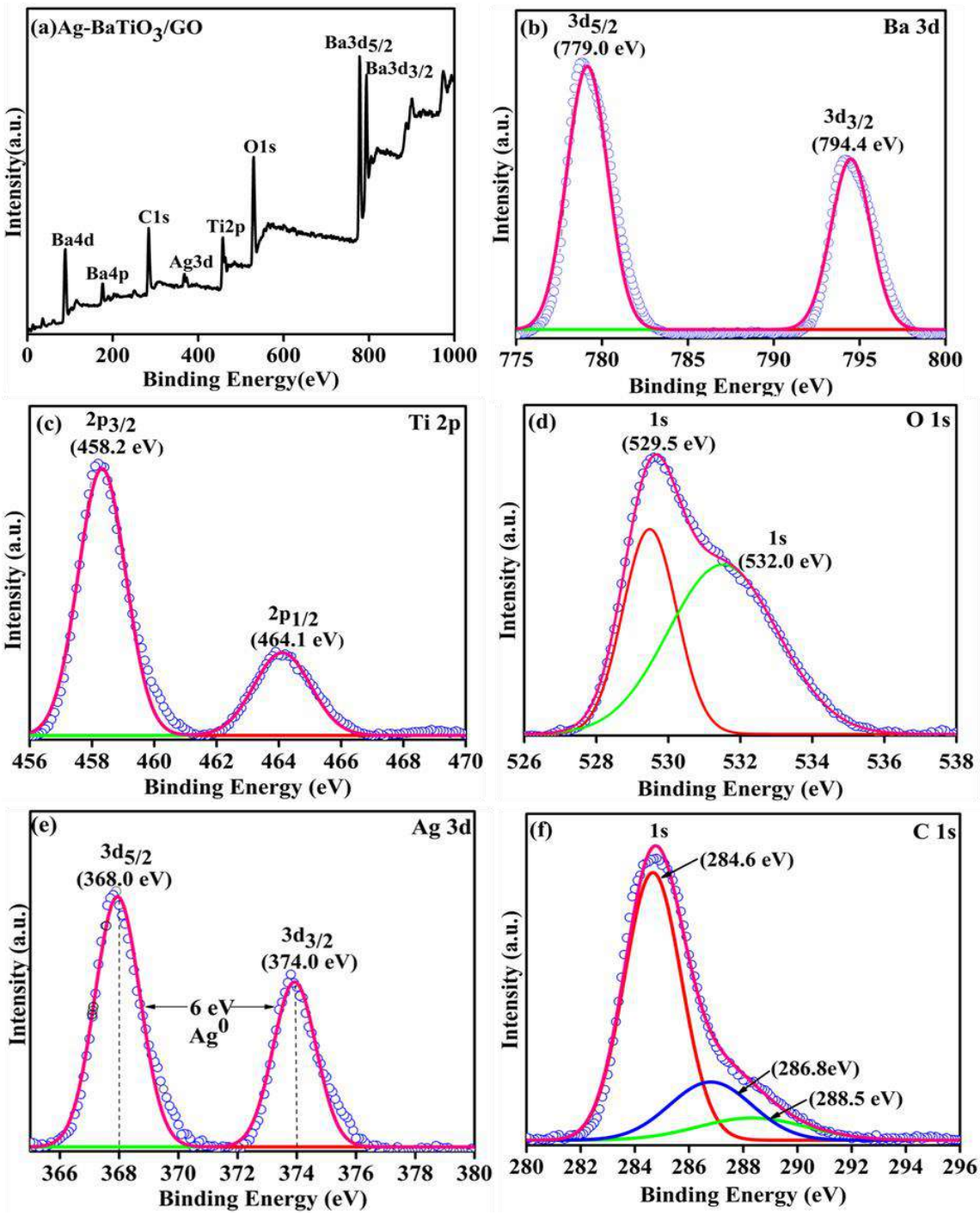

Fig. 3.5: XPS spectra of Ag-$BaTiO_3$/GO nanocomposite (a) survey scan (b) Ba 3d, (c) Ti 2p, (b) O 1s, (d)

Ag 3d, and (e) C 1s spectrum.

As anticipated, the elemental peaks of Ba, Ti, O, Ag, and C can be clearly observed in the survey spectrum **(Fig. 3.5(a))**. The XPS spectrum of Ba (3d) **(Fig. 3.5(b))** manifests two peaks at 794.4 eV and 779.0 eV representing the splitting of the Ba $3d_{5/2}$ and Ba $3d_{3/2}$ spin states, respectively, which suggest the presence of Ba^{+2} in the composite. **Fig. 3.5(c))** illustrates two binding energy peaks (B.E.) positioned at 458.2 eV and 464.1 eV which can be identified and designated to the distinct Ti $2p_{3/2}$ and Ti $2p_{1/2}$ signals, witnessing the presence of titanium in four oxidation state (Ti^{4+}). **Fig. 3.5(d)** displays the deconvoluted spectrum of O1s, fitted into two different peaks. One at a (B.E.) of 529.5 eV is allocated to oxygen in the $BaTiO_3$ crystal lattice, and other peak at 532.0 eV is ascribed to the oxygen atom of hydroxyl groups (O-H) adsorbed on the surface of $BaTiO_3$ or graphene oxide in the composite. The spectrum of Ag 3d **(Fig. 3.5(e))** contains two peculiar peaks, Ag $3d_{5/2}$ (368.0 eV) and Ag $3d_{3/2}$ (374.0 eV). The 3d doublet's spin-orbit splitting value is 6.0 eV, which is compatible with the typical spin energy separation of silver in zero oxidation state (Ag^0), validating the presence of Ag metal in the ternary composite [32,43,44]. Furthermore, the C1s XPS spectrum, **(Fig. 3.5(f))** is deconvoluted into 3 peaks with B.E. of 284.6, 286.8 and 288.5 eV, respectively. Peak at 284.6 eV corresponds to a C-C bond with the "sp^2"orbital. Additional peaks positioned at 286.8 eV, 288.5 eV attributes to the C-O and C=O, demonstrating the presence of functional groups with O_2 in the GO [45].

3.3.4 Porosity and Surface area analysis

Fig. 3.6(a) represents the BET surface area with corresponding BJH pore-size distribution graphs of bare $BaTiO_3$ and Ag-$BaTiO_3$/GO ternary nanocomposite, respectively. According to the IUPAC classification, both samples' nitrogen (N_2) adsorption-desorption isotherms showed type-IV Langmuir patterns with distinctive H3-shaped hysteresis loops, indicating their multilayer and mesoporous behavior. The inset is their pore size distribution plots. Pore size of both the samples is mainly observed to be distributed between 2 and 20 nm, which further confirms that the catalysts have properties as of mesoporous material. Mesoporosity is usually of wrinkled, sheet-like structure, and this result is consistent with FESEM images. As depicted in **Table-3.1**, the Ag-$BaTiO_3$/GO composite (22.786 m^2/g) possesses two times larger BET specific surface area in comparison with pristine $BaTiO_3$ (11.247 m^2/g). Additionally, it was noted that the ternary composite's pore volume and size distribution were both somewhat increased. The enlargement observed in the various BET parameters could be ascribed to the incorporation of GO with special 2-D structural features along with the decoration of metallic Ag NPs onto the $BaTiO_3$ surface, which would offer abundant active sites for the adsorption of contaminants, and facilitate rapid transportation of reactants and

products thus, beneficial for attaining high photocatalytic activity.

S.No.	Photocatalyst	Surface area (m^2g^{-1})	Total Pore Volume (cm^3g^{-1})	Mean Pore diameter (nm)
1	$BaTiO_3$	11.247	0.021	2.246
2	Ag-$BaTiO_3$/GO	22.786	0.063	2.550

Table-3.1: Textural properties of pristine $BaTiO_3$ and ternary Ag-$BaTiO_3$/GO nanocomposite.

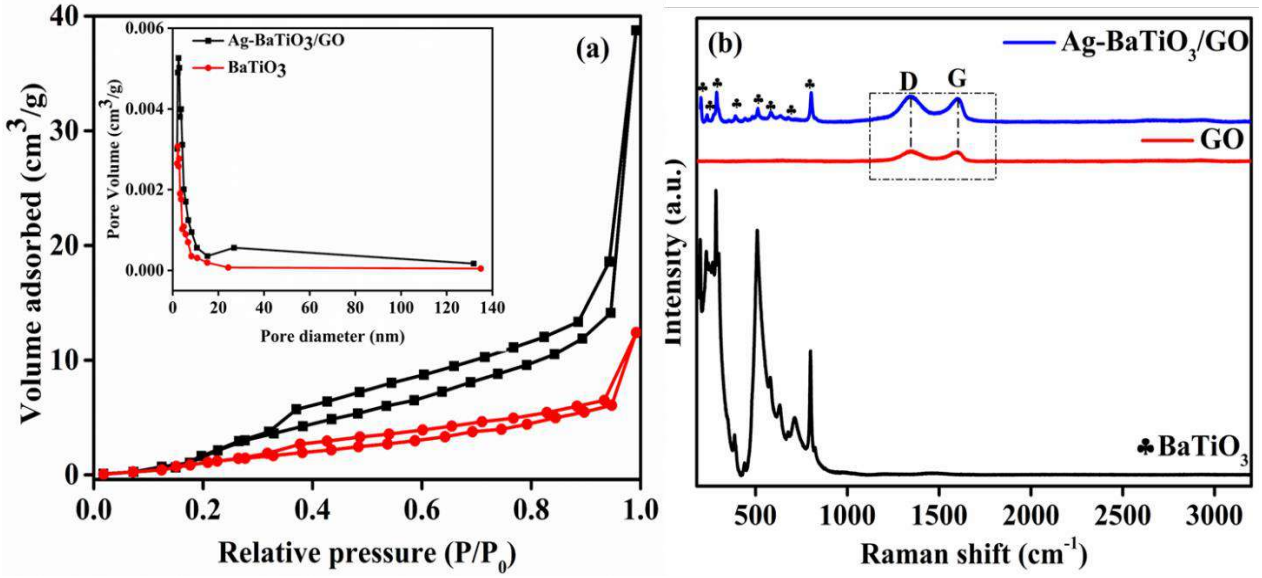

Fig. 3.6: (a) N_2 adsorption isotherms and the corresponding BJH pore size distributions curves (inset) of $BaTiO_3$ and Ag-$BaTiO_3$/GO nanocomposite. (b) Raman spectra of $BaTiO_3$, GO and the Ag-$BaTiO_3$/GO nanocomposite.

3.3.5 Raman analysis

Fig. 3.6(b) illustrates the comparative Raman spectra of GO, Ag-$BaTiO_3$/GO, and $BaTiO_3$ samples respectively. Raman spectrum of pure $BaTiO_3$ exhibits several characteristic peaks positioned at 205, 229, 281, 302, 380, 515, 577, 629, 718 and 806 cm^{-1} which are associated with the [A1(TO), E(LO)], [A1(TO)], [B1, E(TO + LO)], [A1(LO) + E(TO)], [A1, E(TO)], [A1, E(LO)], modes of $BaTiO_3$[46–48]. Sharp peak seen at 302 cm^{-1} is the clear evidence of the existence of $BaTiO_3$ in the tetragonal phase, which is consistent with the XRD findings. The peaks appearing at low wavenumbers 205, 229 cm^{-1} are mostly caused by the vibrations between the atoms of Ba and O. broad and sharp signals at 281 and 302 cm^{-1} attributes to the O-

Ti-O bending vibration, i.e due to the vibrations within the TiO6 group of $BaTiO_3$. Band at 515 cm^{-1} is associated with the asymmetric stretching vibration, a vibration that occurred by the displacement of oxygen atoms. Likewise, the higher frequency peak assigned at 718 cm^{-1} represents the symmetric Ti-O stretching vibration while existence of the small peak at 806 cm^{-1} might be related to the internal lattice defects and/or vacancies. Besides, the raman spectrum of GO, discloses 2 prominent bands centered at 1349 and 1600 cm^{-1} which were ascribed to the renowned D and G bands of GO. The D band is related to the breathing modes of rings of κ-point photons with A_{1g} symmetry and G band is assigned to E_{2g} mode of sp^2 hybridized carbon atoms[45]. Further, the raman analysis of Ag-$BaTiO_3$/GO composite, reveals the existence of similar characteristic peaks corresponding to pure $BaTiO_3$ as well as D and G bands originating from GO. This combination strongly witnesses the successful formation of Ag-$BaTiO_3$/GO nanohybrid. However, in comparison with $BaTiO_3$, the peak intensities of the ternary hybrid decreased greatly, which might be due to the surface coverage by GO, this additionally supports the intimate contact developed between the individual components.

3.3.6. Optical and charge transfer properties

UV-Vis Diffuse reflectance spectra

To further study the light absorption characteristics of $BaTiO_3$ nanorods, GO-$BaTiO_3$, Ag-$BaTiO_3$, and Ag-$BaTiO_3$/GO nanocomposites, the UV-vis DRS spectra was examined, and the outcomes are presented in **Fig. 3.7(a).** The spectrum of pristine $BaTiO_3$ shows some absorption in visible region, as implied by its absorption onset around 428 nm. The observed absorption onset in synthesized $BaTiO_3$ corresponds to the electronic transitions from its VB (O^{2-}2p) to the CB (Ti^{3+}3d). In addition, the effect of morphology i.e. rod like shape of $BaTiO_3$ adds to its light harvesting ability towards the visible region. Although the extent of absorption in this region is very low, but it is not negligible, e^-–h^+ pairs can be generated, upon irradiation with visible light. Notably, the DRS spectra of binary composite (GO-$BaTiO_3$) reveal that the incorporation of GO significantly improves the light absorption property of $BaTiO_3$ with a continuous absorption tail towards the visible light region (400-800 nm). This enhancement in the absorption power might be credited to the presence of carbon centers on $BaTiO_3$ surface, which typically functions as a photosensitizer, and reduces the reflection of light[49]. Moreover, a new strong and broad absorption band (plasmonic band) in the range of 450-730 nm is noticed in the Ag loaded $BaTiO_3$ sample, which is due to the red shift of the absorption wavelength resulting from the LSPR of metallic Ag NPs[50] . Besides this, the intensity and light absorption range of Ag-$BaTiO_3$/GO further gets extended towards the higher wavelength, making the ternary composite the best

choice for harvesting visible light among all the candidates, indicating that Ag, $BaTiO_3$, and GO work together in a synergistic manner.

Additionally, the color changes observed **(below Fig. 3.7)** from typical white ($BaTiO_3$) to finally dark grey (Ag-$BaTiO_3$/GO) also confirm the increment in light absorption property of the modified catalysts towards the visible light region of the spectrum.

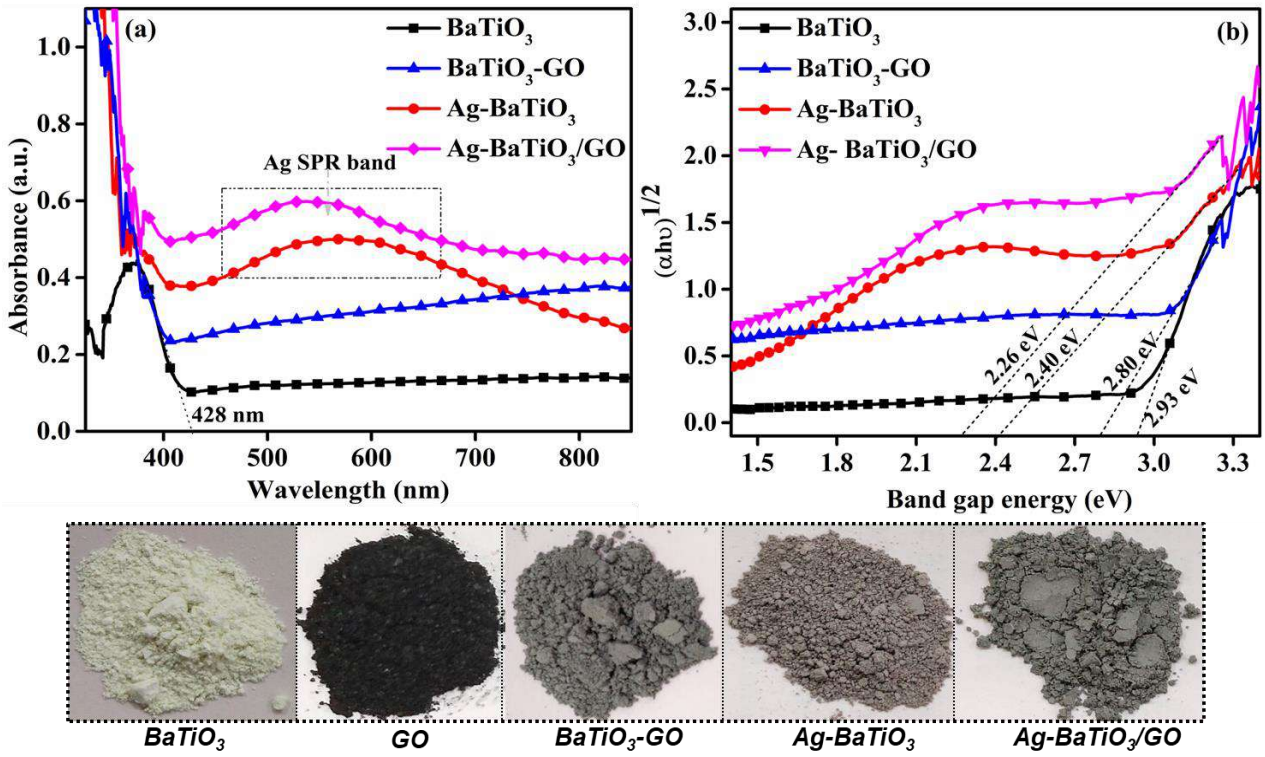

Fig.3.7: (a) UV-vis diffuse reflectance spectra and corresponding (b) Tauc plots of pristine $BaTiO_3$, binary $BaTiO_3$-GO, Ag-$BaTiO_3$ and ternary Ag-$BaTiO_3$/GO nanocomposites.

The bandgap energy of the as-prepared photocatalysts was also calculated by employing Tauc's equation:

$$ahv = A\,(hv - E_g)^{1/2} \quad (5)$$

Here α denotes the coefficient of absorption, A = constant, *h* = Planck's constant, υ = light's frequency and E_g is the energy of the bandgap. As displayed in **Fig. 3.7(b)**, the E_g values of pristine $BaTiO_3$, GO-$BaTiO_3$, Ag-$BaTiO_3$ and Ag-$BaTiO_3$/GO samples, were formulated to be 2.93 eV, 2.80 eV, 2.40 eV and 2.26eV, respectively. It is apparent that the E_g value reduces markedly from 2.93 to 2.26 eV upon the simultaneous addition of Ag and GO onto the $BaTiO_3$ surface. In comparison with $BaTiO_3$, Ag-$BaTiO_3$/GO catalyst possesses a narrowed band gap. From the results of the DRS spectra, it can be inferred that the strengthening of the visible-light harvesting capability here would favour the production of abundant charge carriers and

consequently, could boost the photocatalytic performance of the fabricated ternary composite.

Photoluminescence measurement

Fig. 3.8 displays the PL emission spectra of all the synthesized samples at a 335 nm excitation wavelength. It has been observed that, the PL spectrum of pure $BaTiO_3$ nanoparticles exhibits emissions in both the UV [Near band gap emission (NBE)] and visible regions, [Defect-related deep level emission (DLE)]. A sharp, UV emission peak at 380 nm (NBE), is typically caused by band gap emission, which is the reconciliation of photogenerated e^- - h^+ in conduction as well as valence bands. Usually, because of the charge transference from the Ti^{3+} ion to a nearby O^{2-} ion in the $TiO6^{8-}$ octahedron.

And other two weaker, green emission bands at 468 and 535 nm (DLE) could be the result of various intrinsic structural defects like oxygen vacancies, OH^- defects, surface states, along with the noncentral symmetric Ti^{3+} in the nanophase $BaTiO_3$. Additionally, all of the samples display similar emission peaks centered at 380, 468, and 535 nm [51,52]. Based on the PL results, it can be elucidated that the lifetimes of the photoinduced carriers in the as-prepared photocatalysts decrease in the order Ag-$BaTiO_3$/GO > Ag-$BaTiO_3$ > $BaTiO_3$-GO > $BaTiO_3$, which was also found to be in good accordance with the photocatalytic activity results. Among all the samples, $BaTiO_3$ had the highest PL intensity, implying a high rate of recombination and reduced efficiency of photoinduced charge carrier separation. Meanwhile, the intensity of PL peaks diminished sharply, upon the introduction of Ag and GO. This significant PL quenching is due to the effective migration of photoexcited electrons from $BaTiO_3$ onto the surfaces of silver and graphene oxide. Actually, the Schottky barrier generated at the Ag-$BaTiO_3$ interface is supposed to behave like electron reservoir to impede the reunion of electron-hole couples. Also, due to the excellent electronic conductivity of GO, there exists an easy pathway for the transference of electrons in the $BaTiO_3$-GO composite resulting in a low charge recombination rate. Besides, the highest PL quenching happens in the ternary Ag-$BaTiO_3$/GO composite. This suggests that the synergistic interaction between the photo-deposited Ag NPs, $BaTiO_3$, and GO, as well as the formation of multiple electron transfer channels, all together significantly prolongs the lifetime of photoinduced charge carriers which ultimately benefits in the adequate charge separation, and greater suppression of PL intensity.

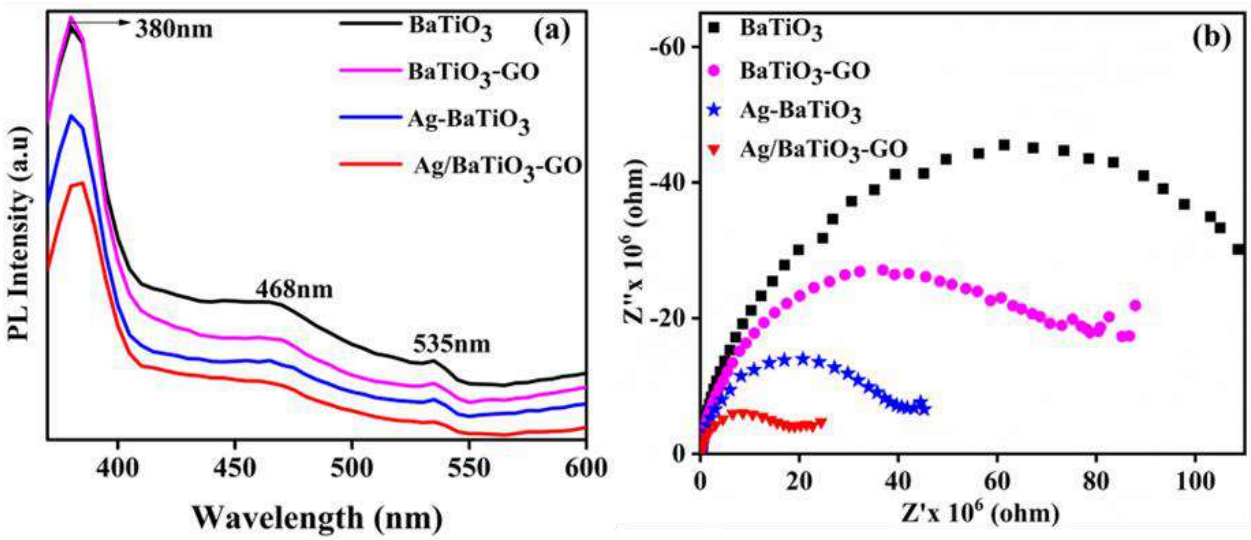

Fig. 3.8: (a) Photoluminescence (PL) spectra (b) Nyquist impedance plots of all the as-synthesized photocatalysts.

Impedance analysis

Furthermore, impedance measurements were performed to probe the interfacial charge transfer behavior of the as-fabricated samples. In general, the arc radius in the EIS Nyquist plot depicts the electron transfer resistance of the photocatalyst, and a smaller arc radius indicates higher conductivity, an effective charge separation rate with less resistance and a lower rate of electron-hole pair reconciliation [53]. The arc radii of the four samples, as displayed in **Fig. 3.8 (b)** followed the sequence of $BaTiO_3$ > $BaTiO_3$-GO > Ag-$BaTiO_3$ >Ag-$BaTiO_3$/GO composites. Comparatively, the ternary composite Ag-$BaTiO_3$/GO possess the smallest arc radius among all the samples, suggesting that modifying $BaTiO_3$ with both Ag and GO could promote its conductivity, accelerate the charge transference and minimize the extent of recombination of photoinduced carriers. Hence, the combined results of PL spectra and EIS measurements confirmed that Ag-$BaTiO_3$/GO photocatalyst possesses superior charge carrier separation and migration capacity.

3.4. Photocatalytic activity

3.4.1. Photodegradation reaction

The photocatalytic performance of the Ag-$BaTiO_3$/GO ternary composite was evaluated first by studying the visible-light induced degradation of the highly toxic dye Crystal Violet (CV) **(Fig.3.9)**. For comparison, the removal of CV over pristine $BaTiO_3$, binary (Ag-$BaTiO_3$, and $BaTiO_3$-GO), composites were also performed. In addition to photocatalysis, tests on photolysis and adsorption were also conducted, and results

are displayed in **Fig. 3.9(a)**. In the absence of photocatalyst (photolysis), only 14% of CV is observed to be degraded after 75 min of visible-light treatment, indicating its high stability.

After 30 min of dark adsorption, the adsorption efficiencies of various photocatalysts were calculated as $BaTiO_3$: 16.27%; Ag-$BaTiO_3$: 22.90%; $BaTiO_3$-GO : 26.72%, and Ag-$BaTiO_3$/GO : 31.45%. In comparison with the unmodified $BaTiO_3$, all other samples exhibit higher adsorption towards CV, and when both Ag and GO are incorporated onto $BaTiO_3$'s surface, its adsorption capacity becomes the largest, which is attributed to the increased BET surface area and adsorption sites. Further, in order to boost the removal efficiency, the photocatalytic process was preceded by the irradiation of visible light. After being exposed to light for 75 min, the catalytic ability of the as-prepared photocatalysts progress in the following order: Ag-$BaTiO_3$/GO (98.5%) > Ag-$BaTiO_3$ (83.4%) > $BaTiO_3$/GO (75.3%) > $BaTiO_3$ (47.6%) **{Fig. 3.9(a)}**. Thus, the multicomponent sample with Ag and GO synergy with $BaTiO_3$ demonstrates dynamic CV removal, which is consistent with the earlier characterization results.

Additionally, using a pseudo-first-order rate kinetics equation, the associated reaction rate constants (k) were quantitatively determined,

$$\{\ln(C_t/C_0) = -kt\} \quad (6)$$

Here C_0 is the starting concentration of CV, C_t is its concentration at the time (t), and k denotes the rate constant (min^{-1}).

Fig. 3.9(b) compares the values of $\ln(C_t/C0)$ for the various samples as a function of the amount of time they were exposed to light. Interestingly, the highest CV degradation rate constant of (0.053 min^{-1}) was observed for the Ag-$BaTiO_3$/GO hybrid photocatalyst which is about ~6.62, ~2.94, and 2.208 folds greater than those of the pristine $BaTiO_3$ NRs, $BaTiO_3$-GO, and Ag-$BaTiO_3$, respectively.

.

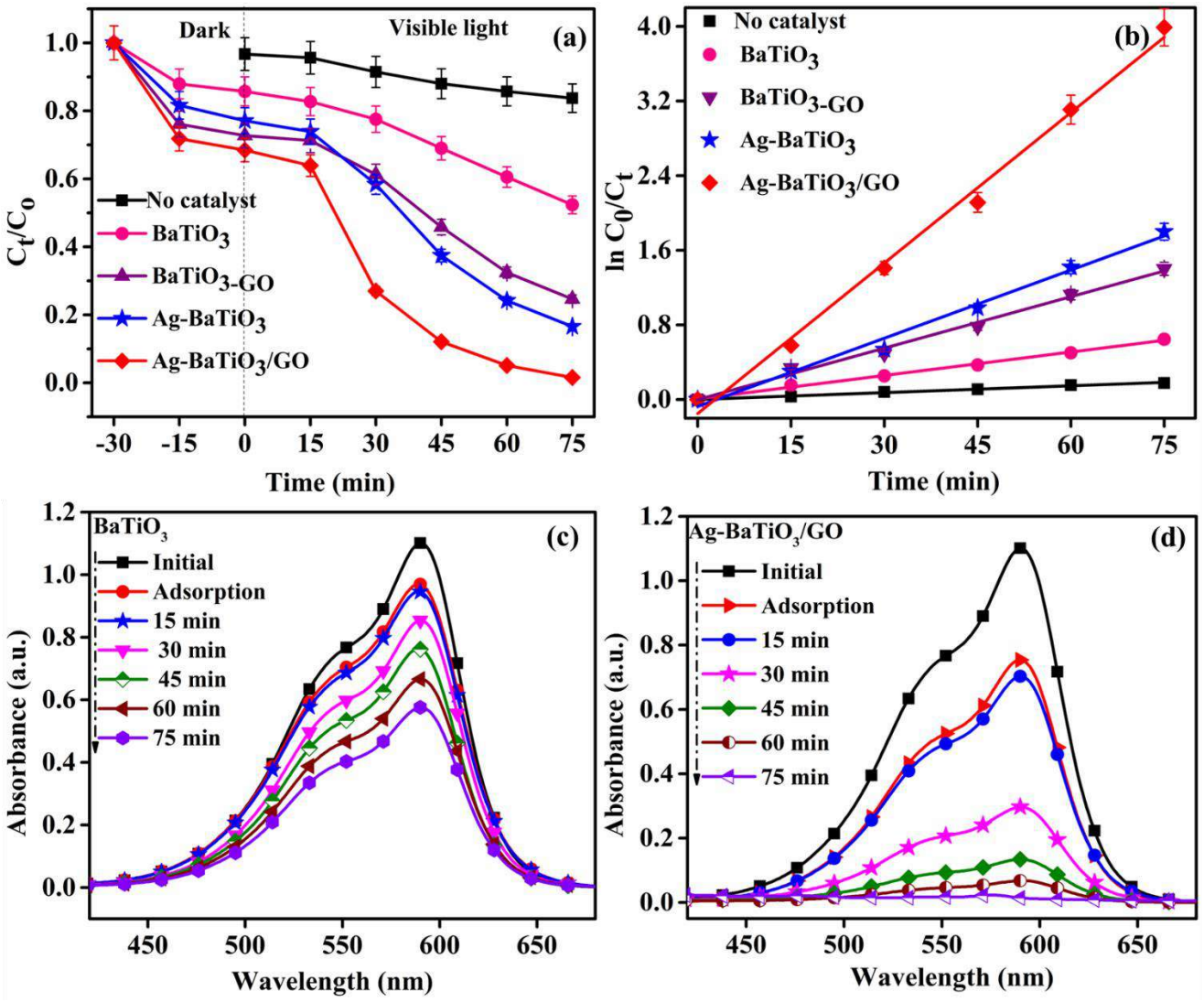

Fig. 3.9: (a) Time course-kinetic plots and (b) corresponding variations in apparent reaction rate constants (k) values obtained for the degradation of CV dye in the presence of different photocatalysts (c) Time-dependent UV-vis spectral absorption changes of CV solution over pristine $BaTiO_3$ and (d) Ag-$BaTiO_3$/GO ternary nanocomposite under 75 min LED-light irradiation.

Fig.3.9(c-d) illustrates the changes in the UV-vis absorption spectrum of the CV dye solution over various catalysts (bare $BaTiO_3$ and the ternary Ag-$BaTiO_3$/GO sample) at different irradiation times. It is clearly evident that as illumination time increases during the degradation process, the intensity of the characteristic maximum absorption peak of CV at 589 nm is observed to gradually diminish by both catalysts. The ternary sample, however, experienced a much greater decrease after 75 minutes of visible light exposure. The complete flattening trend of the CV spectral profile highlights the superior photocatalytic response of Ag-$BaTiO_3$/GO suggesting that the synergy of both metallic silver and graphene oxide is helpful in enhancing

the photocatalytic activity of $BaTiO_3$

Besides this, in order to assess the effectiveness of using Ag-$BaTiO_3$/GO in the treatment of antibiotic pollutants, a colorless pollutant (ofloxacin) was selected. The general trend in the results of OFL photodegradation is similar to that for CV elimination. Photolysis (without catalysts) was found to be ineffective for OFL elimination as only about a ~10% reduction in the absorbance was accounted for 100 min of light treatment. The adsorption efficiency of the ternary nanocomposite (33%) was the highest among others and almost threefold compared to the bare $BaTiO_3$ (11.4%). Notably, the ternary nanocomposite also exhibited significantly ameliorated photocatalytic performance towards the removal of OFL among all the synthesized samples, with nearly 96.1% of the OFL being degraded after 100 min of visible-light illumination, in contrast to the OFL degradation of only 53.3%, 72.1%, and 88% achieved over pure $BaTiO_3$, $BaTiO_3$-GO, and Ag-$BaTiO_3$, respectively, under the same conditions. (Depicted in **Fig. 3.10 (a)**). According to the pseudo-first-order reaction kinetic plots (**Fig.3.10(b)**), ternary Ag-$BaTiO_3$/GO catalyst displays the highest OFL decomposition rate (0.033 min^{-1}), which is approximately 4.7, 2.7, 1.5 times greater than those observed for $BaTiO_3$ (0.007 min^{-1}), $BaTiO_3$-GO (0.012 min^{-1}), and Ag-$BaTiO_3$ (0.021min^{-1}), respectively. **Fig.3.10(c-d)**, displays the temporal evolution of the spectral absorption variations during the OFL degradation over pure $BaTiO_3$ and ternary Ag-$BaTiO_3$/GO samples with the assistance of visible light. Apparently, it can be observed that in contrast with the unmodified $BaTiO_3$, with the extension of the irradiation duration, the intensity of the initial absorption peak of the OFL molecule, situated at λ_{max} = 288 nm, declined rapidly with little shifting from the absorption maxima towards the shorter wavelength. i.e there is a steady hypsochromic shift in the absorption maxima during the degradation, this is linked to the de-ethylation process.

The complete kinetic analysis data with histograms for removal of both the hazardous pollutants is depicted in **Fig. 3.11 (a-b).**

The above photocatalytic activity results strongly suggest that Ag-$BaTiO_3$/GO is excellent visible light-active catalyst, not only for colored dye pollutants but also for colorless water contaminants.

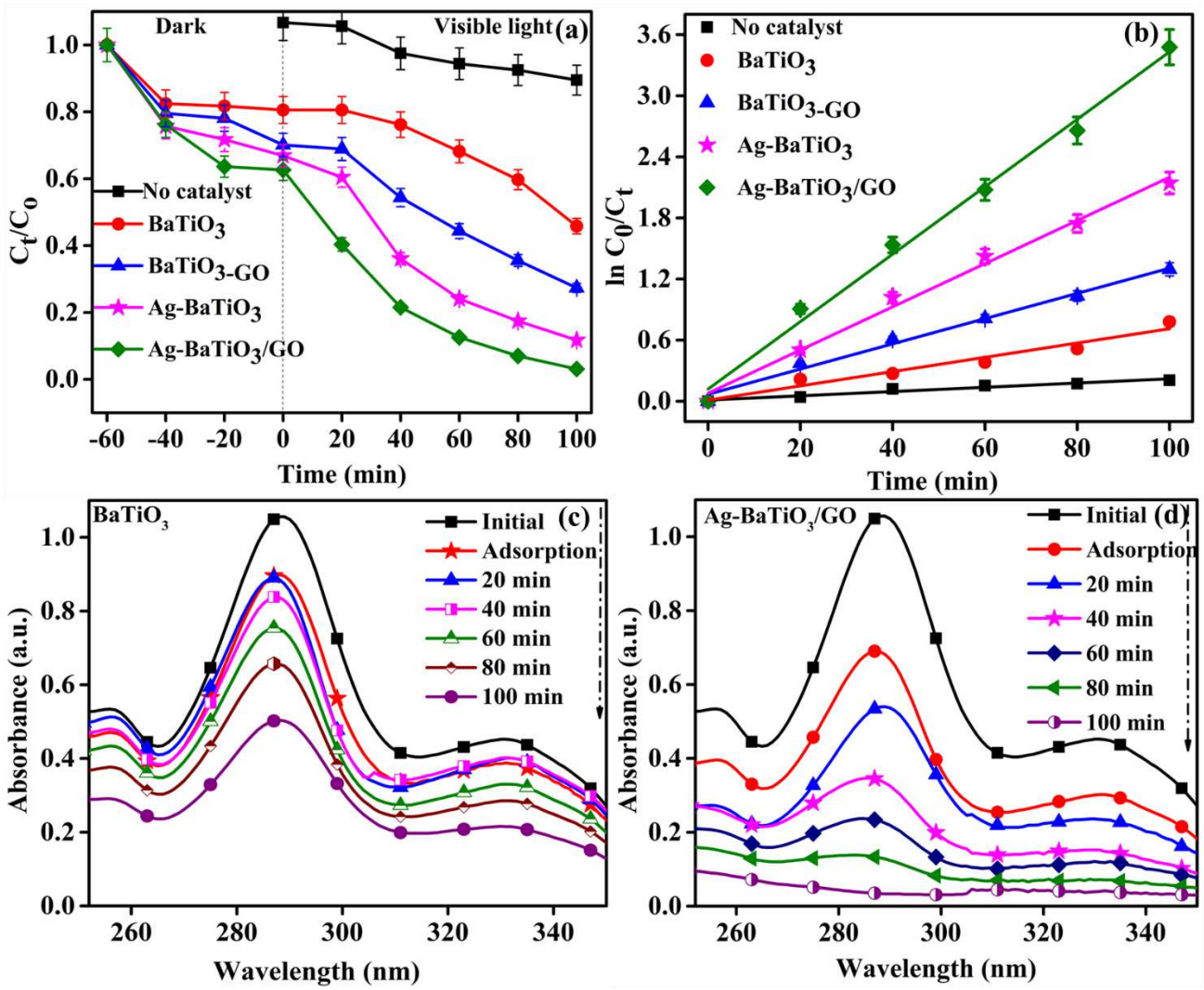

Fig. 3.10: (a) Time course-kinetic plots and (b) corresponding variations in apparent reaction rate constants (k) values obtained for the degradation of OFL antibiotic in the presence of different photocatalysts (c) Time-dependent UV-vis spectral absorption changes of OFL solution over pristine $BaTiO_3$ and (d) Ag-$BaTiO_3$/GO ternary nanocomposite under 100 min LED-light irradiation.

The superior photocatalytic behavior of the as-fabricated ternary hybrid in contrast with bare $BaTiO_3$ and other binary photocatalysts could be credited to the following benefits:

(i) Much better enhancement of the light absorption ability in the visible range, upon deposition of plasmonic Ag with a specialized LSPR effect onto its surface.

(ii) Boosting up of its photoinduced charge separation ability as a result of GO's exceptional conductivity and electron storage capability of GO.

(iii) Well-designed nanostructure, with favorable morphology and increased surface area along with the

development of multi-channel electron transfer pathways, which can efficiently suppress the reconciliation extent of charge carriers in $BaTiO_3$ thereby extending the life-time of the charge carriers.

Additionally, the AQEs of Ag-$BaTiO_3$/GO for 10 ppm CV degradation at different incident wavelengths (450, 500, 550, 600, 650) nm were estimated to be 39.68%, 35.72%, 32.47%, 29.76%, and 27.47%, respectively. And for degradation of 20 ppm OFL, AQE values reached upto 64%, 57.68%, 52.43%, 48.06%, 44.36% at 450, 500, 550, 600, 650 nm wavelengths.

The result further, demonstrates the great potential of the ternary Ag-$BaTiO_3$/GO photocatalyst by exhibiting significantly high AQEs.

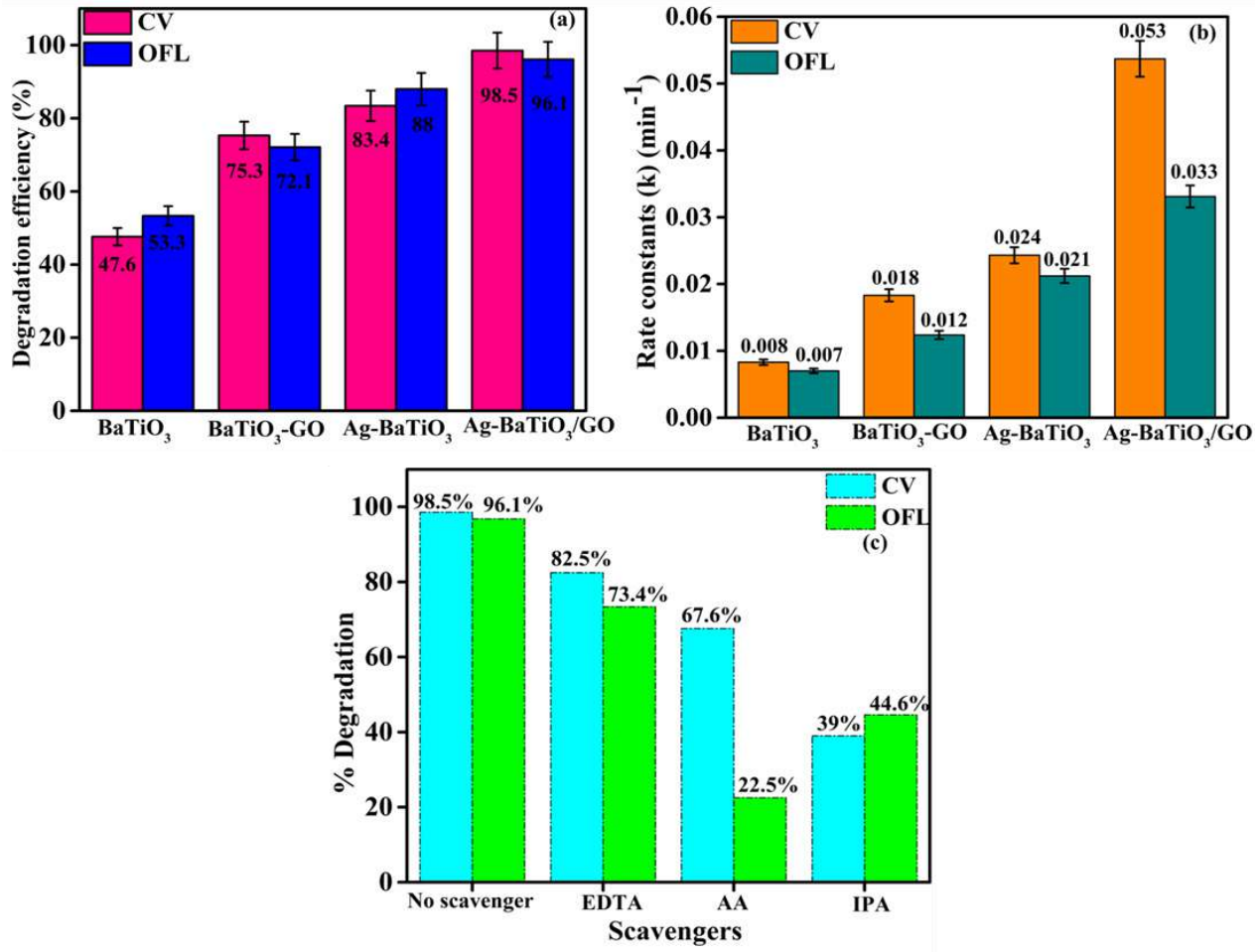

Fig.3.11: Histograms showing comparative (a) photodegradation efficiencies (b) reaction rate constants (k) values exhibited by different as-synthesized photocatalysts for removal of CV and OFL. (c) effect of series of scavengers on CV and OFL degradation by Ag-$BaTiO_3$/GO photocatalyst.

Moreover, we contrasted the photocatalytic performance of the as-fabricated Ag-$BaTiO_3$/GO nanocomposite with that of the majority of other recently reported photocatalysts for CV and OFL degradation (as tabulated

in **Table-3.2 and 3.3**). The findings recommend, that this newly designed photocatalyst is a strong contender for application in wastewater treatment.

S.No	Photocatalyst	Initial CV concentration (ppm)	Light Source	Degradation efficiency time (min)	References
1.	m-$BiVO_4$ nanoparticles	10	300W xenon lamp [Visible light]	96.23% in 120	[54]
2.	$Ce_2(MoO_4)_3$	5	Two 200 W Incandescent light bulbs [Visible light]	89% in 300	[55]
3.	$BiSI/MoS_2$	5	OSRAM 250W lamp [Visible light]	80% in 240	[56]
4.	In_2O_3 nanocapsules	10	~70W/cm^2 [Natural sunlight]	90% in 180	[57]
5.	$BaCr_xFe_{12-x}O_{19}$	10	200 W Argon lamp [Visible light]	91% in 90	[58]
6.	Mesoporous titania nanoparticles (MTN-8)	5	Four 8W Philips lamps [UV-light]	85% in 150	[59]
7.	Sb_2S_3-$Sb_4O_5Cl_2$	10	15 W LED bulb [Visible light]	96.2% in 270	[4]
8.	Ag-$BaTiO_3$/GO	10	50 W LED bulb [Visible light]	98.5% in 75	**This work**

Table- 3.2: Summary of comparison of different photocatalysts for CV degradation.

S.No	Photocatalyst	Initial OFL concentration (ppm)	Light Source (Visible light)	Degradation efficiency time (min)	References
1.	ZnO/CdS	10	15 W	73% in 240	[60]
2.	CdS/TiO_2	10	85W oreva bulb	86% in 180	[61]
3.	Bi_2S_3/Bi_2WO_6	20	150W Xenon lamp	87% in 180	[62]
4.	$MoO_3/Ag/C_3N_4$	20	300W Xenon lamp	89% in 100	[63]
5.	Bi_2MoO_6-rGO-TiO_2	4×10^{-5} M	150 W tungsten lamp	92.3% in 120	[64]
6.	Bi_2WO_6/Au-400˚C	20	300W Xenon lamp	95% in 180	[65]
7.	g-C_3N_4/NH_2-MIL-88B(Fe)	10	300 W xenon lamp	96.5% in 150	[66]
8.	Ag-$BaTiO_3$/GO	20	50 W LED bulb	96.1% in 100	**This work**

Table-3.3: Summary of comparison of different photocatalysts for OFL degradation.

3.4.2. Pollutants Mineralization

As mineralization is the ultimate goal of pollutant treatment, TOC measurement was thus executed to recognize the real mineralization of contaminant molecules during photocatalysis. The TOC value actually monitors the total amount of organic compounds present in the solution, and its decline represents the level of mineralization near the end of the photocatalytic process. The TOC removal effectiveness of ternary Ag-$BaTiO_3$/GO photocatalyst towards the removal of CV and OFL was investigated by dichromate based

chemical method. The obtained results reveal that the TOC values of CV dye declined from 26.8 to 12.1 mg/l after 75 min of visible light irradiation, corresponding to 54.8% TOC reduction. Similarly, without any pretreatment, the TOC of an OFL antibiotic was 14.9 mg/L, which decreased to 7.35 mg/L after 100 minutes of reaction time. i.e ofloxacin's TOC was reduced by 50.6%. The lower TOC values suggests that Ag-$BaTiO_3$/GO photocatalyst could mineralize both CV and OFL contaminants. In addition, it was worth noting that the mineralization activity was lower than degradation efficiencies as evaluated by the UV–Vis spectrophotometer. The incomplete mineralization of pollutants demonstrates that photodegradation proceeded at a slower rate so is the mineralization. This is mainly attributable to the generation of intermediate products. Total mineralization of the remaining intermediates might be possible, but it will most likely take more time of visible light irradiation.

3.4.3. Active species detection

To cognize the exact role of active species, engaged in the photocatalytic eviction of CV and OFL over Ag-$BaTiO_3$/GO composite and further propose the photocatalytic mechanism, the radical capturing experiments were conducted. 10^{-3}M solutions of AA, IPA, and EDTA were selected as scavengers of $O_2^{\bullet-}$, •OH, and photoproduced holes (h^+), respectively. The conditions for both the free radical trapping and degradation experiments were kept identical. As presented in **Fig. 3.11(c)**, photo removal efficiency of OFL reduced in the presence of scavengers with the order of significance following AA > IPA > EDTA, suggesting that the superoxide radical, ($O_2^{\bullet-}$) followed by the hydroxide radical (•OH) significantly contributed to the degradation process of OFL, while the valence band (h^+) plays a minor role.

On examining the photodegradation of CV dye, somewhat similar results were observed. The degradation efficiency was extremely screened by the introduction of IPA, revealing that •OH are highly accountable for the photocatalytic activity. However, when AA, and EDTA were added, the degradation process was affected only to a small extent, manifesting that $O_2^{\bullet-}$, and h^+ played an insignificant role during the degradation. Additionally, their rates were close to that of the control experiment (no scavenger). The attained results suggest that both •OH and $O_2^{\bullet-}$, radical species are the prime reactive species engaged in the photocatalytic degradation of OFL, while only "•OH" has a significant impact on the removal of CV dye.

3.4.4. Probable degradation mechanism

Since the energy-band potentials of photocatalysts are linked to the redox power of charge carriers, it is crucial to ascertain these potentials so as to comprehend the photocatalytic mechanism of the ternary composite. Using the following empirical equations, the energy (E) of CB and VB positions of $BaTiO_3$ are

determined as:

$E_{CB} = \chi - E_e - 1/2E_g$ (7)

$E_{VB} = \chi - E_e + 1/2E_g$ (8)

where, χ denotes the absolute electro-negativity of $BaTiO_3$ (5.242 eV)[54], E_e is the free e^-'s energy on H_2 scale (4.50 eV vs. NHE), E_g is the band gap energy of $BaTiO_3$ (2.93 eV). Consequently, the E_{CB} and E_{VB} of $BaTiO_3$ vs. NHE were found to be -0.723 eV and +2.207 eV, respectively. A probable mechanism for photocatalytic decomposition of dye (CV) and antibiotic (OFL) over the Ag-$BaTiO_3$/GO nanocomposite is explained through the schematic diagram displayed in **Scheme-3.2.**

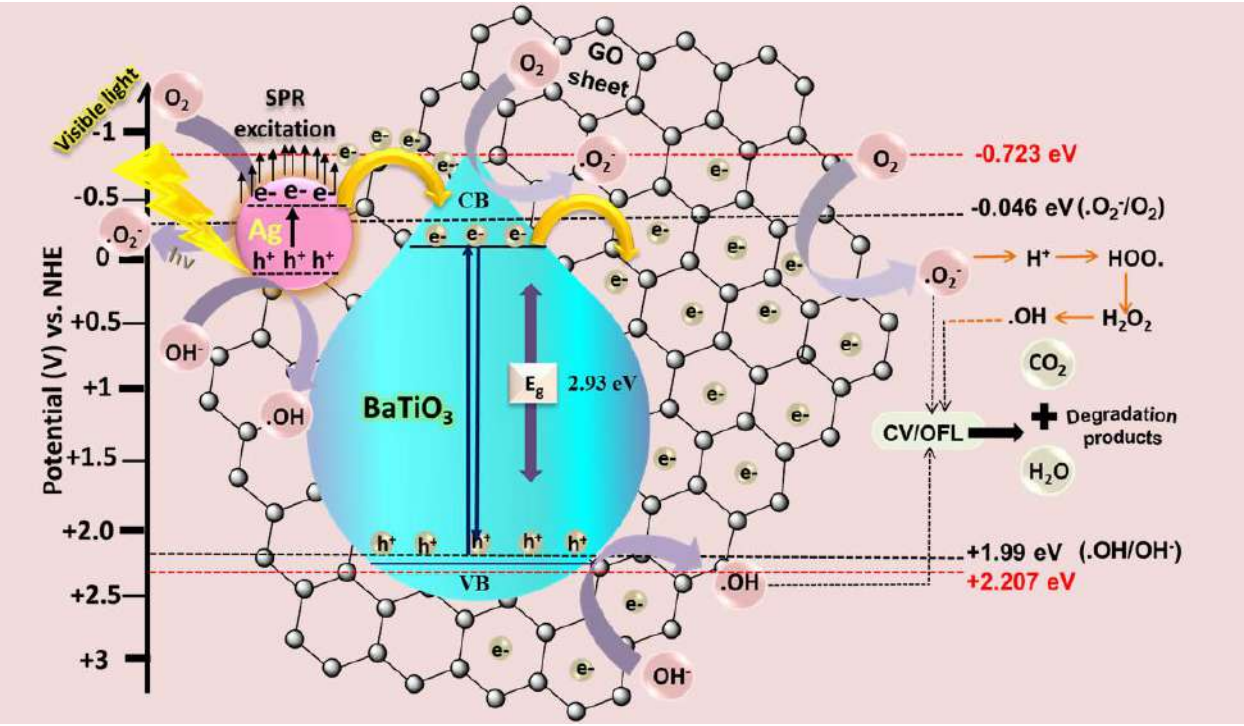

Scheme.3.2. A possible mechanism for the photocatalytic degradation of pollutants using ternary Ag-$BaTiO_3$/GO photocatalyst under LED- light irradiation

When exposed to visible light radiations, as-synthesized $BaTiO_3$ with a rod-like structure and absorption onset around 428 nm, exhibits some affinity towards this irradiated light, which results in its excitation to produce electrons in the CB and holes in the VB. Similarly, the plasmonic effect also causes the deposited Ag NPs to photogenerate e^-– h^+pairs, and when these Ag NPs come into contact with $BaTiO_3$ nanorods, the LSPR-induced extremely energetic hot electrons quickly jump towards the CB of $BaTiO_3$, leaving behind holes on the metal surface. Since, graphene is known to be a good electron acceptor, and its energy levels (-

0.08 eV vs. NHE) lies below the $BaTiO_3$ CB (-0.723 eV), excited electrons further get transferred onto the graphene oxide sheets, thereby inhibiting the charge recombination process in $BaTiO_3$. Further, the excessive electron's on the Ag NPs surface as well as those assembled on the $BaTiO_3$ and GO's surface might easily react with dissolved O_2 in the aqueous solution to produce reactive superoxide radical anion ($\bullet O_2$-), owing to their sufficiently negative reduction potential. (−0.723 eV vs. NHE) in contrast with the standard redox potential of $\bullet O_2$-, $E^0(\bullet O_2^-/O_2)$ (-0.046 eV vs. NHE) [55,56]. $\bullet O_2$- radical anion further gets protonated to generate hydro-peroxyl radical HOO·, and subsequently hydrogen peroxide (H_2O_2) which then dissociates into extremely reactive species (•OH). At the same time, photoinduced holes left in the VB of $BaTiO_3$ and Ag and tend to react with the surface OH^- ion to form another strong oxidant OH• radicals, owing to the higher positive standard redox potential of E_{VB} of $BaTiO_3$ than the E^0 (•OH/OH-) (+1.99 eV vs. NHE)[54]. The analysis was also consistent with the result of scavenging experiment. Ultimately, generation of plenty of these energetic species ($\bullet O_2$- and OH•) in the photocatalytic system would result in efficient degradation of hazardous contaminants (CV and OFL) into the organic intermediates and finally into H_2O and CO_2, as environment friendly products.

Summing up the above analysis, the major routes involved in the photocatalytic degradation mechanism over Ag-$BaTiO_3$/GO are listed in Eqs. (9–21) as follows:

$$Ag + hv \rightarrow Ag\ (h^+ + e^-) \quad (9)$$

$$BaTiO_3 + hv \rightarrow BaTiO_3\ (h^+ + e^-) \quad (10)$$

$$Ag\ (e\text{-}) + BaTiO_3 \rightarrow BaTiO_3\ (e^-) + Ag \quad (11)$$

$$BaTiO_3\ (e^-) + GO \rightarrow BaTiO_3 + GO\ (e^-) \quad (12)$$

$$GO\ (e\text{-}) + O_2 \rightarrow GO + \bullet O_2^- \quad (13)$$

$$BaTiO_3\ (e\text{-}) + O_2 \rightarrow BaTiO_3 + \bullet O_2^- \quad (14)$$

$$Ag\ (e\text{-}) + O_2 \rightarrow Ag + \bullet O_2^- \quad (15)$$

$$\bullet O^{2-} + H^+ \rightarrow .OOH \quad (16)$$

$$2.OOH \rightarrow O_2 + H_2O_2 \quad (17)$$

$$H_2O_2 + (e\text{-}) \rightarrow .OH + OH^- \quad (18)$$

$$Ag\ (h^+) + OH^- \rightarrow \bullet OH \quad (19)$$

$$BaTiO_3\ (h^+) + OH^- \rightarrow \bullet OH \quad (20)$$

$$\bullet O^{2-} / \bullet OH + CV + OFL \rightarrow CO_2 + H_2O \text{ (degradation products)} \quad (21)$$

This transfer pathway in the ternary catalyst, is expected to remarkably suppress the charge carrier reconciliation, thereby effectively upgrading the photocatalytic performance.

3.4.4. Photodegradation pathway

For grasping a deeper knowledge on photocatalytic degradation of OFL antibiotic and CV dye, the degradation intermediates generated in the photocatalysis process with Ag-$BaTiO_3$/GO catalyst were inspected via LC-MS technique and identified by interpretation of their m/z value (Here (m) denotes the intermediate's molecular weight in the mass spectra and (z) is the charge number). **Scheme.3.3.(a)** depicts the mass spectrum of the OFL antibiotic, having characteristic peak detected at m/z 362.58. Several by-products (BP) were identified during various stages of degradation. Based on LC-MS data, quenching tests and previous reports, [57–61] the degradation routes of OFL were proposed as illustrated in **Scheme.3.3(b).**. Generally, the degradation pathway of OFL involves the piperazinyl dealkylation, demethylation of the piperazinyl ring, carboxylation/decarboxylation processes, hydroxylation, cleavage of the piperazine ring, oxidation of hydroxyl groups and defluorination of the OFL molecule. The first pathway proceeded through piperazine ring oxidation. OFL (m/z 362.58) gets oxidized to open this ring with the generation of BP1 (m/z 392.60). Further, the loss of the -CO group allowed BP1 (m/z 392.60), to be transformed into BP2 (m/z 364.57). BP3 with (m/z 254.31) might be produced through hydroxyl group addition i.e. the hydroxylation process. This BP3 underwent ring-opening and could generate BP4 (m/z 217.37) by defluorination. Another pathway was the piperazine ring dealkylation. BP5 (m/z 346.53) could be formed by the cleavage of methyl group affixed with the piperazine ring. Cleavage of $–C_2H_4$ and $–C_2H_4$-NH-CH_3 from the piperazine ring can result in the intermediates, BP6 (m/z 333.49) and BP7 (m/z 280.48). Aside from that OFL through dehydration results in the formation of another intermediate BP8 (m/z 330.46). By another pathway OFL could be decarboxylated to BP9 (m/z 312), which could then be transformed into BP10 with m/z 333.49 by adding a hydroxyl group to the piperazine substituent. As the electron donating capacity of a methyl is superior than the H-atom substituted at N4 of the piperazenyl so, intermediate (m/z 272.35) could be formed through demethylation and its repetition again results in a new product with m/z 261.45. Finally, (m/z 261.45) through an ethylene linkage could form BP11 (m/z 236.25). Ultimately, the detected transformation products from all the routes eventually disintegrate into smaller, oxygen containing molecules before being transformed into CO_2 and H_2O.

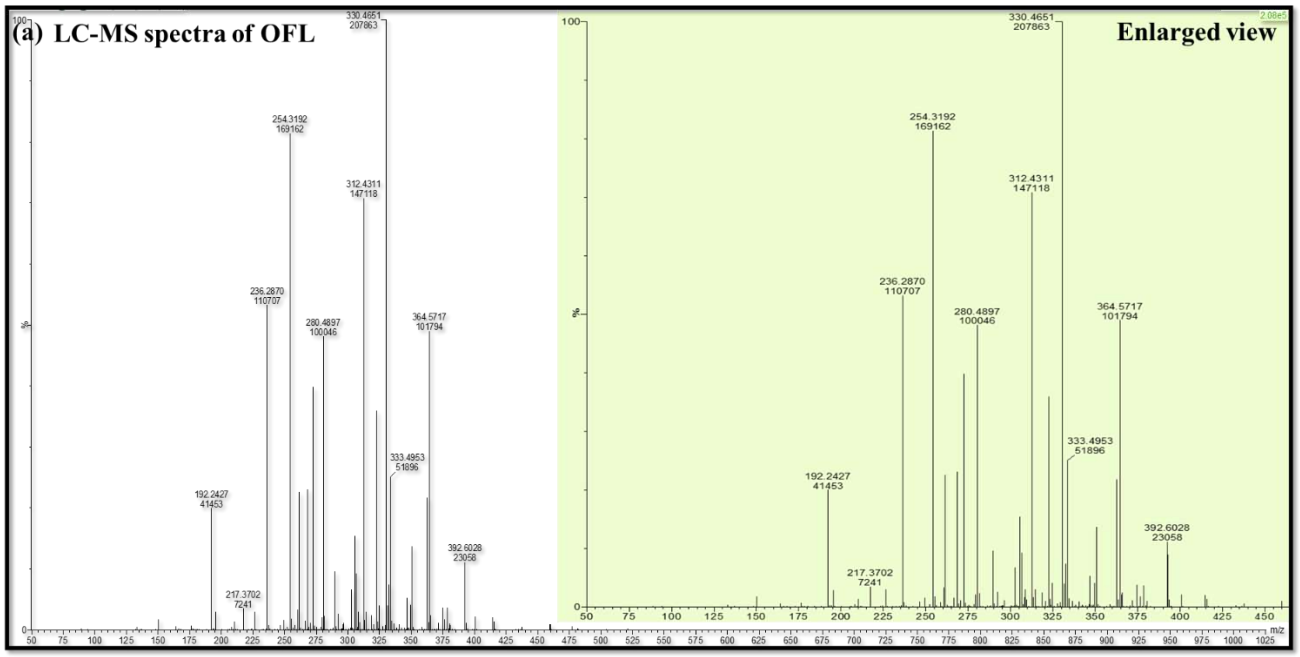

Scheme.3.3(a): LC-MS chromatogram of the intermediates generated from OFL degradation using Ag-$BaTiO_3$/GO nanocomposite after 100 min of LED-light illumination.

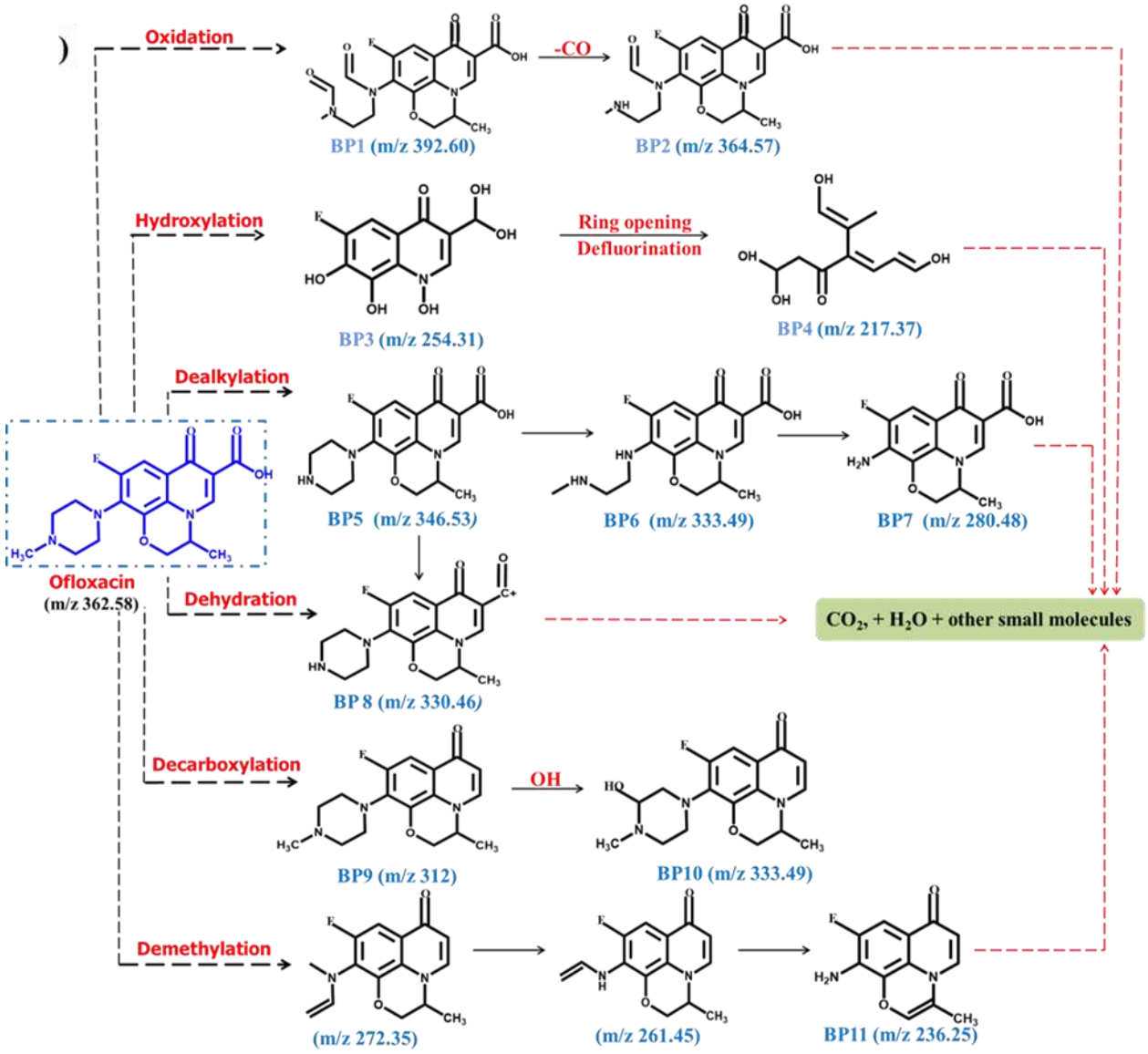

(b)

Scheme.3.3(b): Proposed photocatalytic degradation pathway of OFL antibiotic by Ag-$BaTiO_3$/GO nanocomposite.

.

Similarly, the LC-MS technique was also used to find the intermediates involved in the degradation of CV dye **(Scheme.3.4(a)).** It's decomposition is believed to occur via two photodegradation pathways, one is the stepwise N-de-methylation, and other is the destruction of the conjugated triphenylmethane structure [62–65]. Several distinct m/z peaks were detected in its mass spectrum, including 372.2, 330.3, 288, 166, and 138. **((Scheme.3.4(b)).** Based on the ion characteristic peak at m/z = 372.2, the substance was identified to be CV. By-products BP1(m/z 288) and BP2 (m/z 330.3), were mainly the N-de-methylated intermediates

that occurred by the attack of (.OH) species on CV's N,N-methylamino group. Once the triphenylmethane ring in the CV structure was broken, low molecular intermediates such as organic acids, BP3 (m/z 166) and BP4 (m/z 166) and BP5 (m/z 138) corresponding to terephthalic acid, phthalic acid, and 3-hydroxybenzoic acid, respectively, were most likely to form. Finally, the progressive cleavage of the aromatic intermediates would lead to the formation of carboxylic acids, which would then undergo transformation into simpler products.

The generation of the aforementioned intermediates and products as encountered by LC-MS approach implies that OFL and CV are likely transformed to a nearly mineralized condition over the synthesized Ag-$BaTiO_3$/GO.

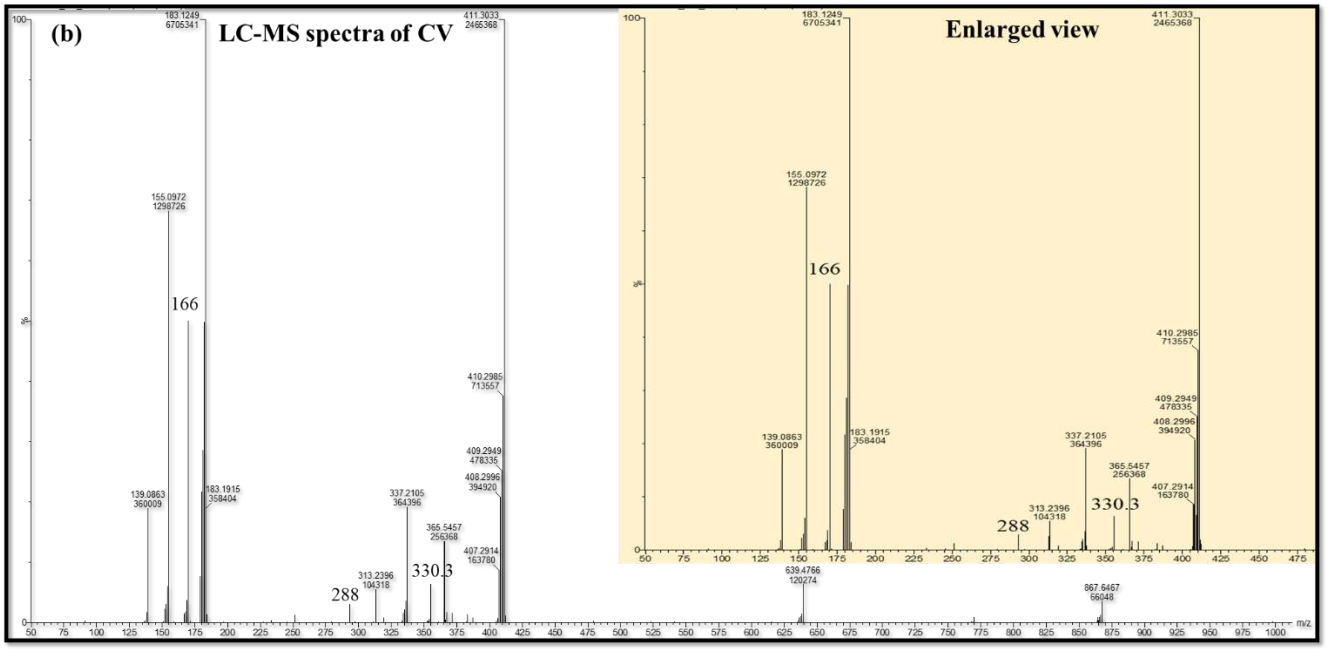

Scheme.3.4(a):LC-MS chromatogram of the intermediates generated from CV degradation using Ag-$BaTiO_3$/GO nanocomposite after 75 min of LED-light illumination.

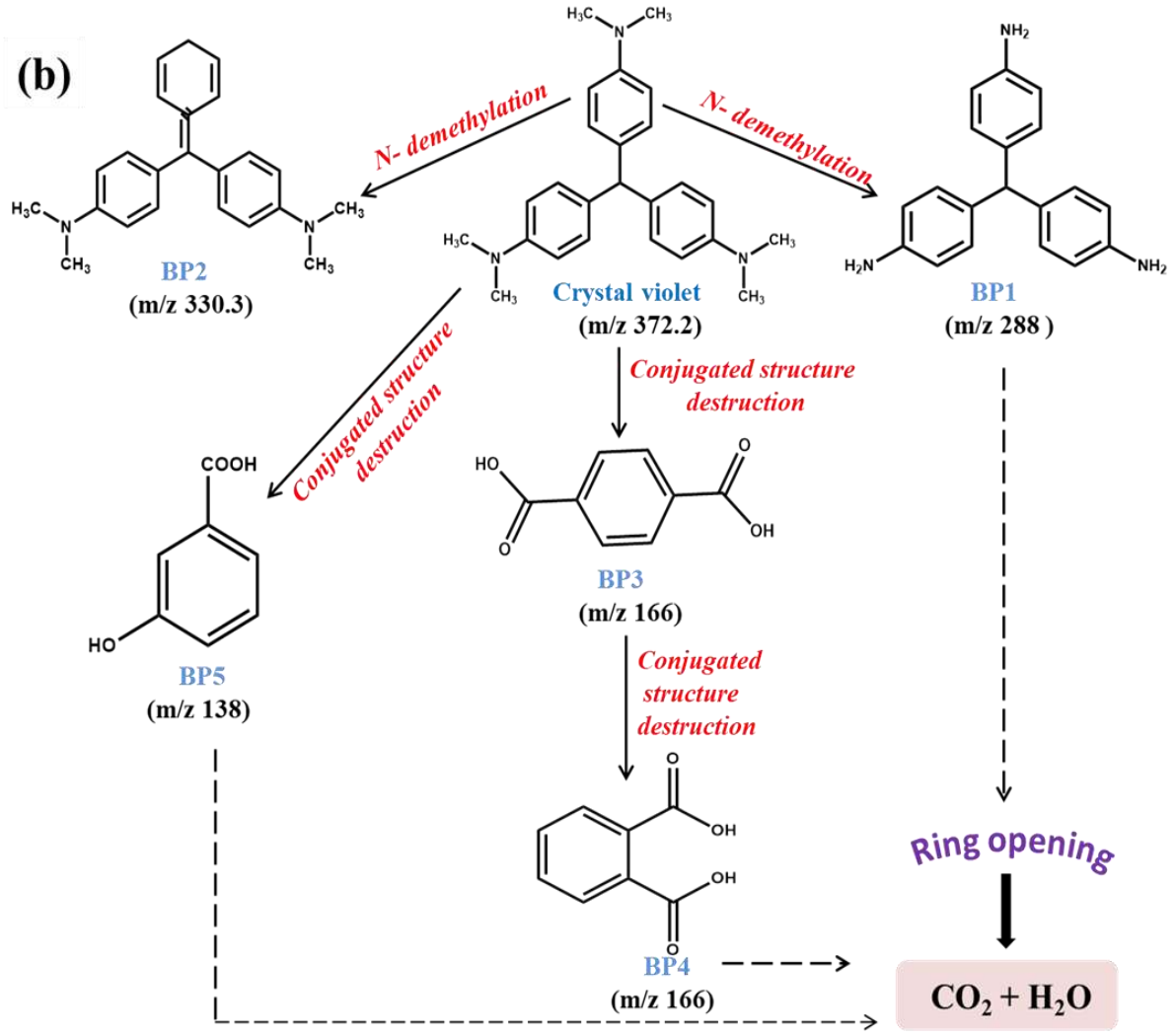

Scheme.3.4(b): Proposed photocatalytic degradation pathway of CV dye by Ag-$BaTiO_3$/GO nanocomposite.

3.4.5. Recyclability studies

From a practical point of view, reusability and stability are vital parameters affecting the photocatalyst's performance. Hence, to investigate these, successive recycling experiments for photodegradation of CV using a ternary Ag-$BaTiO_3$/GO composite were conducted for four consecutive cycles accompanying the similar approach as described in the experimental portion. Each cycle included 75 min of reaction. In every progression except for the first, the photocatalyst of the previous cycle was recovered by centrifugation, and after washing process, it was kept for drying for its next use. **Fig.3.13(a)** clearly demonstrates that the degradation efficiency for CV was only reduced by 19.76% i.e (~20%) from the first to the fourth cycle, implying that the Ag-$BaTiO_3$/GO is highly reusable catalyst. The decline (78.83% from 98.59%) in the degradation performance may be due to the catalyst's inevitable loss throughout the separation and recycling

procedure. Furthermore, to better support this view point, the structural stability of the photocatalyst was also assessed. **Fig.3.13(b,c)** represents the XRD pattern, and FESEM image of the recycled Ag-$BaTiO_3$/GO acquired before and after the 4 times recycling experiments. In all the cases, the results look similar, and no drastic changes were seen before and after the reaction.

No variation in the peak positions, peak parameters, and crystallinity was detected in the XRD pattern **Fig.3.13(b)** of the recovered composite, implying that the components retain their crystal structure intact. However, a minimal reduction in the intensity of the XRDs peaks is noticed after the recycling process. FESEM image **Fig.3.13(c)** provides additional evidence for the photocatalyst's exceptional stability, demonstrating that the morphology remains consistent and not significantly disturbed even after numerous cycles of use. Hence, considering the superb degradation activity, regeneration ability, and powerful photostability, the present Ag-$BaTiO_3$/GO composite can be deemed as a promising material for photocatalytic applications.

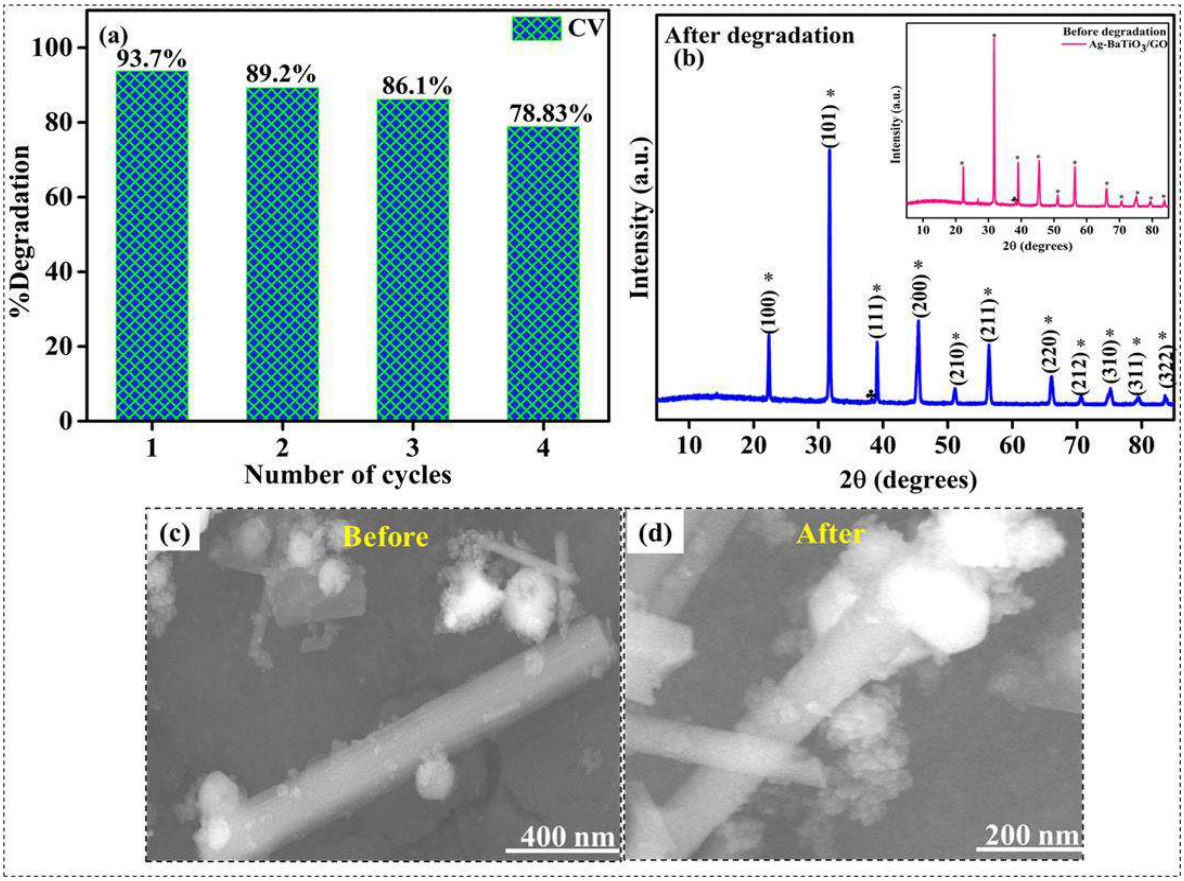

Fig.3.12:(a) Reusability studies, (b) XRD spectra, (c) FE-SEM images of Ag-$BaTiO_3$/GO nanocomposite before and after four cycles of CV dye degradation.

Conclusion

Visible light active Ag-$BaTiO_3$/GO ternary photocatalyst was synthesized for the first time and has been thoroughly studied with regard to its chemical composition, structural and optical properties. Notably, the well-designed composite displayed significantly enhanced photocatalytic degradation activity (98.5% CV removal efficiency within 75 min and 96.1% OFL degradation efficiency in 100 min) under LED-light illumination, which is much greater than that achieved for pristine $BaTiO_3$, binary (Ag-$BaTiO_3$, and $BaTiO_3$-GO) hybrids. The extended visible-light response of $BaTiO_3$ due to the SPR effect of metallic Ag NPs, and the excellent electron transport properties of graphene oxide inhibiting the rapid recombination of photoinduced charge carriers, favorable morphology as well as the strong synergistic interaction among the three components Ag, $BaTiO_3$, and GO, all together contributed to the superior degradation performance of the ternary nanocomposite. Moreover, the developed photocatalyst exhibited good stability, even after four consecutive degradation cycles, with a little loss in performance. Additionally, according to the results of the LC-MS, as well as trapping experiments, the probable intermediate products and reaction mechanism have been presented in detail, that demonstrates $\bullet O_2^-$ and •OH as the pivotal active species responsible for pollutants removal. Mineralization efficiency of the developed photocatalyst was also evaluated by a TOC test. Overall, the present study illustrated a promising prospect for an avenue for using the Ag/$BaTiO_3$-GO composite with a unique architecture as an environmentally-friendly approach and a highly-effective visible light activated catalyst for elimination of toxic pollutants from wastewater.

References

[1] R. Al-Tohamy, S.S. Ali, F. Li, K.M. Okasha, Y.A.G. Mahmoud, T. Elsamahy, H. Jiao, Y. Fu, J. Sun, Ecotoxicology and Environmental Safety 231 (2022) 113160.

[2] A. Rafiq, M. Ikram, S. Ali, F. Niaz, M. Khan, Q. Khan, M. Maqbool, Journal of Industrial and Engineering Chemistry 97 (2021) 111–128.

[3] R. Kumar, M. Qureshi, D.K. Vishwakarma, N. Al-Ansari, A. Kuriqi, A. Elbeltagi, A. Saraswat, Case Studies in Chemical and Environmental Engineering 6 (2022) 100219.

[4] R. Makhloufi, S.E. Hachani, A. Fettah, W. Tair, Z. Zekri, Chemical Data Collections 39 (2022) 100867.

[5] S. Mani, R.N. Bharagava, Exposure to Crystal Violet, Its Toxic, Genotoxic and Carcinogenic Effects on Environment and Its Degradation and Detoxification for Environmental Safety, 2016.

[6] R. Anjali, S. Shanthakumar, Journal of Environmental Management 246 (2019) 51–62.

[7] A. Rahmah, D. Ahmad, S.S. Imam, W. Da Oh, R. Adnan, (2020).

[8] V.M.F. Frade, M. Dias, A.C.S.C. Teixeira, M.S.A. Palma, Brazilian Journal of Pharmaceutical Sciences 50 (2014) 41–54.

[9] D. Zhu, Q. Zhou, Environmental Nanotechnology, Monitoring and Management 12 (2019) 100255.
[10] G. Mamba, A.K. Mishra, Applied Catalysis B: Environmental 198 (2016) 347–377.
[11] M. Passi, B. Pal, Powder Technology 388 (2021) 274–304.
[12] R. Djellabi, M.F. Ordonez, F. Conte, E. Falletta, C.L. Bianchi, I. Rossetti, Journal of Hazardous Materials 421 (2022) 126792.
[13] S.K. Ray, J. Cho, J. Hur, Journal of Environmental Management 290 (2021) 112679.
[14] T. Xian, H. Yang, L.J. Di, J.F. Dai, Journal of Alloys and Compounds 622 (2015) 1098–1104.
[15] Y.Y. Yang, H.P. Feng, C.G. Niu, D.W. Huang, H. Guo, C. Liang, H.Y. Liu, S. Chen, N. Tang, L. Li, Chemical Engineering Journal 426 (2021).
[16] H.Y. Liu, C.G. Niu, H. Guo, C. Liang, D.W. Huang, L. Zhang, Y.Y. Yang, L. Li, Journal of Colloid and Interface Science 576 (2020) 264–279.
[17] A.T. Montoya, E.G. Gillan, ACS Omega 3 (2018) 2947–2955.
[18] A. Kumar, P. Choudhary, A. Kumar, P.H.C. Camargo, V. Krishnan, Small (2021).
[19] G. Ren, H. Han, Y. Wang, S. Liu, J. Zhao, X. Meng, Z. Li, Nanomaterials 11 (2021).
[20] Y.S. Fu, J. Li, J. Li, Nanomaterials 9 (2019).
[21] Y.Y. Yang, X.G. Zhang, C.G. Niu, H.P. Feng, P.Z. Qin, H. Guo, C. Liang, L. Zhang, H.Y. Liu, L. Li, Applied Catalysis B: Environmental 264 (2020).
[22] X.G. Liu, H.Y., Niu, C.G., Guo, H., Huang, D.W., Liang, C., Yang, Y.Y., Tang, N. and Zhang, Journal of Colloid and Interface Science 610 (2022) 953–969.
[23] Z. Wu, Y. Zhang, X. Wang, Z. Zou, New Journal of Chemistry 41 (2017) 5678–5687.
[24] Y. Yan, H. Yang, Z. Yi, R. Li, X. Wang, Micromachines 10 (2019) 1–16.
[25] K.H. Reddy, S. Martha, K.M. Parida, Nanoscale 10 (2018) 18540–18554.
[26] B. Luo, D. Xu, D. Li, G. Wu, M. Wu, W. Shi, M. Chen, ACS Applied Materials and Interfaces 7 (2015) 17061–17069.
[27] N. Zhang, Y. Zhang, Y.J. Xu, Nanoscale 4 (2012) 5792–5813.
[28] F. Khan, M.S. Khan, S. Kamal, M. Arshad, S.I. Ahmad, S.A.A. Nami, Journal of Materials Chemistry C 8 (2020) 15940–15955.
[29] H.A.A. Jamjoum, K. Umar, R. Adnan, M.R. Razali, M.N. Mohamad Ibrahim, Frontiers in Chemistry 9 (2021) 1–24.
[30] C. Prasad, Q. Liu, H. Tang, G. Yuvaraja, J. Long, A. Rammohan, G. V. Zyryanov, Journal of Molecular Liquids 297 (2020) 111826.
[31] D. Photo-oxidation, A.A. Yaqoob, N. Habibah, A. Serr, M. Nasir, M. Ibrahim, (2020).
[32] R.X. Wang, Q. Zhu, W.S. Wang, C.M. Fan, A.W. Xu, New Journal of Chemistry 39 (2015) 4407–4413.
[33] H.H. El-Maghrabi, A.A. Nada, K.R. Diab, A.M. Youssef, A. Hamdy, S. Roualdes, S. Abd El-Wahab, Journal of Photochemistry and Photobiology A: Chemistry 365 (2018) 86–93.
[34] N. Ben Saber, A. Mezni, A. Alrooqi, T. Altalhi, Journal of Materials Research and Technology 12 (2021) 2238–2246.
[35] T. Wang, T. Tang, Y. Gao, Q. Chen, Z. Zhang, H. Bian, Physica E: Low-Dimensional Systems and Nanostructures 112 (2019) 128–136.

[36] R. Beura, R. Pachaiappan, T. Paramasivam, Journal of Physics and Chemistry of Solids 148 (2021) 109689.
[37] J. Chen, B. Yao, C. Li, G. Shi, Carbon 64 (2013) 225–229.
[38] T. Bora, D. Zoepfl, J. Dutta, Scientific Reports 6 (2016) 1–10.
[39] X. Li, Journal of Chemistry 2018 (2018).
[40] P.M. Nithya, L.G. Devi, Surfaces and Interfaces 15 (2019) 205–215.
[41] T. Fafal, P. Taştan, B.S. Tüzün, M. Ozyazici, B. Kivcak, South African Journal of Botany 112 (2017) 346–353.
[42] E. Lin, Z. Kang, J. Wu, R. Huang, N. Qin, D. Bao, Applied Catalysis B: Environmental 285 (2021).
[43] S. Zhang, B. Zhang, S. Li, Z. Huang, C. Yang, H. Wang, 6 (2017) 1–10.
[44] D. Ye, Z. Zhong, H. Xu, C. Chang, Z. Yang, Y. Wang, Q. Ye, L. Zhang, Cellulose 23 (2016) 749–763.
[45] F.T. Johra, J.W. Lee, W.G. Jung, Journal of Industrial and Engineering Chemistry 20 (2014) 2883–2887.
[46] K. Das Sangram, K. Roul Binod, S. Keshari Das, B. Kumar Roul, Chinese Physics B 24 (2015) 2–9.
[47] J. Pokorný, U.M. Pasha, L. Ben, O.P. Thakur, D.C. Sinclair, 114110 (2011).
[48] E. Chávez, S. Fuentes, R.A. Zarate, L. Padilla-campos, (2010).
[49] N. Mirikaram, Á. Pérez-molina, S. Morales-torres, A. Salemi, F.J. Maldonado-hódar, L.M. Pastrana-martínez, Nanomaterials 11 (2021).
[50] L. Bai, Q. Xu, Z. Cai, Journal of Materials Science: Materials in Electronics 29 (2018) 17580–17590.
[51] R. Vijayalakshmi, V. Rajendran, Digest Journal of Nanomaterials and Biostructures 5 (2010) 511–517.
[52] M.A.M. Khan, S. Kumar, J. Ahmed, M. Ahamed, A. Kumar, Materials Chemistry and Physics 259 (2021) 124058.
[53] W. Zhang, X. Dong, Y. Liang, Y. Sun, F. Dong, Applied Surface Science 455 (2018) 236–243.
[54] M.M. Sajid, N. Amin, N.A. Shad, S.B. khan, Y. Javed, Z. Zhang, Materials Science and Engineering B: Solid-State Materials for Advanced Technology 242 (2019) 83–89.
[55] M. Dargahi, M. Masteri-Farahani, S. Shahsavarifar, M. Feizi, Environmental Science and Pollution Research 27 (2020) 12047–12054.
[56] S. Bargozideh, M. Tasviri, New Journal of Chemistry 42 (2018) 18236–18241.
[57] K.K. Pawar, L.S. Chaudhary, S.S. Mali, T.S. Bhat, A.D. Sheikh, C.K. Hong, P.S. Patil, Journal of Colloid and Interface Science 561 (2020) 287–297.
[58] Misbah, I. Bibi, F. Majid, S. Kamal, K. Jilani, B. Taj, Z. Nazeer, M. Iqbal, Journal of Saudi Chemical Society (2022) 101533.
[59] S. Mallakpour, V. Ramezanzade, Journal of Environmental Management 291 (2021) 112680.
[60] T. Senasu, T. Chankhanittha, K. Hemavibool, S. Nanan, Materials Science in Semiconductor Processing 123 (2021) 105558.
[61] A. Kaur, A. Umar, W.A. Anderson, S.K. Kansal, Facile Synthesis of CdS/TiO2 Nanocomposite and Their Catalytic Activity for Ofloxacin Degradation under Visible Illumination, Elsevier B.V., 2018.
[62] S. Adhikari, D.H. Kim, Chemical Engineering Journal 354 (2018) 692–705.

[63] S. Adhikari, H.H. Lee, D.H. Kim, Chemical Engineering Journal 391 (2020).
[64] A. Raja, N. Son, M. Kang, Environmental Research 199 (2021) 111261.
[65] Y. Tian, L. Ma, X. Tian, Y. Nie, C. Yang, Y. Li, L. Lu, Z. Zhou, Chemosphere 269 (2021) 128717.
[66] Q. Su, J. Li, H. Yuan, B. Wang, Y. Wang, Y. Li, Y. Xing, Chemical Engineering Journal 427 (2022).
[67] S. Kappadan, S. Thomas, N. Kalarikkal, Materials Chemistry and Physics 255 (2020) 123583.
[68] S. Yang, L. Zhang, C. Shao, X. Li, X. Li, S. Liu, R. Tao, Y. Liu, Journal of Sol-Gel Science and Technology 97 (2021) 610–621.
[69] S.M. Ghoreishian, G.S.R. Raju, E. Pavitra, C.H. Kwak, Y.K. Han, Y.S. Huh, Applied Surface Science 489 (2019) 110–122.
[70] G. Zhao, J. Ding, F. Zhou, X. Chen, L. Wei, Q. Gao, K. Wang, Q. Zhao, Chemical Engineering Journal 405 (2021) 126704.
[71] H. Guo, Z. Li, S. Lin, D. Li, N. Jiang, H. Wang, J. Han, J. Li, Chemosphere 265 (2021) 129089.
[72] J. Liu, X. Wu, J. Liu, C. Zhang, Q. Hu, X. Hou, Molecular Catalysis 465 (2019) 61–67.
[73] Z. Geng, M. Yang, X. Qi, Z. Li, X. Yang, M. Huo, J.C. Crittenden, Journal of Chemical Technology and Biotechnology 94 (2019) 1660–1669.
[74] Y. Pi, J. Feng, M. Song, J. Sun, Chinese Science Bulletin 59 (2014) 2618–2624.
[75] H.A. Abbas, R.A. Nasr, R. Abu-Zurayk, A. Al Bawab, T.S. Jamil, Royal Society Open Science 7 (2020).
[76] P.P. Thattil, A. Leema Rose, Rasayan Journal of Chemistry 13 (2020) 1166–1173.
[77] S. Ameen, M.S. Akhtar, M. Nazim, H.S. Shin, Materials Letters 96 (2013) 228–232.
[78] H. He, S. Yang, K. Yu, Y. Ju, C. Sun, L. Wang, Journal of Hazardous Materials 173 (2010) 393–400.

CHAPTER-4

Fe(III) and GO loaded $SrTiO_3$ nanocomposite for the LED-light driven photocatalytic degradation of norfloxacin antibiotic

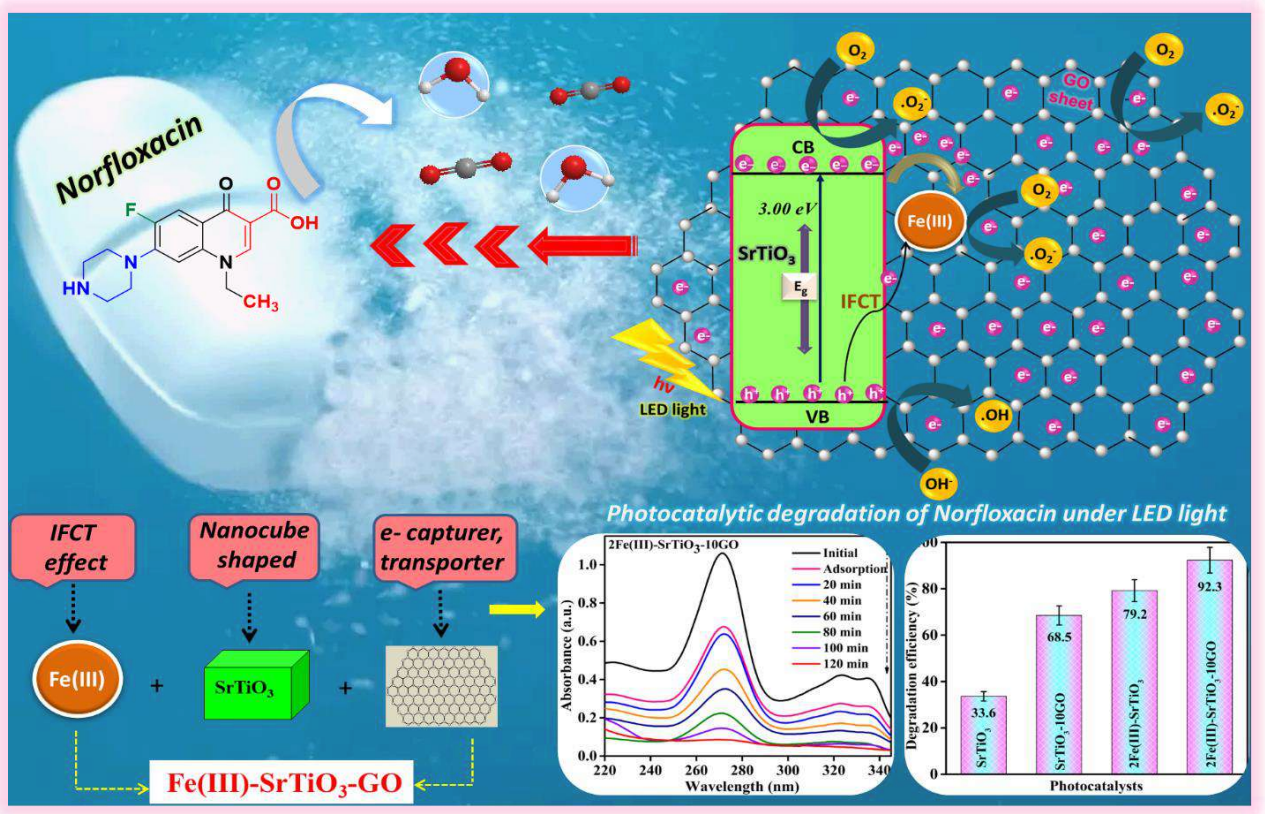

Schematic summary

A dual cocatalyst modified Fe(III)-$SrTiO_3$-GO photocatalyst was fabricated by anchoring Fe(III) species and GO sheets onto $SrTiO_3$. Outperforming its counterparts, the optimized (2Fe(III)-$SrTiO_3$-10GO) nanocomposite commendably degraded 92.3% of the norfloxacin drug after 120 min of LED light exposure. The heightened performance is credited to the trio-hybrid's unique design, combining the benefits of $SrTiO_3$ (nano-cubic morphology), GO (high conductivity), and Fe(III) species (IFCT effect) to accelerate the transference and separation of e^--h^+ pairs and extend the light absorption range.

4.1. Introduction

For more than 50 years, antibiotics have been used as an elixir to safeguard human beings and animals from a wide range of pathogens, and in recent years, both their production and consumption have escalated. Antibiotic proliferation in the environment particularly in the water sources (surface water, wastewater, groundwater, and drinking water) and their persistent nature are a global concern due to the adverse environmental impacts and potential harm to the botany and fauna in aquatic systems. As a result, these are now considered as emerging pollutants. Pharmaceutical industries, municipal wastewater (from human and animals excrement), hospital wastewater, and sewage treatment plants are the main sources of their presence in aquatic environments [1,2]. Norfloxacin (NOF), a second-generation synthetic fluoroquinolone antibiotic (FQ), has been used in human (respiratory, bacterial infections) and veterinary medicine, as well as in livestock farming and aquaculture, due to its broad antimicrobial activity against microscopic organisms [3]. Due to the stability of the quinolone backbone, low metabolic rate and incomplete biodegradability, only partial removal of these antibiotics is accomplished in conventional wastewater treatment plants and significant quantities are deliberately released into the environment in their pharmacologically active forms [4]. As the NOF is highly mutagenic, teratogenic, and embryotoxic, even trace amounts of its residues and derivatives can eutrophize ecosystems and contaminate food and drinking water sources. For instance, by inhibiting DNA replication and inducing antibiotic resistance in bacteria, it may irreparably harm water bodies, posing serious risks to both human security and the ecology [5,6]. Therefore, it is vital to develop feasible technologies for eliminating NOF from the environment. Among the various environmental remediation strategies implemented, semiconductor-mediated photocatalysis has recently received considerable attention as an effectual method in the field of water treatment, owing to its incomparable superiority in terms of being environmentally friendly, sustainability, affordability, high efficiency, and stability [7,8]. In general, this technique works by generating e^--h^+ pairs in the SC materials via light absorption, which are then detached and transported to the target object for redox reactions. Thus, finding a suitable SC photocatalyst with high redox capacity is critical for achieving the mission of clean water.

Alkaline earth metal titanates, a distinctive class of oxide SC's, have been proven to be one of the renowned photocatalysts. Strontium titanate ($SrTiO_3$), a multipurpose n-type titanium oxide with a perovskite structure, is one of them. Owing to its unique and outstanding properties such as superior ferroelectricity/piezoelectricity behavior, strong oxidizing power, multiple crystal phases, corrosion resistance, structural simplicity, availability of large number of alteration sites, nontoxicity, compatibility with other materials, flexibility as well as good stability, it is widely utilized in a variety of photocatalytic

energy and environmental applications [9,10]. Despite the incredible potential, its widespread application and usage is impeded by the ultrafast reconciliation of the photoinduced charge transporters, low quantum efficiency, slow charge transport and insufficient absorption of light. (due to wide band gap typically > than 3 eV) [11]. To circumvent these obstacles, it is exigent to design and fabricate a highly effective photocatalytic system for boosting $SrTiO_3$ photocatalytic activity.

Surface modification of semiconductive oxides with transition metal ions, specifically Cu (II), Fe (III), or Cr (III), has recently piqued the interest of researchers as a promising strategy for developing visible light active photocatalysts with adequate charge carriers' separation capability via a popular IFCT mechanism. This involves direct e^- migration from the SC's VB to the surface deposited nanoclusters, which serve as e- reduction sites, while leaving a vacancy in the catalyst's VB. Induced separated excitons (i.e., e^- in the co-catalysts and photoexcited h^+ in VB) jointly forms the reactive species through multiple pathways which may then contribute to the pollutant degradation. These systems not only employ the photoproduced electrons through the reduction process of the deposited metallic ions, utilizing the deep VB holes for the oxidation reactions, but they also extend the optical response in order to harvest greater quanta of visible light [12,13]. For instance, Hashimoto et al. prepared a series of visible-light active catalysts by Cu(II)/Fe(III) clusters grafting onto TiO_2 surface, leading to magnified photocatalytic activity [14,15]. According to Qiu et al., [16] grafting Fe(III) clusters onto micro flowers shaped BiOCl can improve BiOCl performance due to the IFCT interaction of the components (Fe(III) clusters and BiOCl). Likewise, Sun group demonstrated the enhanced degradation of Orange II over the Fe (III)-modified Bi_2O_3 [17]. Because of its low cost, non-toxicity, and abundance, Fe is a popular co-catalyst for designing and developing high performance photocatalysts via surface modification.

Furthermore, Graphene oxide (GO), a rising star in the carbon family, is another frequently used ideal support material for the construction of various advanced functional nanocomposites, with superior photocatalytic activity. Its enticing properties, such as rich pore structure, large specific surface area, unique conjugated structure with (π–π) interactions, ultrafast e- carrier mobility, strong e- storage ability, abundant reactive oxygen groups, etc, endow the GO-incorporated composites with a plethora of excellent functionalities all at once. These mainly involves (i) increasing the adsorption capacity of target pollutants, (ii) extending the light absorption ranges, (iii) providing efficient pathway for charge transportations and separations, (iv) inhibiting the e^--h^+ recombination rate, which are the ideal traits of a photocatalyst we have been pursuing for [18,19]. To date, a variety of SCs, including BiOCl [20], CdS [21], $BaTiO_3$ [22], and others, have been attempted to construct GO-supported composites with performance greater than single-

component counterparts. Jiaguo Yu et al. [23] reported a BiOI-GO composite with a distinct structure, that demonstrated outstanding photodegradation efficiency towards phenol. Excellent MB dye removal results were recently obtained using porous graphene-$SrTiO_3$ composite [24]. In these composites, GO has been observed to play the role of e- acceptor and mediator. This extends the lifetime of the charge carriers and as a result, facilitates the efficient decomposition of toxic contaminants in wastewater. Considering the distinct properties of $SrTiO_3$, Fe(III) and GO, in photocatalysis, it is intriguing to combine their merits, into one trio system with a potential multiplex synergism among each components.

Inspired by the above concept, the current work developed a new and highly efficient dual cocatalyst modified $SrTiO_3$ photocatalyst, i.e. (Fe(III)-$SrTiO_3$-GO), via a simple two-step route that included the initial anchoring of Fe(III) ions onto the $SrTiO_3$ surface via impregnation followed by coupling of GO sheet via hydrothermal method. The morphology, structure, and optical properties of hybrid has been well scrutinized through series of characterizations. The close interfacial contact developed between the individual components, in the composite contributed to the improvement in the segregation of the charges and increment in the visible light absorption. The efficacy of the as-fabricated ternary hybrid is investigated through the elimination of pharmaceutical pollutant NOF under LED-light exposure. Moreover, the critical role of GO and the impact of Fe(III) species in advancing $SrTiO_3$ activity are thoroughly examined. A photoactivity comparison study has been carried out between the ternary Fe(III)-$SrTiO_3$-GO, the corresponding binary composites (Fe(III)-$SrTiO_3$, and $SrTiO_3$-GO), and the single ($SrTiO_3$). The photocatalyst's stability, mineralization power are also evaluated. Besides, the mechanism of synergism between $SrTiO_3$, Fe and GO has been explored using quenching experiments and the plausible degradation pathway of NOF has been discussed. As far as we know, no investigation has been reported on building such an innovative trio hybrid with multi-channel electron transport routes for ameliorating the photocatalytic behavior of $SrTiO_3$ and expanding its applicability area.

4.2. Experimental section

4.2.1. Chemicals and Reagents

Strontium chloride hexahydrate ($SrCl_2.6H_2O$, 99%), potassium permanganate ($KMnO_4$, 97%), sodium hydroxide (NaOH, 97%) graphite powder (98%), sodium nitrate ($NaNO_3$, 99%), sulphuric acid (H_2SO_4, 98%), hydrogen peroxide (H_2O_2, 30wt%), ethylenediaminetetraacetic acid ($C_{10}H_{16}N_2O$, 99%), isopropyl alcohol (C_3H_8O, 99.5%), ascorbic acid ($C_6H_8O_6$, 99%), hydrochloric acid (HCl, 35%), methanol (CH_3OH, 99%), ethanol (C_2H_5OH, 99.9%), Iron chloride hexahydrate ($FeCl_2.6H_2O$, 98%) were acquired from Loba

Chemie (India). Commercially available Titanium dioxide (P25-TiO_2, [70% anatase + 30 % rutile form]) was obtained from Degussa Corporation Germany. All these reagents were of analytical grade and were used any pre-treatment. Norfloxacin ($C_{16}H_{18}FN_3O_3$) tablet (400 mg) was purchased from the pharmaceutical company Bharat Health Care Ltd. Triple deionized water utilized throughout the entire study was procured from Organo Biotech Laboratories Pvt. Ltd.

4.2.2. Synthesis of $SrTiO_3$ nanocubes

$SrTiO_3$ nanocubes were fabricated via a hydrothermal route. To begin, 3 mmol of $SrCl_2.6H_2O$ was dissolved in 20 mL of DI water (marked as solution A); then, 3 mmol of P25-TiO_2 was dispersed in 20 mL of DI water (designated as suspension B); and 0.2 mol of NaOH was dispersed in 40 mL of DI water (referred as C). For 30-minute, solutions A and B were stirred separately. The suspension B was then gradually added dropwise to the solution A, followed by the solution C. After 1h of uniform mixing and magnetic stirring, the reaction mixture was transferred into a (100 mL) Teflon-lined autoclave and subjected to a 24h hydrothermal treatment at 200°C. Upon completion, the autoclave was allowed to cool down naturally. The product was collected by centrifugation, repeatedly washed with DI water and ethanol, and then dried in a hot air oven at 65°C for 4 hours. Finally, white colored $SrTiO_3$ nanocubes were obtained.

4.2.3. Synthesis of Graphene oxide

Graphene oxide (GO) was effectively prepared from graphite powder via the modified Hummer's approach. [25]

4.2.4. Synthesis of Fe(III) deposited $SrTiO_3$ nanocomposite

The wet impregnation method was employed for the deposition of iron species on $SrTiO_3$. For this purpose, 100 mg of the as-synthesized $SrTiO_3$ powder was dispersed in a round bottom flask containing 20 mL of distilled water. The required amount of $FeCl_2.6H_2O$ solution (0.1M) corresponding to distinct weight percentages (1, 2 3) of Fe was then appended dropwise to it. The resulting solution was kept under continuous magnetic stirring for 12h. The transformation of the solution's colour from white to orange indicates successful Fe deposition. The obtained product was centrifuged, washed with DI water and ethanol several times, and dried in an oven at 65°C for 3h. The various 1, 2, and 3wt% Fe(III) impregnated $SrTiO_3$ composites synthesized in this manner were abbreviated as 1Fe(III)-$SrTiO_3$, 2Fe(III)-$SrTiO_3$, and 3Fe(III)-$SrTiO_3$, respectively.

4.2.5. Synthesis of Fe(III)-$SrTiO_3$-GO ternary nanocomposite

The synthesis of the ternary Fe(III)-$SrTiO_3$-GO nanocomposite was performed by using a hydrothermal process. To begin, 10 mg of GO was dispersed in 40- and 20-mL mixture of distilled water and ethanol ultrasonically for 2 hours to thoroughly re-exfoliate the GO. Following that, 100 mg of the as-prepared Fe(III)-$SrTiO_3$ composite was added to this GO dispersion and stirring was continued for 1hour to achieve a homogeneous suspension. The obtained suspension was then loaded to an autoclave and heated to 120°C for 3 hours. After cooling naturally, the grey color precipitates were recovered through centrifugation, thoroughly washed with distilled water and ethanol thrice, and kept for drying in an oven at 65°C for 3 h to obtain the desired xFe(III)-$SrTiO_3$-10GO nanocomposite. (x% Fe, fixed 10% GO by wt%).

The complete fabrication process of 2Fe(III)-$SrTiO_3$-10GO nanocomposite is schematically displayed in **Scheme-4.1.**

4.2.6. Synthesis of $SrTiO_3$-GO binary nanocomposite

$SrTiO_3$-GO nanocomposite was also prepared in a similar manner for comparison. Briefly, 10 mg of GO was firstly dispersed in a ethanol (40mL): water (20mL) mixture ultrasonically, then (100mg) of prepared $SrTiO_3$ nanocubes were added to it. After 1 hour of uniform mixing and stirring, the final mixture was heat treated at 120°C for 3 hours. Finally, a (10 wt% GO loaded, $SrTiO_3$-10GO) binary nanocomposite was obtained following a centrifugation, washing and drying procedure.

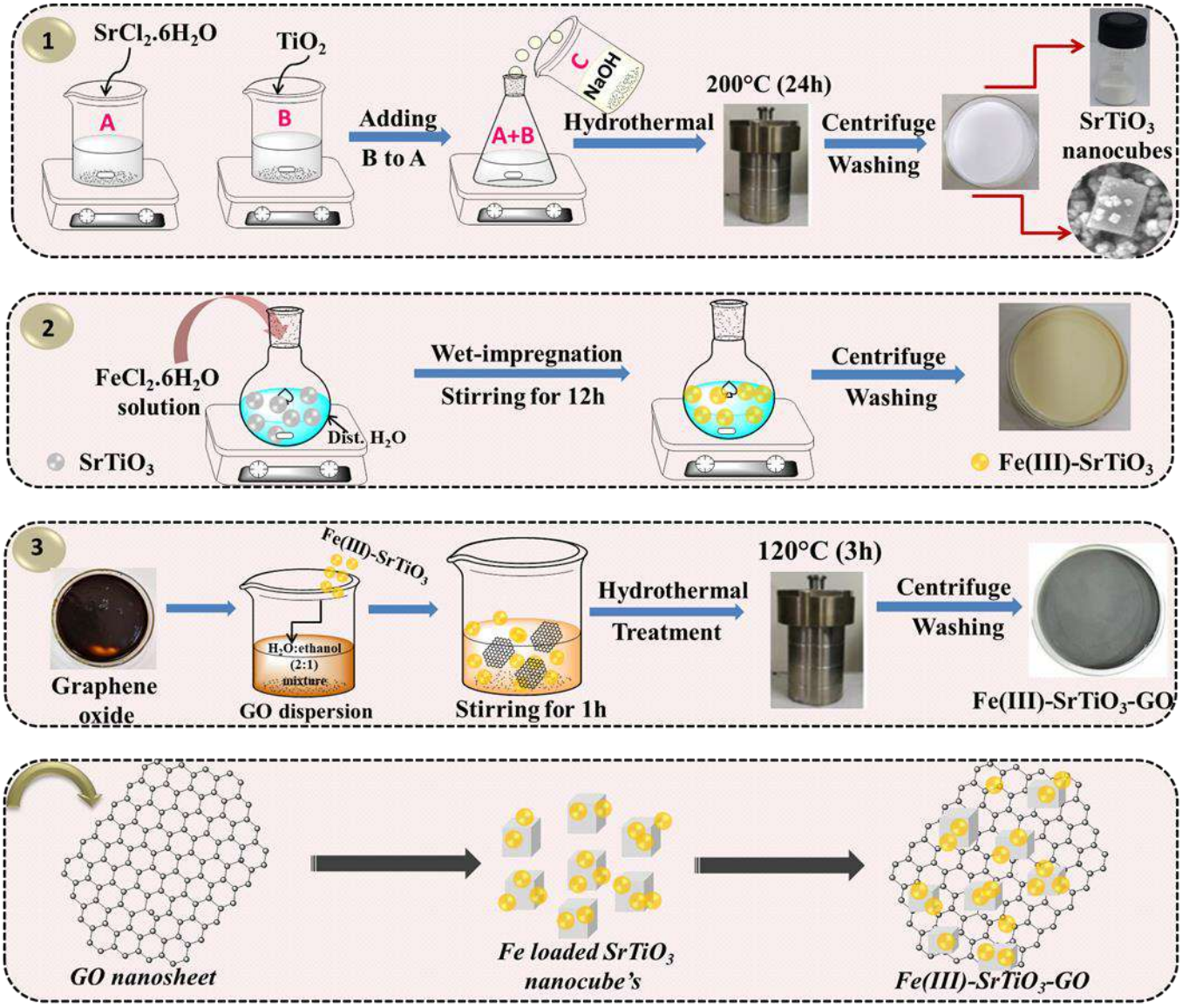

Scheme-4.1: Schematic illustration of the fabrication process of the ternary Fe(III)-$SrTiO_3$-GO nanocomposite.

4.2.7. Characterization

The crystal structures and phase purity of the as-fabricated photocatalysts were examined by the XRD technique using Rigaku Smart Lab SE Japan X-ray diffractometer, with Cu Kα target as an irradiation source (λ = 1.5406 Å) operated in the range of 5° to 85° (2θ). The surface chemical compositions and binding energies of constitutional elements were investigated using an XPS spectrometer (Thermo Fisher ESCALAB Xi+). The morphology and structural characteristics were appraised though FE-SEM, (Carl Zeiss SIGMA 500), HR-TEM (JEOL, JEM 2100 PLUS) electron microscopes. The EDS spectra and mapping images were captured on the Bruker EDS system. Furthermore, optical absorption spectra of each sample were collected

in a diffuse reflectance mode with a UV-vis spectrophotometer (JASCO, V-750) across region of 200-800 nm with $BaSO_4$ as a reference. The PL experiments were performed at room temperature using a SHIMADZU RF-6000 spectrofluorimeter excited at 330 nm wavelength. The functional groups were identified with FT-IR spectra taken on a SHIMADZU, IR Tracer-100 spectrophotometer using KBr pellets as reference. Raman spectra were obtained from Labram HR, a Horiba micro-Raman spectrometer with a excitation laser of 532 nm. Changes in the absorption spectra observed during the degradation of toxic pollutant were recorded on a (Shimadzu, UV-2600) UV-Vis spectrophotometer. Electrical conductivity data was obtained on a Solartron analytical impedance analyzer set at room temperature (Model: SI 1260). Besides, the surface area and distribution of pore sizes were measured using the Quantachrome Nova-1000 surface analyzer by BET and BJH methods, respectively. (Analysis gas: Nitrogen, Outgas and bath temperature: 180^{o}C and 77.3 K respectively, Outgas Time: 6 h).

4.2.8. Photocatalytic activity test

The photocatalytic performances of pure $SrTiO_3$, and its nanocomposites (Fe(III)-$SrTiO_3$, $SrTiO_3$-GO, and Fe(III)-$SrTiO_3$-GO) were examined by analyzing the degradation of a model pharmaceutical pollutant, NOF, under LED light irradiation. The photocatalytic reactions were executed in separate test tubes. Typically, 5 mg of a sample was dispersed into each test tube containing 5 mL of a 20 ppm NOF aqueous solution. Before being exposed to light radiations, the suspension was stirred magnetically for 40 minutes in the dark to ensure that the catalyst and NOF molecules were in a state of adsorption-desorption equilibrium. The photocatalytic degradation processes were then commenced by illuminating the test tubes containing different catalysts with a 50-W LED lamp (Wipro Garnet B22, with ~100W/m^2 intensity) for 120 min. At appropriate time intervals, each catalyst was separated from the test tube via a centrifugation at 6,000 rpm for 10 min to remove any residual solid particulates. A UV-visible spectrophotometer was then used to analyse the supernatant. Changes in NOF concentration were monitored by observing changes in the absorbance spectra at λ_{max} = 272 nm.

The (%) of NOF degradation was calculated from the below-mentioned relation:

$$\text{Degradation (\%)} = \{(C_0 - C_t)/C_0\} \times 100 \quad (1)$$

where, C_0 and C_t signifies the NOF concentrations at the initial stage at time '0' and after exposure to light irradiation at time 't' respectively.

To inspect the mineralization capability of Fe(III)-$SrTiO_3$-GO, TOC evaluation experiment was executed, using the titrimetric method.

The TOC value was reckoned by the following equation with distilled water as a blank:

$$TOC\ (mg/L) = \frac{(Blank-Sample)\times Normality\ of\ FAS\times 12000}{Sample\ volume\times 4} \quad (2)$$

The extent of mineralization was ascertained by the given equation:

$$Mineralization\ (\%) = \frac{TOC\ initial-TOC\ final}{TOC\ inital}\times 100\% \quad (3)$$

Where, $TOC_{initial}$ is the total organic carbon of NOF (mg/L) before degradation; TOC_{final} represents the total organic carbon of NOF after degradation process of 120 min (mg/L). Further, the degraded products of NOF were identified with LC-MS system (Waters Micromass QTOF Micro mass spectrometer) coupled with a quadrupole time-of-flight high resolution mass spectrometer. Aqueous solutions of 0.1% of formic acid and acetonitrile with HPLC grade were taken as mobile phases.

4.3. Results and Discussion

4.3.1. Structural study

XRD analysis

The crystalline phases of the as-fabricated ternary (2Fe(III)-$SrTiO_3$-10GO) and binary ($SrTiO_3$-10GO, 2Fe(III)-$SrTiO_3$) nanocomposites along with the bare GO and $SrTiO_3$ samples, were recognized using XRD patterns, and the results are depicted in **Fig.4.1(a)**. For pure GO, the typical sharp peak at a 2θ value of 11.6° has been observed, which corresponds well to the (001) lattice plane [26]. The result indicates the conversion and oxidation, of pristine graphite into graphene oxide. Further, the XRD profile of parent $SrTiO_3$ shows characteristic peaks located at 2θ = 22.78˚, 32.34˚, 39.8˚, 46.4˚, 52.34˚, 57.7˚, 67.6˚, 72.04˚, 77.09˚, which can be well indexed to the (100), (110), (111), (200), (210), (211), (220), (221), and (310) diffraction planes of cubic-structured $SrTiO_3$. (JCPDS No.79-0174), respectively [27]. The XRD profiles of the two binary samples, (2Fe(III)-$SrTiO_3$, $SrTiO_3$-10GO) as well as the ternary 2Fe(III)-$SrTiO_3$-10GO sample, were found to be similar to those of pristine $SrTiO_3$. No peaks associated with Fe_2O_3, Fe_3O_4, FeOOH, or other iron-based oxides/hydroxides have been observed in XRD diffractogram of Fe impregnated samples, which might be because of the low amount of Fe species or their high dispersion on the $SrTiO_3$ surface. However, the presence and distribution of Fe (III) species have been additionally validated through FE-SEM, EDX, and XPS technique. Meanwhile, the enlarged principal peak corresponding to the (110) crystal plane at (2θ = 32.39˚) clearly indicates that the Fe(III) deposition did not induce any noticeable shift even in the peak positions of $SrTiO_3$ in respective 2Fe(III)-$SrTiO_3$ and 2Fe(III)-$SrTiO_3$-10GO samples (**Fig.4.1(b)**). This

suggests that Fe ions are well adhered on the surface instead of being embedded into the $SrTiO_3$ lattice [28]. Additionally, in the case of the GO hybridized system, negligible diffraction peaks belonging to the GO were detected in the XRD profiles of $SrTiO_3$-10GO and 2Fe(III)-$SrTiO_3$-10GO nanocomposites. The absence of such a peak could be due to the relatively small content, low diffraction intensity and nice dispersion of GO in the composites. Besides, the sharp peaks and lack of any impurity related peaks demonstrates the purity and highly crystalline nature of the prepared materials.

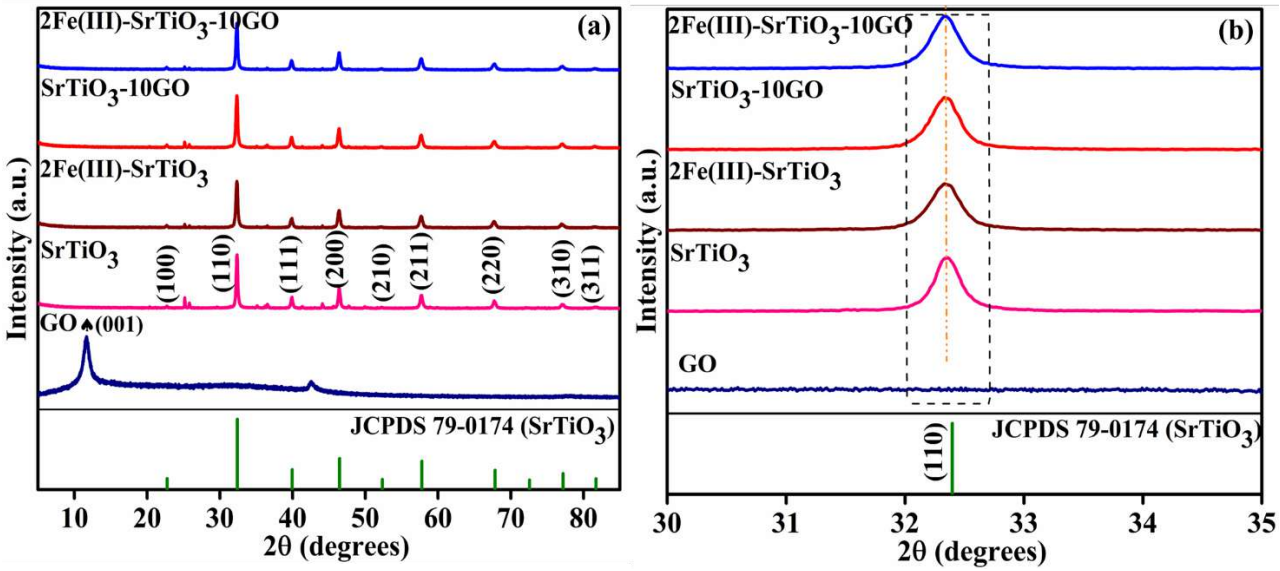

Fig.4.1: (a) XRD patterns of GO, pristine $SrTiO_3$, binary [2Fe(III)-$SrTiO_3$, $SrTiO_3$-10GO], and ternary 2Fe(III)-$SrTiO_3$-10GO samples (b) their corresponding magnified XRD patterns with an enlarged (110) crystal plane.

4.3.2 Raman analysis

The existence of GO in 2Fe(III)-$SrTiO_3$-10GO is further ascertained by Raman spectroscopy. **Fig.4.2** compares the Raman spectra of the GO and various $SrTiO_3$ samples, with Raman shifts ranging from 100 cm^{-1} to 2000 cm^{-1}. The spectra of parent $SrTiO_3$, exhibit a broad continuum in the range of 100-1150 cm^{-1}. Peaks corresponding to first order raman modes in $SrTiO_3$ are observed at 179.9, [254.7, 289.4, 366.7], 544.5 cm^{-1} which are associated with the TO_2 (O-Sr-O), TO_3 (O-Sr-O), and TO_4 (O-Sr-O), modes respectively, while the second order raman bands are occurring at [621.3, 685.0, 712.2], 802.2 cm^{-1} are allocated to the LO (Ti-O-Ti) and LO_4 (Ti-O) modes respectively [27,29]. After depositing iron species, no shift or broadening of Raman peaks is observed in 2Fe(III)-$SrTiO_3$, demonstrating that the $SrTiO_3$ structure remains intact. The well-known D (1349 cm^{-1}) and G (1598 cm^{-1}) bands of GO, were clearly visible in the

raman spectrum of GO. The D band is due to the presence of disorders in sp^2-hybridized carbons, arising from breathing mode of k-point phonons with A_{1g} symmetry and the G band is caused by the phonon vibration of sp^2 carbons with E_{2g} mode [30,31]. Both the binary and ternary composites ($SrTiO_3$-10GO and 2Fe(III)-$SrTiO_3$-10GO) exhibit all of the characteristic bands analogous to pristine $SrTiO_3$ and GO, confirming the successful attachment of graphene oxide sheets. However, when compared with pure $SrTiO_3$, the peak intensities of the hybrids were significantly lowered due to the strong bonds between the various components, or the surface coverage by GO, and Fe(III) species. This further advocates the intimate contacts developed between the individual components of the ternary hybrid.

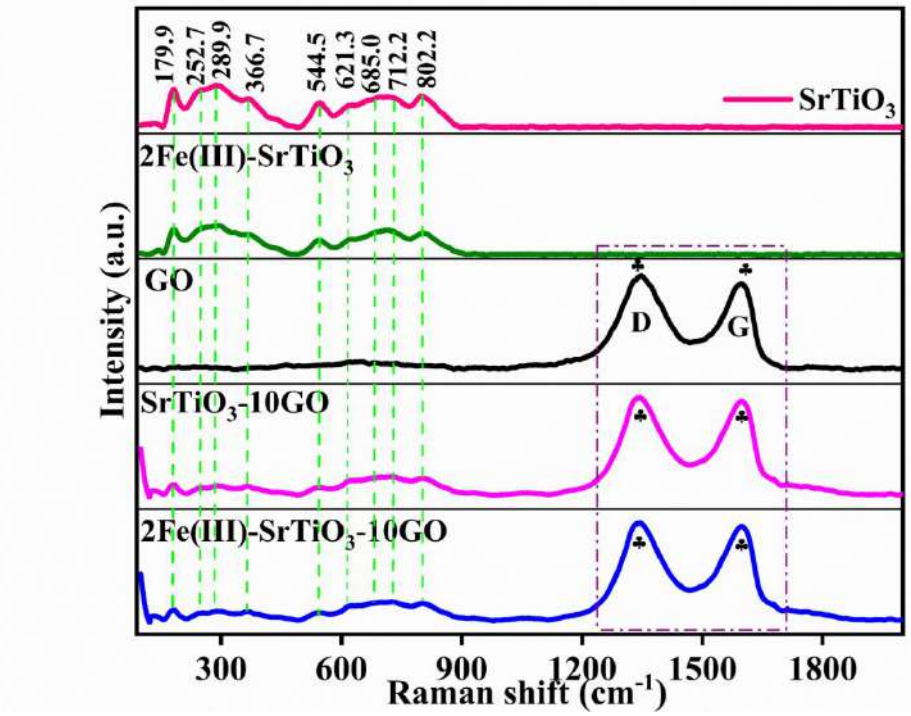

Fig. 4.2: Raman spectra of GO, pristine $SrTiO_3$, and various $SrTiO_3$ nanocomposites.

4.3.3 FT-IR analysis

FT-IR analysis was done to investigate the differences in chemical structure and study the bonding interactions in pure GO, $SrTiO_3$, 2Fe(III)-$SrTiO_3$, $SrTiO_3$-10GO, and 2Fe(III)-$SrTiO_3$-10GO samples, and the results are depicted in **Fig. 4.3.** The FTIR spectrum of synthesized GO, revealed the existence of several O_2-containing functional groups on its surface such as the band at 934 cm^{-1} belongs to the C−H bending vibration, while, 1044 cm^{-1} refers to the C−O stretching vibration. Band around 1248 cm^{-1} relates to the (C−O−C) epoxy group's asymmetric stretching vibration. An absorption peak at 1381 cm^{-1} relates to carboxyl (C-O) group's bending vibrations. The band noticed at 1598 cm^{-1} corresponds to the aromatic stretching vibration mode of the sp^2 carbon skeletal network (C=C) and the other at 1720 cm^{-1} was

characterized as C = O stretching vibration of the carboxyl (COOH) group. The C-H bond vibrations in sp^3 hybridization corresponds to the band at 2987 cm^{-1}. Finally, a broad band in the high frequency region of 3000-3500 cm^{-1} associates with the stretching, bending vibrations of O-H groups of water molecules adsorbed on GO surface[32,33].

For the $SrTiO_3$ NC's, the characteristic absorptions were observed at 540, 855, 1646 and 3430 cm^{-1}. Peak at 540 cm^{-1} corresponds to the Ti-O stretching mode. This implies the existence of TiO6 octahedrons and the formation of $SrTiO_3$ perovskite-like structure. The weak peak at 855 cm^{-1} is from the stretching vibrations of Sr–O bond. Broad absorption peaks around 1646 cm^{-1} and the band at

3430cm^{-1} are the bending and stretching vibration modes of O-H group from the adsorbed water molecules [34,35]. Compared to pristine $SrTiO_3$, small amount of O_2 functional groups (C-O, C-O-C, C=O) characteristic of GO, are additionally detected in the spectrum of both $SrTiO_3$-10GO, and 2Fe(III)-$SrTiO_3$-10GO nanocomposites, strongly demonstrating the existence of chemical bonding with GO in the synthesized composites. However, no functional groups of Fe(III) species were found in iron modified composites (Fe(III)-$SrTiO_3$, and Fe(III)-$SrTiO_3$-GO), most likely due to the low loading amount and high dispersion. Besides, no discernible differences were observed in comparison to $SrTiO_3$, indicating that anchoring of Fe(III) species did not alter the chemical structure of $SrTiO_3$.

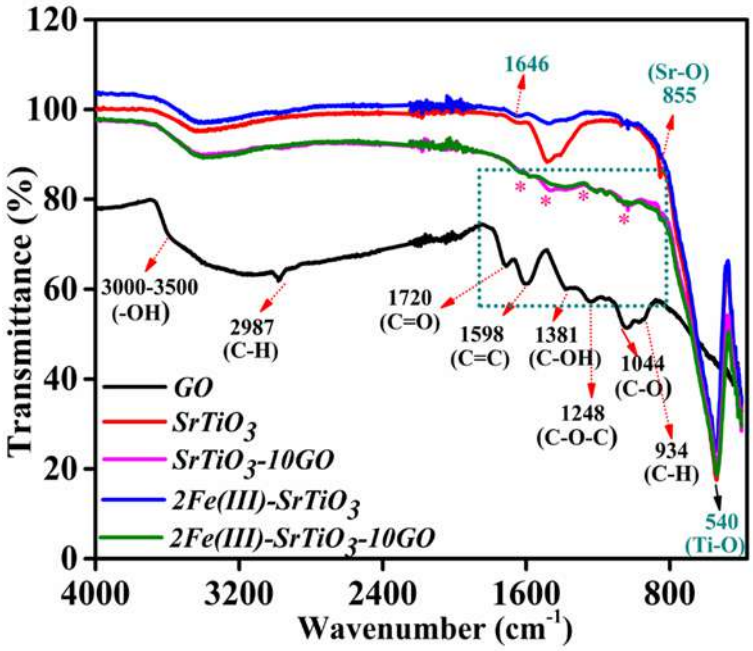

Fig. 4.3. FT-IR spectra of GO, pristine $SrTiO_3$, and various $SrTiO_3$ nanocomposites

4.3.4 XPS analysis

XPS measurements **(Fig. 4.4)** were done to examine the surface elemental composition as well as chemical state of the multi-component 2Fe(III)-$SrTiO_3$-10GO nanocomposite. As depicted in **(Fig.4.4(a))**, the XPS survey scan spectrum clearly show that the composite consists of Sr, Ti, O, Fe, and C elements, this is in accordance with the EDS mapping analysis discussed later. The high-resolution XPS spectrum of Sr (3d) **(Fig.4.4(b))**, exhibits 2 prominent peaks that are allocated to Sr $3d_{5/2}$ (133.7 eV) and Sr $3d_{3/2}$ (135.3 eV), respectively, suggesting that the strontium element exists in the Sr^{2+} state. One deconvoluted peak appearing at 132.2 eV related to the metallic Sr^0. The Ti (2p), XPS spectra **(Fig.4.4(c))** presents two distinct peaks, centered at 458.4 eV and 464.1 eV, corresponding to the Ti $2p_{3/2}$ and Ti $2p_{1/2}$ binding signals respectively[36]. The difference in B.E's between these two peaks was observed to be 5.7 eV, suggesting that the chemical state of Ti in the 2Fe(III)-$SrTiO_3$-10GO composite was Ti^{4+} [37]. The spectrum **(Fig.4.4(d))** of O (1s) was fitted to 2 deconvoluted peaks at B.E.'s 530.0 eV and 532.0 eV. The high peak at 530 eV correspond to crystal lattice oxygen of $SrTiO_3$, whereas the other peak at 532.0 eV attributes to the adsorbed oxygen from the OH bond (surface hydroxyl group) attached to the composite's surface.Furthermore, the XPS spectra of Fe 2p **(Fig.4.4(e)**, exhibits two main peaks centered at 710.6 eV (Fe $2p_{3/2}$), 724.0 eV (Fe $2p_{1/2}$) and a satellite peak at (719.3 eV) which are characteristic of Fe in trivalent oxidation state (Fe(III)). Moreover, the peak separation ($\Delta = 2p_{1/2} - 2p_{3/2} = 13.4$ eV) , is comparable to that of Ferric ion [38]. This is also corroborated by the satellite peak of Fe^{+3} which is located at higher B.E. of about 8.7 eV from the main Fe $2p_{3/2}$ peak, which matches well with the B.E. energy difference reported in literature and rules out the presence of Fe^{2+} species. These findings strongly suggest that, the surface deposited Fe species in the synthesized composite, are in Fe(III) oxidation state, which corresponds to the iron in its oxide (Fe_2O_3) or hydroxides (FeOOH) form. However, it should be noted that many reports, including one by Kirstin et al.[39], clearly show the presence of the aforementioned Fe peaks, which are associated with the α-Fe_2O_3 (Hematite) phase of iron. **(Fig.4.4(f))**, displays the GO, C1s XPS spectrum, which is deconvoluted into three peculiar peaks. The peak at 284.5 eV referred to the typical C-C bonds in the aromatic network for GO, while the other two weaker peaks positioned at the 286.2 and 288.6 eV corresponded to the epoxy (C-O), carbonyl (C=O) functional groups suggesting the existence of oxygen-containing groups in GO[20]. From the XPS results, it can be strongly inferred that the formation of the ternary Fe(III)-$SrTiO_3$-GO composite was successful.

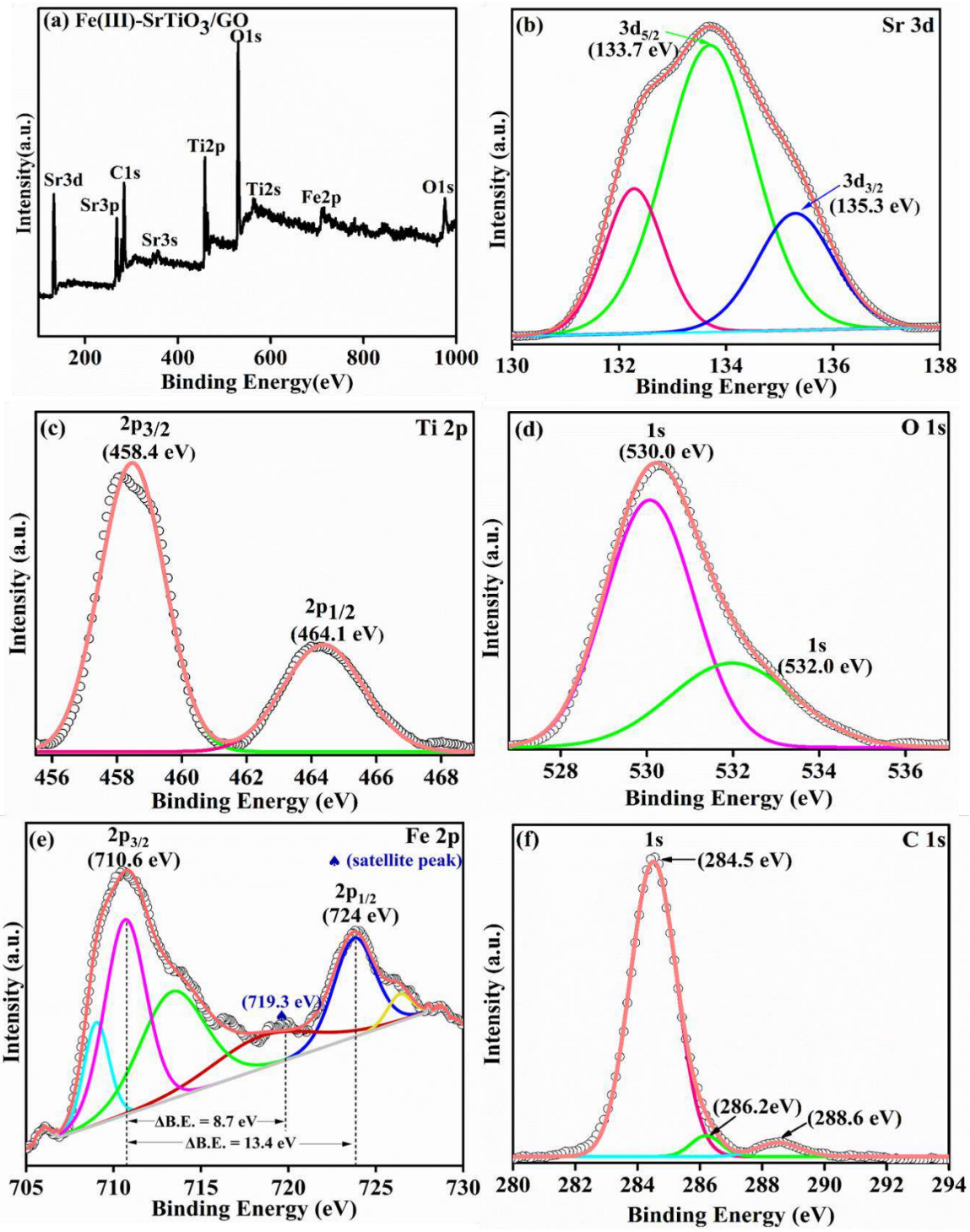

Fig. 4.4: XPS spectra for 2Fe(III)-$SrTiO_3$-10GO nanocomposite (a) survey scan (b) Sr 3d, (c) Ti 2p, (b) O 1s, (d) Fe 2p, and (e) C 1s spectrum.

4.3.5 Morphology studies

FE-SEM, EDS-Mapping and HR-TEM analysis

In order to understand the morphological and structural features of newly designed ternary 2Fe(III)-$SrTiO_3$-10GO nanocomposite, FE-SEM, TEM and HR-TEM analysis were carried out. As evident from the FE-SEM micrograph **Fig.4.5(a),** pristine $SrTiO_3$ has a well-defined nanocube's like morphology with a smooth surface. In the ternary 2Fe(III)-$SrTiO_3$-10GO system, **Fig.4.5(b)**, some tiny Fe(III)NPs with irregular shapes can be seen tightly anchored on the surface of $SrTiO_3$ nanocube's, all of which interacted well with the 2-D lamellar structure of GO. The tightly packed surface morphology of the composite particles is expected to result in a smooth pathway for the efficient electron transportation and collection.

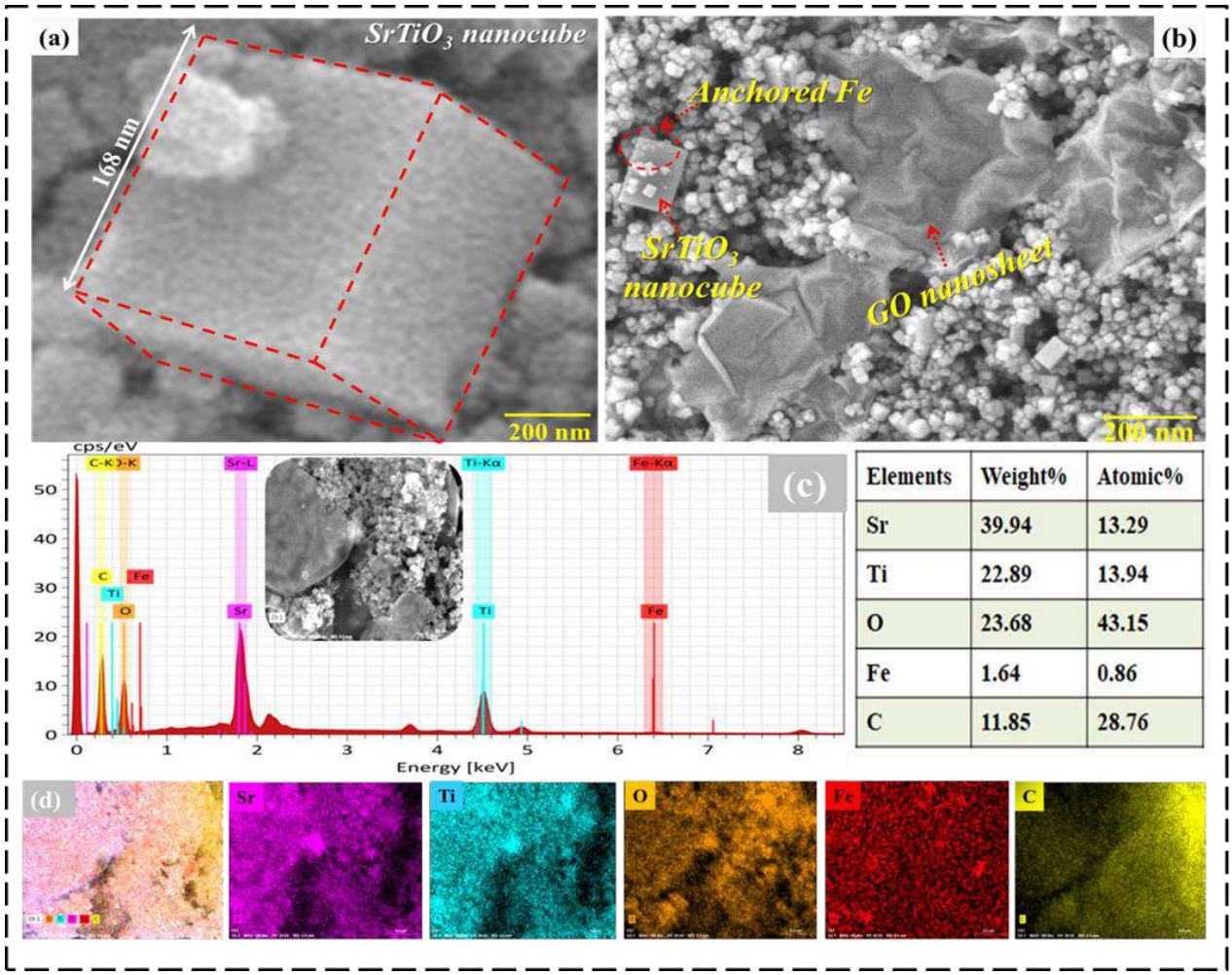

Elements	Weight%	Atomic%
Sr	39.94	13.29
Ti	22.89	13.94
O	23.68	43.15
Fe	1.64	0.86
C	11.85	28.76

Fig.4.5: (a-b) FE-SEM images, **(**c) corresponding EDX spectrum; and (d) elemental color mapping images of different elements (Sr, Ti, O, Fe, C) present in ternary 2Fe(III)-$SrTiO_3$-10GO nanocomposite.

Further, the images of EDS spectrum and corresponding elemental distribution with colored dot mapping **(Fig. 4.5(c-d))** testify the co-existence of Sr (pink), Ti (azure), O (orange), Fe (red) and C (yellow) constituent

elements in the hybrid, affirming the successful configuration of the Fe(III)-$SrTiO_3$-GO trio with high elemental purity and even distribution of Fe(III) species deposited $SrTiO_3$ nanocube's over the GO surface. The atomic percentage of each element is revealed in the inserted table in **Fig. 4.5(c)**, which shows that $SrTiO_3$ is more abundant in the sample than GO and Fe species, this is consistent with the findings of SEM analysis.

Fig. 4.5((a)-(d)) displays the TEM images of the 2Fe(III)-$SrTiO_3$-10GO nanocomposite. Similar to FE-SEM, $SrTiO_3$ NPs were found to have a cube like structure with an average length of 24 nm (as measured by the particle size distribution pattern). On each $SrTiO_3$ nanoparticle, dark colored patches in the range of 2-10 nm are observed, which are believed to be the Fe(III) species adhered to the $SrTiO_3$ surface. The photographs clearly show the accumulation of Fe(III)-impregnated $SrTiO_3$ NCs on layered GO sheets. These images depict the perfect development of the desired ternary composite with close contacts.

The HR-TEM analysis was then used to investigate the effectual integration of the three components in the developed hybrid. The image **(Fig. 4.6(e))** clearly shows, the presence of two distinct sets of well-resolved lattice fringes, one of which is associated with (110) crystal plane of cubic $SrTiO_3$ with an interplanar spacing (d) of 0.271 nm [36] and another with a lattice spaces of 0.375 nm, attributing to the (012) diffraction plane of Fe(III) species from α-Fe_2O_3 (JCPDS No. 33-0664). This provides an authentication that the anchored Fe(III) ions are in the form of iron oxide i.e. alpha hematite [40]. And, GO nanosheets served as the support for both the anchored Fe(III) species and $SrTiO_3$. Likewise, the SAED pattern **Fig. 4.6(f),** displays numerous concentric diffraction rings with bright spots, which are congruent to peculiar ring pattern of $SrTiO_3$ [(110), (200), (220), (311)], α-Fe_2O_3 [(006)], and (001) plane of GO, which further demonstrated that impregnated iron species were firmly anchored on $SrTiO_3$ NCs and are nicely supported by GO sheets[36,40]. According to HR-TEM results, the Fe(III) clusters formed by the impregnation method were in the grown in the form of Fe_2O_3. Furthermore, the diffraction spots in the SAED pattern demonstrated the hybrid material's polycrystalline nature.

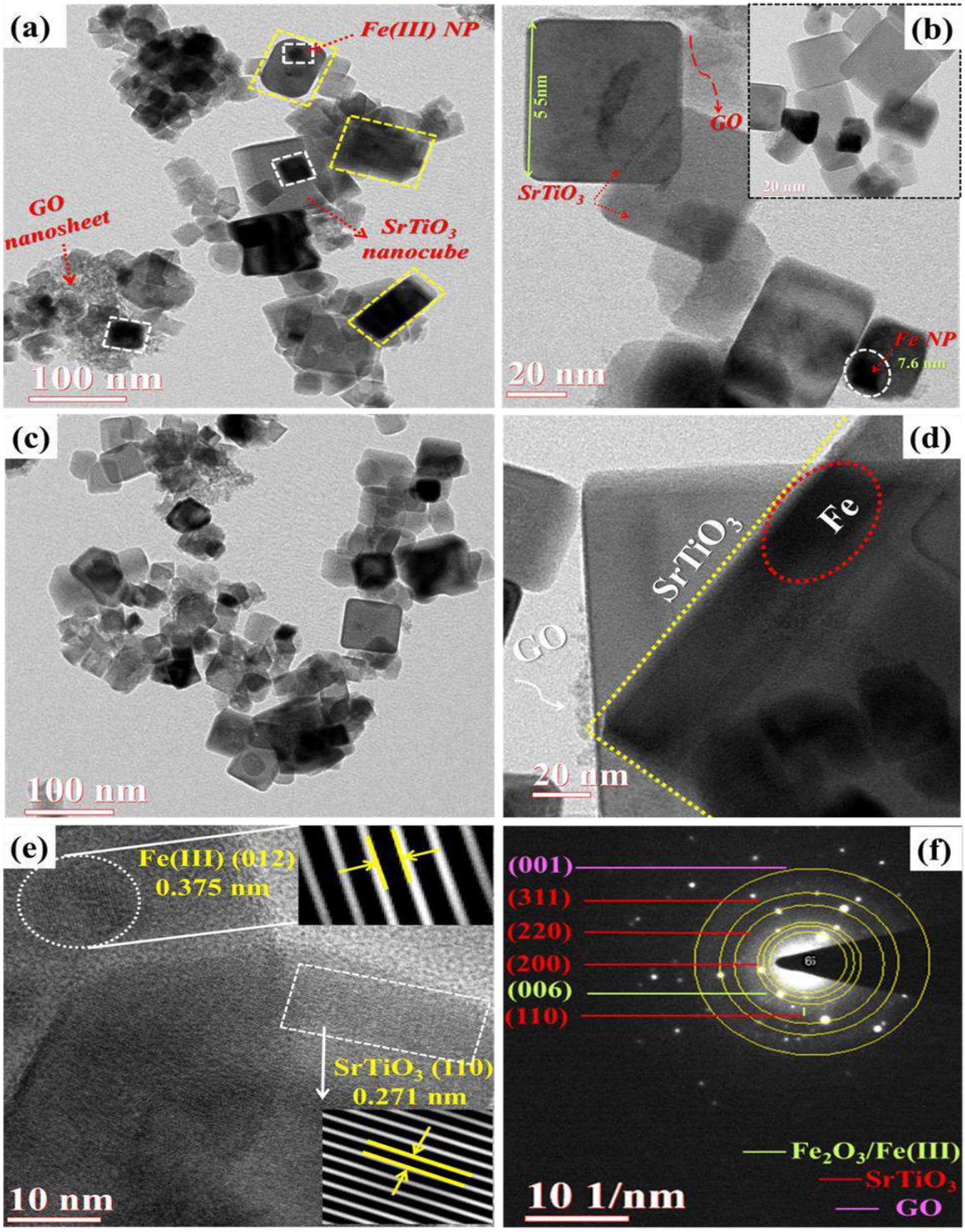

Fig.4.6: (a-d) HR-TEM images (e) Lattice fringes and (f) SAED pattern of 2Fe(III)-$SrTiO_3$-10GO nanocomposite.

Overall, the FE-SEM and HR-TEM observations jointly evidenced successful fabrication of the dual (iron) and (graphene oxide) modified $SrTiO_3$ nanocomposite with development of strong and close contacts along

with existence of multiple e- transfer routes between the individual constituents (Fe(III) species, $SrTiO_3$ NCs and GO sheets) in trio hybrid. This could be beneficial for the adequate charge carrier's migration as well as segregation in the composite ultimately resulting in an amelioration in $SrTiO_3$'s photocatalytic activity.

4.3.6 Porosity and surface area study

In photocatalytic degradation reaction, a large surface area allows the adsorption of more reactants on the catalyst's surface, while a larger pore volume promotes the fast diffusion of numerous reactants and products, thus, upgrading the photocatalytic ability for removing pollutants efficiently[41,42]. Hence, characterizing the photocatalyst's surface area and distribution of pore size is beneficial for investigating the material's photocatalytic features. The N_2 adsorption-desorption experiments were carried out to explore these textural properties (porosity and surface area) of pristine $SrTiO_3$ as well as ternary 2Fe(III)-$SrTiO_3$-10GO nanocomposite and the findings are portrayed in **Fig. 4.7.**

According to the IUPAC, the curve shape **(Fig. 4.7(a))**, of both samples resembles the classic type-IV isotherm with typical H3 hysteresis loops at pressures ranging from (P/P_0), [0.8- 1.0], representing the formation of slit-like pores that are generally associated with aggregates of platelike particles typical mesoporous nature of nanostructures.[43]The BJH analysis curves **((Fig. 4.7(b))**, indicated that for both the samples, the majority of the pores lie in the range of 2-25 nm which further signals the existence of a mesoporous structure.

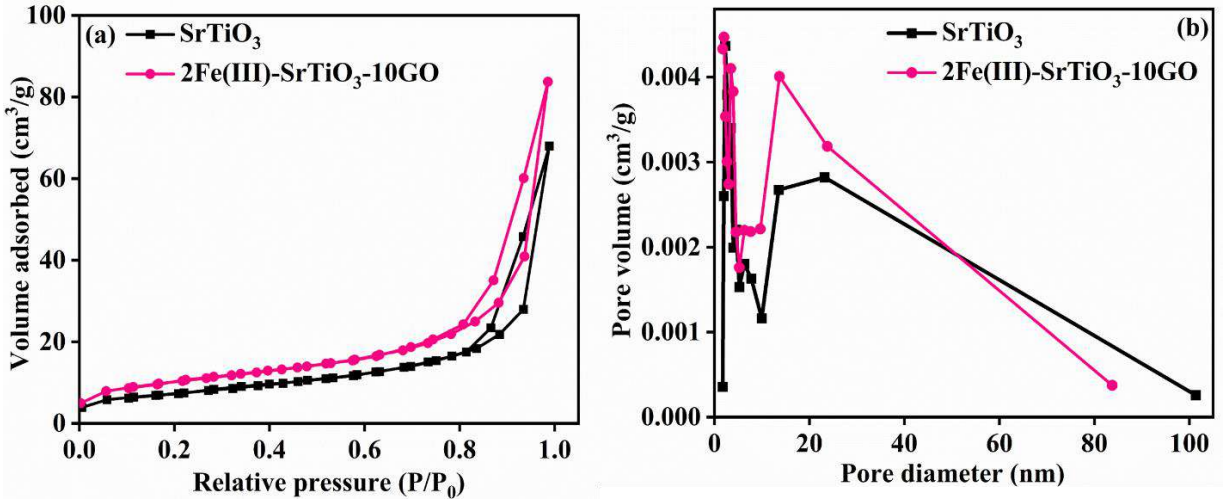

Fig. 4.7: (a) N_2 adsorption isotherms and (b) the corresponding BJH pore size distributions curves of pristine $SrTiO_3$ and 2Fe(III)-$SrTiO_3$-10GO nanocomposite.

The associated textural properties of pristine $SrTiO_3$ and ternary 2Fe(III)-$SrTiO_3$-10GO nanocomposite are

presented in **Table-4.1.**

S.No.	Photocatalyst	Surface area (m^2g^{-1})	Total Pore Volume (cm^3g^{-1})	Mean Pore diameter (nm)
1	$SrTiO_3$	25.635	0.109	2.297
2	2Fe (III)-$SrTiO_3$-10GO	36.137	0.132	2.030

The calculated BET surface area of the optimal 2Fe(III)-$SrTiO_3$-10GO sample (36.137 m^2/g) was approx. 1.4 folds larger than that of pure $SrTiO_3$ (25.635 m^2/g). The enlargement observed in the surface area could be owed to the surface deposition of Fe(III) and the inclusion of a wonderful carbonaceous material such as GO, with excellent supportability and a high adsorption capacity. Likewise, the pore volume of the ternary composite was also found to be larger compared to those of pure $SrTiO_3$ NC's, which means that in composite there is enough volume to hold and transport the contaminant molecules. However, the average pore size is observed to be slightly reduced in 2Fe(III)-$SrTiO_3$-10GO, may be due to the interaction between the three components in the hybrid. Thus, the ternary photocatalyst with a mesoporous feature, extended BET surface area and higher pore volume is capable of supplying plenty of surface-active sites during the photocatalysis, which is conducive for ameliorating the photocatalytic degradation performance.

4.3.7 Optical and charge transfer properties

UV−Vis Diffuse reflectance spectra

The light absorption properties of as-fabricated samples were visualized using diffuse reflectance spectroscopy and the outcomes are presented in **Fig.4.8. (Fig. 4.8(a))** clearly depicts that, pure $SrTiO_3$ absorbs strongly in the UV range, with an absorption maximum around 392 nm. This absorption is attributed to the transition of e- from the O 2p orbital of VB) to the Ti 3d orbital of the CB. [44] In comparison to the limited light absorption of pristine $SrTiO_3$, the two binary composites (2Fe(III)-$SrTiO_3$, $SrTiO_3$-10GO), and the ternary (2Fe(III)-$SrTiO_3$-10GO) hybrid demonstrated strong absorption intensities from 400 to 800 nm. Anchoring Fe(III) nanoparticles on $SrTiO_3$'s, surface significantly improves its optical absorption property by extending the absorption tail to above 500 nm. According to the literature, the d-d transition of the Fe(III) cocatalyst may play a role in this. In addition, a new absorption band in the region of 450-550 nm has been observed in Fe(III) impregnated $SrTiO_3$ sample. This could be ascribed to the IFCT process occurring from $SrTiO_3$'s, VB electrons to the surface Fe(III) species that greatly reduces the transition distance [12,13,45].

The incorporation of GO further enlarges the visible light response, a considerable red shift is noticed in the absorption edges, which is credited to the chemical interaction among the $SrTiO_3$ surface and the GO functional groups via the Ti-O-C bond [46]. Moreover, the fact that it is a blackbody material aids in improving the sample's absorption capacity.

After compounding both Fe and GO, with $SrTiO_3$, the resultant hybrid not only exhibits an increase in absorption intensity but also has a much wider absorption band across the entire visible spectrum[47]. As a result, the combined IFCT phenomenon coming from the deposited Fe(III) species and photosensitization by GO results in the highest optical absorption strength and favors more efficient visible light utilization.

The observation was in close agreement with the colors of the corresponding samples which varied from white for pristine ($SrTiO_3$) to bright orange for binary (2Fe(III)-$SrTiO_3$), and finally to dark grey for trio (2Fe(III)-$SrTiO_3$-10GO).

Besides this, the band gap energies of E_g of each photocatalyst were assessed using the empirical equation [48]:

$$ahv = A\,(hv - E_g)^{1/2} \quad \textbf{(4)}$$

Here α , *h* , υ and A, represents the absorption coefficient, planck's constant, frequency of incident light, proportionality constant, and bandgap energies respectively.

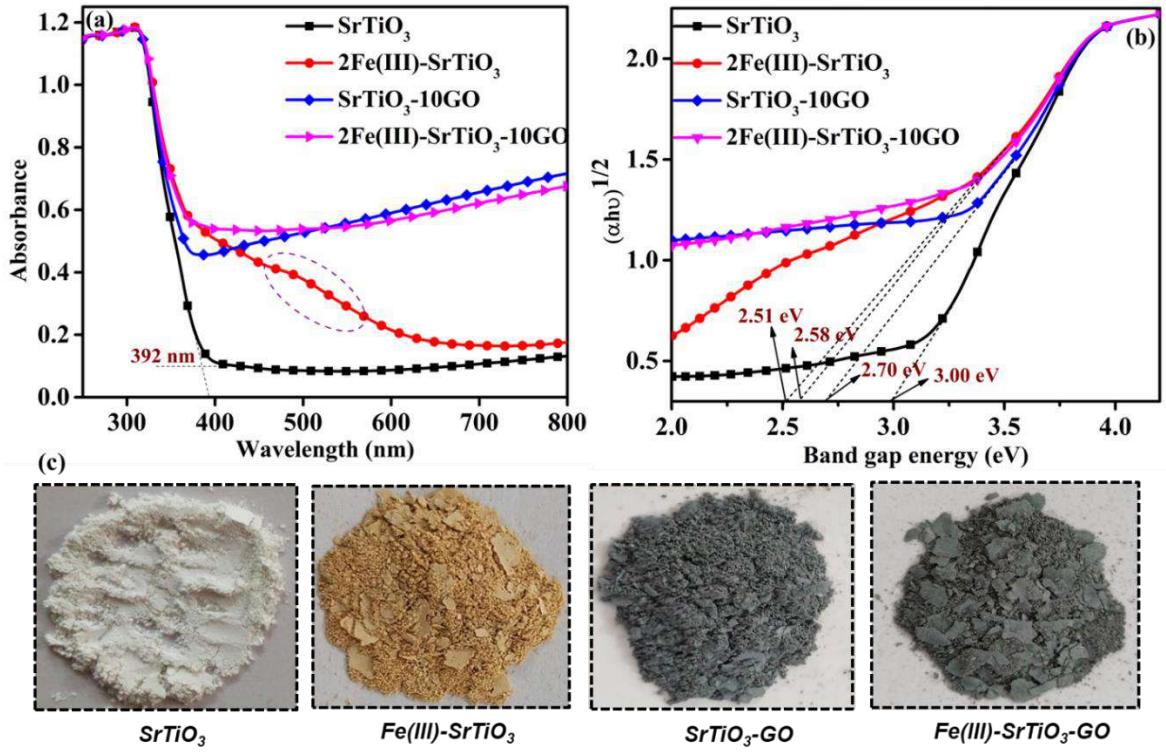

Fig. 4.8: (a) UV-Vis diffuse reflectance spectra and the corresponding (b) Tauc plots of pristine $SrTiO_3$, binary 2Fe(III)-$SrTiO_3$, $SrTiO_3$-10GO, and ternary 2Fe(III)-$SrTiO_3$-10GO samples.

As depicted in (**Fig. 4.8(b))**, in comparison to the larger band gap energies of bare $SrTiO_3$ (3.00 eV), $SrTiO_3$-10GO (2.70 eV), and 2Fe(III)-$SrTiO_3$ (2.58 eV), the ternary photocatalyst 2Fe(III)-$SrTiO_3$-10GO had the smallest optical bandgap energy (2.51eV), indicating that the energy demand for exciting the electrons from the VB to the CB is significantly lowest in the trio 2Fe(III)-$SrTiO_3$-GO nanocomposite. These findings suggest that combining $SrTiO_3$, simultaneously with both Fe and GO played a vital role in reducing the band gap, and successfully induced and broadened the visible light response range of parent $SrTiO_3$ towards longer wavelengths. Thus, the newly designed Fe(III)-$SrTiO_3$-GO composite with the strongest visible-light harvesting capacity is expected to reap abundant photons, which could generate more charge carriers, subsequently boosting its photocatalytic efficiency.

Photoluminescence measurement

The efficient segregation of photoinduced electrons and holes is considered as a prominent factor for an ideal photocatalyst. In this regard, the PL emission spectra was studied for the investigation of the migration, separation, and rejoining extent of e^--h^+ pairs. Lower PL intensity usually indicates improved separation and transfer of the photo-produced carriers which enhances the photocatalytic ability. **Fig. 4.9(a)** illustrates the PL emission spectra of the samples measured at (λex = 335 nm). The PL spectrum of pristine $SrTiO_3$ NCs has been observed to emit both in the UV and visible regions. At 380 nm [Near band gap emission (NBE)], a strong UV emission peak appears, which could be caused by recombination of free excitons and corresponds to the typical band edge emission of $SrTiO_3$ perovskite. Other weaker blue and green emission bands [Defect-related deep level emission (DLE)], observed at 469 and 536 nm attributes to several intrinsic structural defects such as OH-defects, oxygen vacancies (V_O), surface states, and recombination of self-trapped excitons (STE) formed between the CB and VB of $SrTiO_3$ [49–52]. However, M. L. Crespillo et al., study reveals that both blue and green emissions may be associated with STE center transitions from unbound (blue) to bound (green) excited states [53]. Moreover, all the curves display similar emission peaks positioned around 380, 469, and 536 nm with the intensity of the PL spectrum decreasing in the order of 2Fe(III)-$SrTiO_3$-10GO > 2Fe(III)-$SrTiO_3$ > $SrTiO_3$-10GO > $SrTiO_3$. Among all, $SrTiO_3$ exhibits the most intense PL signal, indicating high extent of reconciliation and a low proficiency of charges partition. However, the peaks intensities decreased markedly, after being modified with Fe(III) species as well as GO, suggesting that the carrier lifetime is longer in the composites. Reduced fluorescence signals here, reveals

the beneficial roles of these co-catalysts in prohibiting the joining of e^--h^+ pairs. Notably, the intensity of the PL emission was highly quenched in 2Fe(III)-$SrTiO_3$-10GO, implying that the charge reunion process gets further delayed in the ternary composite.

Two major factors can be imputed to the observed quenching effect: (i) the role of impregnated Fe species, in facilitating the adequate e- transference from the $SrTiO_3$ VB to Fe(III) surface and effectively consuming the photoinduced electrons via IFCT and multielectron reduction reactions, ultimately suppressing the reunion of e^--h^+ pairs [54]. (ii) as a carbonaceous material, GO possesses excellent electronic conductivity and a high storage capacity, which accelerates the transportation of photoexcited carriers from the CB of $SrTiO_3$ to its large surface and then to the active sites, thereby extending charge carrier lifetime and contributing to the superior photocatalytic activity of Fe(III)-$SrTiO_3$-GO. The outcomes of the PL analysis, shows that by fabricating a ternary nanocomposite with strong coordination between the individual components (deposited Fe(III), active $SrTiO_3$ NC's , and GO), it is possible to achieve efficient charge carrier transfer system with a lower recombination rate, which benefits the increased photocatalytic ability.

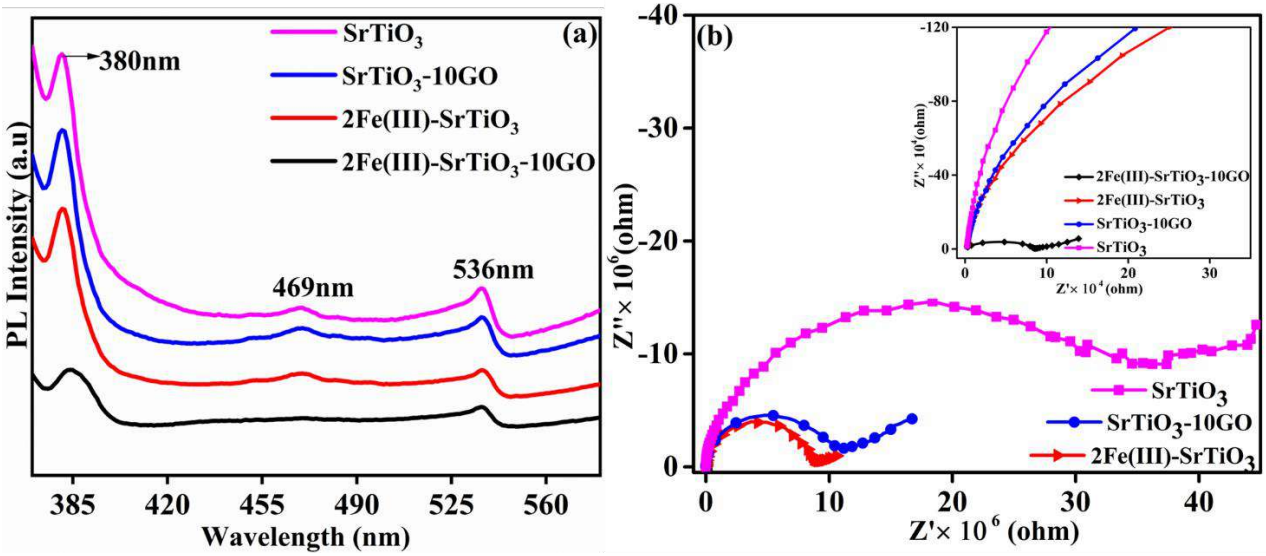

Fig. 4.9: (a) Photoluminescence (PL) spectra and (b) Nyquist impedance plots of as-fabricated samples.

Impedance analysis

Furthermore, the EIS measurements were performed to gain deeper insight into the charge transfer efficiency of the pristine $SrTiO_3$ and its nanocomposites. Generally, a smaller arc radii in the Nyquist plot corresponds to faster interfacial charge transport and ameliorated charge segregation efficiency [55]. The arc radius here, followed the sequence of $SrTiO_3$ > $SrTiO_3$-10GO > 2Fe(III)-$SrTiO_3$ > 2Fe(III)-$SrTiO_3$-10GO. As can be

perceived from (**Fig. 4.9(b))** that there was a decline in the arc radius when co-catalysts Fe and GO were introduced into the $SrTiO_3$ sample, suggesting that the formation of composites could reduce the electron transfer resistance and minimize the rate of e^--h^+ pairs recombination, resulting in a superior interfacial charge carrier transport system. Compared to binary composites, the ternary 2Fe(III)-$SrTiO_3$-10GO composite owned the smallest arc radius, demonstrating that it holds the highest electrical conductivity, more accelerated charge carrier migrations, as well as adequate separation of photoinduced carriers. The obtained EIS results are consistent with the above PL analysis and unambiguously reveal the valuable role of constructing a ternary hybrid (2Fe(III)-$SrTiO_3$-10GO) for promoting the separation of photo-produced charges.

4.4. Photocatalytic activity

4.4.1. Photodegradation reaction

Photocatalytic efficiencies of the as-fabricated Fe(III)-$SrTiO_3$-GO ternary composite were examined by monitoring the photodegradation of NOF, a typical fluroquinolone antibiotic drug, under LED-light illumination. For comparison, the NOF removal over pure $SrTiO_3$, and binary (Fe(III)-$SrTiO_3$, $SrTiO_3$-GO) composites were also investigated. The degradation process was studied by tracking the main absorption peak of NOF at 272 nm over different time spans. Several Fe(III)-$SrTiO_3$ compositions were probed in order to determine the optimal loading of impregnated Fe onto the $SrTiO_3$. Aside from photodegradation, control tests on self-photolysis and dark adsorption were performed.

As presented in **Fig. 4.10(a)**, photolysis (in absence of catalysts) was seen to be ineffective for NOF removal with only a ~7% decrease in absorbance observed after 120 minutes of LED light treatment. The faint degradation capacity of direct photolysis, certifies that NOF is photostable. About 36.1% of NOF molecules were adsorbed when the 2Fe(III)-$SrTiO_3$-10GO and NOF reached the adsorption-desorption balance (40 min) in the dark, while 13.4%, 26.3%, 27.9% 25.8%, and 28.8% of NOF were adsorbed over pristine $SrTiO_3$, [1Fe(III)-$SrTiO_3$, 2Fe(III)-$SrTiO_3$, 3Fe(III)-$SrTiO_3$]; $SrTiO_3$-GO, samples respectively. Clearly, the adsorption capacity of newly designed 2Fe(III)-$SrTiO_3$-10GO was superior to that of all other modified and unmodified samples. This is due to the increased BET surface area with abundant NOF adsorption sites obtained by simultaneously incorporating Fe and GO onto the surface of $SrTiO_3$. Further, to advance the elimination efficacy, the degradation was commenced with the light illumination. Upon exposure to LED light for 120 min, the catalytic performance of synthesized photocatalysts progressed as follows: $SrTiO_3$ (33.6%) < $SrTiO_3$-10GO (68.5%) < 2Fe(III)-$SrTiO_3$ (79.2%) < 2Fe(III)-$SrTiO_3$-10GO (92.3%). The results

show that pristine $SrTiO_3$ can only degrade a limited amount of NOF, owing to its narrow photo-response range, low specific surface area, and ultrafast rejoining of photoinduced e^- and h^+. The deposition of Fe(III) species, is observed to facilitate the performance. Although all of the Fe(III)-$SrTiO_3$ composites had higher photocatalytic activity than the single-component sample. The extent of degradation, however, is strongly dependent on the amount of Fe(III) loaded. With the raise of the Fe(III) content in the composites their removal efficiencies increase gradually and then decline. Among all the iron deposited $SrTiO_3$ composites, the 2Fe(III)-$SrTiO_3$ (with Fe content = 2wt%) exhibited the highest degradation efficiency toward NOF removal. Increasing the amount of Fe(III) further to 3 wt% slightly reduced the NOF removal efficiency. Such a phenomenon can be explained by the following two aspects. When the deposited content of Fe(III) species was lower, photo-generated charge carriers in the 1Fe(III)-$SrTiO_3$ composites could not be effectively partitioned, and would supply insufficient active sites on the surface of $SrTiO_3$, resulting in low photodegradability. While the presence of excessive Fe(III) ions may partially cover the active sites and prevent incident illumination from reaching the catalyst surface, this impeded the photoexcitation of Fe(III) and $SrTiO_3$ in the binary composite, which could act as recombination centers and undermines the charges separation. This eventually reduces the photocatalytic ability. Therefore, the loading of appropriate amount of Fe(III) species is conducive to achieve the optimum synergy effect between Fe(III) and $SrTiO_3$. After further modifying the optimal 2Fe(III)-$SrTiO_3$ composite with graphene oxide, the photocatalytic activity was remarkably improved. Narrower band gap, enhanced light harvesting ability, minimal e^--h^+ pair charge carrier recombination, and stronger adsorption capability all contribute to the 2Fe(III)-SrTiO3-10GO's high photodegradation ability.

Moreover, the photocatalytic degradation kinetics of NOF was quantitatively analyzed by fitting the experimental values to a pseudo-first-order rate equation.

$$\{\ln(C_t/C_0) = -kt\} \quad \textbf{(5)}$$

Here, C_0 and C_t denote the NOF concentration's at (0) and (t) minutes of irradiation, respectively, while k represents the reaction rate constant (min^{-1}). **Fig. 4.10(b)**, depicts the linear relationships between $\ln(C_0/C_t)$ and reaction time using as-synthesized samples. Interestingly, in line with the degradation efficiency, the degradation rate constant (k) of 2Fe(III)-$SrTiO_3$-10GO is the highest (0.019 min^{-1}), which is approximately ~9.5, ~2.1, and 1.58 folds greater than those of the $SrTiO_3$ NCs (0.002 min^{-1}), $SrTiO_3$-10GO (0.009 min^{-1}), and 2Fe(III)-10$SrTiO_3$, (0.012 min^{-1}). As previously discussed, the exceptional photocatalytic ability of the 2Fe(III)-$SrTiO_3$-10GO sample, demonstrated that the synergy of both anchored Fe(III) species and GO is fruitful in magnifying the photocatalytic response of $SrTiO_3$.

Additionally, the temporal variations in the absorption spectrum of NOF over bare $SrTiO_3$ and the ternary 2Fe(III)-$SrTiO_3$-10GO catalysts during the degradation process were monitored and the outcomes are displayed in **Fig.4.10((c)-(d))**. The degradation profiles clearly show that with an increase in the irradiation period, during the degradation course, the intensity of the maximum absorption peak of NOF ($\lambda_{max=}$ 272nm) is noticed to gradually diminished by both the catalysts. 2Fe(III)-$SrTiO_3$-10GO, however, accomplished a quite larger reduction after 120 min of LED irradiation. The flattening of the NOF spectral profile emphasizes the commendable degradation efficiency of 2Fe(III)-$SrTiO_3$-10GO in contrast with the unmodified $SrTiO_3$ sample.

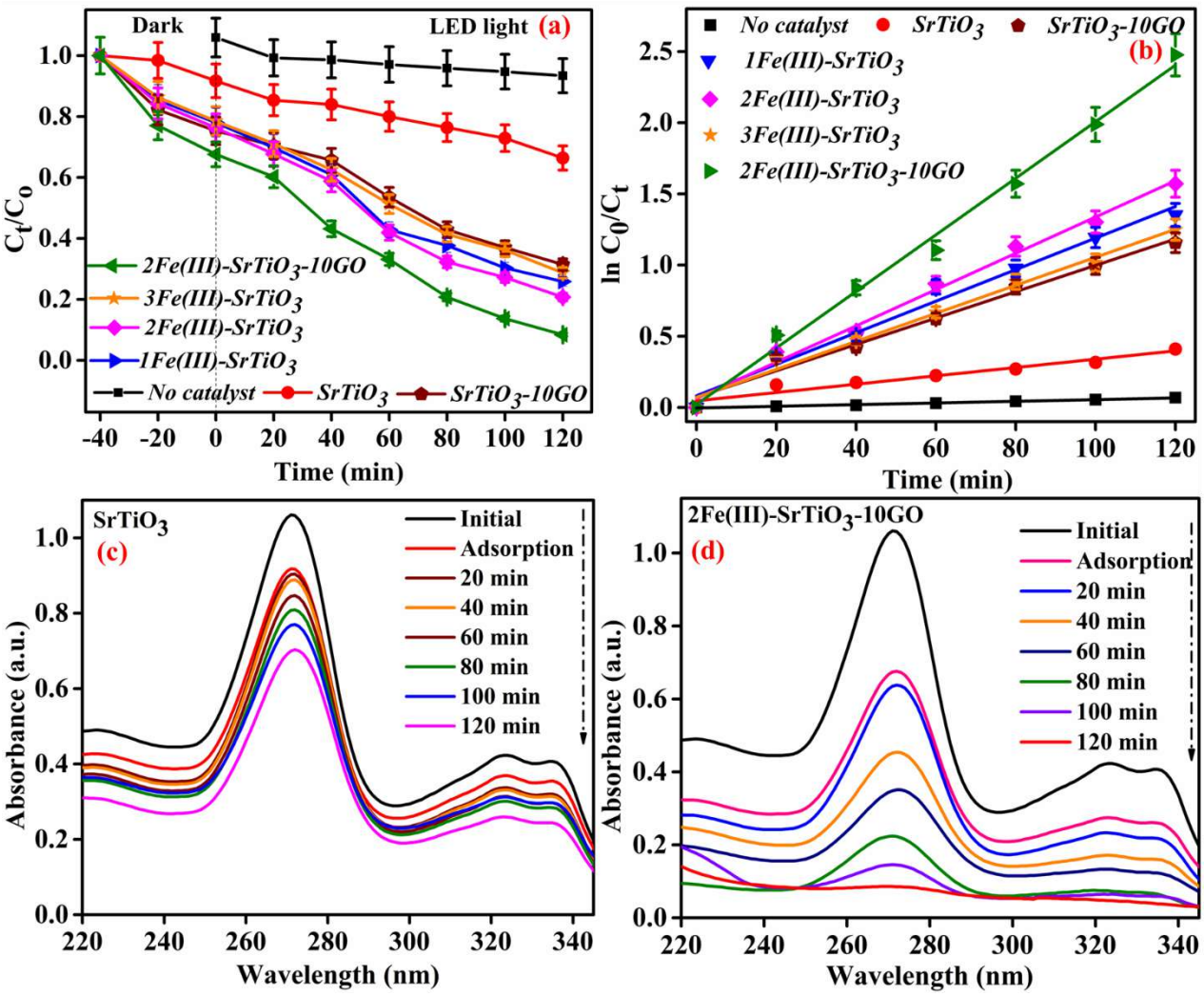

Fig. 4.10: (a) Time course-kinetic plots and (b) corresponding variations in apparent reaction rate constants (k) values obtained for the degradation of NOF antibioitc in the presence of different photocatalysts (c) Time-dependent UV-vis spectral absorption changes of NOF solution over pristine $SrTiO_3$ and (d) 2Fe(III)-$SrTiO_3$-10GO ternary nanocomposite under 120 min LED light illumination.

Fig.4.11(a-b) displays the complete kinetic analysis data of different photocatalysts with histograms for NOF removal.

The marked augmentation in degradation efficiency of the ternary hybrid over pristine $SrTiO_3$ and other binary catalysts can be associated with these advantages:

(i)Well developed ternary structure with three types of intimate contacts developed simultaneously in the Fe(III)-$SrTiO_3$-GO hybrid, i.e. between $SrTiO_3$ and anchored Fe(III) ions, between Fe(III) and incorporated GO sheets, and between $SrTiO_3$ NC's and GO sheets. All jointly contributes to the extraordinary photocatalytic behavior by providing multi-channel electron transport routes. This expertly suppresses the rejoining extent of e^--h^+ pairs in $SrTiO_3$ thereby prolonging their life-time and thus increasing their participation in the photo degradation process.

(ii) Enlargement in the specific surface area with simultaneous deposition of Fe(III) ions and GO sheets on $SrTiO_3$ nanocube's aids in the provision of more active adsorption sites suitable for adsorption of the pollutant molecules which ultimately facilitates the quicker degradation.

(iii) Increment in visible light absorption extent with considerable red shift in absorption edges achieved through the IFCT process of Fe(III) ions as well as the role of GO as a sensitizer.

(iv) Advancement in the transfer and separation ability of the photoinduced charge carriers owing to the superb electrical conductivity and mobility of GO.

(v) The direct transfer of electrons from $SrTiO_3$ VB to the Fe(III) surface by the IFCT mechanism increases the availability of holes in $SrTiO_3$ VB, resulting in the efficient production of active hydroxyl radicals with high oxidizing power, which promotes the degradation process.

Besides, we compared the photocatalytic performance of the as-synthesized 2Fe(III)-$SrTiO_3$-10GO nanocomposite towards the degradation of NOF removal to that of some other previously reported photocatalysts **(Table-4.2).**

Remarkably, the photocatalytic activity of 2Fe(III)-$SrTiO_3$-10GO outperforms that of the other photocatalytic materials addressed earlier, strongly recommending that this newly designed ternary hybrid holds enormous potential as an efficient nanomaterial for application in field of wastewater treatment.

Table-4.2: Comparison of performance of 2Fe(III)-$SrTiO_3$-10GO with other promising photocatalysts for NOF degradation .

S.No	Photocatalyst	Initial NOF concentration (ppm)	Light Intensity	Degradation efficiency time (min)	References
1.	2BVP/GQDs/PCN	20	300W Xenon lamp (420 nm cut-off filter) [Visible light]	86.3% in 120 min	[56]
2.	TiO_2/Bi_2WO_6/rGO (TBR-0.75%)	20	500W Xenon lamp (400 nm cut-off filter) [Visible light]	87.79% in 60 min	[57]
3.	rGO/Bi_2WO_6	10	300W Xenon lamp [Visible light]	87.49% in 180 min	[58]
4.	$CsPbBr_3$-rGO/Bi_2WO_6	10	300W Xenon lamp (420 nm cut-off filter) [Visible light]	69.79% in 120 min	[59]
5.	3:1BiOBr/β-Bi_2O_3	20	500W Xenon lamp [Simulated Sunlight]	71% in 60 min	[60]
6.	Ag_3PO_4/GO (AG-2)	15	250W Xenon lamp (100 mW cm^{-2}) [Visible-LED light]	83.68% in 100 min	[6]
7.	2Fe(III)-$SrTiO_3$-10GO	20	50 W LED lamp (~100W/m^2) [Visible-LED light]	92.3% in 120 min	**This work**

4.4.1. Pollutant mineralization

One of the primary goals of photocatalytic processes is to mineralize the target organic pollutant. Following that, TOC analysis was employed to determine the extent of mineralization. The amount of organic carbon dissolved in the aqueous solution is generally represented by the TOC value. And the reduction in the TOC concentration reflects the extent of mineralization of the organic content at the end of the reaction [56]. So, to assess the extent of mineralization of NOF antibiotic over the as-prepared trio, (2Fe(III)-$SrTiO_3$-GO) photocatalyst, the TOC was measured both before and after the photodegradation process **(Fig. 4.11(c))**. The obtained results reveal that after 120 minutes of LED light exposure, the removal ability reached 60.0%, indicating that 2Fe(III)-$SrTiO_3$-GO, can mineralize more than half of the NOF molecules which is also adequate to remove the antimicrobial properties of antibiotics and their harmful impacts on the environment and human health. And the low percentage of TOC removal in comparison to degradation efficiency, could be associated with the higher stability of the NOF molecule with its large aromatic ring structure as well as the generation of immense number of intermediate products that could accompany the degradation process and still contribute to the TOC of the solution. As a result, total antibiotic mineralization is difficult to achieve. However, prolonged treatment is expected to provide complete mineralization of NOF from aqueous solutions.

4.4.2. Active species detection

To identify the dynamic agents involved in the photocatalytic removal of NOF over optimal 2Fe(III)-$SrTiO_3$-10GO composite, the radical scavenging experiments were carried out **Fig. 4.11(d))**. The analysis was done by employing 10^{-3}M solutions of AA, IPA and EDTA for trapping ($O_2^{\bullet-}$), (.OH), and (h^+), species respectively. This active species detection test was conducted under similar conditions as the degradation experiments. When compared to the scavenger-free photocatalytic system, the decrease in photocatalytic activity with the addition of scavengers suggests that the photocatalysis of NOF over 2Fe(III)-$SrTiO_3$-10GO is influenced by holes, super oxides, and hydroxyl radicals. However, the addition of EDTA and IPA has an acute suppressing effect on NOF removal, indicating that both h^+ and. OH are the primary active species that were produced and responsible for the degradation, whereas (AA) only marginally affects the photocatalytic rate, implying that $O_2^{\bullet-}$ plays a limited or subordinate role. The contribution of each reactive species to NOF removal was in the following order: $h^+ >$. OH > $O_2^{\bullet-}$. The same phenomenon was observed in the $NiWO_4$@g-

C_3N_4 [57], $Ag/FeTiO_3/Ag/BiFeO_3$ [58], photocatalytic reaction systems. Thus, it can be deduced that, the degradation of NOF is chiefly accomplished by h^+ and. OH active species.

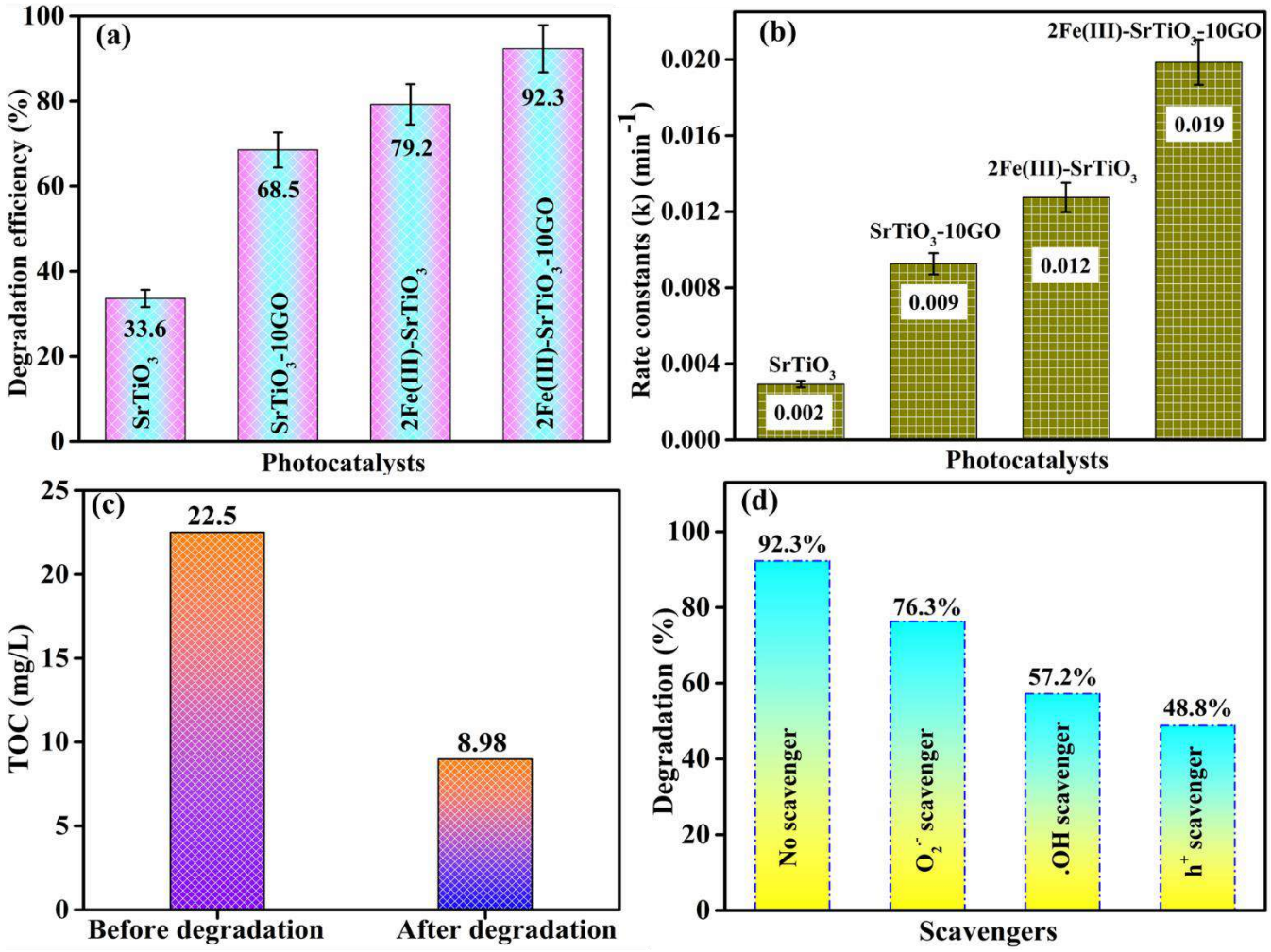

Fig. 4.11: (a) Photodegradation efficiencies (b) reaction rate constants (k) (min^{-1}) values exhibited by different photocatalysts for NOF degradation. (c) TOC removal of NOF using 2Fe(III)-$SrTiO_3$-10GO (d) Influence of various scavengers on the removal effect of NOF in the presence of 2Fe(III)-$SrTiO_3$-10GO photocatalyst.

4.2.3. Probable degradation mechanism

For grasping the photocatalytic mechanism, the transport pathways for photoinduced charge carriers needs to be speculated, by combining the experimental results with the band-edge potential levels of the concerned semiconductor. In this regard, the CB and VB positions of $SrTiO_3$ were formulated by the following formulas:

$E_{CB} = \chi - E_e - 1/2E_g$ **(6)**

$E_{VB} = \chi - E_e + 1/2E_g$ **(7)**

Here, χ denotes the absolute electro-negativity of $SrTiO_3$ (5.34 eV), E_{CB} and E_{VB} are its conduction band and valence band positions, E_e is the energy of free-electrons on the H_2 scale (4.50 eV vs NHE) [59]and E_g refers to observed band gap energy of $SrTiO_3$ (3 eV). Thus, the E_{CB} and E_{VB} values for $SrTiO_3$ were found as -0.66 eV and +2.34 eV, respectively. Based on the information, a conceivable mechanism for the photodegradation of norfloxacin over the ternary Fe(III)-$SrTiO_3$-GO hybrid is presented and elaborated in **Scheme-4.2.**

Previous studies have shown that $SrTiO_3$, with a wide band gap of ≥ 3 eV, is difficult to excite with visible light ($\lambda > 400$ nm). However, under the exposure of LED light irradiation (with $\lambda > 360$ nm), the as-synthesized $SrTiO_3$ with nanocubes like morphology and an absorption onset around 392 nm become partially excited. As a result, when the LED light strikes the surface of Fe(III)-$SrTiO_3$-GO, the $SrTiO_3$ phase elevates, producing e^--h^+ pairs.

Further, when both Fe species and GO, sheet are simultaneously adhered to the $SrTiO_3$ surface and a close interfacial contact is developed between all the three components, the photo-excited electrons are then expected to travel a variety of paths. Some of these electrons would quickly shoot towards the CB of $SrTiO_3$ and undergo reduction reactions. Also, a small fraction of these CB electrons may shift to the deposited Fe(III) cocatalyst due to the higher positive potential of Fe^{3+}/Fe^{2+} (+0.77 eV vs. NHE) in comparison with the CB of $SrTiO_3$ (-0.53 eV vs. NHE). This can upgrade the separation extent of photoinduced e^--h^+ pairs in bulk $SrTiO_3$. Meanwhile, a direct IFCT process from the $SrTiO_3$ VB to the anchored Fe(III) species would also occur due to the strong contact formed between the Fe(III) and $SrTiO_3$ NCs. These transferred electrons would reduce Fe(III) to Fe(II), (Fe(III) + e^- = Fe(II)), and because of the instability, the formed Fe(II) may easily convert back to the original state of Fe(III) via multi-electron oxygen-reduction reactions of Fe(II), [Fe(II) + O_2 + $H_2O \rightarrow$Fe(III) + $\cdot OH$] [45,47]. The Fe(III) species here, serves as an oxygen-reduction site, limiting the reintegration of photoinduced electrons and holes even further [60]. Moreover, the coupled GO sheets, with a Fermi level value (-0.08 eV vs. NHE) lower than the $SrTiO_3$ (-0.66 eV) CB, function as excellent e^- sinks and transporter units by readily capturing the photoinduced electrons from the $SrTiO_3$ surface and then shuttling them to reaction sites [34,61]. This additionally inhibits charge carrier reunion and increases the availability of energetic electrons, potentially upgrading the degradation ability of Fe(III)-$SrTiO_3$-GO[59]. Finally, all the excessive electrons accumulated on the surfaces of *$SrTiO_3$*, *GO sheets*, and *Fe(III) species* may combine with the dissolved O_2 molecules to form a reactive ($\bullet O_2^-$) radical anion, due to their higher negative CB edge potential (−0.66 eV vs. NHE) in comparison with the E^0 ($\bullet O_2^-/O_2$) (-0.046 eV

vs. NHE). The generated $\bullet O_2^-$ is then protonated to produce firs the hydro-peroxyl radical (HOO·), and then H_2O_2, which further dissociates into a highly active (.OH) species. Simultaneously, due to the $SrTiO_3$'s larger positive VB potential value (E_{VB}) than the E^0(OH-/•OH) (+1.99 eV vs. NHE)[62,63], photoinduced holes left on the VB of $SrTiO_3$ can react with surface OH^- ions to generate another powerful oxidant, the OH• radical. Ultimately, the production of numerous reactive species (h^+, OH•, and $\bullet O_2$-) works together in mineralizing the toxic NOF molecules into less harmful intermediates and, eventually, eco-friendly products such as H_2O and CO_2.

The possible reaction steps engaged in the photocatalytic NOF degradation mechanism with Fe(III)-$SrTiO_3$-GO are summarized in equations below **(8-20):**

$$SrTiO_3 + hv \rightarrow SrTiO_3\ (h^+ + e^-) \quad (8)$$

$$SrTiO_3\ (e\text{-}) + O_2 \rightarrow SrTiO_3 + \bullet O_2^- \quad (9)$$

$$SrTiO_3\ (e^-) + Fe\ (III) \rightarrow SrTiO_3 + Fe\ (III)\ (e^-) \quad (10)$$

$$Fe(III) + e^- \Leftrightarrow Fe(II) \quad (11)$$

$$Fe(II) + O_2 + H_2O \rightarrow Fe(III) + \cdot OH \quad (12)$$

$$Fe\ (III)\ (e^-) + O_2 \rightarrow Fe(III) + \bullet O_2^- \quad (13)$$

$$SrTiO_3\ (e^-) + GO \rightarrow SrTiO_3 + GO\ (e^-) \quad (14)$$

$$GO\ (e\text{-}) + O_2 \rightarrow GO + \bullet O_2^- \quad (15)$$

$$\bullet O^{2-} + H^+ \rightarrow .OOH \quad (16)$$

$$2.OOH \rightarrow O_2 + H_2O_2 \quad (17)$$

$$H_2O_2 + (e\text{-}) \rightarrow .OH + OH^- \quad (18)$$

$$SrTiO_3\ (h^+) + OH^- \rightarrow \bullet OH \quad (19)$$

$$\bullet O^{2-} / \bullet OH / h^+ + NOF \rightarrow CO_2 + H_2O + \text{smaller molecules (degradation products)} \quad (20)$$

Overall, the excellent synergetic effect between the dual cocatalysts, Fe (III) and GO, greatly facilitates the separation of photogenerated charges, and offers a convenient electron transport pathway as well as numerous reactive sites for carrying out the oxygen-reduction reactions. Consequently, the photocatalytic performance of the prepared ternary Fe(III)-$SrTiO_3$-GO nanocomposite gets greatly improved.

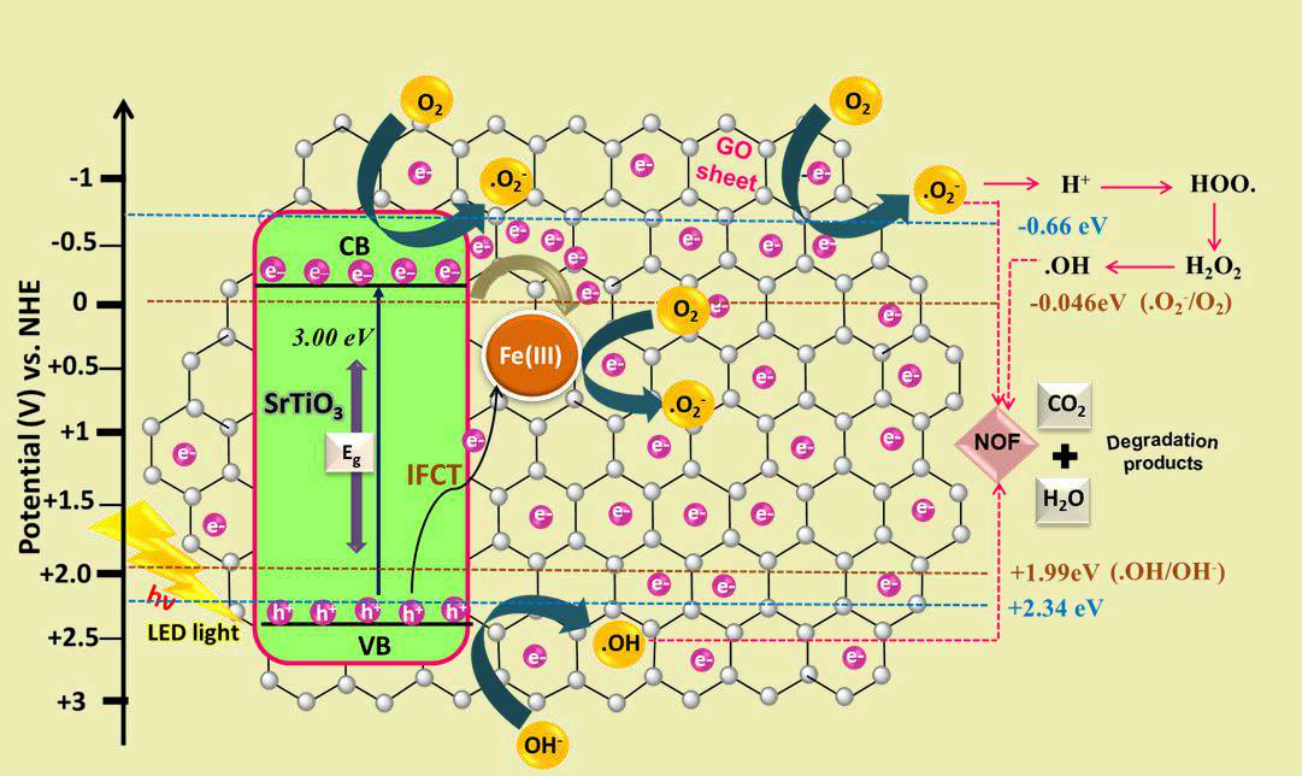

Scheme-4.2: A plausible mechanism for the photocatalytic degradation of Norfloxacin over 2Fe(III)-$SrTiO_3$-10GO nanocomposite under LED light irradiation.

4.2.4. Photo-degradation pathway

To gain a better understanding of the photocatalytic removal of NOF antibiotic, the intermediate products formed in the degradation process by the 2Fe(III)-$SrTiO_3$-10GO catalyst were identified using the LC-MS method, and their chemical structures were suggested based on the description of their m/z value. ((m) represents product's molecular mass and (z) its charge number). The mass spectrum of the possible NOF intermediates is shown in **Fig. 4.12 (a)**. It can be observed that after 120 minutes of photodegradation, the characteristic mass spectrum peak of parent molecule NOF at m/z 320 no longer exists, indicating that NOF molecules were successfully degraded. During the degradation, primarily products (P) with m/z values of 336, 310, 296, 262, 246, and 90 were detected. Based on the results of LC-MS analysis, scavenging experiments, and prior literature reports, the probable degradation pathway of NOF is presented in **Fig. 4.12 (b)**. The pathway is supposed to undergo degradation routes mainly involving piperazinyl ring cleavage, defluorination, decarboxylation, and opening of quinolone and benzene moieties. Owing to the higher e-density, the benzene ring of piperazine in NOR gets easily attacked by free radicals. Therefore, NOF degradation began with the cleavage of the piperazinyl ring reaction via sequential attack of. OH, which

leads to product P1 (m/z: 336). The second pathway involves the opening of quinolone ring to generate product P2 (m/z 310)[64,65]. NOF was then converted to P3 (m/z: 334) by carboxylation of the piperazine ring. Further, defluorination occurs through the attack of .OH radicals on the benzene ring's C-F bond, resulting in the formation of P4 (m/z: 332) and the release of F^- ion from degradation of NOR. P4 gives rise to P5 (m/z: 291) via the piperazine ring opening. Subsequently, after decarboxylation (-COOH), this P5 transformed into product P6 (m/z: 247) [66]. P6 (m/z: 352) can also be formed by the attack of .OH on the C=C in the quinolone moiety, which then resulted in P7 (m/z: 324) and P8 (m/z: 296) via step-by-step decarboxylation pathway[67]. P12 (m/z: 318) can be generated by replacing the (F) atom on the benzene ring with a. OH radical. The piperazine ring is then opened, forming P13 (m/z: 334), which further underwent dihydroxylation reaction to yield P14 with m/z 261) [68,69]. Besides, the quinolone moiety in product P6 (m/z: 352) could be attacked by. OH radical on the C=C bond next to the COOH group, to form P10 (m/z: 280). The ring opening would lead to formation of aliphatic substance, P11(oxalic acid), with the lowest molecular mass (m/z: 90) [68,70]. Finally, by prolonging the reaction time, all these intermediate products (P6, P2, P9, P11 and P14) are expected to be successfully oxidized by the essentially generated reactive species, to form smaller fragments such as molecular acids, which can then mineralize to inorganic compounds such as CO_2, H_2O, NO_3^- , and F^- ions

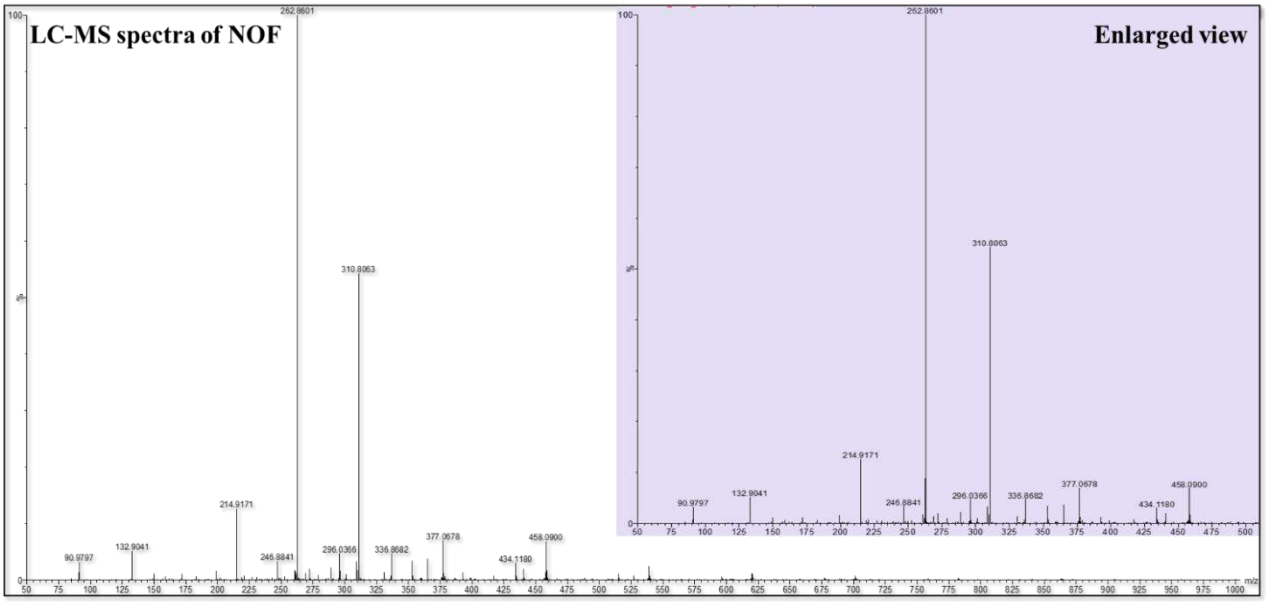

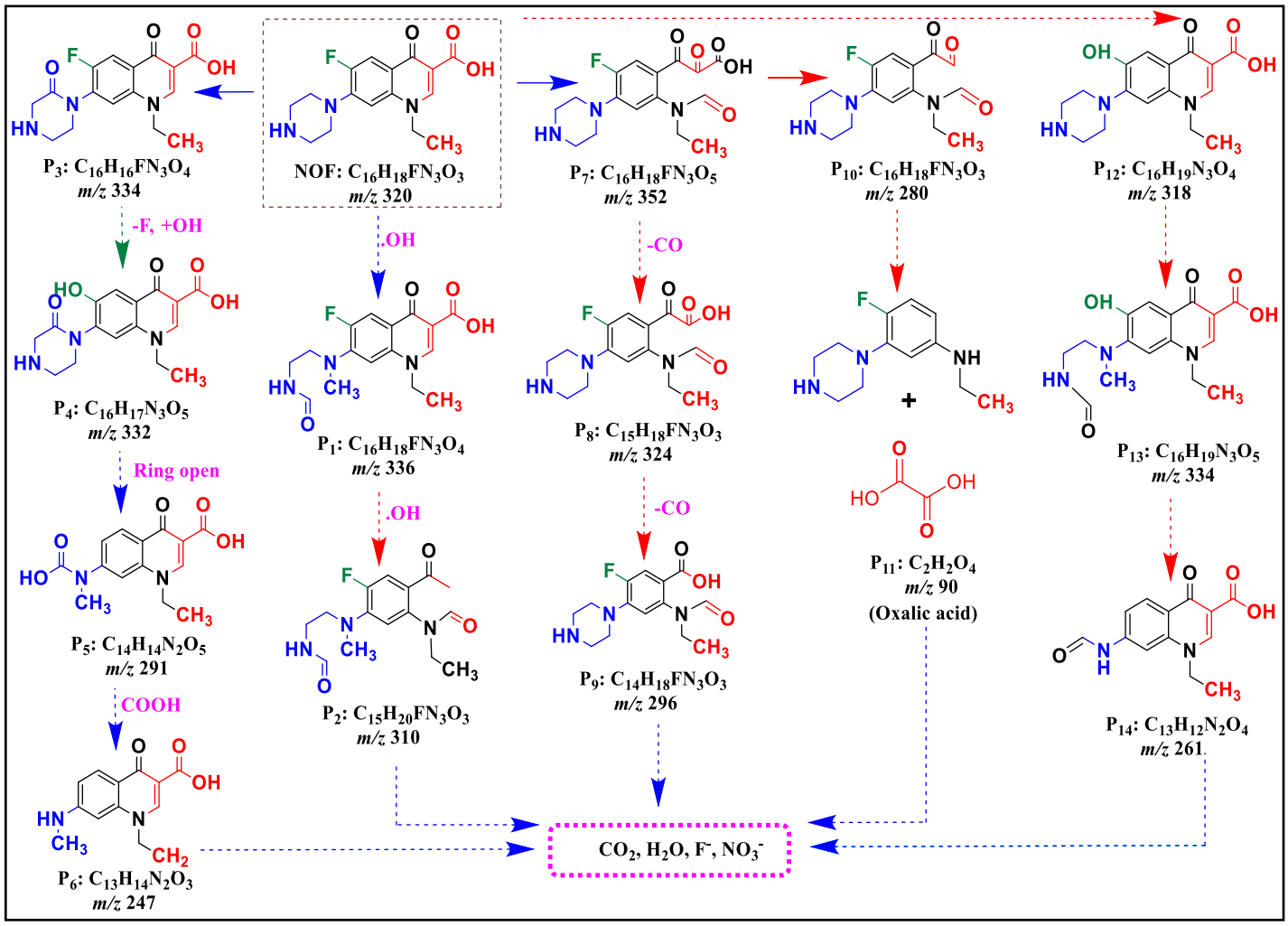

Fig. 4.12 (a): LC-MS chromatogram of the NOF intermediates (b) Proposed photocatalytic degradation pathways generated from NOF degradation using 2Fe(III)-$SrTiO_3$-10GO nanocomposite after 120 min of LED-light illumination.

4.2.5. Recyclability studies

Aside from its catalytic activity, it is critical to assess the service life of a photocatalyst for real-time applications. The, reproducibility and photostability of the as-prepared ternary 2Fe(III)-$SrTiO_3$-10GO photocatalyst were evaluated by performing the successive recycling experiments for the photodegradation of NOF under similar experimental conditions (as described in sec 4.2.8), where the catalyst was subjected to repeated photochemical reactions. After every run, the catalyst was centrifuged, and subjected to washing and drying process before being used in the next cycle. As shown in **Fig. 4.13(a)**, after four consecutive reaction cycles, the degradation rate of NOF is still at about 82.7%, which is down by 9.6% from the first use, implying that the 2Fe(III)-$SrTiO_3$-10GO hybrid is a reusable catalyst. The reduction in the removal

efficiency (92.3% to 82.7%) could be attributed to the catalyst's ineluctable loss during the retrieval process. In addition, during the cycles, a few untreated intermediates may have attached to the catalyst's surface clogging some active sites and pores, and resulting in the reduction in its performance.

Furthermore, after the four cycles, the sample (2Fe(III)-$SrTiO_3$-10GO) was subjected to XRD, **(Fig. 4.13(b))**, to investigate its structural stability. The XRD pattern of the reused sample showed that the positions and intensities of characteristic diffraction peaks remained consistent, and no new diffraction peaks were observed, thereby indicating that the crystal structure of the photocatalyst remained preserved even after four cycles of use. In general, the results suggest that the, newly designed Fe(III)-$SrTiO_3$-GO possesses outstanding regeneration ability and superb stability, thus can be regarded as a robust photocatalyst with long-term applicability in various photocatalytic reactions.

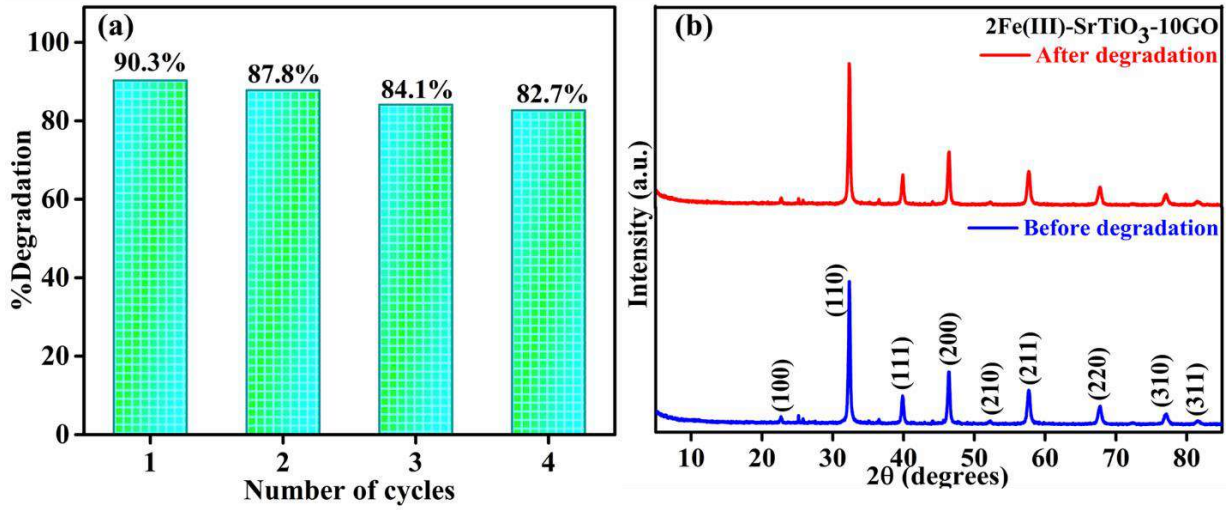

Fig. 4.13: (a) Reusability experiments for the degradation of NOF using 2Fe(III)-$SrTiO_3$-10GO nanocomposite, (b) XRD patterns of 2Fe(III)-$SrTiO_3$-10GO before and after four cyclic runs.

Conclusion

In summary, this work involves the fabrication of a dual cocatalyst modified Fe(III)-$SrTiO_3$-GO ternary photocatalyst by the impregnation and hydrothermal methods. The structural, morphological, chemical composition, optical, and textural properties of the optimal 2Fe(III)-$SrTiO_3$-10GO have been thoroughly studied using a variety of techniques, confirming its successful formation. The characterization results show, that the newly designed trio hybrid with specialized morphology has a relatively larger specific surface area, improved charge separation efficiency, rapid electron transport pathways, a narrower band gap, and a broader photo-absorption range. XPS and HR-TEM analysis revealed the existence of surface deposited iron species

mainly in the form of iron oxide (α-Fe_2O_3), with (Fe) exhibiting a +3-oxidation state. After being exposed to LED light for 120 min, this hybrid (2Fe(III)-$SrTiO_3$-10GO) with nanocube-like $SrTiO_3$, sheet-like GO, and impregnated Fe ions commendably eliminated 92.3% of the toxic norfloxacin antibiotic. Moreover, the degradation efficiency was superior to that of bare $SrTiO_3$ and single-co-catalyst modified composites (such as 2Fe(III)-$SrTiO_3$, $SrTiO_3$-10GO). This tremendous improvement in performance could be credited to the specially-designed ternary system with intimate contact between the constituent components all of which worked synergistically. The anchored Fe (III) species, play a beneficial role in strengthening the light absorption range as well as improving the charge dynamic behavior by e^- capturing through the photoinduced IFCT phenomenon, generating plenty of reactive $OH^{\cdot}$, that are vital for the degradation process. Similarly, the attached GO sheet with strong e^- migration and trapping ability inhibits the e^--h^+ pairs rejoining and provides more surface area with abundant reaction active sites. The 2Fe(III)-$SrTiO_3$-10GO even demonstrated acceptable mineralization ability as well as commendable reusability and stability in 4 successive recycling tests. Furthermore, LC-MS results reveal that the hybrid can decompose the NOF into small molecules with lower toxicity. Finally, based on the outcomes of the LC-MS, band energy analysis and scavenger experiments, the possible photocatalytic mechanism over Fe(III)-$SrTiO_3$-GO was speculated with h^+, **.**OH, playing a paramount role in the degradation process. Therefore, the current study not only validates the potential and practicability of employing low-cost Fe species, and carbonaceous materials like GO to promote $SrTiO_3$ photocatalytic activity, but also proposes a novel strategy for designing efficient visible light active perovskite type ternary hybrids with environmental remediation applications.

References

[1] J. Patel, A.K. Singh, (2020).

[2] and P.P. Pal, S., Z. Ahamed, Separation and Purification Technology 295 (2022) 121249.

[3] M.M. Haque, M. Muneer, Journal of Hazardous Materials 145 (2007) 51–57.

[4] H. Yu, F. Chen, L. Ye, H. Zhou, T. Zhao, Journal of Materials Science 54 (2019) 10191–10203.

[5] W. Liu, T. He, Y. Wang, G. Ning, Z. Xu, X. Chen, X. Hu, Y. Wu, Y. Zhao, Scientific Reports 10 (2020) 1–12.

[6] B. Ji, W. Zhao, J. Duan, L. Fu, L. Ma, Z. Yang, RSC Advances 10 (2020) 4427–4435.

[7] X. Yang, Z. Chen, W. Zhao, C. Liu, X. Qian, M. Zhang, G. Wei, E. Khan, Y. Hau Ng, Y. Sik Ok, Chemical Engineering Journal 405 (2021) 126806.

[8] X. Bai, W. Chen, B. Wang, T. Sun, B. Wu, Y. Wang, International Journal of Molecular Sciences 23 (2022).

[9] R.R. Solís, J. Bedia, J.J. Rodríguez, C. Belver, R.R. Solís, J. Bedia, J.J. Rodríguez, C. Belver, Chemical Engineering Journal (2020) 128110.

[10] S. Patial, V. Hasija, P. Raizada, P. Singh, 8 (2020).

[11] K. Sharifian, V. Mahdikhah, S. Sheibani, Ceramics International 47 (2021) 22741–22752.
[12] U. Alam, S. Kumar, D. Bahnemann, J. Koch, C. Tegenkamp, M. Muneer, Physical Chemistry Chemical Physics 20 (2018) 4538–4545.
[13] S. Li, L. Chen, Z. Liu, M. Zhang, B. Li, C. Lai, Applied Surface Science 566 (2021) 150658.
[14] H. Irie, S. Miura, K. Kamiya, K. Hashimoto, Chemical Physics Letters 457 (2008) 202–205.
[15] H. Yu, H. Irie, Y. Shimodaira, Y. Hosogi, Y. Kuroda, Science And Technology (2010) 1–8.
[16] C. Huang, J. Hu, S. Cong, Z. Zhao, X. Qiu, "Applied Catalysis B, Environmental" 174–175 (2015) 105–112.
[17] W. Sun, H. Zhang, J. Lin, Journal of Physical Chemistry C 118 (2014) 17626–17632.
[18] M. Passi, B. Pal, Powder Technology 388 (2021) 274–304.
[19] M. Al Kausor, D. Chakrabortty, Inorganic Chemistry Communications 129 (2021) 108630.
[20] W. Lin, X. Yu, Y. Zhu, Y. Zhang, Frontiers in Chemistry 6 (2018) 1–13.
[21] P. Gao, J. Liu, D.D. Sun, W. Ng, Journal of Hazardous Materials 250–251 (2013) 412–420.
[22] R.X. Wang, Q. Zhu, W.S. Wang, C.M. Fan, A.W. Xu, New Journal of Chemistry 39 (2015) 4407–4413.
[23] R. He, S. Cao, D. Guo, B. Cheng, S. Wageh, A.A. Al-Ghamdi, J. Yu, Ceramics International 41 (2015) 3511–3517.
[24] H. Bantawal, M. Sethi, U.S. Shenoy, D.K. Bhat, ACS Applied Nano Materials 2 (2019) 6629–6636.
[25] J. Chen, B. Yao, C. Li, G. Shi, Carbon 64 (2013) 225–229.
[26] X. Li, Journal of Chemistry 2018 (2018).
[27] J. Liu, Z. Wei, W. Shangguan, Frontiers in Energy 15 (2021) 700–709.
[28] L. Yin, D. Zhang, J. Wang, J. Huang, X. Kong, J. Fang, F. Zhang, Materials Characterization 127 (2017) 179–184.
[29] L. Gu, H. Wei, Z. Peng, H. Wu, Journal of Materials Research 32 (2017) 748–756.
[30] N. Li, F. Chen, Q. Shen, C. Wang, L. Zhang, Journal of Physics: Conference Series 419 (2013).
[31] M. Iliut, C. Leordean, V. Canpean, C.M. Teodorescu, S. Astilean, Journal of Materials Chemistry C 1 (2013) 4094–4104.
[32] L.C. Sim, K.H. Leong, S. Ibrahim, P. Saravanan, Journal of Materials Chemistry A 2 (2014) 5315–5322.
[33] H. Zhang, X. Wang, N. Li, J. Xia, Q. Meng, J. Ding, J. Lu, RSC Advances 8 (2018) 34241–34251.
[34] G. Venkatesh, S. Vignesh, M. Srinivasan, G. Palanisamy, N. Elavarasan, K. Bhuvaneswari, P. Ramasamy, M. Alam, M. Ubaidullah, M.K. Raza, Colloids and Surfaces A: Physicochemical and Engineering Aspects 629 (2021) 127523.
[35] Z. Wu, Y. Zhang, X. Wang, Z. Zou, New Journal of Chemistry 41 (2017) 5678–5687.
[36] Y. Xia, Z. He, Y. Lu, B. Tang, S. Sun, J. Su, X. Li, RSC Advances 8 (2018) 5441–5450.
[37] Y. Deng, S. Shu, N. Fang, R. Wang, Y. Chu, Z. Liu, W. Cen, Chinese Chemical Letters 34 (2023) 107323.
[38] Y. Yan, H. Tang, F. Wu, R. Wang, M. Pan, Energies 10 (2017).
[39] K. Brezesinski, J. Haetge, J. Wang, S. Mascotto, C. Reitz, A. Rein, S.H. Tolbert, J. Perlich, B. Dunn, T. Brezesinski, Small 7 (2011) 407–414.

[40] B.B. Lv, Z. Liu, H. Tian, Y. Xu, D. Wu, Y. Sun, 201203 (2010) 3987–3996.
[41] S. Kong, Z. An, W. Zhang, Z. An, M. Yuan, D. Chen, Nanomaterials 10 (2020) 1–19.
[42] Y. Li, K. Lv, W. Ho, F. Dong, X. Wu, Y. Xia, Applied Catalysis B: Environmental 202 (2017) 611–619.
[43] S.R. Damkale, S.S. Arbuj, G.G. Umarji, S.B. Rane, B.B. Kale, RSC Advances 11 (2021) 7587–7599.
[44] A.E. Souza, G.T.A. Santos, B.C. Barra, W.D. MacEdo, S.R. Teixeira, C.M. Santos, A.M.O.R. Senos, L. Amaral, E. Longo, Crystal Growth and Design 12 (2012) 5671–5679.
[45] S. Liu, P. Deng, G. Dai, Y. Liang, S. Zhang, Ceramics International 42 (2016) 10094–10098.
[46] Y. Fu, XianzhiZhang, Z.-R. Tang, Y.-J. Xu, ACS Nano 4 (2010) 7303–14.
[47] Q. Liu, Y. Guo, Z. Chen, Z. Zhang, X. Fang, "Applied Catalysis B, Environmental" 183 (2016) 231–241.
[48] Z. Hu, D. Chen, X. Zhan, F. Wang, L. Qin, Y. Huang, Applied Physics A: Materials Science and Processing 123 (2017).
[49] G.L. He, Y.H. Zhong, M.J. Chen, X. Li, Y.P. Fang, Y.H. Xu, Journal of Molecular Catalysis A: Chemical 423 (2016) 70–76.
[50] M. Ganapathy, Y. Hsu, J. Thomas, C.T. Chang, V. Alagan, Journal of Materials Science 56 (2021) 18976–18988.
[51] M.L. Crespillo, J.T. Graham, F. Agulló-López, Y. Zhang, W.J. Weber, Crystals 9 (2019).
[52] S. Dadgostar, J.L. Pura Ruiz, J. Serrano Gutierrez, B. Lepine, P. Schieffer, J. Jimenez, Materials Science and Engineering B: Solid-State Materials for Advanced Technology 283 (2022) 115830.
[53] M.L. Crespillo, J.T. Graham, F. Agulló-López, Y. Zhang, W.J. Weber, Materials Research Letters 7 (2019) 298–303.
[54] G. Ma, Z. Chen, Z. Chen, M. Jin, Q. Meng, M. Yuan, X. Wang, J.M. Liu, G. Zhou, Materials Today Energy 3 (2017) 45–52.
[55] L. Wang, X. Min, X. Sui, J. Chen, Y. Wang, Journal of Colloid and Interface Science 560 (2020) 21–33.
[56] M. Kus, S. Ribbens, V. Meynen, P. Cool, Catalysts 3 (2013) 74–87.
[57] L.P. S., V. Muthuraj, Colloids and Surfaces A: Physicochemical and Engineering Aspects 567 (2019) 43–54.
[58] J. Tang, R. Wang, M. Liu, Z. Zhang, Y. Song, S. Xue, Z. Zhao, D.D. Dionysiou, Chemical Engineering Journal 351 (2018) 1056–1066.
[59] T. Xian, H. Yang, L. Di, J. Ma, H. Zhang, J. Dai, Nanoscale Research Letters 9 (2014) 1–9.
[60] X. Meng, L. Shi, L. Yao, Y. Zhang, L. Cui, Colloids and Surfaces A: Physicochemical and Engineering Aspects 594 (2020) 124658.
[61] S. Ghasemi, S.J. Hashemian, A.A. Alamolhoda, I. Gocheva, S. Rahman Setayesh, Materials Research Bulletin 87 (2017) 40–47.
[62] Z. Yao, X. Liu, H. Sui, H. Sun, Materials Letters 275 (2020) 128007.
[63] Sohrabian,M.,Mahdikhah,V.,Alimohammadi.,Sheibani,S., Applied Surface Science 618 (n.d.) 156682.
[64] Z. Chu, T. Chen, H. Liu, D. Chen, X. Zou, H. Wang, F. Sun, P. Zhai, M. Xia, M. Liu, Chemosphere

282 (2021) 131091.
[65] M. Wang, H. Yu, P. Wang, Z. Chi, Z. Zhang, B. Dong, H. Dong, K. Yu, H. Yu, Separation and Purification Technology 274 (2021) 118692.
[66] M. Xi, K. Cui, M. Cui, Y. Ding, Z. Guo, Y. Chen, C. Li, X. Li, Chemical Engineering Journal 420 (2021) 129902.
[67] C. Bao, J. Zhao, Y. Sun, X. Zhao, X. Zhang, Y. Zhu, X. She, D. Yang, B. Xing, Environmental Science: Nano 8 (2021) 2347–2359.
[68] H. Yu, D. Dou, X. Zhang, L. Zhang, H. Dong, H. Yu, Journal of Cleaner Production 242 (2020) 118548.
[69] Z. Zhu, C. Wang, L. Liang, D. Yu, J. Sun, L. Zhang, S. Zhong, B. Liu, Journal of Nanoscience and Nanotechnology 20 (2019) 2247–2258.
[70] A. Özcan, A. Atılır Özcan, Y. Demirci, Chemical Engineering Journal 304 (2016) 518–526.

CHAPTER-5

Cu decorated $CaTiO_3$-GO hybrid composite for the improved degradation of cefixime and dehydrogenation of alcohol under LED-light

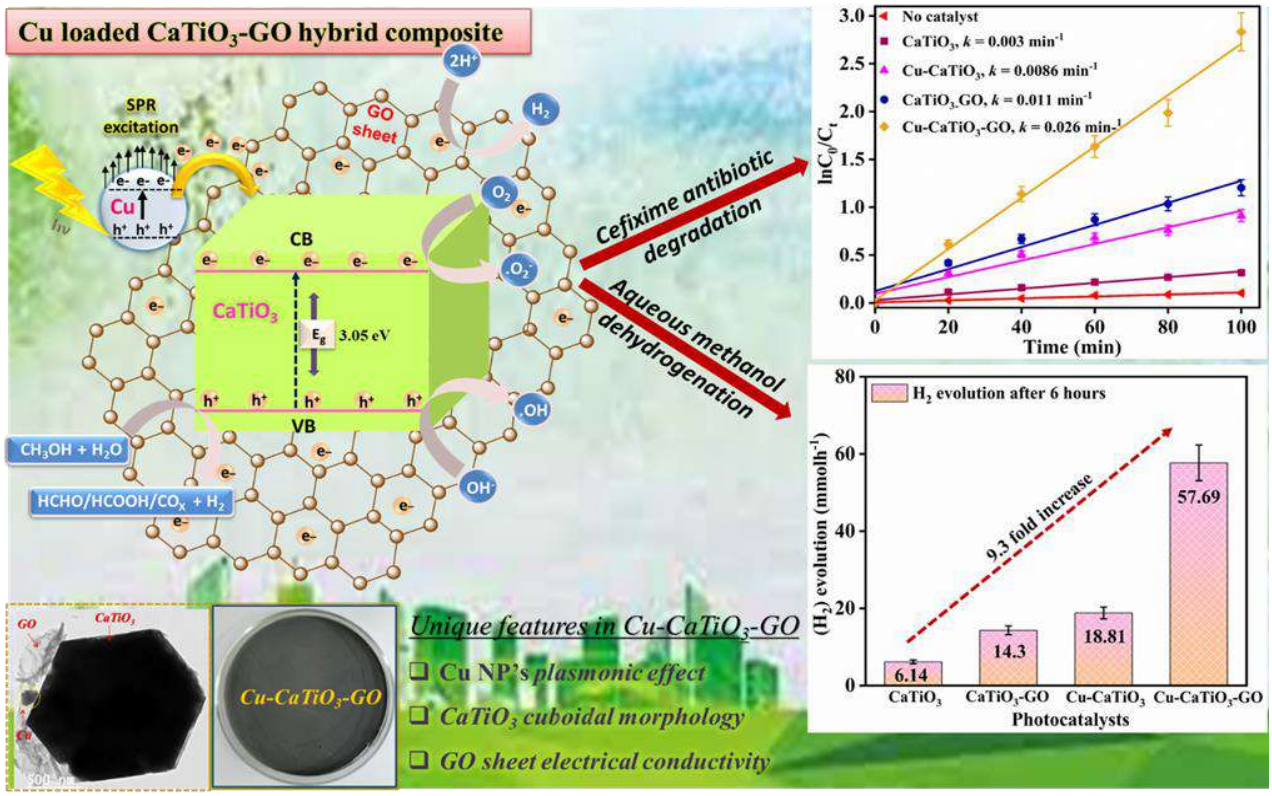

Schematic summary

A multifunctional Cu-$CaTiO_3$-GO tnanocomposite was synthesized, with the dual capability of generating clean energy (H_2) and degrading antibiotic cefixime (CFX) under LED light. The trio hybrid outperformed its counterparts by generating 57.6 $mmolh^{-1}$ H_2 and attaining 94.1% CFX degradation efficiency. The efficient migration and separation of photoinduced charge carriers, the SPR effect of plasmonic Cu NPs, bandgap narrowing, enlarged surface area, favourable cuboidal morphology, and the strong synergy between the three components Cu, $CaTiO_3$, and GO in the developed three-level electron transfer system all contributed to this splendid photocatalytic performance.

5.1. Introduction

Dilemma of sustainable-energy and environmental deterioration have recently emerged as the two major roadblocks to the development of human society. Research priorities are currently cantered on the advancement of new renewable energy and water treatment technology in response to the ongoing depletion of fossil fuels and the rising water pollution problem [1]. H_2 is gaining support as a potential carbon-free renewable clean energy source that can replace fossil fuels owing to its low density, abundant reserves, high calorific value, non-toxicity, easy storage, etc. Among the numerous H_2 production technologies, photocatalytic H_2 generation via water splitting is regarded as a promising method due to the lack of toxic byproducts and environmental friendliness [2,3]. Being an uphill reaction with a high ΔG_0 (+237 kJ/mol) limits water splitting's thermodynamic feasibility. Producing H_2 from a methanol-water mixture, on the other hand, requires less energy (G_0 = +49.51 kJ/mol) than water splitting. In this regard, photocatalytic dehydrogenation of alcohols is being investigated as a high-quantum-yield energy production technique [4].

Similarly, pharmaceutical antibiotics are becoming contaminants because of their indiscriminate usage, continuous input, and persistence in various environments matrices even at lower concentration. Among them, Cefixime (CFX), one of the most active and widely utilized third-generation semisynthetic cephalosporin, from the Beta-lactam family has been extensively produced and applied in agriculture and medicine due to its broad antibacterial spectrum. Ear, throat, lung, and urinary tract infections, as well as gonorrhoea, pneumonia, syphilis, and influenza, are all treatable with CFX antibiotic [5,6]. However, due to insufficient metabolism, most of the CFX is excreted from the living body in its pharmacologically active state via urine and feces and eventually enters the environment (surface and ground-water, drinking water, municipal sewage and soil), posing threat to the human health ecosystem function. Long-term accumulation of CFX residue especially in the water sources may increase bacterial resistance [7]. As a result, it is crucial to employ appropriate treatment technologies to completely remove CFX residues from water bodies [8].

Semiconductor photocatalysis is a potential technology for combating energy scarcity and environmental pollution concerns with the minimum operational cost and time. Thus, efficient SC materials with high efficiency, stability, powerful redox capability, and adequate carrier separation and transmission ability are required. Calcium titanate ($CaTiO_3$), ‘the founding father’ of the perovskite family, is a well-researched SC photocatalysts that excels in a wide range of applications, including artificial photosynthesis, energy storage, water splitting, sensors, wastewater treatment, air adsorbents, the production of H_2 and CO_2 reduction, etc.

As an alkaline earth metal titanate composed of naturally abundant, non-toxic elements, this multifunctional

material possesses incredible characteristics such as perovskite structural stability, multiple crystal phases, superior ferroelectricity, high oxidizing capacity, corrosion resistance, a large number of available alteration sites, compatibility with other materials, compositional flexibility and environmental friendliness. Furthermore, the substantially more negative CB position makes it an appealing candidate for generating H_2 energy [9]. Despite its enormous potential, bottlenecks including lower surface area, quick photo-induced e^--h^+ pair recombination, and limited light harvesting capacity (owing to wide band gap greater than 3 eV), largely hinders its practical applicability scope[10].

To address the aforementioned pitfalls, decorating plasmonic metal NPs (i.e. Au, Ag, Cu, and Pt) over the SC surface is a promising strategy that can drastically upgrade the photo-absorption properties. The improvement is attributed to their unique LSPR effect, which can enlarge the light absorption range to the visible region by efficiently transmitting their plasmonic energy to the $CaTiO_3$ surface, resulting in the generation of abundant charge carriers. Additionally, because of the creation of a Schottky barrier at the M-SC contact, these metal NPs can also behave as e^-trappers, capturing the energetic e^-'s streaming from the $CaTiO_3$ CB. This greatly accelerates the separation of e^--h^+ pairs, contributing to the improvement [11–13]. For instance, Zhen et al. synthesized Ag/α-MoO_3 heterojunctions that accelerated the degradation of thiophene (a refractory S-containing pollutant) by almost 2.5 folds (0.023 min^{-1}) contrast to pure α-MoO_3 (0.009 min^{-1}) [14]. When exposed to UV light, Cu-$SrTiO_3$ photocatalyzed the release of H_2 from a methanol-water solution much better than pure $SrTiO_3$, moreover, the H_2 evolution rate is comparable with Pt- $SrTiO_3$ [15]. Visible light photocatalytic activity with 80.24 μmol$g^{-1}h^{-1}$ CO production and up to 264.5 μmol g^{-1} h^{-1} were obtained with plasmonic Ag-decorated $SrTiO_3$ nanocomposite (ASTO). The extraordinary performance is credited to the enhanced e- extraction and transfer between Ag and STO, and the increased visible light absorption capacity facilitated by the LSPR effect [16]. Likewise, Au/$ZnTiO_3$ [17] nanocomposites exhibit a remarkable increase in H_2 evolution rate (108 μmol h^{-1}) unlike pure $ZnTiO_3$, which exhibits negligible activity in visible light. Due to its affordable cost, natural abundance, high effectiveness, impressive electrical conductivity, and a significant LSPR effect, the non-noble metal Cu has been recognized as an efficient co-catalyst for developing plasmonic photocatalysts [18].

Another approach that has garnered immense attention is the use of graphene oxide (GO), a fantastic member of the carbon family, as a photocatalyst support material for constructing advanced nanocomposites with superb photocatalytic activity. The effectiveness of GO is rooted in its distinctive characteristics, such as its tunable porous structure with (π–π) interactions and abundant reactive oxygen

groups, ultrafast charge carrier mobility, high e^- storage ability, large specific surface area, high mechanical strength, extended absorption, etc. All these fascinating properties offer GO-incorporated composites a plethora of excellent, unprecedented functionalities all in one go. These include (i) enlarging the photo-absorption range and narrowing the band gap; (ii) extending the lifetime of e^--h^+ pairs; (iii) developing a feasible pathway for transporting and separating charge carriers; and (iv) producing an abundance of active sites and offering good absorptivity for target pollutants [9,19,20]. To date, there have been a handful of reports on enhancing the photocatalytic efficiency of SC materials by coupling them with GO. Guo et al. [21] reported a 3-D BiOI-GO composite that exhibited outstanding photodegradation efficiency towards phenol. A porous graphene-$SrTiO_3$ composite was recently used to remove MB dye with great results [22]. Luo et al. [23] used GO as a substrate to support $ZrO(OH)_2$) NPs to remove As(III) and As(V) from the drinking water. Under sunlight exposure, Victoria Blue dye was almost completely degraded (97.95%) in just 90 minutes with V_2O_5 nanorods/GO photocatalyst [24].

Considering the above, the current work used a two-step approach to create a potential Cu-$CaTiO_3$-GO nanocomposite by hydrothermally forming a binary composite of $CaTiO_3$ and GO sheets and then photo-depositing Cu NPs on its surface. Here Cu NPs would boost optical responsiveness, while GO would facilitate the separation and transportation of photoinduced charges, thus enhancing $CaTiO_3$'s photocatalytic behavior. The efficacy of such a ternary hybrid is tested by degrading pharmaceutical pollutant CFX and generating H_2 by dehydrogenating methanol under LED light. The photocatalytic effectiveness of ternary Cu-$CaTiO_3$-GO, binary composites (Cu-$CaTiO_3$ and $CaTiO_3$-GO), and single component $CaTiO_3$ have been compared. The catalyst's reusability is examined in consecutive photocatalytic cycles. The mineralization ability for CFX is also assessed. The role of reactive species has been investigated systematically, and a plausible degradation route for CFX has been suggested. Finally, the mechanism behind this dual-purpose system's increased photocatalytic activity has been addressed. To our knowledge, no research has been proposed for upgrading $CaTiO_3$'s photocatalytic activity by building a trio-hybrid with various charge transfer channels comprising of transition metal (Cu), perovskite ($CaTiO_3$), and carbonaceous material (GO).

5.2. Experimental section

5.2.1. Chemicals and Reagents

Calcium nitrate tetrahydrate ($Ca(NO_3)_24H_2O$, 99%), sodium nitrate ($NaNO_3$, 99%), sodium hydroxide (NaOH, 97%), graphite powder (98%), hydrogen peroxide (H_2O_2, 30%), sulphuric acid (H_2SO_4, 98%), hydrochloric acid (HCl, 35%), ethylenediaminetetraacetic acid (EDTA) ($C_{10}H_{16}N_2O$, 99%), potassium

permanganate ($KMnO_4$, 97%), isopropyl alcohol (IPA) (C_3H_8O, 99.5%), ascorbic acid (AA) ($C_6H_8O_6$, 99%), ethanol (C_2H_5OH), methanol (CH_3OH, 99%), Cupric acetate monohydrate ($Cu(CH_3COO)_2.H_2O$, 99%), were obtained from Loba Chemie (India). Titanium dioxide (P25-TiO_2) was purchased from Degussa Corporation, Germany. These chemicals were all of an analytical grade and were used directly without any pre-treatment. Cefixime ($C_{16}H_{15}N_5O_7S_2$) antibiotic tablet (250 mg) was acquired from the Shine pharmaceutical Ltd. Also, for the entire study, triple deionized water from Organo Biotech Laboratories Pvt. Ltd. was used.

Synthesis

5.2.2. Synthesis of Graphene Oxide (GO)

An improved version of Modified Hummer's method was used to synthesize GO from graphite powder [25].

5.2.3. Synthesis of binary $CaTiO_3$-GO composite

$CaTiO_3$-GO composite was prepared through the hydrothermal route. Briefly, in order to synthesize 5 wt% GO modified $CaTiO_3$, 0.04 g of GO was first ultrasonically dispersed in 80 mL of distilled water for 1 h. Then, while being vigorously stirred, 0.4940 g of $Ca(NO_3)_24H_2O$ was added to it. The resulting suspension was then gradually treated with 19.20 g of NaOH and 0.1190 g of TiO_2 P25. Following 30 minutes of continuous stirring, the mixture was subsequently given a 15-minutes of Ar gas purging. The obtained suspension was then transferred to a 100 mL Teflon-lined autoclave, and hydrothermal treatment was carried out for 12hours at 200˚C. After cooling naturally, the dark gray product ($CaTiO_3$-GO) was acquired, washed multiple times with D.I. water, ethanol, and finally kept for drying in a vacuum oven at 65˚C for 3 h.

5.2.4. Synthesis of $CaTiO_3$ cuboids

A similar procedure was adopted for the synthesis of pristine $CaTiO_3$ as above, but without the inclusion of GO.

5.2.5. Synthesis of Cu deposited $CaTiO_3$-GO composite

To obtain a ternary Cu-$CaTiO_3$-GO composite, plasmonic Cu nanoparticles were deposited onto the $CaTiO_3$-GO composite via the photo-deposition process. In a test tube containing 10 ml of IPA-water (1:1) mixture, 100 mg of as-prepared $CaTiO_3$-GO powder was dispersed, where isopropanol was a hole scavenger. To obtain a Cu loading of 1wt%, the appropriate amount of (0.01M) $Cu(CH_3COO)_2.H_2O$ solution was added dropwise to the above suspension. The test tube was then bubbled with Ar gas for about 15 minutes to make the atmosphere oxygen-free and then sealed with a rubber septum. Further, the prepared suspension was photo-irradiated with a UV lamp (125W Hg arc, 10.4mW/cm^2) for 4 hours while receiving steady magnetic

stirring. Finally, the light gray-colored product (Cu-$CaTiO_3$-GO) was collected by centrifuge, washed a few times with distilled water and ethanol separately, then dried at 50°C for 2 hours in an oven.

The complete fabrication route adopted for ternary Cu-$CaTiO_3$-GO composites is depicted in **Scheme-5.1.**

5.2.6. Synthesis of binary Cu-$CaTiO_3$ composite

For the purpose of comparison, a Cu-deposited $CaTiO_3$ sample was also synthesized with the same protocol and conditions as the ternary composite (**Cu-$CaTiO_3$-GO)** by simply replacing the $CaTiO_3$-GO powder with $CaTiO_3$ in the test tube.

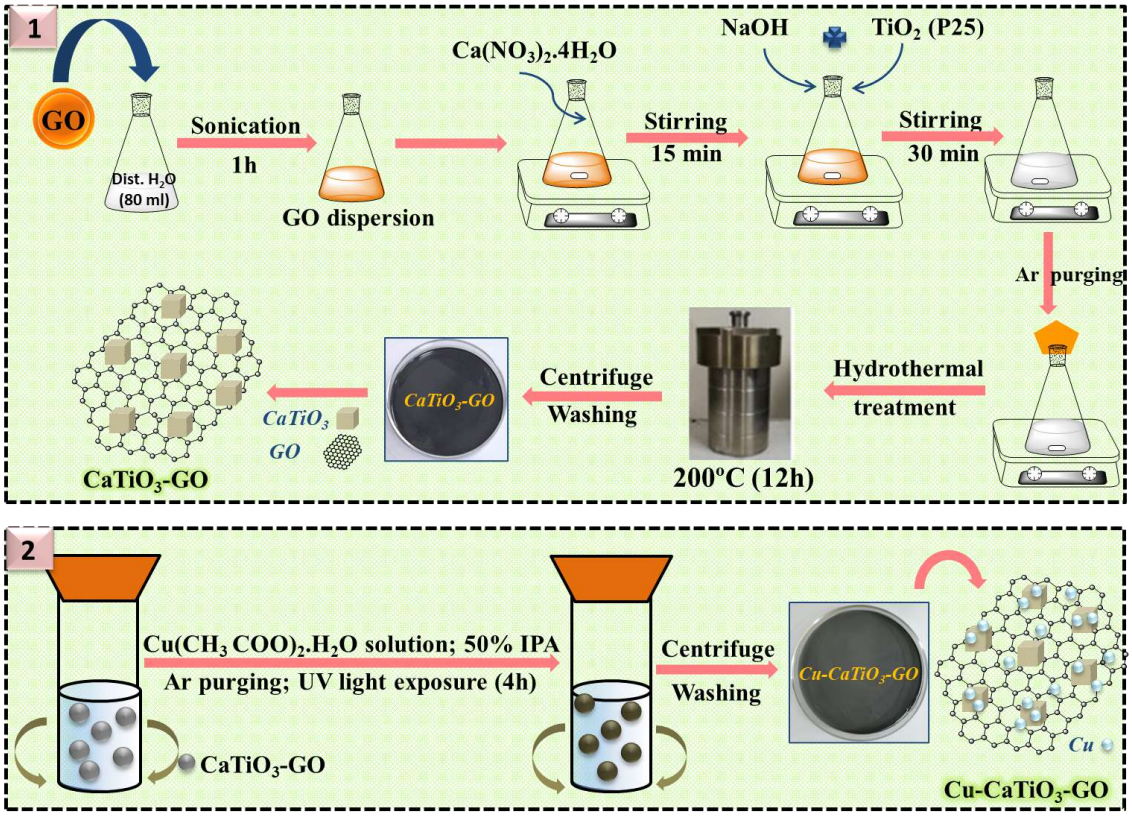

Scheme-5.1. Schematic illustration of the synthesis process of the ternary Cu-$CaTiO_3$-GO composite

5.2.7 Characterization:

The crystal structure of the prepared photocatalysts were investigated through Rigaku, Smart Lab SE Japan X-ray diffractometer) with a monochromatic Cu-Kα radiation source (λ = 1.54056 Å) operated at angle 10° ≤ 2θ ≤ 80°. Surface chemical compositions and oxidation states of constitutional elements were examined by a Thermo Fisher ESCALAB Xi+, X-ray photoelectron spectrometer. Morphology studies were acquired via FESEM (Carl Zeiss SIGMA 500) and HR-TEM (JEOL, JEM 2100 PLUS) electron microscopes.

Elemental composition along with colored mapping images were appraised by collaborating the scanning module of the SEM microscope with an EDX analyzer (Bruker). The SEM microscope scanning module and EDX analyzer (Bruker) were used to evaluate element composition and colored mapping images.

The Quantachrome Nova-1000 analyzer measured surface area and pore structure characteristics using Brunauer-Emmett-Teller (BET) analysis. (Analysis gas: nitrogen, outgas and bath temperature: 180°C and 77.3K respectively, outgas time: 6 h). The diffuse reflectance spectra (DRS) of each sample were monitored using a UV-vis spectrophotometer (JASCO, V-750) 200-800 nm range with a reference standard of $BaSO_4$. A 532 nm laser-excited Labram HR, Horiba micro-Raman spectrometer was used for Raman spectroscopy measurements.The photoluminescence (PL) emission spectra were recorded on a SHIMADZU, RF-6000, spectrofluorimeter with excitation of λ_{max} = 278 nm. An analytical impedance analyzer from Solartron was used to measure electrical conductivities/resistances at room temperature (Model: SI 1260). A UV-vis spectrophotometer (Shimadzu, UV-2600) was employed for observing the photodegradation of the model contaminant.

5.2.8 Photocatalytic activity test

(a) Photodegradation study of the toxic pollutant

The photocatalytic activity of the pristine $CaTiO_3$, and its composites ($CaTiO_3$-GO, Cu-$CaTiO_3$, and Cu-$CaTiO_3$-GO) was assessed by monitoring the degradation of a model pharmaceutical contaminant CFX antibiotic under visible LED light. Typically, about 10 mg of each photocatalyst was dispersed in different test tubes containing 10 ml of aqueous CFX solution (50 ppm). Before photo-irradiation, the suspension was subjected to vigorous magnetic stirring in complete darkness for 40 min to accomplish the equilibrium of adsorption-desorption between the catalyst surface and the CFX molecules. Subsequently, the degradation experiments were performed by illuminating the test tubes with LED light irradiations (a 50-watt LED bulb (Wipro Garnet B22, intensity~100W/m^2) under continuous stirring for different time intervals of 20, 40, 60, 80, and 100 min. After every fixed interval of time, each test tube solution was centrifuged (7000 rpm) to dislodge the catalyst The supernatant was then analyzed by utilizing a UV-visible spectrophotometer. The concentrations of CFX were examined by measuring the absorbance at λ_{max} = 278 nm, respectively. All photocatalytic tests were conducted in triplicates, with averages and error bars presented in graphs (source of error ~7% of data).

The photodegradation efficacy of the catalysts was determined using the equation:

$$\text{Degradation efficiency (\%)} = \frac{C_o - C_t}{C_o} \times 100 \quad (1)$$

where C_0 denotes the initial concentration of "CFX" antibiotic at time '0′ and C_t refers to the concentration of "CFX" at time 't' after photoirradiation.

The CFX degradation intermediates were also detected using LC-MS analysis (Waters Micromass QTOF Micro mass spectrometer) utilizing a mobile phase of acetonitrile, ultrapure water, and 0.2% formic acid.

(b) Photocatalytic H_2 production reaction

The photocatalytic H_2 evolution studies were executed in different test tubes. Typically, 40 mg of each photocatalyst was suspended in a test tube containing 10 mL of aqueous methanol solution (50 vol%). To establish an inert environment inside the medium, Ar gas purging was done for 20 minutes and then sealed with a gas tight rubber septum. The reaction was then initiated by exposing the test tubes containing the reaction mixture to LED light illumination (50W LED lamp of Wipro Garnet B22 with intensity ~100W/m^2, $\lambda > 360$ nm) for 6 hours, with continuous magnetic stirring. After 6 hours, the amount of H_2 evolved from the aqueous solution was identified and quantified periodically by manually injecting 1 mL of the produced H_2 gas into the injector port of a gas chromatography system (GC, Nucon Ltd. India) with a TCD detector, a 5 Å molecular sieve column, and carrier gas (Ar). The oven, injector, and detector temperatures were kept at 40°C, 40°C, and 50°C, respectively. The GC chromatogram was then compared to a reference gas standard, (505 ppm H_2 concentration + 503 ppm CO_2 balanced Argon as acquired from Sigma Gases, India). For comparison, the control and blank (no catalyst) tests were additionally performed under similar experimental conditions.

5.3 Results and discussion

5.3.1. Structural studies

XRD analysis

The phase purity and crystallographic structures of the synthesized samples pure GO, $CaTiO_3$, Cu-$CaTiO_3$, $CaTiO_3$-GO, and Cu-$CaTiO_3$-GO composites, were examined from the XRD patterns, and the results are depicted in **Fig.5.1.** XRD pattern of pure GO shows a prominent peak at $2\theta = 11.6°$, corresponding to the (001) lattice plane [26]. This confirms the oxidation and existence of oxygen-containing functional groups, supporting the notion that pristine graphite is transformed into graphene oxide. The diffraction peaks located at 2θ = 23.3°, 27.4°, 33.1°, 37.2°, 39.0°,40.8°, 47.5°, 53.9°, 59.1, 62.4°, 69.5°, and 79.2° could be perfectly indexed to the respective (1 10), (1 1 1), (121), (102), (031), (220), (202), (311), (123), (231), (242), and (161) planes of the orthorhombic $CaTiO_3$ [27]. The diffraction peaks of the binary samples (Cu-$CaTiO_3$, $CaTiO_3$-GO) and the ternary Cu-$CaTiO_3$-GO sample, were observed to be consistent to those of pristine

$CaTiO_3$. In addition to the $CaTiO_3$, the XRD pattern of Cu-$CaTiO_3$ and Cu-$CaTiO_3$-GO reveals the emergence of one additional low-intensity peak of metallic Cu at 2θ = 74.8°, which can be indexed to the (220) crystal plane (marked with "♣" asterisks)[28]. The absence of any other peaks owing to copper oxides affirms the presence of Cu in metallic form in these composites. Similarly, the lack of variations between the existing peak positions of $CaTiO_3$ and Cu-$CaTiO_3$, suggests that the Cu NPs are well adhered to the surface instead of being embedded into the lattice. Furthermore, no obvious diffraction peak belonging to GO is discerned in the XRD profiles of $CaTiO_3$-GO and Cu-$CaTiO_3$-GO. This might be due to GO's good dispersion and even distribution in the composite or the small content in the sample that cannot be detected using the instrument.

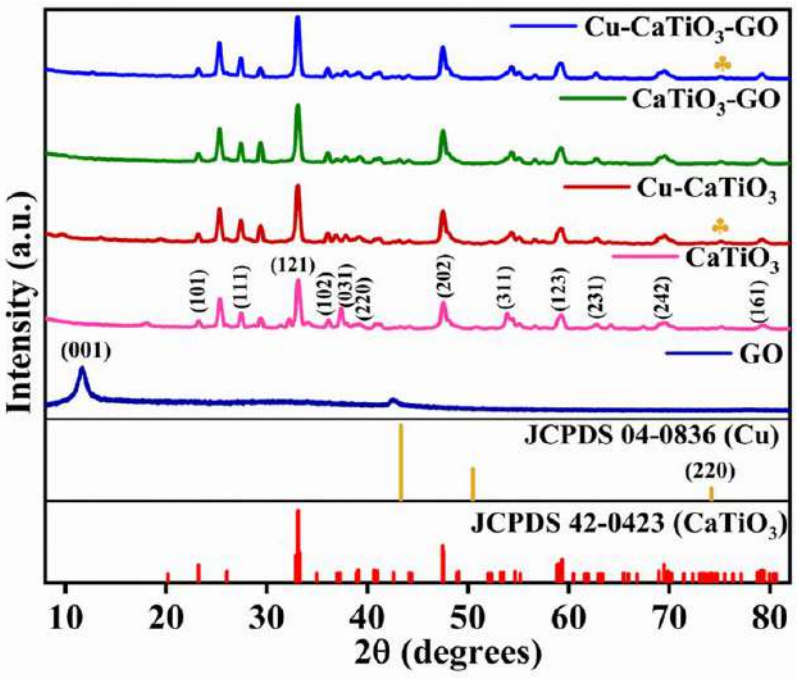

Fig.5.1. (a) X-ray diffraction patterns of prepared GO, pristine $CaTiO_3$, binary (Cu-$CaTiO_3$, $CaTiO_3$-GO) and the ternary Cu-$CaTiO_3$-GO samples

5.3.2. Raman analysis

Fig.5.2. depicts the Raman spectra of the prepared samples. Raman spectra of pristine $CaTiO_3$ show nine peaks observed at 144, 183, 248, 281, 367, 401, 467, 521, and 638 cm^{-1} which can be ascribed to the orthorhombic phase according to prior findings. The peak at 144 cm^{-1} is linked to Ca-TiO_3 lattice vibrations, namely Ca bonding with the TiO_3 group. The bands at 183-367 cm^{-1} correspond to O-Ti-O bending vibration modes. 468 and 521 cm^{-1} represent Ti−O torsional modes (oxygen cage bending or internal vibration). The raman band observed at 638 cm^{-1} arises from the Ti−O symmetric stretching vibrations [29,30]. GO Raman

spectra exhibit two strong bands D and G bands at 1345 cm^{-1} and 1592 cm^{-1}, respectively. D-band originates from the structural defect i.e sp^3 carbon defect with A_{1g} symmetric vibration, while the G band reflects the in-plane vibration of the E_{2g} phonon from the sp^2 bonded carbon atoms [31]. The presence of Raman bands corresponding to pure $CaTiO_3$ as well as GO in the ternary nanocomposite (Cu-$CaTiO_3$-GO) supports the effective attachment of graphene oxide sheets. Furthermore, when compared to pure $CaTiO_3$, the intensity of the Raman peaks of the Cu-$CaTiO_3$-GO was greatly reduced due to the strong interaction between the various components or the surface covering by GO and Cu NPs.

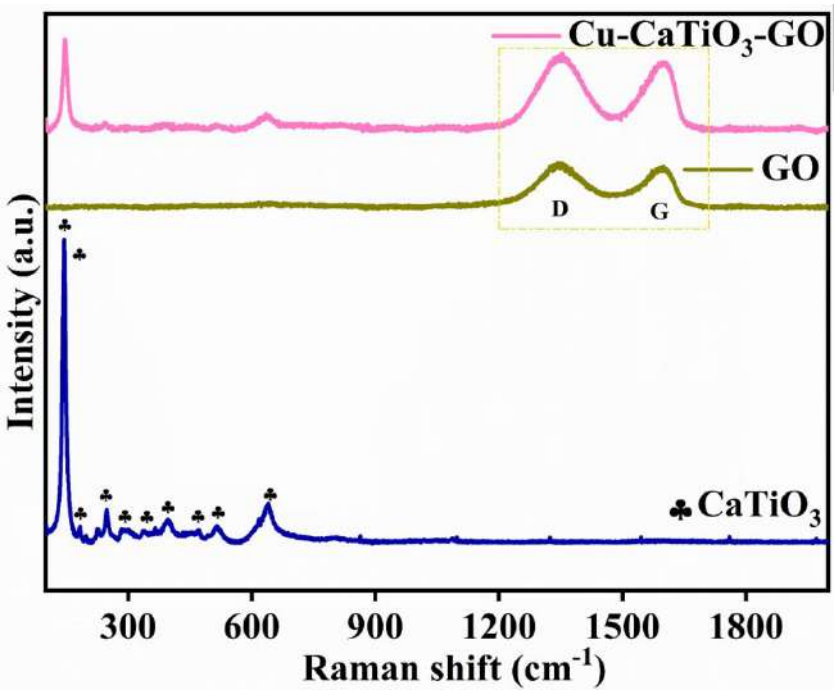

Fig.5.2. Raman spectra of $CaTiO_3$, GO and the Cu-$CaTiO_3$-GO composite**.**

5.3.3. Morphology studies

FE-SEM, EDS-Mapping and HR-TEM analysis

To appraise the morphological and structural properties of the newly developed ternary Cu-$CaTiO_3$-GO composite, FE-SEM, **(Fig.5.3)**, TEM, HR-TEM **(Fig.5.5.(a)-(f))** analysis were executed. The FE-SEM photograph in **Fig.5.3(a)**, shows that the primitive $CaTiO_3$ exhibits a well-defined cuboid-shaped structure. A cross-like cube consisting of some vertically crossing cuboids can also be observed **(Fig.5.3(b)**. The synthesized GO exhibited a flaky or crumpled-sheet like structure. The images, clearly reveal the existence of cuboid-shaped $CaTiO_3$ that are well adhered to the surface of GO sheets. Although the visible presence of

Cu NPs was not observed in the FESEM image of the composite. However, some tiny white spots can be seen randomly deposited on the surface of both $CaTiO_3$ as well as GO, which are assumed to represent the photo-deposited Cu NPs. These photographs depict the perfect creation of the intended ternary hybrid, with tight interactions between each of its components.

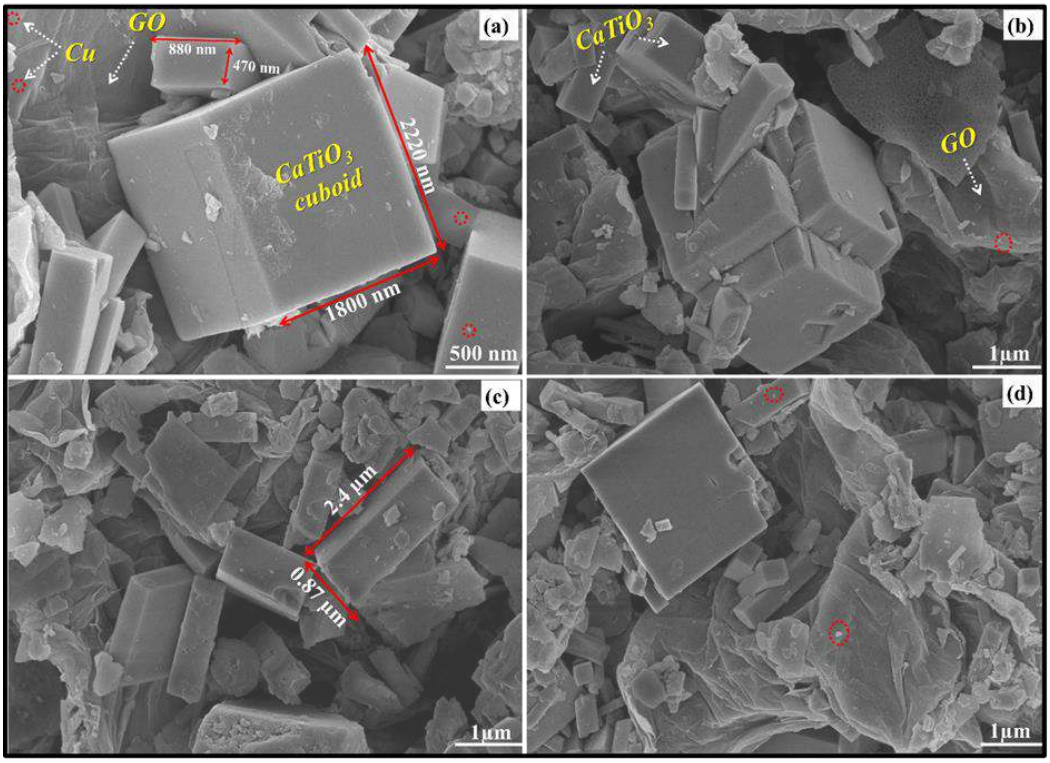

Fig.5.3. FE-SEM images of (a-d) Cu-$CaTiO_3$-GO composite

Further, high elemental purity of the Cu-$CaTiO_3$-GO hybrid is ensured by the EDS spectrum and corresponding elemental mapping images **(Fig.5.4(a) and (b))**, which shows a distribution of Ca (yellow), Ti (azure), O (green), C (red), and Cu (pink) constituent elements in the selected region of the trio composite. It's yet another proof that Cu is successfully deposited on $CaTiO_3$-GO composite.

The detailed morphological characteristics of the ternary composite is further assessed by the TEM and HR-TEM analysis. Similar to FE-SEM analysis, the TEM images **Fig.5.5(a-d)** disclose the cuboid type morphology of $CaTiO_3$ with an average length of 832 nm and a width of about 515 nm, homogenously embedded on the layered GO sheets. Numerous smaller Cu NPs in the form of nanodots (light colored dots) with average size 82 nm are seen to be accumulated on the surface of perovskite $CaTiO_3$ as well as in some portions across the GO sheets. The close attachment of each component in the hybrid (Cu, $CaTiO_3$, GO) is

clearly visible in the TEM photographs. This tightly packed surface morphology of the developed Cu-$CaTiO_3$-GO system is expected to result in a smooth channel for efficient electron capture and transmission to achieve high degree of photochemical reaction.

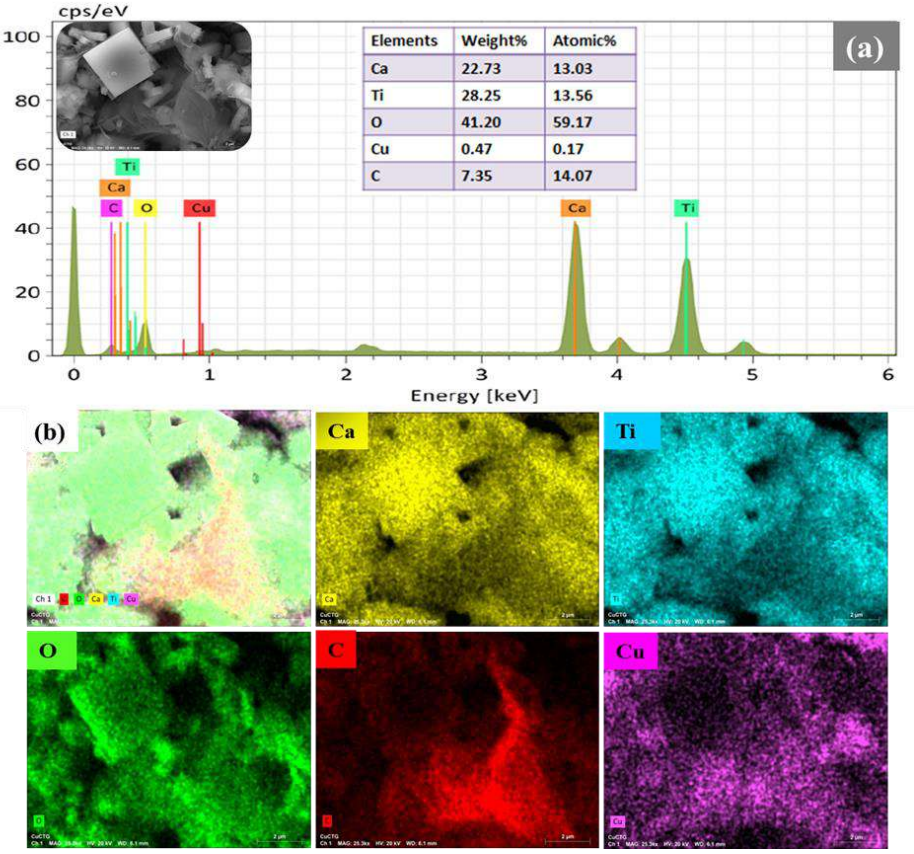

Fig.5.4. (a) EDX spectrum; and (b) elemental color mapping images of different elements (Ca, Ti, O, C, Cu) present in ternary Cu-$CaTiO_3$-GO composite.

Moreover, the HR-TEM images **(Fig. 5(e))** clearly exhibited the presence of two distinct types of lattice fringes, with 'd' spacings of 0.265 nm, and 0.216 nm that can be well correlated to the (121) crystallographic plane of orthorhombic $CaTiO_3$, (111) diffraction plane of metallic cubic Cu respectively[27,32]. In addition, GO nanosheets served as the ground (shown as interface) for both deposited Cu and $CaTiO_3$. This datum provides reliable evidence that the ternary system was indeed formed with all components being in close proximity to one another. Such an intimate interface between different crystal phases could be may be beneficial in accelerating the electron transport across the interface, hence prolonging the life time of charge carriers.

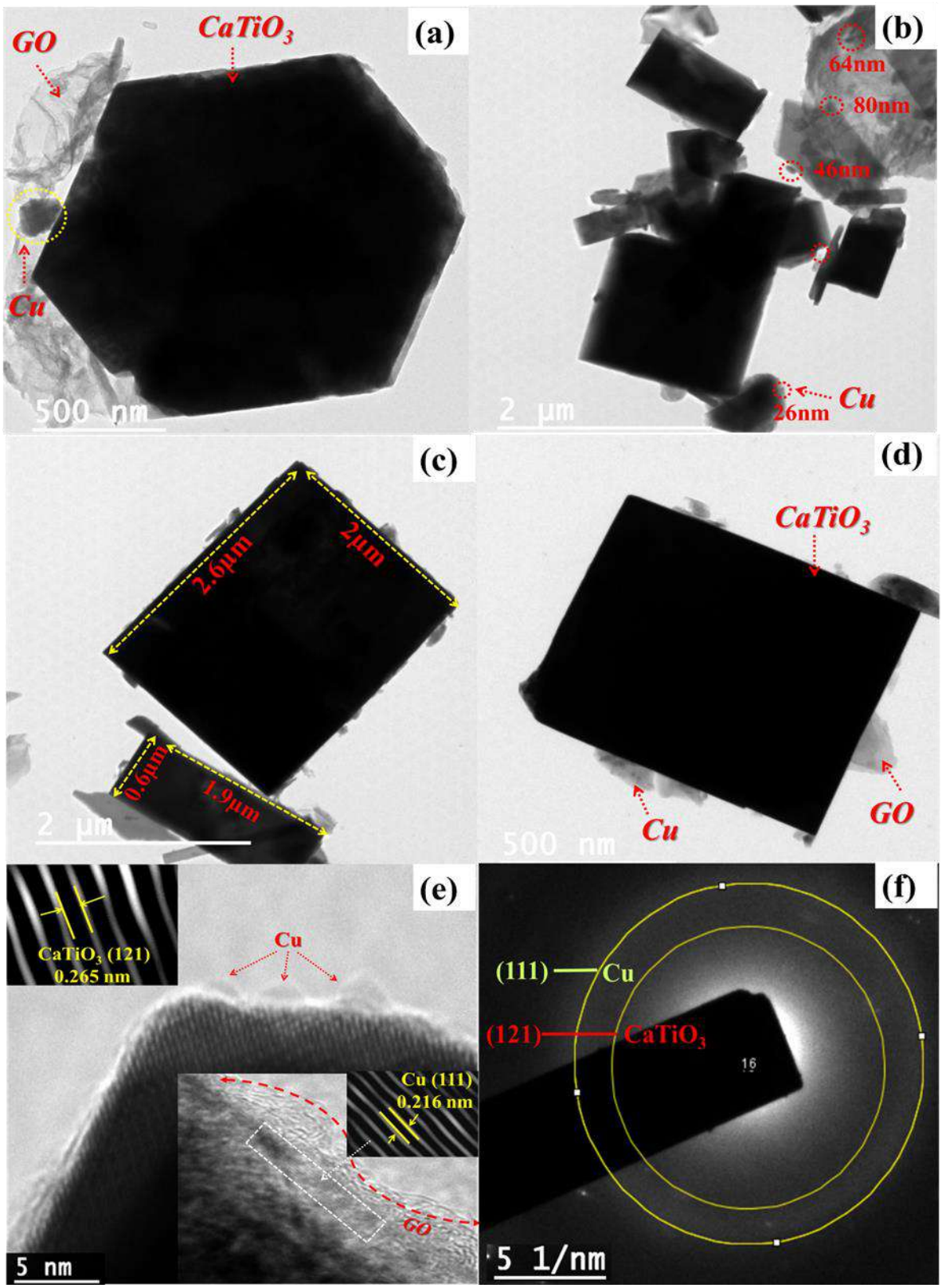

Fig.5.5. (a-d) HR-TEM images (e) Lattice fringes and (f) SAED pattern of Cu-$CaTiO_3$-GO composite.

Likewise, the SAED pattern **Fig.5.5(f)**, shows concentric diffraction rings with spots, matching well with the peculiar ring pattern of orthorhombic phase of $CaTiO_3$ [(121) with d = 0.266 nm], Cu [(111) with d = 0.21nm], further indicated that the Cu NPs are nicely loaded on $CaTiO_3$ nanostructures which are further in good support with graphene oxide sheets. These results are consistent with the XRD patterns. The findings of the FE-SEM and HR-TEM analysis evidenced the successful fabrication of the Cu and GO co-loaded $CaTiO_3$ nanocomposite with intimated contacts along with existence of multiple e- transfer routes among the individual constituents. This could be conducive for the adequate transfer as well as segregation of charge carriers in the composite thus, ameliorating $CaTiO_3$'s photocatalytic activity.

5.3.4 XPS analysis

The elemental compositions and chemical states of the multicomponent Cu-$CaTiO_3$-GO composite were comprehended by XPS analysis (**Fig.5.6)**. The full XPS survey scan spectrum **(Fig.5.6(a))** clearly reveals the existence of five elements (Ca, Ti, O, Cu, and C) in the composite. The high-resolution Ca(2p) XPS spectrum (**Fig.5.6.(b**) exhibits two prominent peaks centered at 345.9 eV and 349.5 eV, that are assigned to the Ca $2p_{3/2}$ and Ca $2p_{1/2}$ binding signals, respectively, suggesting that the calcium element exists in the +2-oxidation state. Similarly, the existence of two distinct peaks in the Ti (2p) **(Fig.5.6.(c)** positioned at 458 eV ($Ti2p_{3/2}$), 463.6 eV ($Ti2p_{1/2}$), with an energy difference of 5.6 eV, indicates the existence of titanium in the (Ti^{4+}) state. The deconvoluted O (1s) spectra of oxygen **(Fig.5.6.(d))**, manifest two peaks. Peak at a 529.5 eV belongs to the crystal lattice oxygen of $CaTiO_3$, and peak at 531.7 eV could relates to the adsorbed O_2 from the OH bond absorbed onto the composite's surface [33]. Cu (2p) spectrum **(Fig.5.6.(e))** shows two peaks at B.E. of 932.6 eV (corresponding to Cu $2p_{3/2}$) and 952.5 eV (corresponding to Cu $2p_{1/2}$). These peaks suggest that the surface deposited Cu exists in two variable oxidation states, 0 and +1, which are assigned to metallic Cu or Cu_2O species.[34] Since no Cu_2O was identified in XRD and HRTEM analysis, so the peaks may be from metallic Cu only. The GO, C(1s) XPS spectra (Fig. 5b) are deconvoluted into three peaks. Peak at 284.5 eV related to the typical C-C bonds with the "sp^2" configuration, while the other two weaker peaks at 286.2 and 288.6 eV belonged to the epoxy (C-O), carbonyl (C=O) functional groups, witnessing oxygen-containing functional groups in GO[35]. Overall, the XPS investigation strongly supported the formation of a Cu-$CaTiO_3$-GO hybrid composite.

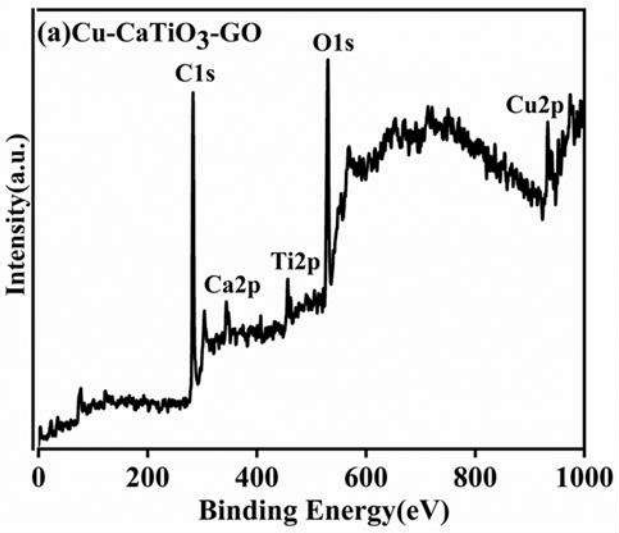
(a)Cu-CaTiO3-GO
C1s
O1s
Cu2p
Ti2p
Ca2p
Intensity(a.u.)
0
200
400
600
800
1000
Binding Energy(eV)

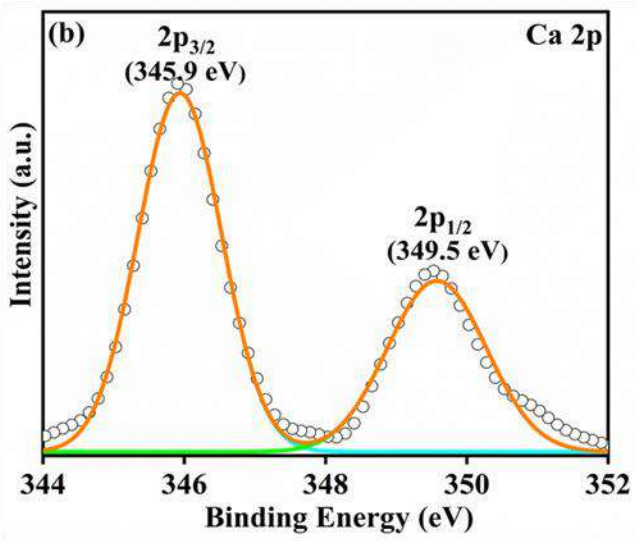
(b)
2p3/2
(345.9 eV)
Ca 2p
2p1/2
(349.5 eV)
Intensity (a.u.)
344
346
348
350
352
Binding Energy (eV)

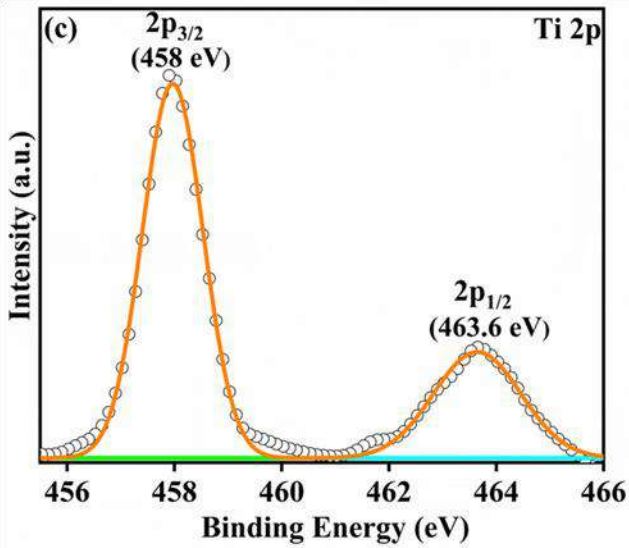
(c)
2p3/2
(458 eV)
Ti 2p
2p1/2
(463.6 eV)
Intensity (a.u.)
456
458
460
462
464
466
Binding Energy (eV)

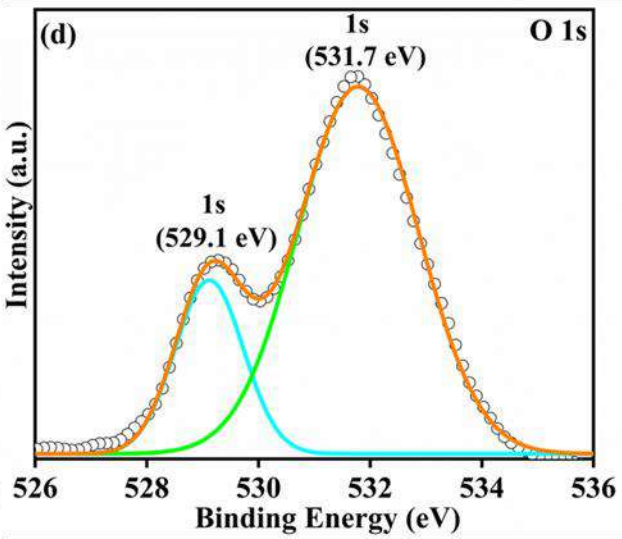
(d)
1s
(531.7 eV)
O 1s
1s
(529.1 eV)
Intensity (a.u.)
526
528
530
532
534
536
Binding Energy (eV)

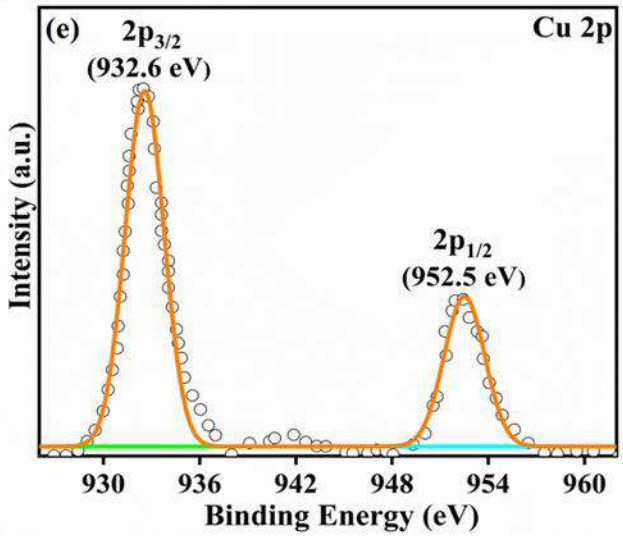
(e)
2p3/2
(932.6 eV)
Cu 2p
2p1/2
(952.5 eV)
Intensity (a.u.)
930
936
942
948
954
960
Binding Energy (eV)

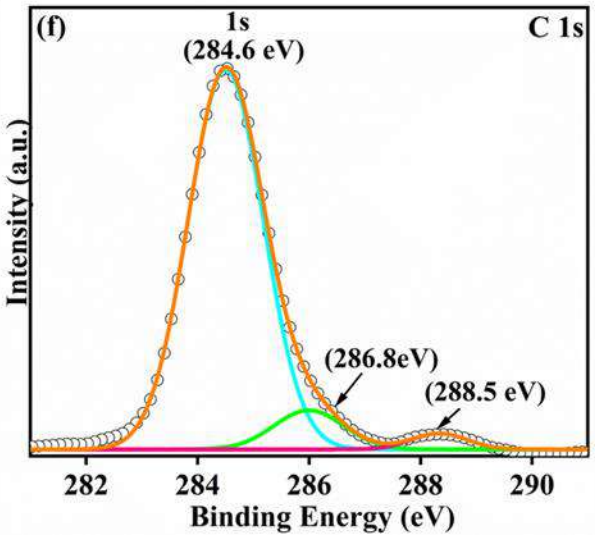
(f)
1s
(284.6 eV)
C 1s
(286.8eV)
(288.5 eV)
Intensity (a.u.)
282
284
286
288
290
Binding Energy (eV)

Fig.5.6. XPS spectra for Cu-$CaTiO_3$-GO nanocomposite (a) survey scan (b) Ca 2p, (c) Ti 2p, (b) O 1s, (d) Cu 2p, and (e) C 1s spectrum

5.3.5 Porosity and surface area study

The textural properties (surface area and porous nature) of the pristine $CaTiO_3$, and the ternary Cu-$CaTiO_3$-GO composite were examined by the N_2 adsorption desorption technique. As depicted in **Fig.5.7(a)**, both samples exhibit a type-IV isotherm pattern with H3 hysteresis loops, at vapor pressures ranging from 0.1 to 0.9 P/P_0, indicating their mesoporous nature [36,37]. The pore size distribution plots of the samples (**Fig.5.7(b)**) further reflect this. It can be perceived from **Table 5.1,** that the BET surface area of the newly designed Cu-$CaTiO_3$-GO ternary framework (22.82 m^2/g) is approximately 8 times larger than that of bare $CaTiO_3$ (2.84 m^2/g). These results demonstrate that the addition of GO sheets with 2-D structural features, as well as the surface deposition of Cu NPs, significantly increased the surface area of $CaTiO_3$. The greater surface area of the hybrid makes it capable of delivering a greater number of surface-active sites for adsorption of the pollutant molecules, subsequently alleviating the photocatalytic effectiveness. Likewise, the samples' pore volume and pore size distribution exhibited the same increasing trend as the surface area, which could allow the speedy diffusion of numerous reactants and products in the photocatalytic process, thereby, upgrading the photocatalytic activity and eliminating pollutants more quickly [38]. With its mesoporous structure, greater BET surface area, and larger pore volume, the ternary photocatalyst holds huge potential for use in photocatalytic processes.

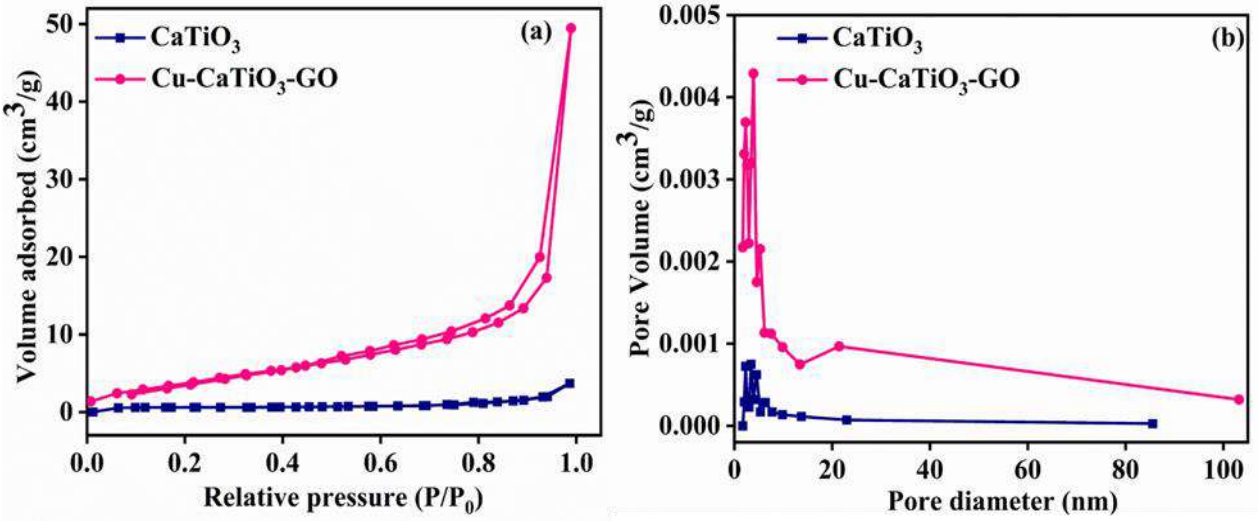

Fig.5.7. (a) N_2 adsorption isotherms and (b) the corresponding BJH pore size distributions curves of pristine $CaTiO_3$ and Cu-$CaTiO_3$-GO composite.

S.No.	Photocatalyst	Surface area (m^2g^{-1})	Total Pore Volume (cm^3g^{-1})	Mean Pore diameter (nm)
1	$CaTiO_3$	2.846	0.007	3.405
2	Cu-$CaTiO_3$-GO	22.829	0.080	3.909

Table 5.1: Textural properties of pristine $CaTiO_3$ Cu-$CaTiO_3$-GO composite

5.3.6. Optical and charge transfer properties

UV-Vis Diffuse reflectance spectra

The optical absorption characteristics of as-fabricated samples were appraised through UV-vis diffuse reflectance spectroscopy, and the resulting spectra along with the color images are displayed in **Fig.5.8. Fig.5.8(a)** clearly depicts that, pristine $CaTiO_3$ exhibited absorption in the UV light region, with an absorption onset around 380 nm. The observed absorption edge corresponds to the electron transference from its VB (O 2p orbital) to CB (Ti 3d orbital)[39]. While the dual composites (Cu-$CaTiO_3$, $CaTiO_3$-GO) show high absorption efficiency in the visible region (400-800 nm). A considerable redshift is clearly observed in the absorption edges of these hybrid composites. In the case of $CaTiO_3$-GO sample, this significant shift, could be attributed to the interaction between the $CaTiO_3$ surface and the graphene oxide functional groups via the Ti-O-C chemical bond [40,41]. Apart from this, an additional intense and broad band in the region of 500-800 nm (with maxima around 700 nm) was observed in the Cu loaded composites, which results from the typical LSPR effect of photo-deposited Cu NPs[42]. The results indicate that the incorporation of GO and plasmonic Cu has a positive effect on the optical property of $CaTiO_3$. In comparison to the hybrids (Cu-$CaTiO_3$, $CaTiO_3$-GO), the absorption band of Cu-$CaTiO_3$-GO was found to be broader and more intense, making it the best choice among all contenders for capturing visible light. The results were consistent with the colors of corresponding samples changing from white $CaTiO_3$ to, finally light gray Cu-$CaTiO_3$-GO.

The band gap energies of these photocatalysts were also evaluated by employing Tauc's equation:

$$ahv = A\,(hv - E_g)^{1/2} \quad (2)$$

where α is an absorption coefficient, h = Planck's constant, υ represents the light frequency, A refers to an energy-independent constant, and E_g denotes the band gap energy. As depicted in **Fig.5.8(b)**, the E_g values of $CaTiO_3$, $CaTiO_3$-GO, Cu-$CaTiO_3$, and Cu-$CaTiO_3$-GO composites were measured as 3.05, 2.85, 2.77, and 2.67 eV, respectively. Clearly, the differences in band gap values show that Cu, $CaTiO_3$, and GO interact

well, which proves that the trio hybrid was formed. The electronic interaction, interfacial bonding, and synergistic effects between carbon-related materials such as GO and the plasmonic metal Cu clearly reduced the band gap of $CaTiO_3$ from 3.05 to 2.67 eV indicating that energy required to excite electrons from the VB to the CB is substantially lower in the Cu-$CaTiO_3$-GO nanocomposite. DRS spectra demonstrate that modifying $CaTiO_3$'s surface with Cu and GO broadens the light absorption range and shortens the composite's bandgap.

Therefore, on account of the improved optical absorption property, it is expected that the newly constructed Cu-$CaTiO_3$-GO composite will be able to accomplish more efficient visible energy use by generating numerous charge carriers, hence improving its photocatalytic efficacy.

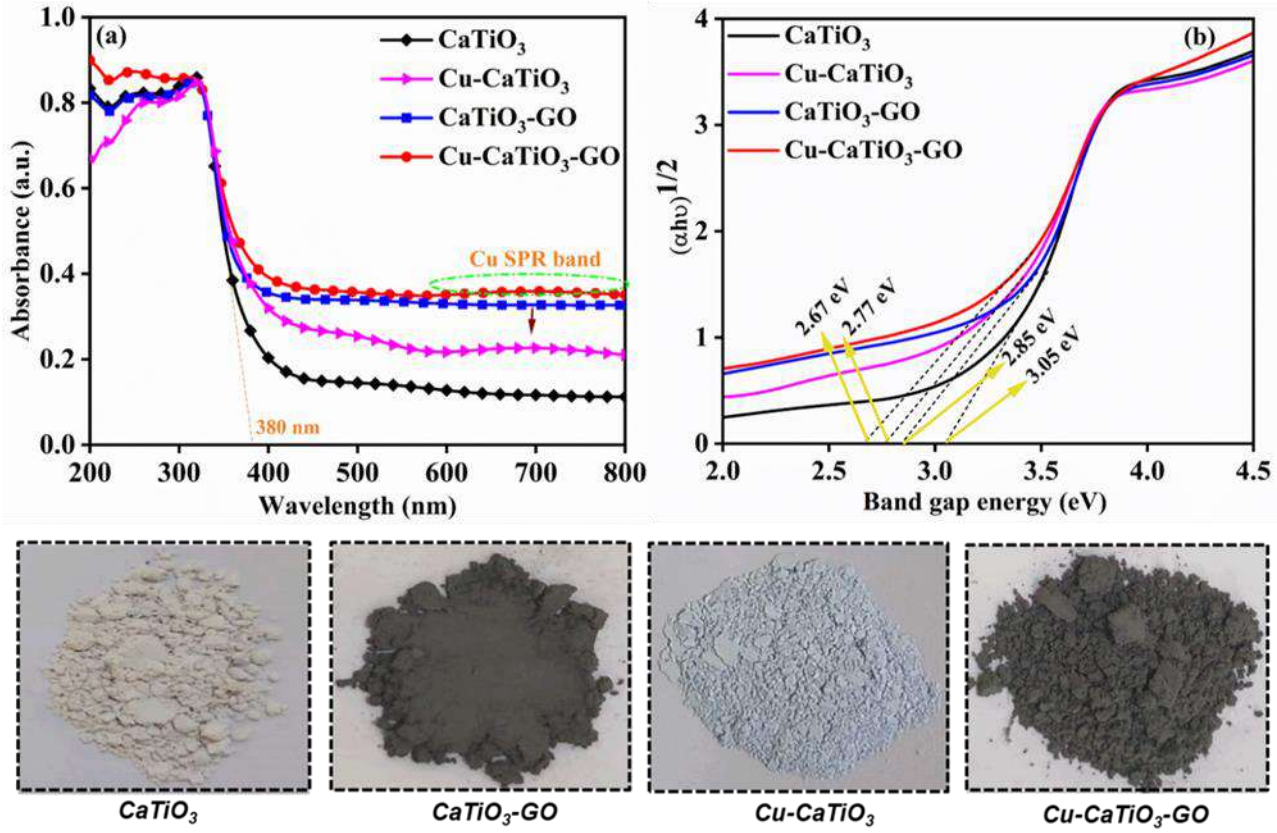

Fig.5.8 (a) UV-Vis diffuse reflectance spectra and the corresponding (b) Tauc plots of pristine $CaTiO_3$, binary Cu-$CaTiO_3$, $CaTiO_3$-GO, and ternary Cu-$CaTiO_3$-GO samples

Photoluminescence measurement

PL spectroscopy is an efficient method to probe the recombination of photoexcited charge carriers. Generally, the PL emissions arise from the reconciliation of the e^--h^+ pair, lower PL intensities suggest a

slower recombination rate [43]. **Fig.5.9(a)** illustrates the PL emission spectra of the $CaTiO_3$ and its composites at the 370 nm wavelength. With the exception of peak intensities, all the samples have similar emission peaks. Defect-related deep-level emission (DLE) caused by inherent structural defects including oxygen vacancies, surface states, and OH- defects, produces two PL bands at 467 nm (blue region) and 553 nm (green region)[44]. The PL intensities here followed the sequence of $CaTiO_3$ > Cu-$CaTiO_3$ > $CaTiO_3$-GO > Cu-$CaTiO_3$-GO. The intensity of the PL peaks in dual composites (Cu-$CaTiO_3$ and $CaTiO_3$-GO) decreased markedly, indicating that the reunion extent of photoinduced e^--h^+ pairs has been suppressed. The Schottky barrier formed at the Cu-$CaTiO_3$ interface may act as an electron reservoir in the Cu-$CaTiO_3$ sample, limiting the reconciliation process. Because of the superior electronic conductivity of the GO sheets in the $CaTiO_3$-GO composite, electrons could be transported quickly from $CaTiO_3$ to the latter, resulting in a decreased recombination rate. The PL spectral intensity was further suppressed in the ternary Cu-$CaTiO_3$-GO composite, indicating that the rejoining of e^--h^+ couples is prevented to a greater extent. This could be because of the strong interaction and synergistic effect between the different parts (metallic Cu NPs, perovskite $CaTiO_3$, and GO sheets), as well as the creation of multiple electron transfer channels, which would help with the segregation and transfer of photoproduced charges Thus, the PL results point out the importance of designing the ternary system for prolonging the lifetime of charge carriers, which could be one of the contributing factors for Cu-$CaTiO_3$-GO's superior photocatalytic performance.

Impedance analysis

To further explore the charge migration and transfer processes in pristine $CaTiO_3$, and its composites, impedance measurements were carried out, and the results are depicted in **Fig.5.9(b)** in terms of Nyquist plots. Generally, the arc on the impedance spectrogram represents the magnitude of the charge transfer resistance, and the smaller the arc radii, the lower the electron transport resistance, indicating a higher segregation efficiency of charge transfer in the material [45]. As shown, Cu loaded $CaTiO_3$-GO owned the smallest arc radii than any other sample which suggests that incorporating both the cocatalysts Cu and GO simultaneously onto $CaTiO_3$ NCs results in higher conductivity, rapid interfacial charge transport, and adequate separation of photoinduced e^--h^+ pairs. The above findings are well consistent with those of PL measurements. Based on the above-mentioned conclusions, it can be inferred that the highly ameliorated photocatalyst performance of the ternary hybrid (Cu-$CaTiO_3$-GO) could not only be credited to its enlarged visible light absorption but also to its improved charge carrier separation and migration ability.

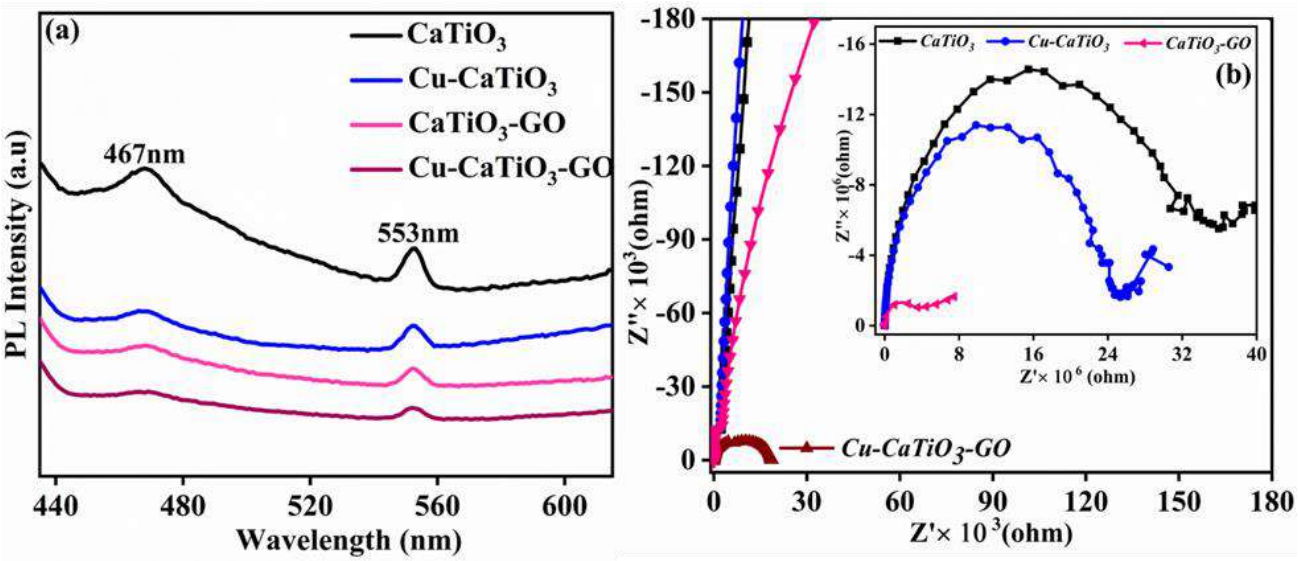

Fig.5.9 (a) PL spectra and (b) Nyquist impedance plots of as-fabricated samples.

5.4. Photocatalytic activity

5.4.1. Photocatalytic degradation reaction

The photocatalytic efficiencies of the prepared samples were initially assessed by monitoring the degradation of the antibiotic, cefixime (CFX) under LED light irradiation. **Fig 5.10(a)** depicts the CFX removal rate curve in terms of C_t/C_0 with light irradiation time (t). As apparent from **Fig.5.10(a)**, no significant degradation of CFX is encountered in blank tests (absence of catalyst), indicating that CFX is extremely photostable and its direct photolysis can be ignored. After 40 min of equilibration in the dark, the adsorption capabilities of different photocatalysts were computed as $CaTiO_3$: 9.6%; $CaTiO_3$-GO: 30.2%; Cu-$CaTiO_3$: 19.2%, and Cu-$CaTiO_3$-GO: 39.1%. Clearly, the adsorption capacity of all the modified samples was better in comparison with the unmodified $CaTiO_3$, and when both Cu and GO were deposited simultaneously on the $CaTiO_3$ surface to develop a trio hybrid, the adsorption capacity was maximized, most likely due to the enhanced BET surface area with abundant reactive adsorption sites that enable this composite system to offer strong adsorption ability. For the further advancement in the removal efficacy, the photocatalytic process was commenced with LED light irradiation. After 100 minutes of photocatalytic treatment, the catalytic performance of synthesized photocatalysts proceeded as follows: $CaTiO_3$ (27%) < $CaTiO_3$-GO (71.4%) < Cu-$CaTiO_3$ (59.8%) < Cu-$CaTiO_3$-GO (94.1%). The minimum photocatalytic performance was observed in the case of pristine $CaTiO_3$, which could be ascribed to its wide band gap, limited light harvesting ability, low surface area, and more prominent charge carrier recombination. Among all the, Cu-$CaTiO_3$-GO

presented exceptionally striking capabilities with the dynamic removal of CFX drug under identical conditions. The cumulative outcome of some promising features like a reduced band gap, extended light harvesting ability, better generation, separation, and transfer of photo-induced e^--h^+ pairs, and stronger adsorption capability ultimately results in its superior pollutant degradation performance.

Additionally, the reaction kinetics of the CFX degradation, were examined quantitatively using a pseudo-first-order rate equation:

$\{\ln(C_t/C_0) = -kt\}$ .....(3)

Here, C_0 and C_t represent the CFX concentrations at (0) and (t) minutes of irradiation, and (k) is the reaction rate constant (min^{-1}). **Fig. 5.10(b)**, depicts the linear correlation between $\ln(C_0/C_t)$ and irradiation time (t) using as-fabricated samples.

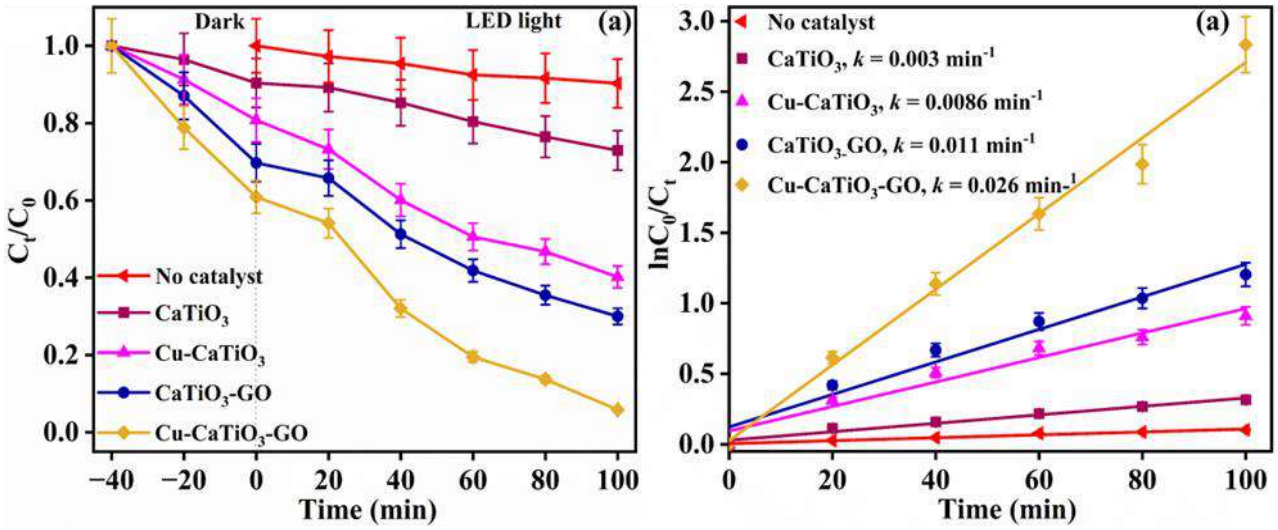

Fig. 5.10(a) Time course-kinetic plots and **(b)** corresponding variations in apparent reaction rate constants (k) values obtained for the degradation of CFX antibiotic in the presence of different photocatalysts

Certainly, in accordance with the degradation efficiency, the ternary Cu-$CaTiO_3$-GO hybrid presents the greatest degradation rate constant (0.026 min^{-1}), which is 8.6, 2.36, and 2.5 folds higher greater than observed for the single $CaTiO_3$ NCs (0.003 min^{-1}), binary $CaTiO_3$-GO (0.011 min^{-1}), and Cu-$CaTiO_3$ (0.008 min^{-1}), respectively. As previously mentioned, the remarkable photocatalytic ability of the multi-component system, demonstrated that the synergy of both photo-deposited Cu and coupled GO is beneficial in amplifying the photocatalytic response of $CaTiO_3$. Moreover, the temporal changes in the absorption spectra of the CFX solution in the presence of bare $CaTiO_3$ and ternary Cu-CaTiO3-GO samples were monitored throughout the

degradation process, and the degradation profiles reveal that with an extension in the irradiation duration, the intensity of the typical absorption peak of CFX appearing at λ = 278 nm gradually diminishes for both catalysts. Cu-$CaTiO_3$-GO, however, experienced a quite large reduction. After 100 minutes of LED light exposure, the prominent band loses its identity, and the absorption hump almost reaches the ground suggesting that most of the CFX molecules get destroyed. Complete flattening trend of the target CFX spectral profile demonstrates the admirable photocatalytic skills of Cu-$CaTiO_3$-GO in contrast with the unmodified $CaTiO_3$ sample.

Fig.5.11(a-b) displays the histograms of CFX degradation kinetic analysis results over different photocatalysts

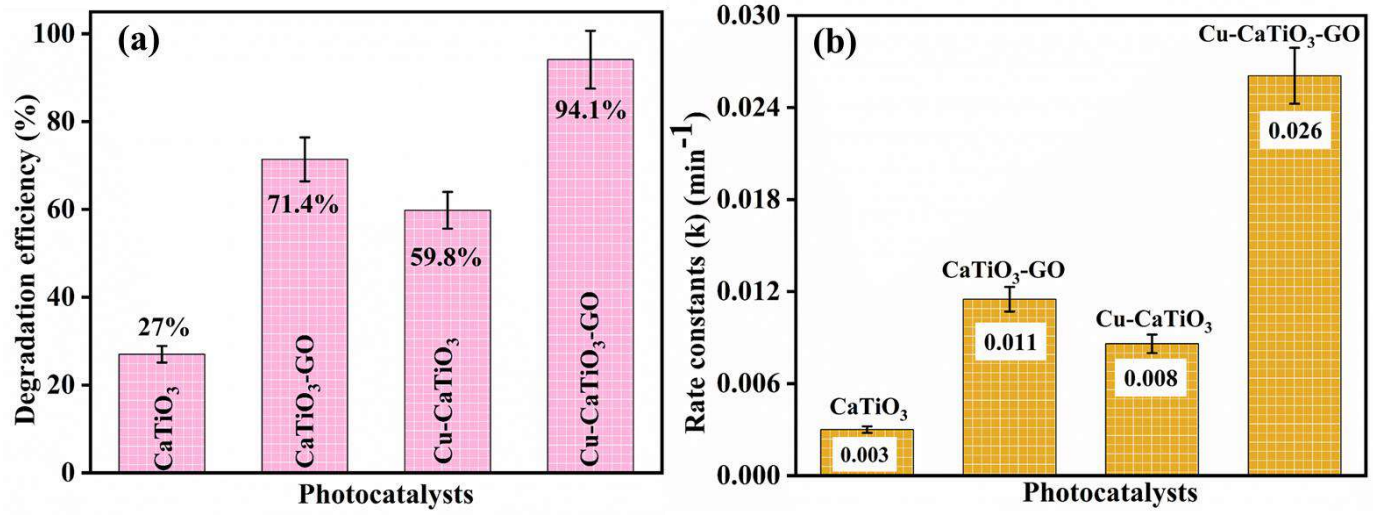

Fig.5.11 Histograms showing comparative (a) photodegradation efficiencies (b) reaction rate constants (k) values exhibited by different synthesized $CaTiO_3$ based photocatalysts for CFX removal.

5.4.2 Photocatalytic H_2 evolution reaction

Due to their suitable band potentials, the prepared $CaTiO_3$ samples, were also tested for photocatalytic hydrogen production through the dehydrogenation of an aqueous methanol solution. In order to determine the H_2 capabilities of different photocatalysts, several experiments were performed. Both photolysis studies (without a catalyst) and dark tests (without light exposure) revealed no appreciable evolution of H_2, showing that H_2 was solely produced through the photocatalytic process. **Fig. 5.12.** illustrates the amount of H_2 gas generated over pristine $CaTiO_3$ and its composites after 6 hours of LED-light irradiation. Similar to the CFX degradation study, pure $CaTiO_3$ exhibits a relatively lower H_2 evolution rate (6.14 $mmolh^{-1}$), owing to its wide band gap, reduced surface area, and quick restriction of interfacial charge carriers. However, the H_2

evolution rates were progressively enhanced with the inclusion of GO and Cu NPs. The maximum H_2 production, of 57.69 $mmolh^{-1}$, was observed over Cu-$CaTiO_3$-GO after irradiation for 6 h, which reveals that the majority of charge carrier electrons are accessible for proton reduction. This rate was about 3.06, 4.03, and 9.39 folds higher than those of Cu-$CaTiO_3$ (14.3$mmolh^{-1}$), $CaTiO_3$-GO (14.3$mmolh^{-1}$) and bare $CaTiO_3$ (6.14 $mmolh^{-1}$), respectively.

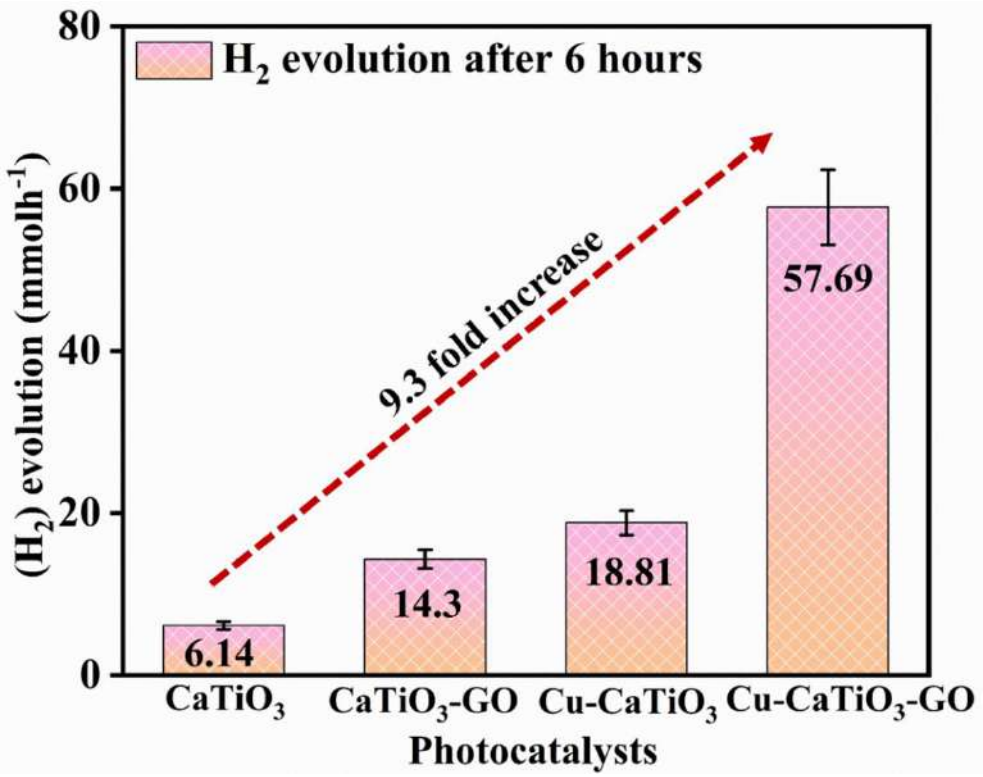

Fig.5.12. Photocatalytic dehydrogenation of methanol for H_2 generation by different catalysts

The fact that the trio hybrid is much better at photocatalysis than $CaTiO_3$ and other photocatalysts can be explained as follows:

(i) The design of a unique multicomponent framework with three types of close contacts between $CaTiO_3$ and deposited Cu NPs, between Cu and incorporated GO sheets, and between $CaTiO_3$ and GO. Together, they all play a role in the splendid photocatalytic performance by offering multi-channel electron transport pathways. This expertly hampers the rejoining probability of e^--h^+ pairs in $CaTiO_3$, thereby extending their life-time and thus improving their involvement in the photodegradation process.

(ii) Extension in the visible light harvesting ability and reduction in the band gap value as attained by the

loading of plasmonic Cu NPs with an unique LSPR effect, as well as the role of GO as a sensitizer permitting the production of vast charge carriers for the purpose of efficient photocatalytic activity.

(iii) Existence of adequate band edge positions in the trio Cu-$CaTiO_3$-GO system, favorable for simultaneous H_2 production and photocatalytic degradation reactions.

(iv) Enlargement of the surface area with the simultaneous inclusion of Cu NPs and GO sheets with $CaTiO_3$ nanocuboids results in the creation of numerous active sites ideal for the adsorption of the pollutant molecules, which eventually accelerates the degradation activity.

(v) Promotion in the charge flow as well as advancement in the transfer and segregation extent of the e^--h^+ pairs due to the exceptional conductivity and electron storage capacity of GO. [46].

5.4.3. Active species detection

To determine the primary oxidative species involved in photocatalytic CFX elimination over Cu-$CaTiO_3$-GO composites, the radical scavenging experiments were executed. For this, the photocatalytic degradation of CFX in the optimal conditions was carried out in the presence of (AA, 10^{-3}M), (IPA, 10^{-3}M) and (EDTA, 10^{-3}M), as the ($O_2^{\bullet-}$), (•OH), and (h^+) scavengers, respectively. **Fig 5.13** depicts the effect of various scavengers on the photodegradation of CFX into Cu-$CaTiO_3$-GO catalysts. In comparison with the scavenger-free experiments, the presence of revealed the most significant decline in degradation efficiency, confirming that •OH plays a key role in the degradation of CFX. AA also suppresses degradation efficiency, suggesting that the $O_2^{\bullet-}$ is also actively involved in the degradation of CFX. However, the addition of EDTA shows only a small inhibition in the photocatalytic activity of the Cu-$CaTiO_3$-GO composite, demonstrating that •OH has a limited contribution to the CFX elimination. Similar results were seen in the sillenite $Bi_{12}TiO_{20}$ [8], and MIL-53(Fe)/urchin-like g-C_3N_4 [47] photocatalytic reaction systems. Thus, these experimental findings proposed that the •OH and $O_2^{\bullet-}$ were likely the prime active species and the h^+ performed a secondary role (not directly participating) in the presented photocatalytic degradation process.

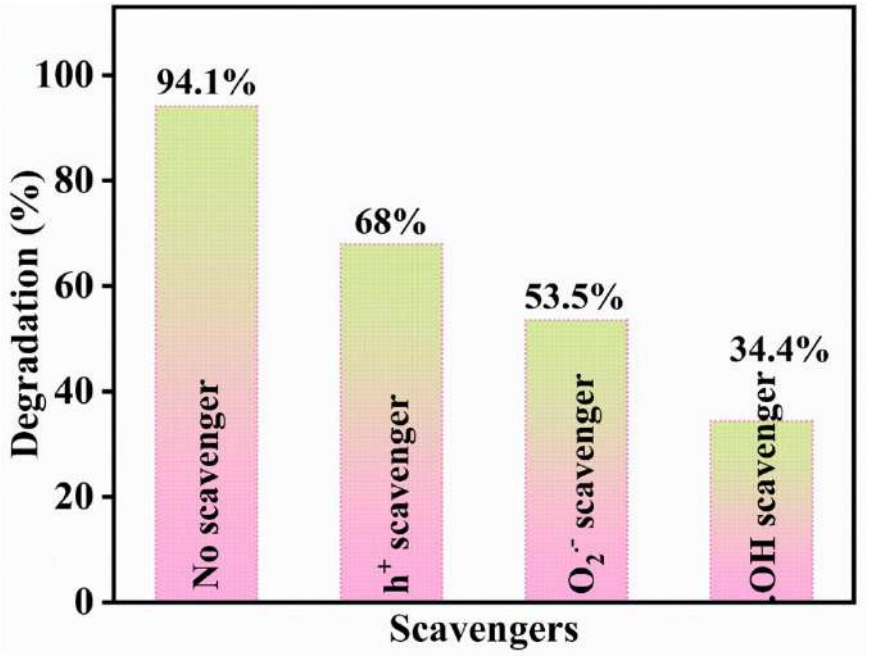

Fig.5.13. Effect of series of scavengers on CFX degradation by Cu-$CaTiO_3$-GO photocatalyst

5.4.4. Probable degradation mechanism

To gain a better understanding of the origins of the synergy between $CaTiO_3$, Cu, and GO in CFX degradation, as well as the improved activity of the nanocomposite, we investigated the photocatalytic charge transfer mechanism. In this regard, the conduction (E_{CB}) and valence band (E_{VB}) potentials of $CaTiO_3$ were reckoned by using the following equations:

$$E_{CB} = \chi - E_e - 1/2E_g \quad (4)$$

$$E_{VB} = \chi - E_e + 1/2E_g \quad (5)$$

where, χ represents the absolute electro-negativity of $CaTiO_3$ (5.105 eV)[48], E_e is the free energy of e- on the H_2 scale (4.50 eV vs. NHE), E_g is energy of the $CaTiO_3$ band gap (3.05 eV). As a result, the E_{CB} and E_{VB} of $CaTiO_3$ vs. NHE were determined to be -0.92 eV and +2.13 eV, respectively. Based on the foregoing results and discussions, a possible photodegradation mechanism of CFX over Cu-$CaTiO_3$-GO ternary nanocomposite is proposed and depicted schematically in **Scheme-5.2.**

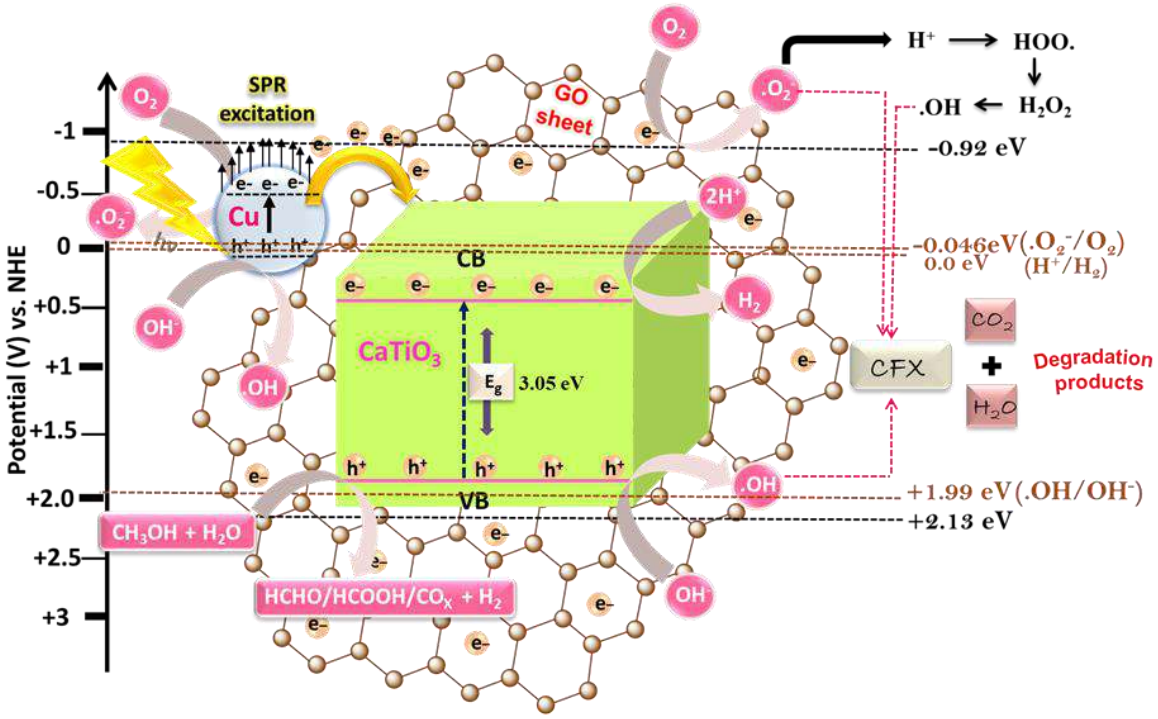

Scheme-5.2: Probable photocatalytic mechanism for degradation of cefixime (CFX) and H_2 evolution through methanol dehydrogenation over Cu-$CaTiO_3$-GO composite

When the Cu-deposited $CaTiO_3$-GO composite is subjected to LED light irradiations (with $\lambda > 360$ nm), the $CaTiO_3$ phase, which has a cuboid-like morphology and an absorption onset at 380 nm, shows some affinity for the irradiation light and elevates to create electrons and holes in its CB and VB. Similarly, under this LED light, photo-generated e^--h^+ pairs can also be produced on deposited plasmonic Cu NPs due to the localized SPR effect, and when these Cu NPs come in contact with $CaTiO_3$ cuboids, the LSPR-induced highly energetic hot electrons overcome the Schottky barrier and rapidly channel to the CB of $CaTiO_3$, leaving behind holes on the Cu surface [49–51]. Furthermore, the photoexcited electrons accumulated in the $CaTiO_3$ CB have a proclivity to flow into the graphene oxide sheets since GO's energy level (-0.08 eV vs. NHE) is much positive than the $CaTiO_3$ CB (-0.92 eV), and GO possess strong electron-accepting behavior [52]. This type of electron transfer route of Cu → $CaTiO_3$ → GO, efficiently suspends the charge recombination process hence, facilitates the photocatalytic performance. Finally, the excessive electrons on the plasmon-excited Cu NPs surfaces and those gathered on the $CaTiO_3$ and GO's surfaces may react with dissolved O_2 in the aqueous solution to generate a highly striking superoxide radical anion ($\bullet O_2^-$), because of their much negative CB potential (-0.92eV vs. NHE) in comparison with the $E^0(\bullet O_2^-/O_2)$ (-0.046 eV vs. NHE). In addition to this, the protonation of $\bullet O_2^-$ creates the hydro-peroxyl radical HOO·, which dissociates

into highly reactive (.OH) species. Meanwhile, owing to $CaTiO_3$'s higher positive VB potential in contrast with the E^0 ($\bullet OH/OH^-$, +1.99 eV vs. NHE), the residual holes within the VB of $CaTiO_3$ and Cu may react with the surface OH^- ion to generate another active species, OH• radicals [31,53–55]. Eventually, the generation of abundant active species ($\bullet O_2^-$, h^+, and OH•) could satisfactorily lead to the destruction of the target CFX moieties by several oxidation and reduction reactions, which is in accordance with the results of the quenching experiments **(Fig. 8a)**.

To sum up, the possible reactions equations occurring during the photocatalytic degradation of CFX over Cu-$CaTiO_3$-GO hybrid composite are expressed below:

$$Cu + hv \rightarrow Cu\,(h^+ + e^-) \quad (6)$$

$$CaTiO_3 + hv \rightarrow CaTiO_3\,(h^+ + e^-) \quad (7)$$

$$Cu\,(e\text{-}) + CaTiO_3 \rightarrow CaTiO_3\,(e^-) + Cu \quad (8)$$

$$CaTiO_3\,(e^-) + GO \rightarrow CaTiO_3 + GO\,(e^-) \quad (9)$$

$$GO\,(e\text{-}) + O_2 \rightarrow GO + \bullet O_2^- \quad (10)$$

$$CaTiO_3\,(e\text{-}) + O_2 \rightarrow CaTiO_3 + \bullet O_2^- \quad (11)$$

$$Cu\,(e\text{-}) + O_2 \rightarrow Cu + \bullet O_2^- \quad (12)$$

$$\bullet O_2^- + H^+ \rightarrow .OOH \quad (13)$$

$$2.OOH \rightarrow O_2 + H_2O_2 \quad (14)$$

$$H_2O_2 + (e\text{-}) \rightarrow .OH + OH^- \quad (15)$$

$$Cu\,(h^+) + OH^- \rightarrow \bullet OH \quad (16)$$

$$CaTiO_3\,(h^+) + OH^- \rightarrow \bullet OH \quad (17)$$

$$\bullet O_2^- / \bullet OH + CFX \rightarrow CO_2 + H_2O + \text{smaller degradation products} \quad (18)$$

Likewise, a potential mechanism for generating H_2 via dehydrogenation of methanol solution is described as follows:

The primary condition of an ideal semiconductor for the H_2 production is that the E_{CB} and E_{VB} positions must straddle within the limits of methanol-water mixture decomposition reaction in accordance with the NHE, the E_{CB} has to higher than the redox potential of H_2O i.e H^+/H_2 (0 V vs NHE) and E_{VB} needs to be more positive than the redox potential of water O_2/H_2O (1.23 V vs NHE) and methanol CH_3OH (0.016V). The prepared catalyst, fulfills this condition, and is suitable for the use for H_2 evolution reactions.

As discussed above, when the Cu-$CaTiO_3$-GO catalyst is triggered by LED light, e^-/h^+ pairs are produced in its different components. Since the CB of $CaTiO_3$ is much negative in contrast with the reduction potential of H^+/H_2 (0 eV), the electrons that have accumulated on its CB could drive the generation of molecular H_2.

The H^+ ions could also be converted to H_2 gas by the electrons amassed on the surface of the $CaTiO_3$ and GO sheet. Meanwhile, the photoinduced VB holes with strong oxidation potential, will move to the catalyst's surface, where they will oxidize adsorbed methanol molecules and produce formaldehyde (HCHO) and hydrogen ions. Additionally, the holes can even oxidize water molecules to generate O_2 and H_2 ions [56].

The overall reactions involved in the photocatalytic dehydrogenation of methanol are presented below:

$$Cu\text{-}CaTiO_3\text{-}GO + hv \rightarrow Cu\text{-}CaTiO_3\text{-}GO\ (h^+ + e^-) \quad (19)$$

Reduction:

$$2H^+ + 2(e\text{-}) \rightarrow H_{2\,(g)} \quad (20)$$

Oxidation:

$$CH_3OH + 2(h^+) \rightarrow 2H^+ + HCHO \quad (21)$$

$$CH_3OH \Leftrightarrow H_2 + HCHO \quad (22)$$

$$2H^+ + H_2O \rightarrow 1/2O_2 + 2H^+ \quad (23)$$

The cumulative effect of Cu, $CaTiO_3$, and GO, promote the separation and multistep transference of photoproduced charge carriers, leading to the development of a promising Cu-$CaTiO_3$-GO ternary photocatalyst with heightened performance.

5.4.5. Cefixime photodegradation pathway

To delve deeper into the photocatalytic removal of CFX antibiotic, the reaction intermediates generated in the degradation process were identified via the LC-MS technique, and their structures were deduced from their m/z value. ((m) represents the intermediate's molecular weight, and (z) denotes the charge number.) **Fig.5.14(a)** illustrates the mass spectrum of possible CFX intermediates. After 100 minutes of photodegradation, the characteristic mass spectrum peak of the parent molecule CFX with m/z 453 no longer exists, suggesting that CFX molecules were effectively degraded. However, several products (P) with m/z values of 409, 289, 226, 199, 182, 158, and 91 were detected. Combining the findings of LC-MS analysis, quenching experiments, and previous literature reports, the plausible CFX degradation pathway using Cu-$CaTiO_3$-GO catalyst is suggested and presented in **Fig.5.14(b).**

P1(m/z:226) was generated by the removal of the complete (Z)-2-(2-amino-4-thiazolyl)-2-(carboxymethoxyimino) acetylmoiety from the CFX molecule (m/z 453) [57]. Following that, deamination and dethylation result in the production of P2 (m/z: 199). Next, the β-lactam ring opens up via the sequential attack of active species (·OH and $O_2^{\bullet-}$), which further underwent carboxylation to yield product P3 (m/z: 217). The ring-opening and bond cleavage further lead to the formation of P4 (m/z:182) [58]. The direct

generation of P5 (m/z: 289) from CFX (m/z: 453) occurs by the removal of the aminothiazole ring, opening of the β-lactam ring, and losing the carboxyl group[59]. In another pathway, after being attacked by the. OH radical and losing its carbon dioxide functional group, CFX (m/z: 453) transforms to P6 (m/z: 409). The product P7 (m/z: 337) is then formed by separating another CO_2 group. As the .OH attack proceeds, P7 (m/z: 337) loses its ethylene group and gains the OH group in its place. The enol form is then converted to ketone, resulting in the formation of product P8 (m/z: 313). Subsequently, the attack of several radical groups results in the breakdown of one of the rings generating P9 (m/z: 158). The removal of branching of the thiazole ring converts this product to P11 thiazol-2-ol with m/z 101. Eventually, the ring-opening occurs, leading to a product with a lower molecular mass, P12 (m/z: 91) [60]. Finally, with further oxidation reactions and longer processing times, all these intermediate products (P4, P5, and P12) are expected to decompose into smaller fragments, such as molecular acids of lower toxicity, which can subsequently mineralize into inorganic compounds such as CO_2, H_2O, NH_4^+, and SO_4^{2-} ions.

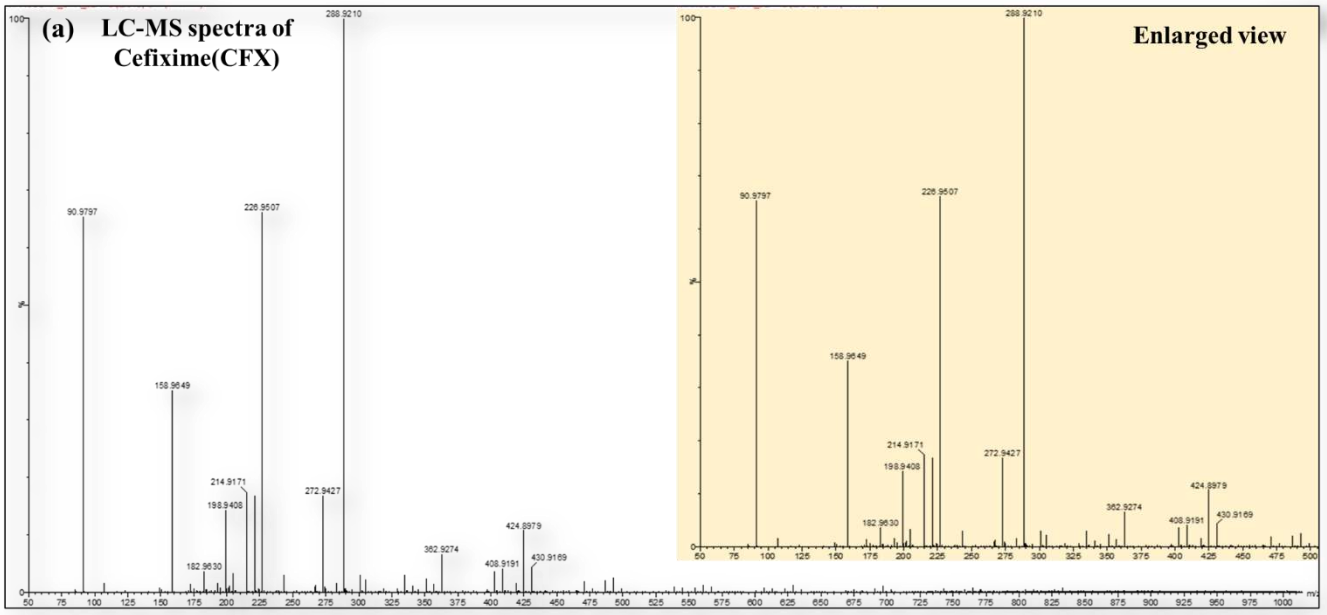

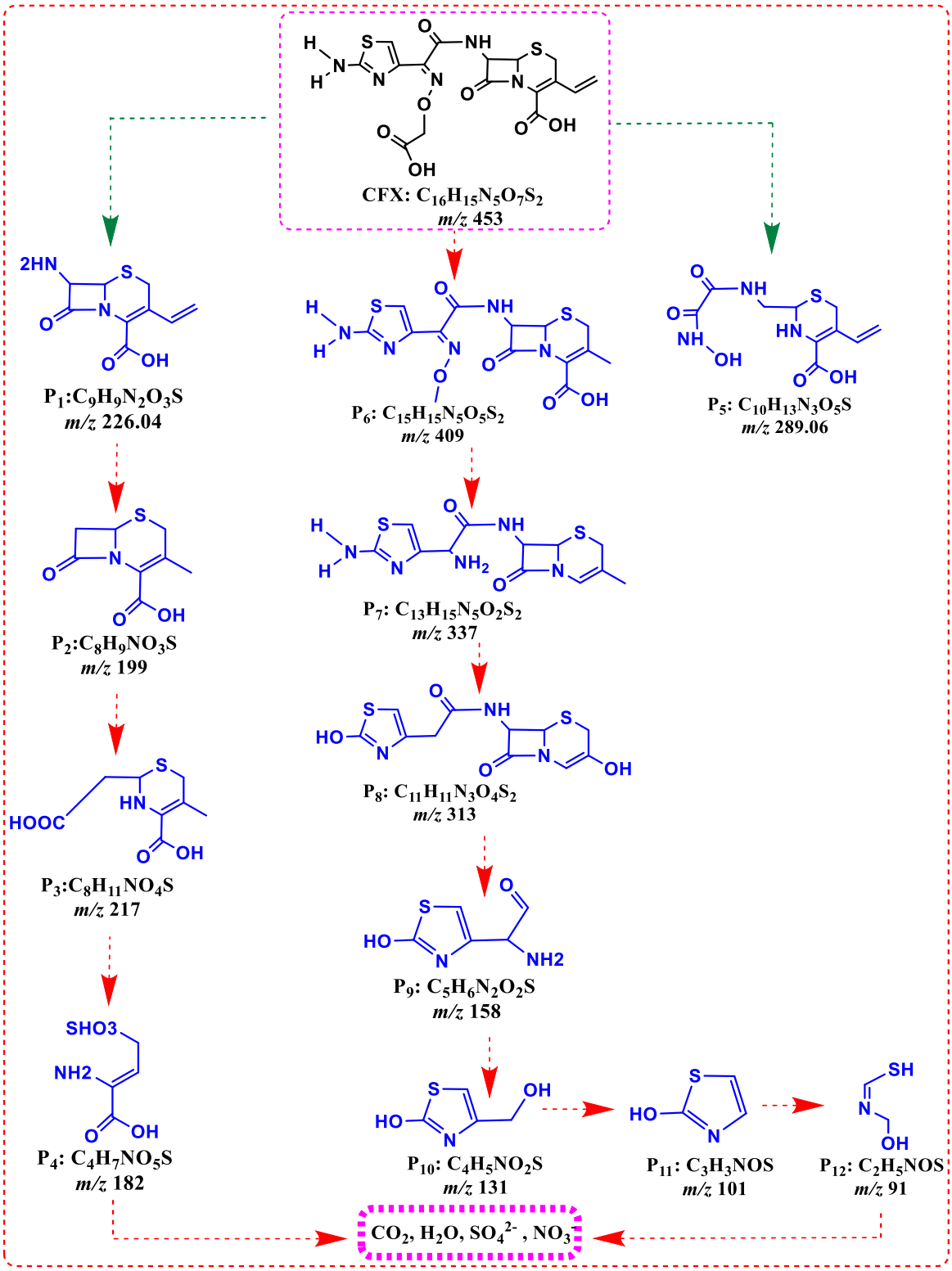

Fig.5.14(a): LC-MS chromatogram of the CFX intermediates **(b)** Proposed photocatalytic degradation pathways generated from CFX degradation using Cu-$CaTiO_3$-GO composite after 100 min of LED-light illumination.

5.4.6. Recyclability studies

In order to scrutinize the durability and reusable nature of the as-prepared ternary Cu-$CaTiO_3$-GO ternary photocatalyst for real-time applications, the recyclability experiments for degradation of CFX and H_2 production were carried out for 4 repetitive cycles by following the similar steps as mentioned in the experimental section. Each cycle was continued for 100 minutes. After every run, the catalyst was recovered from the suspension, washed with distilled water and ethanol, and finally kept for drying at 65°C for 2 hours in a vacuum before being utilized in the next cycle. It can be seen that after 4 successive reaction cycles, the degradation efficiency of the Cu-$CaTiO_3$-GO hybrid declined about 14.7%, however, the catalyst still exhibits 79.4% removal efficiency for CFX (**Fig.5.15(a**), demonstrating excellent reusability of the prepared composite. The observable drop in its removal efficiency (79.4% from 94.1%) could be due to the unavoidable loss of the catalyst during the retrieval process. It is also possible that, during the sequential cycles, a few untreated intermediates would have adhered to the catalyst's surface, blocking certain active pores and contributing to the decrease in its photocatalytic activity. Likewise, after four consecutive reaction cycles, the rate of H_2-evolution still stays at 52.51 $mmolh^{-1}$, which is slightly down by 8.97% from the first use. Formaldehyde, formic acid, and other byproducts of methanol oxidation may contribute to this loss by altering the solution's pH and decreasing the charge carriers' life.

Additionally, no significant changes in the locations and intensities of characteristic diffraction peaks could be seen in the XRD patterns of the ternary composite before and after the 4^{th} degradation cycle (**Fig.5.15(b)**, further validating the inactness of its crystal structure. This ratifies that the constructed Cu deposited $CaTiO_3$-GO composite possesses commendable stability, with acceptance for long-term repetitive applications such as environmental remediation and clean energy production.

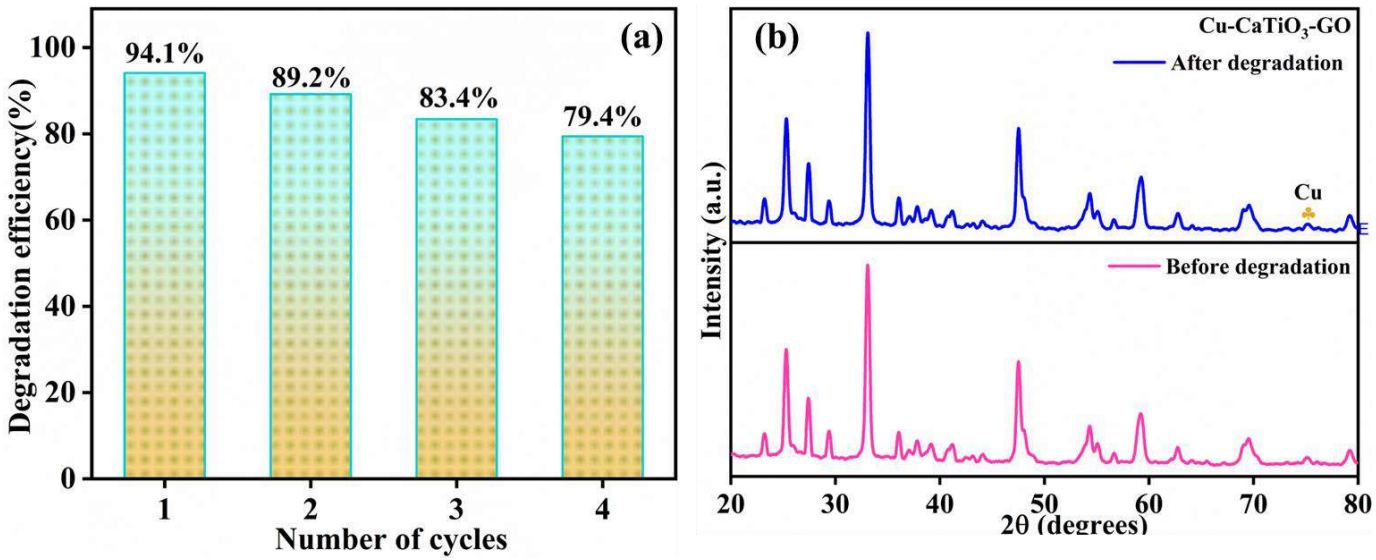

Fig.5.15. (a) Reusability studies, (b) XRD spectra, of Cu-$CaTiO_3$-GO composite before and after four cycles of CFX degradation

Conclusion

In this study, a new Cu-$CaTiO_3$-GO ternary composite was synthesized using hydrothermal and photo-deposition techniques. Characterization results confirmed the successful creation of the trio-hybrid with intimate contacts between the individual components. HR-TEM images validate the existence of cuboid shaped $CaTiO_3$ in close proximity with the GO sheets, and the buildup of tiny Cu nanodots on the surfaces of both. The smaller arc radius of the EIS Nyquist plots and substantially weaker PL intensity corroborate the efficient distance between the photogenerated charge carriers in this composite. Additionally, in comparison to pure $CaTiO_3$, a significant red shift was observed in the optical absorption edge, indicating its stronger visible light sensitivity. The effectiveness of the ternary composite was assessed under LED light via degradation of the antibiotic CFX and the generation of green energy (H_2). Compared to pristine $CaTiO_3$, and its binary ($CaTiO_3$-GO, and Cu-$CaTiO_3$) counterparts, the newly developed three-level system (Cu-$CaTiO_3$-GO) exhibited enormously high photocatalytic performance, with a H_2 generation rate of 57.6 mmolh-1 from a methanol-water mixture in 6 hours and an cefixime degradation rate of 94.1% in a short span of 100 min. This splendid enhancement in the photocatalytic performance of the Cu-$CaTiO_3$-GO composite could be accredited to the following merits: effective generation, migration, and partition of photoinduced e^--h^+ pairs, enlargement in light captivation because of the SPR effect of plasmonic Cu NPs, a lower bandgap, a larger specific surface area, the design of a unique three-level electron transfer system with beneficial morphology, along with strong synergy between the 3 components Cu, $CaTiO_3$, GO jointly

contributed to the drastic improvement. Additionally, this trio system showed stupendous structural and photocatalytic stability even after four cycles of its progressive use. The predominant role of •OH, and $O_2^{\bullet-}$ species in the degradation process was affirmed by scavenger studies. The mineralization degree of the CFX was gauged through TOC measurements. The photocatalytic degradation route was determined by LC-MS, proving that the ternary hybrid could decompose the CFX molecules into smaller, less hazardous compounds. Finally, based on the scavenger tests, and band energy calculations, a probable mechanism of dual functional photocatalysis with Cu-$CaTiO_3$-GO was also mapped out. In conclusion, this study offers a new thought for the design and synthesis of a noble-metal-free Cu-$CaTiO_3$-GO type versatile photocatalyst that can simultaneously produce hydrogen and purify wastewater, thereby providing both energy-saving and environmental restoration functionalities.

References

[1] Y. Zhu, Y. Cui, B. Xiao, J. Ou-yang, H. Li, Z. Chen, Materials Science in Semiconductor Processing 129 (2021) 105767.

[2] S. Escobedo, H. de Lasa, Catalysts 11 (2021).

[3] I. Tateishi, M. Furukawa, H. Katsumata, S. Kaneco, Catalysts 9 (2019).

[4] B. Ulejczyk, Ł. Nogal, P. Jóźwik, M. Młotek, K. Krawczyk, Catalysts 11 (2021).

[5] M.M. Elham Sadat Behineh a, Ali Reza Solaimany Nazar a, Mehrdad Farhadian a, Journal of Environmental Management 316 (2022) 115195.

[6] B. Erim, Z. Ciğeroğlu, M. Bayramoğlu, Journal of Molecular Structure 1234 (2021).

[7] J.F. c Yanyan Zhao a, Cuifen Ji b, Yuyu Wang a, Xuhua Liang a, Colloids and Surfaces A: Physicochemical and Engineering Aspects 635 (2022) 128024.

[8] A.A.A. c Oussama Baaloudj a, Noureddine Nasrallah a, Rachida Bouallouche a, Hamza Kenfoud a, Lotfi Khezami b, Journal of Cleaner Production 330 (2022) 129934.

[9] M. Passi, B. Pal, Powder Technology 388 (2021) 274–304.

[10] J. Han, Y. Liu, F. Dai, R. Zhao, L. Wang, Applied Surface Science 459 (2018) 520–526.

[11] Y. Yan, H. Yang, Z. Yi, R. Li, X. Wang, Micromachines 10 (2019) 1–16.

[12] A. Kumar, P. Choudhary, A. Kumar, P.H.C. Camargo, V. Krishnan, Small (2021).

[13] M. Passi, B. Pal, Korean Journal of Chemical Engineering 39 (2022) 942–953.

[14] Y.Z. Zhen, J. Wang, J. Li, M. Fu, F. Fu, Y.Z. Zhang, J.H. Feng, Journal of Materials Science: Materials

in Electronics 29 (2018) 3672–3681.

[15] D.N. Bui, J. Mu, L. Wang, S.Z. Kang, X. Li, Applied Surface Science 274 (2013) 328–333.

[16] S. Wan, M. Chen, M. Ou, Q. Zhong, Journal of CO2 Utilization 33 (2019) 357–364.

[17] K.H. Reddy, S. Martha, K.M. Parida, Nanoscale 10 (2018) 18540–18554.

[18] M.H. e Zhuogen Li a, Gangqiang Zhu a, Weibin Zhang b, Lujun Zhu a, Baowei Cao c, Jianzhi Gao a, Xianjin Shi d, Yu Huang d, Peng Liu a, Chemical Engineering Journal 452 (2023) 139378.

[19] J. Prakash, Photochem 2 (2022) 651–671.

[20] F. Khan, M.S. Khan, S. Kamal, M. Arshad, S.I. Ahmad, S.A.A. Nami, Journal of Materials Chemistry C 8 (2020) 15940–15955.

[21] R. He, S. Cao, D. Guo, B. Cheng, S. Wageh, A.A. Al-Ghamdi, J. Yu, Ceramics International 41 (2015) 3511–3517.

[22] H. Bantawal, M. Sethi, U.S. Shenoy, D.K. Bhat, ACS Applied Nano Materials 2 (2019) 6629–6636.

[23] X. Luo, C. Wang, L. Wang, F. Deng, S. Luo, X. Tu, C. Au, Chemical Engineering Journal 220 (2013) 98–106.

[24] M. Beaula Ruby Kamalam, S.S.R. Inbanathan, K. Sethuraman, A. Umar, H. Algadi, A.A. Ibrahim, Q.I. Rahman, C.S. Garoufalis, S. Baskoutas, Environmental Research 199 (2021) 111369.

[25] J. Chen, B. Yao, C. Li, G. Shi, Carbon 64 (2013) 225–229.

[26] X. Li, Journal of Chemistry 2018 (2018).

[27] A. Kumar, C. Schuerings, S. Kumar, A. Kumar, V. Krishnan, Beilstein Journal of Nanotechnology 9 (2018) 671–685.

[28] T. Ahmad, Material Science & Engineering International Journal 2 (2018).

[29] A. Kumar, S. Kumar, A. Bahuguna, A. Kumar, V. Sharma, V. Krishnan, Materials Chemistry Frontiers 1 (2017) 2391–2404.

[30] G. Dong, X. Xiao, L. Zhang, Z. Ma, X. Bao, M. Peng, Q. Zhang, J. Qiu, Journal of Materials Chemistry 21 (2011) 2194–2203.

[31] M. Passi, B. Pal, Separation and Purification Technology 308 (2023) 122839.

[32] Z. Zhang, Y. Ji, J. Li, Z. Zhong, F. Su, RSC Advances 5 (2015) 54364–54371.

[33] J. Pan, Z. Jiang, S. Feng, C. Zhao, Z. Dong, B. Wang, J. Wang, C. Song, Y. Zheng, C. Li, International Journal of Hydrogen Energy 43 (2018) 19019–19028.

[34] M. Chen, H. Wang, X. Chen, F. Wang, X. Qin, C. Zhang, H. He, Chemical Engineering Journal 390 (2020) 124481.

[35] G. Gao, D. Liu, S. Tang, C. Huang, M. He, Y. Guo, X. Sun, B. Gao, Scientific Reports 6 (2016) 1–8.

[36] Z. Huang, S. Zhao, Y. Yu, Chinese Journal of Catalysis 41 (2020) 1522–1534.

[37] X. Chen, L. Di, H. Yang, T. Xian, Journal of the Ceramic Society of Japan 127 (2019) 221–231.

[38] S. Kong, Z. An, W. Zhang, Z. An, M. Yuan, D. Chen, Nanomaterials 10 (2020) 1–19.

[39] J.S. Jang, P.H. Borse, J.S. Lee, K.T. Lim, O.S. Jung, E.D. Jeong, J.S. Bae, H.G. Kim, Bulletin of the Korean Chemical Society 32 (2011) 95–99.

[40] L.M. Pastrana-Martínez, S. Morales-Torres, S.K. Papageorgiou, F.K. Katsaros, G.E. Romanos, J.L. Figueiredo, J.L. Faria, P. Falaras, A.M.T. Silva, Applied Catalysis B: Environmental 142–143 (2013) 101–111.

[41] M. Asif, M. Saeed, M. Zafar, U. e. S. Amjad, A. Razzaq, W. Young Kim, Results in Physics 42 (2022) 105997.

[42] R.A. Rather, S. Singh, B. Pal, Journal of Nanoscience and Nanotechnology 17 (2017) 1210–1216.

[43] M. Murugalakshmi, G. Mamba, V. Muthuraj, Applied Surface Science 527 (2020) 146890.

[44] M.L. Moreira, E.C. Paris, G.S. do Nascimento, V.M. Longo, J.R. Sambrano, V.R. Mastelaro, M.I.B. Bernardi, J. Andrés, J.A. Varela, E. Longo, Acta Materialia 57 (2009) 5174–5185.

[45] H.R. Ali, E.A. Motawea, ACS Omega 6 (2021) 22047–22064.

[46] A. Bouddouch, B. Akhsassi, E. Amaterz, B. Bakiz, A. Taoufyq, S. Villain, F. Guinneton, A. El Aamrani, J.R. Gavarri, A. Benlhachemi, Catalysts 12 (2022).

[47] H.R.S. Maryam Salimi a b, Ali Esrafili a b, Ahmad Jonidi Jafari a b, Mitra Gholami a b, Inorganic Chemistry Communications 111 (2020) 107565.

[48] X. Yan, X. Huang, Y. Fang, Y. Min, Z. Wu, W. Li, J. Yuan, L. Tan, International Journal of Electrochemical Science 9 (2014) 5155–5163.

[49] W. Hao, L. Zhao, X. Li, L. Qin, S. Han, S.Z. Kang, International Journal of Hydrogen Energy 46 (2021) 6461–6473.

[50] G.Y. Yao, Z.Y. Zhao, Q.L. Liu, X.D. Dong, Q.M. Zhao, Solar Energy Materials and Solar Cells 208 (2020) 110385.

[51] L. Clarizia, G. Vitiello, G. Luciani, I. Di Somma, R. Andreozzi, R. Marotta, Applied Catalysis A: General 518 (2016) 142–149.

[52] T. Xian, H. Yang, Y.S. Huo, Physica Scripta 89 (2014).

[53] V. Lalan, V.P. Mahadevan Pillai, K.G. Gopchandran, Journal of Science: Advanced Materials and Devices 7 (2022) 100468.

[54] G. Wang, W. Guo, D. Xu, D. Liu, M. Qin, Symmetry 12 (2020).

[55] B. Tan, Y. Fang, Q. Chen, X. Ao, Y. Cao, Optical Materials 109 (2020) 110470.

[56] K. Kočí, M. Reli, M. Edelmannová, I. Troppová, H. Drobná, A. Rokicińska, P. Kuśtrowski, D. Dvoranová, L. Čapek, Journal of Photochemistry and Photobiology A: Chemistry 366 (2018) 55–64.

[57] V.T. Gawande, K.G. Bothara, C.O. Satija, Acta Chromatographica 30 (2018) 212–218.

[58] T. Zhang, R. Zhou, P. Wang, A. Mai-Prochnow, R. McConchie, W. Li, R. Zhou, E.W. Thompson, K. (Ken) Ostrikov, P.J. Cullen, Chemical Engineering Journal 421 (2021) 127730.

[59] N. Das, J. Madhavan, A. Selvi, D. Das, 3 Biotech 9 (2019) 1–14.

[60] K. Hasani, A. Peyghami, A. Moharrami, M. Vosoughi, A. Dargahi, Arabian Journal of Chemistry 13 (2020) 6122–6139.

Conclusion and Future Outlook

Semiconducting perovskite oxides such as metal titanates ($ATiO_3$, A = C, Ba, and Sr) have attracted significant interest from researchers as potential photocatalytic materials. Yet, their fully-fledged efficiency has been hampered by issues such as a poor response to visible light, quick recombination of photoinduced charge carriers, and a small surface area with a few reaction-active sites. The core focus of this thesis is to synthesize visible light-active perovskite based ($ATiO_3$ = Ca, Ba, and Sr) titanates with efficient e^--h^+ pair separation for photocatalysis using the synergic influence of metal (plasmonic/transition) and graphene oxide (carbonaceous material) on them. The developed nanocomposites, such as Ag/Cu-$CaTiO_3$, Ag-$BaTiO_3$/GO, Fe(III)-$SrTiO_3$-GO, and Cu-$CaTiO_3$-GO, have been found to exhibit improved photocatalytic performance than their individual counterparts (pure titanates and their binary composites) for the photodegradation of several toxic pharmaceutical pollutants and textile dyes. In addition, the Cu-$CaTiO_3$-GO catalyst performed well in tests evaluating its potential for use in the generation of renewable energy (H_2). The enhancement in the photocatalytic properties is credited to the construction of a three-level electron transfer system that features (i) suitable morphologies (nanorod, nano-cube, cuboid), (ii) increased specific surface areas due to the incorporation of GO, resulting in an abundance of photocatalytic active sites (iii) accelerated separation and transport of photoexcited charge carriers across the interface contacts of metal (M), $ATiO_3$, and GO, and (iv) an expanded light absorption range due to surface-deposited metals. Based on the research work, it is anticipated that these modified metal titanates with promising photocatalytic activity and the advantage of perovskite stability can be further investigated in other scientific fields such as sensing, fuel cells, batteries, bacterial disinfection, carbon dioxide (CO_2) reduction, nitrogen oxide (NOx) conversion, hydrogen (H_2) generation from biomass or water splitting, and many more. In extension to this, it is proposed that the strategy of promoting the photocatalysis activity via the combined effect of M and GO can be expanded for the modification of other perovskites oxide such as titanates belonging to the transition metal series ($ATiO_3$, A = Fe, Co, Ni, Mn etc.)

List of Publications

1.1. Related to PhD work (Objectives)

I. **Manjusha Passi** and Bonamali Pal, "Influence of Ag/Cu photodeposition on $CaTiO_3$ activity for degradation of Rhodamine B dye." ***Korean Journal of Chemical Engineering,*** **39, (2022), 942-953. (I.F = 3.30).**

II. **Manjusha Passi** and Bonamali Pal, "Design of a novel Ag-$BaTiO_3$/GO ternary nanocomposite with enhanced visible-light driven photocatalytic performance towards mitigation of carcinogenic organic pollutants." ***Separation and Purification Technology,*** **308, (2023), 122839. (I.F.= 8.6).**

III. **Manjusha Passi** and Bonamali Pal, "A novel ternary Fe(III)-$SrTiO_3$-GO nanocomposite for LED-light-driven photocatalytic degradation of norfloxacin antibiotic: Performance, mineralization ability, degradation pathway, and mechanistic insight." ***Chemical Engineering Journal,*** **479, 147685, (2023). (I.F = 15.1)**

IV. **Manjusha Passi** and Bonamali Pal, "Synthesis and application of Cu-$CaTiO_3$-GO ternary composite: A new visible-light active multifunctional photocatalyst efficient towards antibiotic cefixime degradation and H_2 evolution reaction." ***Applied Materials Today,*** ***(I.F = 8.3).*** **(Under review)**

1.2. Review articles

I. **Manjusha Passi** and Bonamali Pal, "A review on $CaTiO_3$ photocatalyst: Activity enhancement methods and photocatalytic applications." ***Powder Technology,*** **388, (2021), 274-304. (I.F = 5.2).**

II. **Manjusha Passi** and Bonamali Pal, "Recent advances on visible light active non-typical stoichiometric oxygen-rich $Bi_{12}O_{17}Cl_2$ photocatalyst for environment pollution remediation, ***Journal of Environmental Chemical Engineering,*** **10, (2022), 107688. (I.F = 7.7).**

Conferences and Workshops

I. International **Webinar** on "An Overview of Semiconductor-Lab to Fab, organized by Surana College, Bangalore, on 18th August, 2023.

II. Volunteered in **SCI-FEST 2023**, held at Thapar Institute of Engineering and Technology, Patiala, on 18th March, 2023.

III. Volunteered and participated in 7 days, Hands on training program on insights into the applications of high-end instruments in chemical sciences, under the **DST-STUTI** scheme held at Thapar Institute of Engineering and Technology, Patiala. 21th-27th February, 2023.

IV. Attended short term course on Chemistry of advanced functional materials **(CAFM-2020)**, organized by NIT, Srinagar. 21th-25th September, 2020.

V. 12th National conference on chemical and environmental sciences: advanced innnovations-2020 **(CESAI-2020),** held at Punjabi University, Patiala. 19th-20th February, 2020.

VI. ***Poster presentation on the topic***, "Surface modification of $CaTiO_3$ perovskite with Ag/Cu nanoparticles for environmental application". International conference on emerging trends in science and technology, **(ICETST-2022)**, organized by Punjab Engineering College, Chandigarh. 10th-11th June, 2022.

VII. ***Oral presentation on the topic,*** "Fabrication of a novel Ag-BaTiO3/GO ternary photocatalyst for boosting pollutants degradation under visible light." Ist International conference on recent advances in chemistry-2023, **(CRAC-2023),** held at Punjabi University, Patiala. 23th-24th February, 2023.

Korean J. Chem. Eng., 39(4), 942-953 (2022)
DOI: 10.1007/s11814-021-0975-1

pISSN: 0256-1115
eISSN: 1975-7220

Influence of Ag/Cu photodeposition on $CaTiO_3$ photocatalytic activity for degradation of Rhodamine B dye

Manjusha Passi and Bonamali Pal†

School of Chemistry and Biochemistry, Thapar Institute of Engineering & Technology, Patiala-147004, Punjab, India
(*Received 22 July 2021 • Revised 30 September 2021 • Accepted 5 October 2021*)

Abstract–The present work outlines a simple sol-gel method for the synthesis of $CaTiO_3$ (CTO) nanoparticles followed by modification with Ag, Cu via photodeposition. Different amounts (1 to 5 wt%) of Ag and Cu were loaded over CTO to form Ag/Cu-CTO nanocomposites. Several characterization techniques, such as XRD, UV-DRS, SEM, EDS, HRTEM and photoluminesence, were employed to study their structural and physicochemical properties. The photocatalytic performance of as-prepared samples was assessed by degrading Rhodamine B dye under UV irradiation. Results indicate that Ag/Cu deposition significantly enhanced the photocatalytic activity of CTO, depending upon the amount of metal loading. It found that 1 wt% Ag-CTO composite exhibited the highest (98%) photoactivity within 90 mins in contrast to 82% and 57% degradation achieved by 1 wt% Cu-CTO and bare CTO, respectively. The degradation process followed pseudo-first-order kinetics with rate constants of $k=4.5\times10^{-2}$ min^{-1} for Ag-CTO relative to $k=1.8\times10^{-2}$ min^{-1} of Cu-CTO and $k=0.86\times10^{-2}$ min^{-1} of bare. The improved photocatalytic activity was credited to the increased optical absorption and quick transfer of photoinduced electrons from $CaTiO_3$ conduction band to Ag and Cu deposits that probably retards the charge-carriers recombination as evident by their observed photoluminance behavior.

Keywords: Ag/Cu-$CaTiO_3$ Nanocomposites, Ag/Cu Cocatalysis, Photoactivity of Perovskite Nanostructures, RhB Degradation by Metal Loaded $CaTiO_3$, Calcium Titanate Photocatalysis, Ag and Cu Photodeposited $CaTiO_3$

INTRODUCTION

Global environmental problems have become more of more concern due to severe pollution, especially reacalcitrant toxic organic pollutants. For its effectiveness, simplicity, and environmentally-friendly nature, semiconductor-based photocatalysis, one of the advanced oxidation technologies, has been regarded as the most appealing method in treating waste water. It basically involves absorption of photons with energy equal to or higher than the band gap of the semiconductor to produce electron-hole pairs which then react with the oxygen and hydroxyl ions to generate active radicals that can degrade the water contaminants readily and quickly [1,2]. In this regard, a variety of semiconductor systems and their composites have been extensively developed and studied so far. Among the large assemblage of catalytic materials explored to date, perovskite oxides of the form ABO_3 are gaining huge attention because of their immense potential in diverse applications [3-5]. Owing to their remarkable physicochemical and optoelectronic properties, such as structural flexibility, electron-mobility, band gap tunability, low-cost fabrication, high thermal and photocorrosion stability, enormous efforts have been made on utilizing perovskite oxides as photocatalysts [6-8]. Recently, Calcium titanate ($CaTiO_3$), a typical titanium-containing oxide semiconductor with a perovskite-type structure has been examined in various fields including energy conversion [9-12], environmental remediation [13-15] and industrial processes [16,17]. Its unique perovskite structure offers a large platform for designing new and efficient photocatalytic materials by alteration at its A, B and O sites [18]. In addition, this n-type semiconductor even possesses conduction band potential value more negative than the benchmark photocatalyst TiO_2, making it a good substitute for the industrial catalyst TiO_2 [19,20].

Although $CaTiO_3$ is a highly photoactive material, however because of its wide bandgap and low quantum efficiency, its overall photocatalytic performance is restricted. Several factors are of relevance, but majorly two are important: ultrafast recombination of photoexcited electron-hole pairs and the limit of optical response only to UV-light [21]. Thus, the two most crucial points for achieving the high photocatalytic performance of $CaTiO_3$ are necessity to efficiently separate the photogenerated charge carriers and to expand its absorption range to the visible region. Up to now, many attempts have been made for its modification, including elemental doping [22-24], metal deposition [25,26], surface functionalization [27], heterojunction formation [28-30], and coupling with carbon materials [31-33]. Among these, depositing metal nanoparticles on semiconductors has been an important strategy to overcome these shortcomings. Generally, metal deposition on semiconductors is known to form a metal-semiconductor (M-SC) interface or Schottky barrier that furnishes an effective pathway for capturing, storing and discharging of photogenerated electrons. The contact metal actually serves as an electron trap. The Schottky barrier created at the interface permits the flow of electrons from the semiconductor to the deposited metal till the equilibration of Fermi levels. This process is influenced by nature, electronegativity, reduction potential and Fermi energy/work function of the metal [34]. Metals with

†To whom correspondence should be addressed.
E-mail: bpal@thapar.edu
Copyright by The Korean Institute of Chemical Engineers.

Separation and Purification Technology 308 (2023) 122839

Contents lists available at ScienceDirect

Separation and Purification Technology

journal homepage: www.elsevier.com/locate/seppur

Design of a novel Ag-$BaTiO_3$/GO ternary nanocomposite with enhanced visible-light driven photocatalytic performance towards mitigation of carcinogenic organic pollutants

Manjusha Passi, Bonamali Pal *

School of Chemistry and Biochemistry, Thapar Institute of Engineering & Technology, Patiala 147004, Punjab, India

ARTICLE INFO

Keywords:
$BaTiO_3$
Crystal violet
Ofloxacin
Photocatalytic degradation
Ag-$BaTiO_3$/GO
Ternary composites

ABSTRACT

Herein, a novel visible-light responsive, photocatalyst (Ag-$BaTiO_3$/GO) was fabricated by depositing Ag nanoparticles and GO sheets onto the surface of $BaTiO_3$ nanorods via a combination of photodeposition and hydrothermal methods.The as-prepared ternary photocatalyst was comprehensively characterized for its structural, morphological, and optical properties using XRD, XPS, Raman, HR-TEM, FE-SEM, EDS-mapping, BET, EIS,UV–vis DRS, and PL analysis. The photoactivity was assessed by degrading crystal violet dye (CV) and antibiotic ofloxacin (OFL) under visible light illumination. In comparison with pristine $BaTiO_3$, and binary composites Ag-$BaTiO_3$, $BaTiO_3$-GO, the newly designed ternary hybrid exhibited superior activity with ~ 98.5% and 96.1% degradation efficiency for CV and OFL at high rate constants (0.053 and 0.033 min^{-1}, respectively). The heightened photocatalytic performance is attributed to the SPR effect of Ag, which broadens the visible light range, as well as strong adsorption capacity, excellent electron mobility, and greater surface area of GO that facilitates the charge transfer process. Moreover, the catalyst could be easily reused for four sequential cycles, maintaining up to 78.83% efficiency for CV removal. Trapping experiments disclosed the eloquent role played by the (hydroxyl) $^{\bullet}OH$ and $O_2^{\bullet-}$ (superoxide) radicals in pollutant degradation. Also, the degradation pathways of CV and OFL were determined based on the LC–MS analysis. TOC test was conducted. Eventually, on account of the results, a photocatalytic reaction mechanism was presumed. This work offers a propitious strategy, for successful eradication of multiple perilous pollutants from wastewater using a combination of metal titanates, plasmonic Ag nanoparticles, and GO based highly efficient ternary photocatalyst.

1. Introduction

The relentless expansion of industrialization and urbanization has exacerbated some of the world's most pressing issues, such as the energy crisis and environmental pollution. Particularly, the accumulation of hazardous contaminants (lethal dyes, pharmaceutical drugs etc.) in natural water bodies is a major threat to human beings as well as the aquatic life [1–3]. Crystal violet (CV), a well-known synthetic cationic dye belonging to the triphenylmethane group, is extensively utilised in a variety of ways, including biological staining, veterinary medicine, dermatological agents, bacteriostatic agents, and as an poultry feed additive etc. This recalcitrant dye enters the aquatic systems through the effluents of the textile and paint industries, as well as the medical and biotechnology industries. Because of its mutagenic, teratogenic, carcinogenic, and mitotic poisoning properties, it has a considerable deleterious impact on flora and fauna [4,5]. Similarly, antibiotics, which account for a large proportion of pharmaceutical and personal care products are another common emerging organic micropollutant. Dumping of pharmaceutical industrial effluents into water streams and improper disposal of tonnes of unwanted medications into the environment are two of the pathways through which these contaminants predominate in our water resources [6]. For instance, Ofloxacin (OFL),

Abbreviations: FESEM, Field emission scanning electron microscopy; HRTEM, High-resolution transmission electron microscope; EDX, Energy dispersive X-ray; XPS, X-ray photoelectron spectroscopy; DRS, Diffuse reflectance spectrophotometer; BJH, Barrett–Joyner–Halenda; LC-MS, Liquid chromatography-mass spectrometry; BET, Brunauer-Emmett-Teller; CB, Conduction band; VB, Valence band; AA, Ascorbic acid; IPA, Isopropyl alcohol; EDTA, Ethylenediaminetetraacetic acid; $O_2^{\bullet-}$, Superoxide anion radical; $^{\bullet}OH$, Hydroxyl radical; H_2, Hydrogen; NPs, Nanoparticles; MO, Methyl orange; RhB, Rhodamine B; MB, Methylene blue; NCs, Nanocuboids.

* Corresponding author.
E-mail address: bpal@thapar.edu (B. Pal).

https://doi.org/10.1016/j.seppur.2022.122839
Received 12 October 2022; Received in revised form 26 November 2022; Accepted 30 November 2022
Available online 5 December 2022
1383-5866/© 2022 Elsevier B.V. All rights reserved.

Chemical Engineering Journal 479 (2024) 147685

Contents lists available at ScienceDirect

Chemical Engineering Journal

journal homepage: www.elsevier.com/locate/cej

A novel ternary Fe(III)-$SrTiO_3$-GO nanocomposite for LED-light-driven photocatalytic degradation of norfloxacin antibiotic: Performance, mineralization ability, degradation pathway, and mechanistic insight

Manjusha Passi, Bonamali Pal *

School of Chemistry and Biochemistry, Thapar Institute of Engineering & Technology, Patiala 147004, Punjab, India

ARTICLE INFO

Keywords:
$SrTiO_3$
Norfloxacin
Interfacial charge transfer effect (IFCT)
Photocatalytic degradation
Fe-$SrTiO_3$-GO
Ternary composites

ABSTRACT

The widespread production and use of pharmaceutical antibiotics is wreaking havoc on the environment. To address this issue, a semiconductor photocatalyst with high photocatalytic efficiency must be developed in order to eliminate antibiotics from wastewater. Herein, an efficient ternary photocatalyst (Fe(III)-$SrTiO_3$-GO) was synthesized by anchoring Fe(III) species and GO sheets over the surface of $SrTiO_3$ nanocubes. The optimized (2Fe (III)-$SrTiO_3$-10GO) nanocomposite displayed superior photoactivity by degrading 92.3 % of NOF within 120 min of LED light exposure in contrast with pristine $SrTiO_3$ (33.6 %) and binary composites ($SrTiO_3$-10GO) (68.5%), (2Fe(III)-$SrTiO_3$) (79.2%). The meliorative performance is credited to synergic effects of GO (with high conductivity), $SrTiO_3$ (specialized morphology) and Fe(III) species (IFCT effect) all together in the trio-hybrid that accelerated the transference and separation of photoinduced carriers, and extends the visible-light responsive range. (h^+), ($^{\cdot}OH$) were the predominant reactive species liable for the degradation process. Further, the plausible photocatalytic mechanism and degradation pathways of NOF were speculated with several intermediates identified. The current study provide a new perspective on construction of innovative, reusable and cost-effective photocatalyst based on transition metal ion and GO co-catalyzed metal titanates for wastewater remediation.

1. Introduction

For more than 50 years, antibiotics have been used as an elixir to safeguard human beings and animals from a wide range of pathogens, and in recent years, both their production and consumption have escalated. Antibiotic persistence in water sources is a global concern due to their adverse environmental impacts and potential harm to aquatic life. As a result, these are now recognized as emerging pollutants. Pharmaceutical industries, municipal wastewater, hospital wastewater, and sewage treatment plants are the main sources of their presence in aquatic environments [1,2]. Norfloxacin (NOF), a second-generation synthetic fluoroquinolone (FQ) antibiotic, has been used in human (respiratory, bacterial infections) and veterinary medicine, livestock farming and aquaculture, due to its broad antimicrobial activity [3]. Due to the stability of the quinolone backbone, low metabolic rate and incomplete biodegradability, only partial removal of these antibiotics is accomplished in conventional wastewater treatment plants and significant quantities are deliberately released into the environment in their pharmacologically active forms [4]. Since, NOF is highly mutagenic, teratogenic, and embryotoxic, even trace amounts of its residues and derivatives can eutrophize ecosystems and contaminate food and drinking water sources. By inhibiting DNA replication and inducing antibiotic resistance in bacteria, it may irreparably harm the water bodies [5,6]. Therefore, for its eradication, viable technologies are required. Semiconductor-mediated photocatalysis has received considerable attention as an effectual water treatment method, owing to its incomparable superiority in terms of environment friendliness, sustainability, affordability, high efficiency, and stability [7,8]. In general,

Abbreviations: NOF, Norfloxacin; SC, Semiconductor; CB, Conduction band; VB, Valence band; IFCT, Interfacial charge transfer; VLA, Visible-light active; (e^-), Electron; (h^+), Hole; AA a, scorbic acid; IPA, Isopropyl alcohol; EDTA, Ethylenediaminetetraacetic acid; NC, Nanocube; DI, Distilled; FESEM, Field emission scanning electron microscopy; HRTEM, High-resolution transmission electron microscope; EDX, Energy dispersive X-ray; XPS, X-ray photoelectron spectroscopy; DRS, Diffuse reflectance spectrophotometer; BJH, Barrett–Joyner–Halenda; LC-MS, Liquid chromatography-mass spectrometry; BET, Brunauer-Emmett-Teller; TOC, Total organic carbon; B.E's, Binding energies; $O_2^{\cdot-}$, Superoxide anion radical; $^{\cdot}OH$, Hydroxyl radical; H_2O_2, Hydrogen peroxide.

* Corresponding author.
E-mail address: bpal@thapar.edu (B. Pal).

https://doi.org/10.1016/j.cej.2023.147685
Received 9 September 2023; Received in revised form 4 November 2023; Accepted 25 November 2023
Available online 27 November 2023
1385-8947/© 2023 Elsevier B.V. All rights reserved.

Powder Technology 388 (2021) 274–304

Contents lists available at ScienceDirect

Powder Technology

journal homepage: www.elsevier.com/locate/powtec

Review

A review on $CaTiO_3$ photocatalyst: Activity enhancement methods and photocatalytic applications

Manjusha Passi, Bonamali Pal *

School of Chemistry and Biochemistry, Thapar Institute of Engineering & Technology, Patiala 147004, Punjab, India

ARTICLE INFO

Article history:
Received 12 January 2021
Received in revised form 14 April 2021
Accepted 20 April 2021
Available online 28 April 2021

Keywords:
$CaTiO_3$ photocatalyst
Titanate
Modification strategies
Hydrogen production
Carbon-dioxide reduction
Pollutant degradation

ABSTRACT

Calcium titanate ($CaTiO_3$) a multi-metal oxide has received extensive attention in recent years, due to its unique structural features, high chemical stability, optimum band edge positions, strong catalytic activity, inexpensiveness, low toxicity and easy synthesis. The current review summarizes various synthesis methods that have been carried out for the preparation of $CaTiO_3$ nanomaterials, their structural properties, their modification strategies including elemental doping, noble metal deposition, heterostructure formation, hybridization with carbonaceous materials like graphene, graphitic-carbon nitride and photocatalytic applications related to environmental and energy fields such as photodegradation of organic pollutants, carbon-dioxide reduction, and production of green currency of energy (hydrogen). Besides, efforts are also made to provide a perspective for future research. Overall this review aims to provide useful information for specialists dealings with calcium titanate.

© 2021 Elsevier B.V. All rights reserved.

Contents

* Corresponding author.
E-mail address: bpal@thapar.edu (B. Pal).

https://doi.org/10.1016/j.powtec.2021.04.056
0032-5910/© 2021 Elsevier B.V. All rights reserved.

Journal of Environmental Chemical Engineering 10 (2022) 107688

Contents lists available at ScienceDirect

Journal of Environmental Chemical Engineering

journal homepage: www.elsevier.com/locate/jece

Recent advances on visible light active non-typical stoichiometric oxygen-rich $Bi_{12}O_{17}Cl_2$ photocatalyst for environment pollution remediation

Manjusha Passi, Bonamali Pal *

School of Chemistry and Biochemistry, Thapar Institute of Engineering & Technology, Patiala 147004, Punjab, India

ARTICLE INFO

Editor: Teik Thye Lim

Keywords:
$Bi_{12}O_{17}Cl_2$
Visible-light active
Photocatalyst
Environment-remediation
Pollutant degradation
Layered materials

ABSTRACT

As a fascinating visible-light active material, $Bi_{12}O_{17}Cl_2$ has become a new research hotspot in the arena of semiconductor photocatalysis and drawn broad interdisciplinary attention as highly potent catalysts for solar energy conversion and environmental protection. The uniqueness of these layered bismuth-based oxides materials are their potential to harness energy in the visible range, their relative ease of synthesis, cost-effectiveness, great chemical stability, high photoactivity, strong adsorptivity, biologically inert nature, less toxicity, appropriate flat band potential, narrow band gap and environmentally benign. However, the quick reconcilation of the photoproduced charge carrier is a persistent bottleneck in this material. This issue generally manifests in the form of reduced lifetime of photoexcited e^--h^+ decreasing the quantum efficiency of diverse light-driven applications. In current years, an enormous research interest is devoted in fabricating $Bi_{12}O_{17}Cl_2$ based robust photocatalysts. This review summarizes the diverse strategies such as morphology control, growth mechanism, metal/non-metal doping, decoration with plasmonic metals, heterojunction/composite formation, the creation of oxygen vacancies etc adopted for improving photocatalytic performance of $Bi_{12}O_{17}Cl_2$. Besides this, relevant achievements of pristine and $Bi_{12}O_{17}Cl_2$-based photocatalysts on the removal of harmful emerging environmental pollutants such as dyes, pesticides, personal care-products, heavy metal ions, pharmaceutical waste, bacteria, gaseous pollutants etc have been discussed in detail. Moreover, efforts are also made to provide a perspective for future research. It is hoped that this review will offer vision by providing some valuable guidance for designing $Bi_{12}O_{17}Cl_2$ as a cocatalyst to fabricate more effective photocatalysts for practical application in environmental pollution management.

1. Introduction

In the past decades, with the acceleration of the human population and rapid development of urbanization and industrialization, environmental contamination has now emerged as a global issue of serious concern. Especially, the unconscionable discharge of wastewater into the natural water bodies poses a significant risk to human health and ecological environment because of their persistence and toxicity. A wide range of industries and chemical factories releases several kinds of toxic and carcinogenic organic pollutants such as dyes, pharmaceuticals (eg, antibiotis, analgesics), personal care products (eg. Hair dyes, Shampoos), heavy metals, phenols, fertilizers, benzene compounds, and halogenated hydrocarbon and so on directly into the rivers without even addressing adequately. This untreated water directly or indirectly relates to the environment pollution [1–4]. To sustain a clean and safe environment and improve the water quality, water pollution issues must be solved urgently. To date, many researchers have attempted to eradicate the wastewater laden with several toxic substances using conventional techniques such as physical adsorption, chemical reactions and biological degradation approaches. However, in spite of some success in the elimination of contaminants from water, several limitations of the conventional strategies such as the undesired generation of secondary

Abbreviations: BPA, Bisphenol A; RhB, Rhodamine B; MO, Methyl orange; CIP, Ciprofloxacin; TC, Tetracycline; MB, Methylene blue; 2,4-DCP, 2,4-dichlorophenol; 4-CP, p-chlorophenol or 4-chlorophenol; SMZ, Sulfamethazine; MBT, 2-mercaptobenzothiazole; CrVI, Hexavalent chromium; $^{\bullet}OH$, Hydroxyl radical; O_2, Oxygen; H_2O, Water; $O_2^{\bullet-}$, Superoxide radical anion; DFT, Density functional theory.

* Corresponding author.
E-mail address: bpal@thapar.edu (B. Pal).

https://doi.org/10.1016/j.jece.2022.107688
Received 26 December 2021; Received in revised form 2 March 2022; Accepted 6 April 2022
Available online 16 April 2022
2213-3437/© 2022 Elsevier Ltd. All rights reserved.